Evaluation and Optimisation of Tubular Receivers with Varied Tube Configuration, Working Fluid and Tube Material

A thesis submitted for the degree of
Doctor of Philosophy of
The Australian National University
by

Meige Zheng

Supervisory Panel

Associate Professor John Pye	Primary Supervisor and Chair
Associate Professor Joseph Coventry	Associate Supervisor

March 2023

© Copyright by Meige Zheng 2023
All Rights Reserved

Except where otherwise indicated, this thesis is my own original work.

Meige Zheng
13 March 2023

Acknowledgments

First and foremost, I would like to express my most sincere appreciation for my primary supervisor, Assoc. Prof. John Pye, and my associate supervisor, Assoc. Prof. Joe Coventry. Their thorough guidance, patience, and generous sharing of their knowledge and experience helped me achieve my milestones.

Secondly, I would like to thank all of my colleagues from the Solar Thermal Group for working with them, which benefited me greatly. Undergoing research with such a renowned group not only developed my interpersonal skills but also broadened my view of solar energy and enabled me to build a solid foundation for my future aspiration.

In addition, I would like to acknowledge the committee of the College of Engineering and Computer Science at the Australian National University for diligently supporting me throughout the spectrum of this significant four-year period. I am also thankful to all school staff who assisted me during the program and created a pleasant working environment on daily basis.

Funding support for this thesis by the Australian Renewable Energy Agency (ARENA), under contract 2014/RND010, is gratefully acknowledged.

Furthermore, I would like to thank my friends outside of work and at the gym for always believing in me. With their support, I have grown faith in myself to progress on my journey without fear. I would not have my accomplishments today without their care and encouragement.

Last but not least, I would like to extend my gratitude to my parents: Baodong Zheng and Yufan Yang. They have given me full support since 6 July 2007 – the day I embarked on the academic journey abroad. They always respected my decisions, whether it is to study in Singapore or Australia, or to pursue postgraduate studies or job hunting, from one thing to the next...

I have been going over these acknowledgements in my mind often lately. I want to compose something eloquent to express my gratitude appropriately, but it does not appear to be enough words here simply because there are truly no words that can adequately voice my heart.

I LOVE YOU! ♡

Abstract

Central tower concentrating solar power (CSP) systems typically focus solar radiation upon a tubular receiver where radiation is absorbed and then transferred, by conduction and convection, into a heat transfer fluid (HTF). High-temperature receivers are critical for third-generation (Gen3) CSP technology to achiever high system efficiencies, and play the role of converting concentrated sunlight into heat. Despite extensive literature on alternative receiver designs, there have been limited efforts to compare optimised receivers with different designs and working fluids using a consistent analysis technique, which leads to a question that there has not been consensus on what the best fluid is for the central receivers. This thesis aims to examine what the optimal receiver design would look like, from the receiver thermal performance point of view. The theme of this thesis is a unified comparison on different working fluids and different tube materials, using one single rigorous model with unified model assumptions, to explore if an optimal receiver performance is caused by the intrinsic benefits of a particular working fluid or the artifact of a particular approach.

First of all, the analysis of tubular receivers for concentrating solar tower systems with a range of working fluids (i.e. molten salt, liquid sodium, air, sCO_2 and water/steam), in exergy-optimised flow-path configurations is conducted. The effects of varying the tube diameter, and tube wall thickness are studied. Results show that liquid sodium performs the best.

The performance of the receiver is strongly constrained by material limits which in turn limit the allowable flux on the receiver. So next, the study seeks to understand the benefits which arise at the receiver as a result of adjusting the flux profile, comparing a simple Gaussian 'spot' with a linear 'ramp' pattern, while respecting an upper limit on the allowable film temperature of the molten salt working fluid.

A novel receiver design concept is capable of improving the efficiency of the receiver by adding a series of horizontal tube banks (aka blades), when compared to a conventional flat receiver. Under a 'virtual experimental' approach, both optimised receivers are designed, built and tested (at CSIRO, Australia). The bladed receiver shows a promising technique performance, in relation to the flux limit remission and the light-trapping enhancement, when compared to the flat receiver. Optimised design models are then reconciled with experimental data, studies show that models are consistent with the earlier experimental results, even though a few discrepancies exist in the temperature- and the pressure-matching due to limited experimental data.

The relationships between material costs, receiver efficiency, and system level design, for a range of working fluids are conducted and developed under a unified analysis, so that a globally optimal choice can be made. The approach of the exergy analysis has the extra benefit of allowing fair comparisons between receivers operating at different temperatures. After optimising across three different operating fluids, three different tube materials, temperature ranges, tube dimensions and flow paths, the optimal configuration is found under a very extensive free-parameter search, which should have sodium as the working fluid and Alloy 740H as the tube material, in the context of the simplified thermal stress and cost analyses.

Lastly, it is found that the exergy destruction in the heat exchanger is not an issue for an optimised sodium–salt system, when compared to an optimised chloride salt system, from a performance point of view. After conducting all the projects mentioned above, it is found that liquid sodium always performed the best in the receivers due to its better heat-transfer characteristics.

List of Publications

Journal articles

1. M. Zheng, J. Zapata, C.–A. Asselineau, J. Coventry and J. Pye, (2020) 'Analysis of tubular receivers for concentrating solar tower systems with a range of working fluids, in exergy-optimised flow-path configurations', in *Solar Energy*, Vol. 211, p999–1016.

Conference articles

1. M. Zheng, S. Guccione, A. Fontalvo, J. Coventry and J. Pye, (2020) 'Exergy analysis of the impact of a heat exchanger on performance of an integrated sodium–salt CSP plant', in *Proceedings of the 26th SolarPACES conference,* Albuguerque, New Mexico, USA. Oral presentation.

2. M. Zheng and J. Pye, (2016) 'Optimization of flat tubular molten salt receivers',in *Proceeding of the Asia–Pacific Solar Research Conference (APSRC),* ANU Canberra, 28–30 Nov. Oral presentation.

3. J. Pye, J. Coventry, J-S Kim, F. Venn, M. Zheng, Y. Wang, M. Rae, M. Collins and J.F. Torres, (2019) 'Experimental testing of the bladed receiver', in *Proceedings of the 25th SolarPACES conference,* Daegu, South Korea. Oral presentation.

4. J. Pye, E. Abbasi, M. Arjomandi, J. Coventry, F. Ghanadi, G Hughes, J-S Kim, L. Ma, A. Shirazi, J.F Torres, F. Venn, Y. Wang and M. Zheng, (2018) 'Towards Testing of a Second-Generation Bladed Receiver', in *Proceeding of the 24th SolarPACES conference,* Casablanca, Morocco, 2–5 Oct. Oral presentation.

Conference presentations

1. M. Zheng, A.Fontalvo, A. Shirazi, J. Coventry, J. Pye, (2019) 'Durability, cost and efficiency trade-offs in tubular receivers with a range of working fluids for CSP', *ASME Power & Energy Conference,* ASME ES 2019, Bellevue, WA, USA, 14–17 Jul. Oral presentation.

2. M. Zheng, Y. Wang, J.F. Torres, J. Coventry, J. Pye, (2018) 'Bladed or conventional flat receivers: which geometry is more efficient?', *ASME Power & Energy Conference,* ASME 2018, Lake Buena Vista, FL, USA, 24–28 Jun. Oral presentation.

3. J. Pye, M. Zheng, Y. Wang, J.F. Venn, F. Torres, L. Ma, J-S Kim, G. Hughes, F. Ghanadi, J. Coventry, M. Arjomandi and E. Abbasi, (2018) 'Reconfiguring and rethinking tubular receivers: Findings from the Bladed Receivers with Active Airflow project', in *Asia-Pacific Solar Research Conference,* Sydney, Dec. Oral presentation.

4. J.F. Torres, Y. Wang, M. Zheng, J. Coventry and J. Pye, (2017). 'Coupled optical-hydrodynamic-CFD modelling of bladed receivers'. *SolarPACES Conference* Chile, Oct. Poster presentation.

Contents

[1]This optical matching was conducted by Wang, as she was involved in the BRAAC project to deal with optical analysis.

List of Figures

List of Tables

Nomenclature

Abbreviations

ARENA	Australian Renewable Energy Agency
ASME	American Society of Mechanical Engineers
ASTRI	Australian Solar Thermal Research Institute
BRAAC	Bladed Receivers with Active Airflow Control
CFD	Computational Fluid Dynamics
COBYLA	Constrained Optimisation by Linear Approximation
CR	Concentration Ratio
CSIRO	Commonwealth Scientific and Industry Research Organisation
CSP	Concentrating Solar Power
CSR	Circumsolar Ratio
DIAPR	Directly Irradiated Annular Pressurized Receiver
DISS	Direct Solar Steam
DN	Nominal Diameter
DNI	Direct Normal Irradiation
DOE	Department of Energy
DSG	Direct Steam Generation
FOM	Figure of Merit
GA	Genetic Algorithms
Gen3	The Third Generation of CSP Technology
HTF	Heat Transfer Fluid
ISCCS	Integrated Solar Combined Cycle System
LBE	Lead Bismuth Eutectic

LCOE	Levelised Cost of Energy
LEC	Levelised Electricity Cost
LFR	Linear Fresnel Reflector
LTES	Latent Thermal Energy Storage
NREL	National Renewable Energy Laboratory
PB	Power Block
PCM	Phase Change Material
PTC	Parabolic Trough Collector
PV	Photovolatic
R&D	Research and Development
RANS	Reynolds-averaged Navier–Stokes
SAM	System Advisor Model
SCRAP	Spiky Central Receiver Air Pre-heater
SE	the scaling exponent of the receiver cost
SFR	Sodium-cooled Fast Reactors
SPT	Solar Power Tower
SST k-w	Shear-Stress Transport k-omega
STES	Sensible Thermal Energy Storage
STHE	Shell and Tube Heat Exchanger
STP	Solar Thermal Power
TEMA	Tubular Exchanger Manufacturers Association
TES	Thermal Energy Storage
TMY	Typical Meteorological Year

Symbols

A	area, m^2
C	concentration ratio
c	cost

c	speed of sound, m/s
c_p	specific heat capacity, kJ/(kg·K)
D	inner tube diameter, m
d	tube diameter, m
E	Young's modulus, Pa
e	exponential function
e	tube roughness, mm
F	safety factor
f	friction factor, factor
G	direct normal irradiance, W/m^2
h	convection coefficient, $W/(m^2 \cdot K)$
h	height of the receiver, m
h	specific enthaply, kJ/kg
J	radiosity, W/m^2
K	minor loss coefficient
k	thermal conductivity, W/(m·K)
L	length (along receiver tube), m
$\dot{m}$	mass flow rate, kg/s
Ma	Mach number
n	number of flow segments, or number of cycles to failure per year
Nu	Nusselt number
N	number of cycles to failure
P	pumping power, MW
Δp	pressure drop through receiver, bar
Pe	Péclet number
Pr	Prandtl number
$\dot{Q}$	heat rate, MW

$\dot{q}$	heat flux, MW/m^2 or kW/m^2
R	specific gas constant, kJ/(kg·K)
r	radius, m
Re	Reynolds number
s	entropy, kJ/(kg·K)
T	temperature
t	thickness, mm
U	overall heat transfer coefficient or U-value, $W/(m^2 \cdot K)$
v	specific volume, m^3/kg
$\mathbf{V}$	velocity, m/s
W	receiver width, m
$\dot{W}$	energy rate, MW
$\dot{X}$	exergy rate, MW
bkw	back wall section of the bladed receiver
blade	blade section of the bladed receiver
edge	edge section of the bladed receiver
mrad	milliradian

Greek symbols

α	absorptivity, solar-weighted
α	linear thermal expansion coefficient, K^{-1}
ϵ	emissivity
η	efficiency, %
μ	dynamic viscosity, kg/(m·s)
ν	Poisson's ratio
ϕ	specific flow exergy, kJ/kg
ρ	density, $kg/(m^3)$
σ	Gaussian spot size

σ	Stefan-Boltzmann constant, $Wm^{-2}\ K^{-4}$/stress, pa
θ	angular coordinate, $^{\circ}$

Subscripts

θ	circumferential direction
abs	absorbed
air	air receiver
allow	allowable stress
amb	ambient
aper	aperture area
A	area, m^2
b	bulk temperature
banks	flow path: number of banks
bend	tube bend
b	tube bend
c	circumferential direction
circum	circumferential
cont	thermal contact resistance
conv	convective heat transfer
con	contraction
c	cold
dest	destroyed within the system
D	Darcy friction factor
eff	effective
elec	electricity output
enl	enlargement
exp	experimental
ext	external wall of receiver tube

E_q	equivalent stress/strain
f	film temperature
flow	flow exergy
fric	friction
F	fabrication
HX	heat exchanger
h	hot
i	for/in one flow segment only
i, o	inlet/inside, outlet/outside
II	second law
in, out	inlet/inside, outlet/outside
inc	incident energy
int	internal wall of receiver tube
I	first law
life	lifespan of the receiver
loss	loss through leaving the system
max	maximum
min	minimum
m	tube material and mass
net	net gain in energy
opt	optical
plate	protective plate for the thermocouple
pr	pressure stress
PU	pump
r	radial direction
rad	radiation due to thermal emission
rec	receiver

refl	energy loss due to reflection
ref	reference
safety	safety factor
shell	shell side of the STHE
sky	sky
spil	loss due to spillage
sun	total energy
th	thermal
tot	total efficiency
tubebanks	number of inter-tube-per-bank
tube	tube side of the STHE
VM	von Mises
wall	wall
water	water receiver
w	wall
z	axial direction

Chapter 1

Background and literature review

The limitation of the long-term supply of fossil fuels and the negative impact of CO_2 emissions on the environment lead to increasing demand for renewable energy supply. Concentrating Solar Power (CSP) systems, specifically central towers, are increasingly being built, owing to their large scale, high efficiency, low operation costs and very low emissions [1, 2]. The receiver is an essential part of a concentrating solar power (CSP) system, and its performance is strongly constrained by material limits which in turn limit the allowable flux on the receiver. A high-efficiency receiver is able to reduce the cost of energy production, and consequently, to make concentrating solar power (CSP) technology a more competitive alternative than other types of renewable energy. In the next sections, the state of the art of the CSP technologies, central receivers in particular, are examined, followed by identifying the limitations of prior analyses on these fields.

1.1 Concentrating Solar Power Plants (CSP)

CSP technology is able to be classified into two categories: point-focus concentrators and line-focus concentrators. Parabolic Trough Collector (PTC, Fig. 1.1a) and Linear Fresnel Reflector (LFR, Fig. 1.1b) are the two design categories of line-focus concentrators, while Parabolic Dish (Fig. 1.1c) and Concentrating Solar Power Tower (SPT, Fig. 1.1d) are classified as point-focus concentrators.

PTC power plants use long, curved, mirrored troughs to reflect the solar radiation onto a glass envelope containing a metal tube filled with heat transfer fluid. Fernández-García et al [3]. presented a summary of the commercialised parabolic trough solar collectors and their applications. GlassPoint proposed a novel design in trough system for Solar Thermal Enhanced Oil Recovery to make those mirrors to be lighter, cheap to build and easy to turn by implementing those mirrors inside a greenhouse [4]. LFR power plants use a number of long mirrors to focus light onto several linear receivers which are located above the mirror field. The largest LFR plant in the world (125 MW) is installed in India, named as "Dhursar", based on the review on LFR plants by Desai et al [5]. LFR has the advantages of mechanical

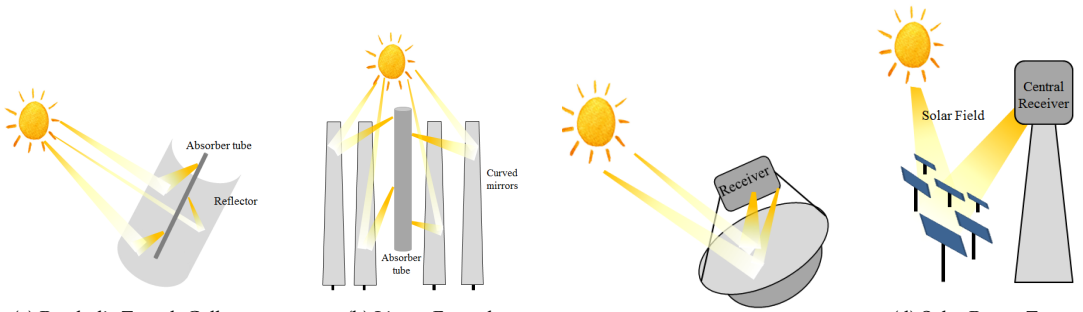

(a) Parabolic Trough Collector (PTC)

(b) Linear Fresnel Reflector (LFR)

(c) Parabolic Dish

(d) Solar Power Tower (SPT)

Fig. 1.1: The sketch of CSP technologies.

simplicity (near-flat mirrors, stationary receiver and pipework) and narrower mirrors that are close to the ground, lowering wind forces. Nevertheless, this technology is not promising so far due to its low optical efficiency [6] and relatively limited commercial uptake.

The Parabolic Dish focuses all the solar radiation that strikes the dish up onto a single point above the dish ideally, and the receiver generate the heat and transforms it into electricity if there is an engine there, e.g. Stirling. The aperture can be smaller than the absorber surface for the cavity receivers. A new tubular cavity receiver for direct steam generation, "SG4", has recently been investigated by researchers at the Australian National University (ANU). This new receiver achieved an average thermal efficiency of around 97%, which is a high efficiency for a solar thermal dish [7]. This higher efficiency, when compared to the previous "SG3", is achieved because of the narrower aperture of the "SG4" receiver, which effectively reduces receiver losses.

CSP tower technology has been developed from a first generation which consists of Direct Steam Generation (DSG) with no storage (e.g. the EURELIOS (1 MW_e) experimental solar power plant in Italy [8], the White Cliffs parabolic dish project in Australia [9]), to a second generation which used molten salt as the HTF and the storage medium (e.g. the Gemasolar plant in Spain [10] and the Crescent Dunes plant in the U.S. [11]). The present effort is to develop a third generation of CSP technology [12] with targets for higher temperatures (>700°C), a higher-efficiency power block (PB), and more cost-effective and reliable technologies in each component. The energy chain for a central tower system primarily consists of a heliostat field, a tower-mounted receiver, a heat exchanger, a thermal energy storage (TES) system and a PB (see Fig. 1.2). The central receiver concept for concentrating and collecting solar energy is based on heliostats which consist of a field of individually tracking mirrors. The incident energy will be reflected from the heliostats onto the receiver at the top of the CSP tower. An HTF will then carry the heat collected from the receiver to a heat exchanger. TES is then incorporated to store energy, which makes CSP a dispatchable electricity supplier. The energy stored in TES can be used to generate steam, and in turn, to generate electricity in a PB. CSP tower technology

is suitable for achieving very high temperature in the receiver, compared to other CSP technologies and therefore, it is more likely to achieve high thermal efficiencies in the PB.

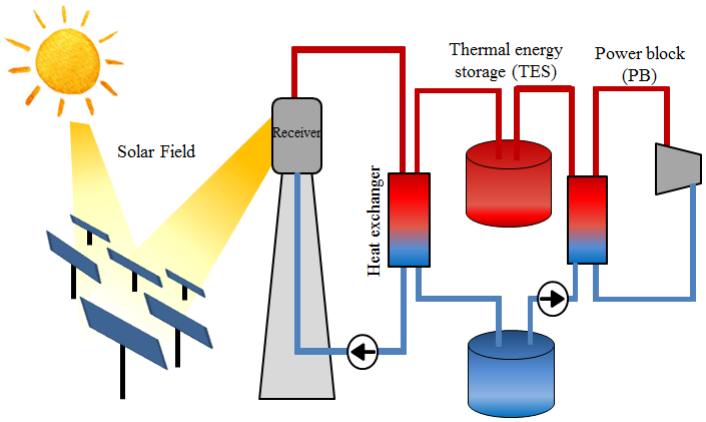

Fig. 1.2: Schematic of a typical CSP tower technology, which consists of a heliostat field, a central receiver, a heat exchanger, a TES and a PB.

Solar One and Solar Two [13, 14, 15] were the two pioneering central tower CSP systems, and operated in California between 1988 and 1999 respectively. Solar Two was a major re-vamp of Solar One with the addition of a molten salt receiver, instead of water as with Solar One. Solar Tres (ultimately renamed "Gemasolar") in Spain was the first commercial solar power plant built using this molten salt receiver technology, about three times the size of Solar Two, and commenced operation in April 2011 [10]. The 110 MW_e Shouhuang Dunhuang "100 MW_e Phase II" commercial solar power plant is the latest of this type by 2018 [16].

A more detailed CSP technology review has been carried out in Section 1.4., according to the type of the working fluid used in the receiver.

1.2 Central receiver system

The receiver is the part of the CSP system where concentrated radiation is focused and where heat transfer fluid circulates and removes the heat for storage. There are three types of receivers for central tower: volumetric receivers, falling particle receivers, and tubular receivers.

There are two types of volumetric receivers: open atmospheric volumetric receiver for the Rankine Cycle and closed pressurised (temperature-resistance windowed) volumetric receiver for the Brayton Cycle. The open volumetric receivers use air as the HTF and they have been under development since the 1980s [1, 17, 18]. For

example, they utilise a porous honeycomb structure to transfer the absorbed heat to the aire passing through the volumetric structure. A review by Ávila-Marín et al. [17] shows that, up to 2011, most of the volumetric receivers were demonstrated in small-scale prototypes. The thermal efficiencies over 20 high-temperature volumetric receivers were in the range of 65%–80%. The main features of volumetric receivers are: good heat transfer in the receiver due to the large internal surface area; high fluid temperature is possible. For instance, the maximum outlet air temperature of DIAPR 30-50 project reached 1200°C at 20 bar [19] and the SOLGATE project, which commenced in 2001, provided gas at 960°C [20]. However, volumetric receivers are not commercially deployed yet, as they require big efforts to solve some issues such as suitable windows for the pressurised receivers and the receiver material selections.

Falling particle receivers utilise sand-like particles that are heated up when they drop through concentrated sunlight [21]. Ceramic and silica-based particles are typically used for high-temperature (> 700°C) falling particle receivers. This technology has the potential to achieve higher temperatures ($\sim$ 1000°C) and greater efficiencies at lower costs in the receivers when compared to the tubular receivers, as it removes the conventional tubes in the receiver to relieve the maximum-flux constraints. The Gen 3 Particle Pilot Plant (G3P3) [22] has demonstrated the ability to heat a working fluid to higher than 700°C with reasonable costs.

Tubular receivers are the dominant type of CSP central receivers, used in both R&D and commercialised projects, due to their simple fabrication, where incident energy is absorbed and transferred through the tubes to the heat transfer fluid (HTF). External and cavity receivers are the two main types of tubular receivers, as shown in Fig. 1.3 [1]. External cylindrical, flat rectangular and cavity tubular receivers are designed and selected accordingly, based on factors such as location of the plant site, receiver concentration ratio, HTF type and the operating temperature range. The design of the heliostat field, flow configuration of the heat transfer fluid, and operating temperature range must be considered, as they in turn will affect the design and performance of the thermal energy storage (TES) and the power cycle.

One successful cavity central tower project is in the eSolar design [23]. This project makes the use of dual-cavity receiver and multiple towers. It states that equator facing fields (as shown in Figure 1.4), unlike the usual surround heliostat fields, are more suitable for multiple smaller towers. The idea of small heliostat aperture area (1.14 m^2) significantly reduces the on-site labour costs as most of the constructional and assembled work can be carried out at factories.

Volumetric and particle receivers are significantly different from gas or liquid tubular receivers in many respects including the optimum receiver geometry. It is very challenging to make a generalised comparison of these receivers using modelling methods suited to gas or liquid tubular receivers, and consequently they are not considered in this thesis.

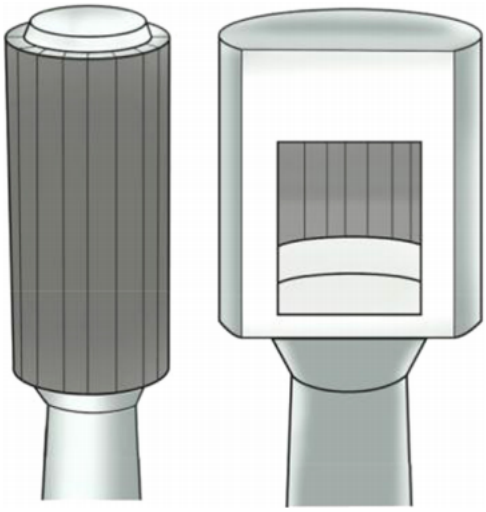

Fig. 1.3: Schematics of tubular external (left) and cavity (right) receivers, picture extracted from Ho et al. [1]

Fig. 1.4: Sierra Suntower Demonstration facility, Lancaster, CA, USA in April 2009. Source extracted from [23]

1.3 Novel configurations of tubular receivers

A number of novel configurations of tubular receivers have been conducted to improve receiver performance, such as the cavity receiver design "Spiky Central Receiver Air Pre-heater (SCRAP)" proposed by Lubkoll et al. [24] and other bladed receiver designs (see Fig. 1.5) to improve light-trapping through the cavity effect, including the "cruciform" receiver proposed by Vant-Hull and Hildebrandt [25], the "bookshelf" receiver proposed by Wanger et al. [26] and the "louvred" bladed receiver. This "louvred" concept was raised by Sandia National Laboratories, USA and the Australian National University to improve the efficiency of the receiver by adding an array of horizontal tube banks (aka blades). Preliminary studies [27, 28, 29] have proven the benefits of implementing bladed tube banks to overcome the flux limits for the molten salt receivers and to increase the light trapping effect by using idealised flux distribution maps.

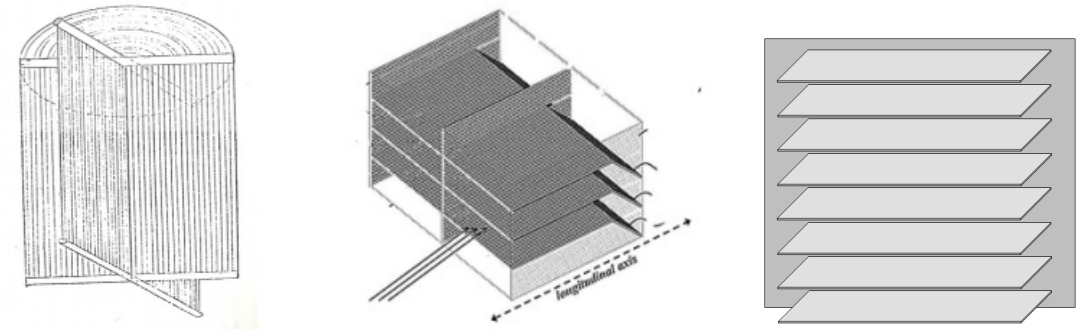

(a) The "cruciform" receiver [30] (b) The "bookshelf" receiver [26] (c) The "louvred" receiver.

Fig. 1.5: Schematic diagrams of the concept of the novel configurations of the bladed receivers.

1.4 Heat Transfer Fluids (HTFs)

The selection of the heat transfer fluid (HTF) is a key factor towards success in CSP, as it transfers the heat from the incident energy source to the power block, which significantly impacts the efficiency of the entire system. A heat transfer fluid can be a gas or a liquid that transfers heat from a receiver to a heat exchanger and then to a thermal energy storage tank. The advantages and limitations of the thermophysical properties of various HTF and TES candidates have been discussed [31, 32, 33, 34]. This section introduces the high-temperature HTFs (i.e. molten salt, chloride salt, liquid sodium, Supercritical CO_2, air, water/steam) considered in the receiver and the heat exchanger in this thesis, and discusses their prior use in CSP.

1.4.1 Molten Salt

Molten salt (60% $NaNO_3$, 40% KNO_3) is arguably the most commonly employed HTF for central tower receivers and TES in parabolic trough collectors and central tower systems, in terms of efficiency, reliability and cost. It has been used widely as a proven technology in the CSP industry, such as in trough and central tower systems. In addition, it is also used in the majority of present-day TES systems for CSP [35] due to its relatively low cost. The Themis Solar Tower was the first large-scale solar tower to use molten salt in its receiver, and was constructed for R&D in France in the 1970s, and could produce 2.5 MW_e [36]. Gemasolar was the first commercial CSP plant to utilise this technology, with a molten salt thermal storage capacity of 15 hours, a 120 MW_{th} receiver power, and a 19.9 MW_e turbine power. This plant has been in operation since Jun, 2011 [10]. The Archimede plant in Italy, was the first power plant in the world to use molten salt as the heat transfer fluid in the collectors of a parabolic trough system [37].

The first utility-scale facility in the world to use molten salt was SolarReserve's Crescent Dunes Solar Energy Facility, located in Nevada USA, which has been under commercial operation since late 2015 [11]. Its 110 MW_e output could power 75,000 homes during peak demand [38]. The Noor III project (150 MW_e) is currently operational and is another utility-scale power tower project with molten salt. This plant has the capacity for up to 7.5 hours storage [39]. The Shouhuang Dunhuang "100 MW_e Phase II" commercial solar power plant began operating in Dec 2018, as a follow-on development to the "10 MW_e Phase I" pilot project, and has the thermal storage with a capacity of 11 hours, using molten salt as the storage fluid [16]. One important limitation of the use of molten salt is its operating temperature constraints. Conventional nitrate salt has to be carefully operated within a bulk temperature range of 290–565°C in order to limit the effects of chemical degradation and corrosion [40].

1.4.2 Chloride Salt

The third generation (Gen3) of concentrating solar power plants will be competitive with conventional ways of electricity generation (e.g. fossil fuels) if a high-efficiency power cycle can be utilised. To achieve this, a high-temperature heat transfer fluid should be developed to be capable of operating at temperatures ($\geq$ 700°C). Chloride-based salts (46.0wt% MgCl2–38.9 wt% KCl–15.1 wt% NaCl) are one of the new categories of HTFs able to work in the range of 400–800°C. Like conventional molten salt, chloride salt has been considered widely in thermal energy storage (TES) due to its low-cost, and high-thermal-stability [41, 42, 43]. The experimental study conducted by Mohan et al. [43] shows the feasibility of using chloride salt as a sensible heat storage (STES) material over 600°C.

Although chloride salts are very promising HTFs for TES, the high-corrosivity requires further investigation. There is some literature indicating methods to reduce

the corrosivity. For instance, an electrolysis method with a Mg anode for reducing the corrosive impurity level has been studied by Ding et al. [44]. A method with thermal treatment for drying and purifying chloride salt is proposed by Fernández and Cabeza [45].

1.4.3 Liquid Sodium

Liquid sodium allows operation at higher temperatures and hence, in principle, with more efficient power cycles. The wide temperature range in the liquidus phase (97.7–873°C) and its exceptionally high thermal conductivity make sodium receivers appealing for high-temperature, high-flux applications [46], at least from the performance point of view. Additionally, its high thermal conductivity makes sodium an exceptional HTF. The availability of sodium metal is sufficient as it is the sixth most abundant metal on earth, but still, the metallic 'form' is relatively expensive and, as such, unsuited to dual operation as both HTF and TES medium, in contrast to molten salt.

Sodium is a highly combustible material when in contact with water or air. Even so, its advantages in certain nuclear applications have attracted the attention of CSP researchers. Sodium has been used as the coolant in the sodium-cooled fast reactors (SFR) in the nuclear industry as early as the 1950s [47]. In a project called IEA-SPSS, the first generation of central sodium receivers, was researched and developed in Spain and Sandia National Laboratories in the U.S. in 1980s [2]. Vast Solar, an Australian CSP company, developed the Jemalong CSP Pilot Plant, which is the first grid-connected CSP plant (1.1 MW_e) project to use sodium as the HTF in the receiver in Australia [32, 48, 49, 50, 51]. So far, this pilot project has successfully demonstrated the possibility of running sodium in CSP. Sodium is also currently under active consideration in the Australian Solar Thermal Research Institute (ASTRI) and the US Gen3 Liquids programs [52], due to its ability to remain liquid at temperatures as high as 700–850°C.

Molten salt was compared with liquid sodium as the HTF in central receivers by Boerema et al. [46]. Molten salt is cheaper and is capable of being used as the storage source, while use of sodium results in more efficient receivers. The in-depth comparison of a range of working fluids is discussed later.

1.4.4 Supercritical CO_2

Supercritical CO_2 (sCO_2), which is compressed carbon dioxide at pressures of 72.9 bar or above, can be used as the working fluid in Brayton cycle power blocks for CSP plants [53]. U.S. DOE's Supercritical Transformational Electric Power (STEP) program aims to demonstrate a pilot scale sCO_2 test facility [54, 55]. As discussed

in 2.2.2, the physical properties of sCO_2, when it is operated above its critical point (31.10°C, 72.9 bar), offers performance advantages for the sCO_2 Brayton cycle over other power cycles (such as steam Rankine). The advanced sCO_2 receiver, proposed by Brayton Energy [56], has the potential to be compatible with the sCO_2 Brayton cycle. The primary interest in sCO_2 arises because sCO_2 is attractive in the PB. Hence, its direct heating in the receiver is of interest. However, the extremely high operating pressure required in the receiver (over 200 bar) brings challenges when combined with the considerations of radiation, thermal stress, thermal resistance and the corrosivity of CO_2.

1.4.5 Air

Air has been considered as an HTF for CSP applications as it is capable of operating at higher temperatures than oil and molten salt, which could increase the thermal-to-electric efficiency for the power block [1, 34]. In addition, air can be used directly as the working fluid in an open or closed air Brayton cycle, which reduces the complexity of the power block by eliminating a heat exchanger. However, the poor conductivity of air is likely to make receivers with this HTF less efficient than others, since it increases the temperature difference between tube wall and the fluid, and results in high exergy destruction in internal convection, but also drives up external losses due to elevated external temperatures. One way to overcome this drawback is to strive to increase the heat transfer coefficient, using rough tubes or internally-finned tubes [57]. The Jülich Solar Tower project is an experimental project using air as the HTF, operating up to 680–700°C [58]. Air at elevated temperature of 800–1000°C has better heat-transfer properties, specifically the internal heat transfer coefficients, but the material constraints of receiver tubes have to be considered carefully. Solugas, a solar hybrid Brayton plant, compressed ambient air up to 9 bar (gauge) and heated it from 300–350°C to 800°C [59]. The heated air was then used in a turbine. This project demonstrated the feasibility of a solar-hybrid plant with gas turbine in Spain. In the PEGASE project in France, pressurised air was heated in a central receiver from 350–750°C at 7 bar, then integrated into a gas-turbine power plant [60].

1.4.6 Water/steam

Water and steam have been used as HTF since the earliest days of CSP. EURELIOS (1 MW_e), in Italy, was the first experimental solar power plant in the megawatt range and the first grid-connected CSP plant. Its construction was completed in the end of 1980 [8]. In the same time frame, the White Cliffs parabolic dish project in Australia [9] successfully demonstrated the possibility of using sun to power a small town, in 1981. Later, direct steam generation, in the DISS (Direct Solar Steam) project, was successfully demonstrated in parabolic troughs from 2004 to 2008, by Zarza et

al [61]. The ANU 500 m^2 Big Dish (SG4, 50 MW_e) is the largest solar paraboloid dish in the world and is able to generate steam up to 550°C at 5 MPa [7]. The PS10 (11 MW_e) and PS20 (20 MW_e) projects in Spain were the world's first commercial SPTs [14], utilising water as the HTF to make saturated steam at about 250–300°C. In 2011, the first commercial solar thermal power plant with parabolic trough collectors using DSG, named "KTSE 9100" (5 MW_e) was tested in Kanchanaburi, Thailand [62]. Khi Solar One is a large commercial CSP plant that generates superheated steam up to 530°C at 120 bar for a 50 MW_e steam Rankine cycle [63]. The plant incorporates an accumulated saturated steam storage with capacity up to two hours. The steam is used directly in the turbine which simplifies the power cycle by eliminating the need for a heat exchanger. Ivanpah, the largest solar thermal power plant in the world (377 MW_e) upon its completion in 2014, uses a solar receiver steam generator [64]. The highest solar tower power plant so far, named "Ashalim Plot B (121 MW)", consisting of steam receiver and steam turbine, was built in Ashalim, Israel, in 2017 [65]. In general, the two-phase flow of water/steam is difficult to handle in the receiver and steam is also corrosive to tubes. Phase change material (PCM) storage could be deployed with DSG to increase the storage efficiency which, however, may increase the complexity and the cost. There are challenges to integrate energy storage with water/steam systems [66].

1.4.7 Thermal oil

Loni et al. [67] compared the performance of water and oil on three types of cavity receivers, with studies showing that water is promising in low-temperature applications (40–90°C) due to its better thermal properties, while a hemispherical cavity receiver with thermal oil has the highest exergetic performance in medium-temperature applications (up to 300°C). Thermal oil has been extensively used in parabolic troughs [3, 68]. However, its maximum working temperature limitation of 398°C excludes this type of HTF for consideration in this thesis.

1.4.8 Figure of Merit (FOM)

Having a figure of Merit is convenient to examine the performance of the working fluids mentioned in Sec.1.4.1 – Sec.1.4.6, as it presents an approach to generalised comparison. It is determined by the thermophysical characteristics of the working fluids. However, it omits important considerations such as tube conduction and external thermal losses, and as such is insufficient for choosing a working fluid. A rigorous receiver model is then required to select the best working fluid. More detailed discussion on FOMs studied by different researchers and their limitations will be covered in Section 2.3.2.

1.5 Flux distribution and limits

Possible approaches to improving the efficiency of receivers are reducing the surface temperature by varying the flux distribution, adopting multi-panel receivers and multi-pass receivers. The IEA-SSPS High Flux Experiment using the advanced sodium receiver with 5 panels, showed the potential for increasing receiver efficiency by reducing the average receiver surface temperature. In the experiment, each receiver panel consists of 39 tubes with an outer diameter of 14 mm, and a wall thickness of 1 mm was used [69]. A schematic diagram of the receiver is shown in Fig. 1.6 (left). Boerema et al. [70] found that multi-pass receivers performed the best for maintaining relatively low surface temperatures, compared with single-pass receivers, due to the increased flow velocity and improved convectional heat transfer coefficient. The cold fluid passes through the other panels first and eventually the hot fluid comes out from the centre panel. Tubes with an outer diameter of 25.4 mm and a wall thickness of 1 mm were used in the study, as shown in Fig. 1.6 (right). Boerema et al. found that such techniques could improve energy efficiency by 1–2% [70].

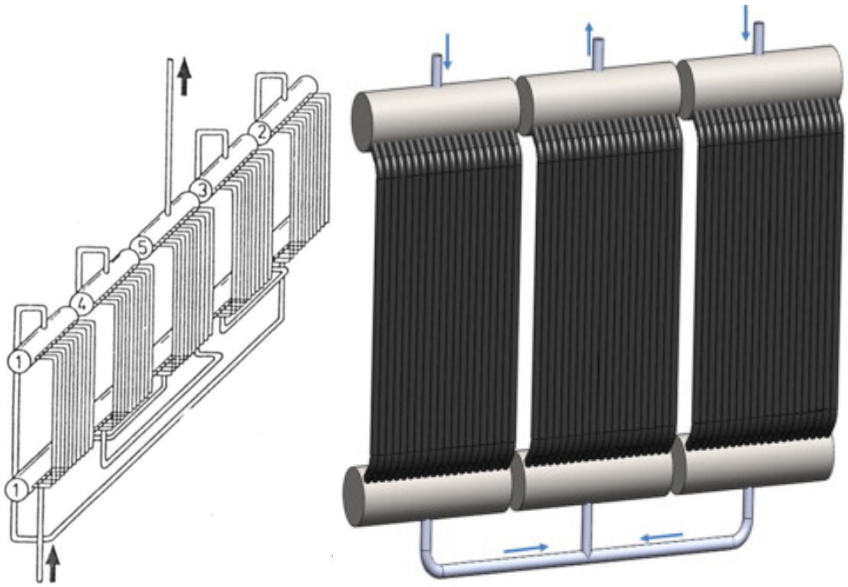

Fig. 1.6: Schematic diagrams of the flow path for the receivers: left: the IEA-SSPS billboard receiver [69]; right: the design proposed by Boerema et al. [70]

1.6 Thermal stresses

Thermal stress is induced due to the change in temperature of a material. If the temperature increases, a material generally expands, whereas if the temperature decreases, the material contracts. Thermal stress can lead to plastic deformation or

the fracture of the material, and therefore, must be considered in design. For instance, thermal stress is one of the most critical constraints in design of molten salt receivers, and was used to determine allowable flux density by Sánchez-González et al. [71]. The allowable flux density is determined based on material creep-fatigue failure models which in turn depend on supporting experimental data. An allowable flux density is developed by modelling how much damage the material experiences during each cycle of operation (daily ramping up, staying hot and cooling down), and adjusting the flux until the receiver lifetime reaches the design specification. This allowable flux density then leads to the need for accurate aiming strategies for the heliostat field. The flux variation on the tube wall in the circumferential direction affects the corresponding temperature and the elastic stress. Logie et al. [72] has used analytical methods to calculate thermoelastic stresses on a single tube and concluded that sodium outperforms salt in relation to higher flux.

Creep is defined as the permanent deformation of a material due to continuous loading. Fatigue of materials is due to loading cycles. Creep and fatigue damage, are important considerations on receiver tube material selection and appropriate tube wall thickness, which have been reviewed by Conroy et al. [73]. González-Gómez et al. [74] studied the creep-fatigue damage on the tubular molten salt receiver using Haynes 230, a nickel-chromium-tungsten-molybdenum alloy, as the tube material. Study showed that stress relaxation could strongly affect the lifetime of the receiver. Augsburger et al. [75] indicated that cloud passage is the main cause of short-time variations and material thermal stresses. They investigated the cloud passage characteristics in meteorological databases and eventually proposed a strategy for start-up/shut-down of heliostats, to minimise the thermal stress on the receiver due to transient flux.

1.7 System-level optimisations

Several tools are capable of handling the system-level optimisation in receiver designs, such as SAM [76] and DELSOL3 [77]. SAM [76] provides the optimal system design that has the lowest levelised cost of energy (LCOE) by searching from the specific variables which are defined in SAM. The discrete combinations of variables are searched for the optimal design based on the specified ranges and step sizes set by the users. DELSOL3 [77], as the latest version of DELSOL, utilises mathematical convolution method for obtaining the optical performance and optimal system design. However, as mentioned, only a range of variables in the "receiver section" could be optimised in these tools which limits the performance of the receivers. For example, inlet and outlet temperatures of the heat transfer fluids play significant roles in the receiver design, which unfortunately, are omitted in the variables that could be optimised in these tools. System-level trade-offs in receiver designs have been conducted widely in STP technology. For example, the performance of the partial receiver and

the related costs are investigated by Gobereit et al. [78]. The levelised electricity cost (LEC) is optimised for the pressurised air receivers coupled with gas turbine by Schwarzbözl et al. [79]. Solar central receiver systems are designed and optimised by Li et al. [80], with an optional compound parabolic concentrator. This study, however, has no heat transfer modelling or heat exchanger being considered. The cavity receiver is assumed as an isothermal, well-insulated blackbody. Techno-economic analysis of liquid sodium and molten salt SPT plants is conducted by Fritsch et al. [81]; however, no optimisation process on the receiver design is approached.

1.8 Exergy analysis

In the optimisation of concentrating solar systems, the second law of thermodynamics plays a significant role as it deals with the degradation of the work potential of energy during a heat transfer process and the associated entropy generation [82]. Exergy analysis proves to be a valuable tool for the investigation of possible configurations of optimised renewable energy systems, since it is able to present the types, causes and locations of thermodynamic losses more clearly than energy analysis on its own, and additionally allows comparison of receivers without needing a TES or a PB model, with regards to temperature [83, 84, 85]. Padilla et al. [86] presented exergy analysis of a parabolic trough solar receiver based on a control volume analysis, which quantifies the variable thermal losses. Baghernejad and Yaghoubi [87] studied the exergetic analysis on the Integrated Solar Combined Cycle System (ISCCS) and showed that the dominant exergy loss throughout the whole system occurs in the combustor which accounts for 29.62% of the total exergy input to the plant. Le Roux et al. [88] emphasised the importance of minimising the irreversibilities (i.e. total entropy generation rate) of the solar thermal Brayton cycle which are due the finite temperature difference between HTF and the receiver walls. This could be achieved by optimising the size of the recuperator and modifying the cavity receiver. A review of exergy analysis on various types of solar collectors and applications of solar thermal systems was presented by Kalogirou et al. [89], emphasising its importance in the design of sustainable energy systems, since exergetic analysis has been involved in designing a wide range of solar collectors including flat-plate collectors, hybrid PV/thermal systems, parabolic trough and dish collectors as well as other applications such as phase change materials.

All of the above published papers have proven the usefulness of exergy analysis in figuring out the optimal operation conditions and evaluating the performance of the CSP systems. By analysing the exergy destroyed by each part in a process it is possible to present the types, causes and locations of thermodynamic losses, and the potential areas on improving the system efficiency can be focused. Exergy can also be used to compare components of a system to help inform design, especially in receiver designs. However, in the detailed exergy analysis of tubular receivers there

still exists a gap, in relation to various phenomena of the losses such as external radiation, external convection, wall conduction, internal convection and internal flow.

1.9 Main research question

Although there have been several studies to optimise the performance of the receivers with individual heat transfer fluids [70, 90, 91, 92, 93, 94], few studies adopt a consistent modelling approach for the comparison of a broad range of HTFs. For example, Boerema et al. [70] optimised the performance of a 2 MW_{th} billboard receiver using liquid sodium as the working fluid, while Potter et al [92] did the optimisation study for a 1 MW_{th} liquid sodium receiver. Rodríguez-Sánchez et al. [90, 95] focused on the optimisation for a 120 MW_{th} cylindrical tubular receiver using molten salt as the working fluid. Laporte-Azcué et al. [96] conducted a comprehensive exergy analysis of a SPT tubular receiver, using molten salt as the heat transfer fluid; however, it was only limited to one fluid type and no optimisation process was conducted in relation to the exergic performance on the receiver. The use of different models and different approaches to design optimisation leaves some doubt as to whether the differences in performance for different fluids are due to intrinsic benefits of the fluids, or due to difference in modelling assumptions and approach. The aim of this thesis is to fill this gap by evaluating and optimising tubular receivers with varied tube configuration, working fluid and tube material, using unified models.

1.10 Chapter outline

Chapter 2 uses a common model and common approach to optimisation across a range of working fluids (e.g. molten salt, liquid sodium, supercritical carbon dioxide (sCO_2), air and two-phase water) and a consistent design space and hence, to conduct a broad high-level comparison. Every fluid is given the chance to work at its best in a tubular receiver configuration, with respect to the HTF degradation and corrosion, HTF melting and boiling temperature limits, pressure stresses on the tube, storage material limits and power block temperature limits through an extensive parameter study. The work includes a novel approach to determining the breakdown of losses in the receiver using exergy analysis. The expected conditions of the TES and power cycle are also considered. Chapter 2 seeks to address the following research questions:

1. How would a range of working fluids perform in relation to energy and exergy efficiencies, assuming uniform flux?

2. How would tube diameter, tube wall thickness or tube-bank flow configuration affect the optimal performance of selected working fluids? What would be the intrinsic benefits of a particular working fluid?

The assumed uniform flux approach in Chapter 2 could not reflect the non-uniform characteristics of solar flux distribution in tubular receiver realistically. Those localised hot spots are expected to affect the performance of the receiver, and more importantly, the life time of the receiver. Chapter 3 seeks to answer:

1. What would be the best flux pattern in term of receiver efficiency, while respecting the allowable film temperature limits on the molten salt tubular receiver?
2. How would varying the tube-bank flow configurations affect the localised maximum external wall temperature on the receiver and consequently, affect the efficiency?
3. How would the non-uniformity of the flux per tube-bank affect the performance of the receiver?

The peak flux limitation is one main constraint on the tubular receiver, as it limits the minimum receiver size and consequently, the optical performance of the receiver [97]. By investigating both convex and concave receiver designs (i.e. flat and bladed) with a single model, and optimising both in order to focus on the hydrodynamic aspects, a deeper understanding on whether a bladed receiver is practical from an internal heat transfer point of view, in comparison to a flat receiver, can be made. Since the structure and the fabrication for bladed designs are more complicated than the flat tubular receivers, the minor losses (e.g. bending, elbows, manifolds), the flow configurations, the choice of HTF, the thermal stress constraints and the rate of return on investment would all affect the decision making for the optimal bladed receiver designs. The work herein was carried out in support of a project titled "Bladed Receivers with Active Airflow Control (BRAAC)"[1] where a realistic comparison was made between a conventional flat receiver and a proposed bladed receiver. The total efficiency improvement of a bladed receiver is evaluated, when compared to a conventional flat receiver.

Furthermore, novel small-scale 'virtual experimental' approach was conducted to indirectly test the performance of the large-scale flat and bladed molten salt receivers, using water and air as the heat transfer fluids. These small-scale receivers were tested on-sun at CSIRO, Australia. Chapter 4 seeks to address the following research questions:

1. What would be the optimal flat or bladed receiver designs, when it comes to the realistic flux distributions?
2. To what extent, could the modelled bladed receiver outperform the modelled conventional flat receiver?

[1]The author was involved in the BRAAC project to develop the hydrodynamic model for both flat and bladed receivers and their prototypes, to assist mechanical engineers with the equipment designs (e.g. the pump size, the pipe sizes and the radiator size), and to reconcile the experimental results and the simulation results.

3. How would the 'virtual experiments' be approached to estimate heat transfer parameters from full-scale testing?

4. If the bladed receiver would still outweigh the flat receiver in relation to the experiments?

Experiments are complicated, expensive and time-consuming. A 2,500-hour experimental test was conducted by Giaconia et al. [98] to analyse the performance of molten salt parabolic troughs. A reconciliation method to deal with the experimental results for refrigeration and power cycle was provided by Dumont et al. [99], in order to efficiently and correctly use experimental measurements. A reconciliation of experiments and models for a piping system with "T shape" was examined by Ryu et al. [100]. However, very limited literature could be found in relation to different approaches to reconcile experiment and simulations of CSP technology. The concept of the bladed receiver has been designed, built and tested, as outlined in Chapter 4. It, therefore, could provide a valuable opportunity to conduct an experiment and simulation reconciliation, which allows matching experimental data with theoretical simulation results and understanding the discrepancies between each other. Chapter 5 conducts key-parameter matching (i.e. flux distributions[2], temperature distributions and pressure drops). In addition, other parameters that were not measured during the testing are examined, such as the external heat transfer coefficient, surface reflectivity of the receiver and the effect of thermocouple configuration. Chapter 5 seeks to address the following research questions:

1. What are the experimental uncertainties in the testing?

2. How large is the discrepancy between simulations and experiments?

3. To what extent could theoretical simulations be optimised or reconciled to better match the experimental results?

The importance of peak flux density and flux distribution on the receiver, as well as the importance of taking thermal stress into account, has been introduced in Section 1.5 and 1.6. Chapter 6 offers an analysis of alternative tubes and working fluids on a thermoelastic creep and fatigue model that considers receiver lifetime and replacement, with the consideration of the non-uniformity of the flux distribution. The relationships between material costs, receiver efficiency, and system level design, for a range of working fluids should be developed under a unified analysis, so that a globally optimal choice can be made. Although numerous studies on receiver design have been conducted, few studies undertake this type of broad comparison. Chapter 6 seeks the answers for the following questions:

1. What would be the best flux distribution from the perspective of thermal efficiencies of the receiver?

[2]The flux distributions were handled by Wang [101]

2. What would be the best Pareto front relationship between efficiency and the cost and how could this be incorporated into a system level analysis?

Both chloride salts and sodium are promising HTF candidates for high-temperature receivers. A question raised here is which of those high-temperature HTFs is more effective considering unified modelling assumptions and the same power block capacity, noting the need for an extra heat exchanger in the case of sodium. Chapter 7 seeks the answer.

Chapter 2

Analysis of tubular receivers for concentrating solar tower systems with a range of working fluids, in exergy-optimised flow-path configurations[1]

2.1 Introduction

This chapter firstly discusses some operating limits on the receiver design, arising from consideration of the thermal energy storage and power block components. Next, the relevance and prior experience of various receiver HTFs are discussed. The examined HTFs are molten salt, liquid sodium, supercritical carbon dioxide (sCO_2), air and water/steam. The properties of these working fluids are compared, together with several 'figures of merit' previously used to evaluate HTF performance directly from their intensive properties. A numerical model of the tubular receiver with uniform flux, with detailed energy and exergy accounting, is subsequently introduced, including consideration of the pumping work and the pressure stresses in the tubes. Calculation results from the model are presented next, with an optimisation of the flow configuration conducted for each HTF. Finally, an overall comparison is presented. Through the analysis, a better understanding is developed of the impacts of working fluid property limitations on receiver performance, including the trade-offs between internal heat transfer, external losses, external flux distributions and pumping losses.

[1]This chapter is based on: M. Zheng, J. Zapata, C.–A. Asselineau, J. Coventry and J. Pye, (2020) 'Analysis of tubular receivers for concentrating solar tower systems with a range of working fluids, in exergy-optimised flow-path configurations', in *Solar Energy*, Vol. 211, p999–1016.

2.2 Sub-system influences on receiver design

The thermal energy storage (TES) and the power block (PB) are explained next, prior to the introduction of the whole system design.

2.2.1 Thermal Energy Storage

Thermal energy storage is an essential component in CSP as it provides the dispatchability at large scale to compete with intermittent alternatives such as PV and wind. In order to understand what temperature ranges are applicable in the receiver for different working fluids, the type of TES should be taken into consideration, together with the rest of the system, such as the power block.

Sensible thermal energy storage (STES) units directly store thermal energy by transferring heat to a storage medium, such as molten salt, oil, water, rocks and particles. STES is frequently incorporated in CSP systems due to its low cost and relative simplicity. It is the most direct way to store heat. Molten salt thermal storage is the most widely used technology in current operational CSP plants. Alternative storage materials and technologies are under development, aiming to improve the power cycle efficiency by operating the turbine at a higher temperature range (beyond the molten salt working temperature range). Jülich Solar Power Tower demonstrates the possibility of storing heat by flowing hot air through ceramic elements [58].

Latent thermal energy storage (LTES) units in CSP are immature but promising technologies to store energy. Phase-change materials (PCMs) represent a category of substances which are able to capture the energy during the melting or solidification process without a temperature rise. Smaller LTES could be achieved using PCMs, when compared to STES with the same capacity. Zalba et al. [102] reviewed over 230 references and summarised that LTES has been widely used in all walks of life such as space, cooling of engines, building applications and thermal storage of food. High-temperature PCM storage is quite challenging to commercialise though, for several reason including, for example, high-temperature corrosion [103]. Besides PCMs, the large-scale PS10 [104], PS20 and Khi Solar One [35] plants use steam accumulators, which accumulate energy in the form of pressurised hot water.

Molten soda-lime silica glass is another category which could be used as a storage medium in high temperature TES unit to store heat between a semi-liquid phase (molten state) at about 1000°C and a solid phase at 500°C [105].

Metallic and metalloid PCMs such as molten aluminium [106] or molten silicon [107] energy storage concept are being considered as other possible contenders for TES.

2.2.2 Power Blocks

The power block is another critical component influencing the temperature ranges for receivers. Design decisions on the receiver models and comparison of working fluids cannot be made without considering available PB options. For example, a sCO_2 Brayton cycle allows use beyond the temperature feasible for a Rankine cycle. The Gen3 CSP tower systems [108] revolve around the use of this emerging concept, using temperatures above 700°C in the receiver to unlock the use of a high temperature Brayton PB. The schematic diagrams, as shown in Fig. 2.1, demonstrate the main components of a steam Rankine cycle with reheat (left) and of a sCO_2 Brayton cycle with recompression (right). The latter involves smaller turbomachinery due to the higher density of the sCO_2, and can achieve high efficiency with relatively simple cycle configurations, and consequently is under active development in anticipation of potential capital cost savings. The cycle could potentially achieve a 50% efficiency if the turbine inlet temperatures were to be raised to 700°C [12]. Recuperation of a large amount of heat affects the thermal efficiency of the cycle [109], by improving cycle efficiency from reducing internal irreversibilities.

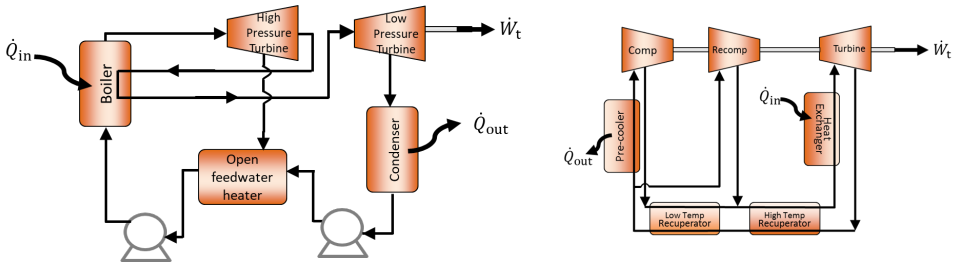

Fig. 2.1: Schematic diagrams. Left: simple Rankine cycle with reheat and regeneration (Source: Cengel et al. [110]; Right: sCO_2 Brayton cycle with recompression (Source: Jeong et al. [111]).

Shouhang and EDF are retrofitting the Dunhuang 10 MW tower plant (Phase I) with an sCO_2 power cycle and plan to commercialise a 100 MW plant (Phase II) with sCO_2 power cycle in the next 5 years [112]. Nevertheless, the sCO_2 power cycle has not yet been proven as a commercial technology. The immaturity of this technology limits the commercialised application due to technical challenges, such as near-critical compressor designs and turbomachinery to deal with high pressure, and non-technical challenges such as cost and safety [113, 114]. The thermal and exergetic efficiency performance of a recompression Brayton cycle power plant would be negatively affected by the sCO_2 solar receiver pressure drop for a direct solar sCO_2 system, which was examined by Vasquez Padilla et al. [115].

2.2.3 Design cases considered in this study

Fig. 2.2[2] shows representative working fluid temperature ranges, the corresponding thermal energy storage and power block throughout various tower receivers with a fixed size of 100 m^2. Systems are defined by the type of HTF in the receiver. The feasible temperature ranges for each HTF are used to determine the possible TES and the power block. The approach temperature differences of heat exchanger are assumed to be 20°C [12]. Fig. 2.2(a) shows the conventional molten salt CSP system used in the current commercialised projects, such as Noor III [116]. Fig. 2.2(b) shows the design of a sodium CSP system. The differences between Fig. 2.2(a) and Fig. 2.2(b) are the HTF and the heat exchanger; otherwise, these systems have the same TES and power block capacities.

As mentioned by Mehos et al. [12], high temperatures ($\geq$ 700°C) are required to achieve high efficiency in sCO_2 Brayton cycle, so sodium could be an appropriate candidate for the HTF in the receiver, which is shown in Fig. 2.2(c). Due to recuperation of CO_2, the temperature rise in the heat exchanger coupled to an sCO_2 Brayton cycle is about 200°C, which is proposed in Gen3 Liquid Pathway [12]. In conjunction with the pinch temperature of 20°C being assumed in the heat exchanger, the temperature range of high temperature salt in the TES is then 520–720°C. Alternatively, sCO_2 could be directly chosen as the HTF in the receiver, as shown in Fig. 2.2(d), although note that in this configuration no TES is considered. One concern with sCO_2 receivers is the stresses in the tube to deal with the high pressure ($\geq$ 200 bar) conditions. The tube wall thickness, especially for the sCO_2, has been carefully studied in the following sub-sections.

Fig. 2.2(e) shows that the inlet and outlet temperature difference of an air receiver is fixed at 200°C. Air can operate at high temperature ranges (e.g. 800–1000°C). However, the resultant effect of pressure and external wall temperature on tube stress may limit its operating temperature. Therefore, the operating temperature range was not specified in this work. The TES is assumed to be a packed-bed air TES [117] and the PB is assumed to be a steam Rankine cycle, if the working temperatures in the air receiver are lower than 700°C. At higher temperatures, a sCO_2 Brayton cycle can be considered. Fig. 2.2(f) shows a water/steam receiver coupled directly to a steam turbine to reduce system cost, again without storage being considered.

In order to make a unified comparison between working fluids in the receiver, the temperature range of steam Rankine cycle is fixed at 270–545°C due to the temperature limitation on molten salt (see Fig. 2.2(a), which in turn limits the operating temperature range of water/steam to 270–545°C). It is worth noting that, in order to show both sCO_2 and water/steam to their best advantage as receiver heat transfer fluids, they are directly coupled to the power block, as adding storage will further

[2]The concepts with 'freely varying' temperature ranges were not considered at this stage of the work, but instead later in Section 6.

lower their second-law efficiencies due to the infeasibility of the direct storage. Identical PBs with equal temperature ranges are considered for all steam Rankine cycles. For different working fluids, the variations of receiver temperatures are assigned accordingly, as shown in Fig. 2.2. A relatively narrow 200°C temperature range is evaluated based on the heat-addition temperature range for some typical recuperated Brayton cycles, for the high-temperature sodium, the sCO_2 and the air cycles. In addition, there is no benefit to lowering the receiver inlet temperature (it reduces exergy efficiency of the receiver, which is equivalent to lowering the energy efficiency of the power block combined with receiver). Meanwhile, raising the receiver outlet temperature is not considered feasible due to material limits.

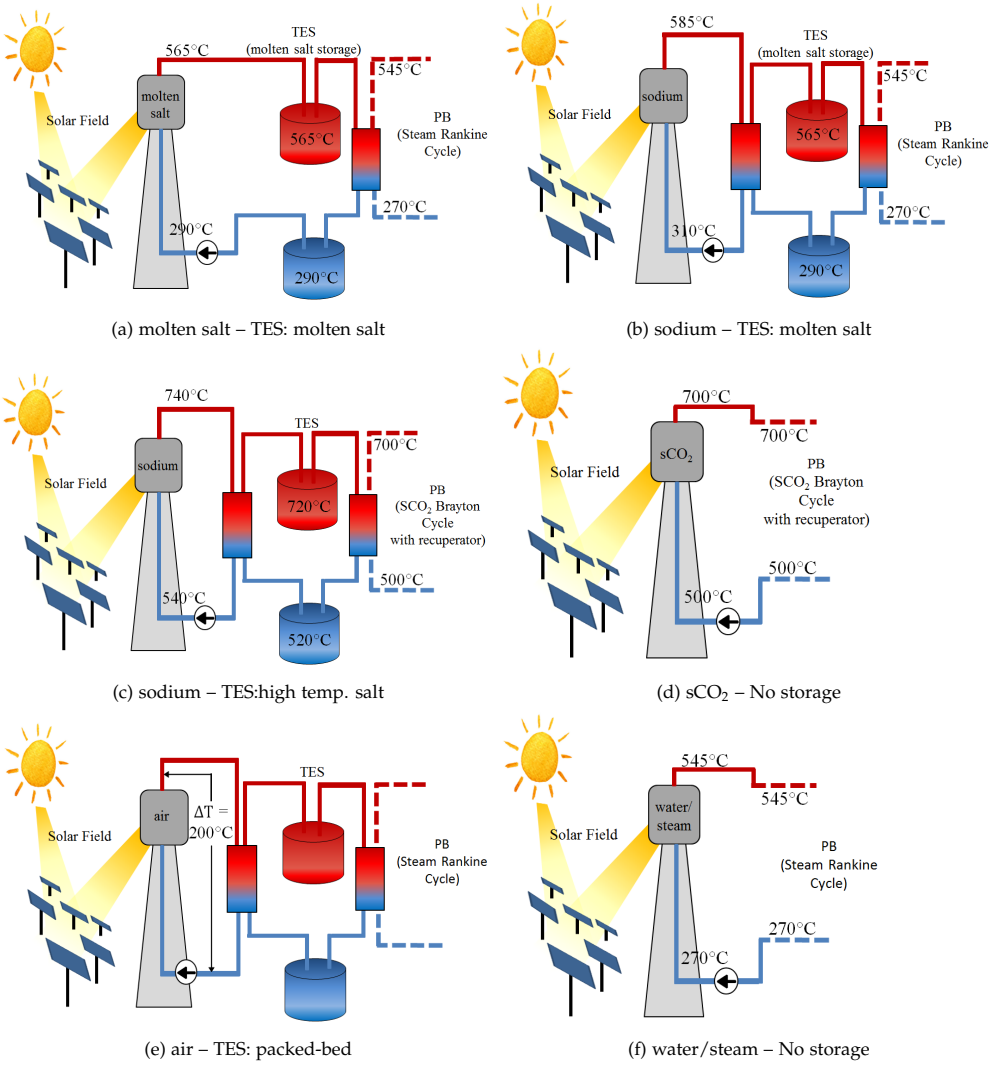

Fig. 2.2: Conceptual designs for tower receivers with the various HTF and the corresponding TES and power block considered in this study.

2.3 Heat Transfer Fluids (HTFs)

This section introduces the high-temperature HTFs considered in this chapter and discusses their prior use in CSP.

2.3.1 Intensive thermophysical properties

The efficiency of the receiver is strongly affected by the heat transfer properties of the HTF in question. Fig. 2.3 shows the main thermophysical properties of the five selected HTFs, at the individually corresponding outlet pressures. Fig. 2.3(a) shows that water/steam has the highest specific heat capacity, which means that it requires more energy to heat up or cool down the fluid across a given temperature range, when compared to other fluids. Fig. 2.3(b) shows the variation of viscosity for the various HTFs. Viscosity influences the energy losses associated with the movement of fluids in the tubes as it generates heat and pressure drop. Also, it influences the turbulence of the flow. Fig. 2.3(c) shows that liquid sodium is the most thermally conductive fluid, and it is two orders of magnitude higher than liquid water and molten salt. Fig. 2.3(d) shows that salt is considered to be a good thermal storage medium in the relatively high temperature range (290–565°C), since it has high density (ρ, kg/m^3) and relatively high specific heat capacity (c_p, kJ/kg/K), resulting in a high volumetric heat capacity (ρc_p, in kJ/m^{3}K), and consequently low storage volume to store same amount of energy, at the same operating temperature range.

2.3.2 Figures of Merit (FOM)

Researchers have tried to find a single way to compare the intensive properties of specific HTFs, as a working fluid for CSP or other applications. It is recognised that improved heat transfer comes at the cost of increased pressure drops [126]. Therefore, it is necessary to control the pressure drop while enhancing the heat transfer. In general, the pumping power required to give the same fluid temperature rise, can be determined as $P = \dot{m}\Delta p/\rho$. The heat transfer is given by $\dot{Q} = \dot{m}c_p\Delta T = hA(T_w - T_f)$. FOMs[3] provided by various researchers are summarised below in Table. 2.1. The detailed derivations will not be presented here. Interested readers can refer to the respective works [127, 128, 129]. Mouromtseff [127] found that the rate of heat transfer, for liquid coolants, at specified velocity and tube size, could be represented using Dittus-Boelter correlation. Bonilla [128] provided one FOM to determine the pumping power required for a given coolant temperature difference between inlet and outlet, at specified heat rate ($\dot{Q}$) and tube size. A smooth tube was assumed. The lower the pumping power, the lower the loss. Thus, the FOM was presented as $\frac{1}{p}$. Another FOM was provided by Bonilla to determine the pumping power required at a specified tube size and temperature difference between tube wall and the fluid

[3]The FOM analysis in this thesis is to show that it is insufficient to select the right working fluids only based on FOM. Several FOMs are used, as an example, to support our statement. A full study of FOM is out of the scope in this thesis.

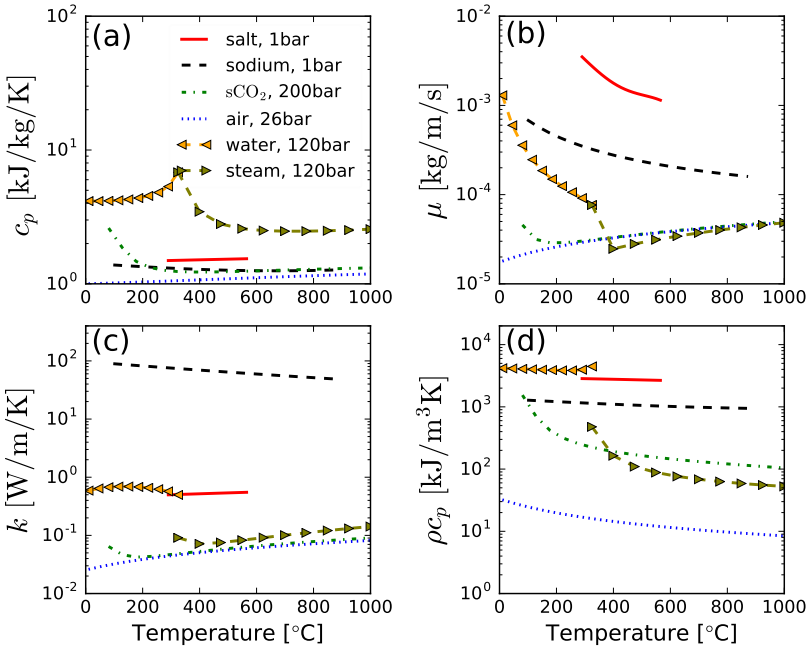

Fig. 2.3: Thermophysical properties of five selected HTFs as functions of temperature. Temperature ranges: salt (290–565°C) [118]; sodium (97.7–873°C) [119]; sCO_2 (31.1–1000°C) [120, 121, 122]; air (0–1000°C) [123, 124]; water (0–324.68°C (liquid), 324.69–1000°C (vapor)) [125]. (a) specific heat capacity; (b) viscosity; (c) thermal conductivity; (d) volumetric heat capacity.

to achieve a specified convection coefficient. Lenert et al. [129] suggested that the pumping power could also be determined at specified heat flux $\dot{q}$, tube length and temperature difference between the external wall and inlet fluid. As discussed above, the performance of the fluid as an HTF is determined by the combination of the thermophysical properties. FOMs are convenient to investigate the performance of the HTFs. By substituting the individual thermophysical properties of each HTF into the FOM proposed by different researchers, the rankings of variable HTFs are obtained as shown in Fig. 2.4. Fig. 2.4 (a), (c) and (d) show very similar trends that sodium performs the best, followed by water. Molten salt is a reasonable choice in the constrained temperature range. sCO_2 could be considered at elevated temperature (> 600°C). Fig. 2.4 (b) ranks water the best without considering the heat transfer through the wall.

However, the best HTF for a tubular receiver cannot be selected based on a limited analysis of only the thermophysical properties of the fluid alone. The FOMs provided above are only valid under specified assumptions. However, for example, different HTFs have different working temperature ranges. The performance of certain HTF would not be best presented if the comparison was constrained within a certain range. In addition, FOMs provide only rankings and no quantified performance difference. Other characteristics such as mechanical stress constraints on the

Table 2.1: Summarised Figures of Merit (FOM), given by various researchers. Full expressions and the corresponding constraints are listed.

No.	Reference	Expression	FOM	Constraint
a	Mouromtseff, 1942 [127]	$h_{\text{int}} = \frac{0.024\mathbf{V}^{0.8}}{D^{0.2}} \left(\frac{\rho^{0.8} {c_p}^{0.4} k^{0.6}}{\mu^{0.4}} \right)$	$\frac{\rho^{0.8} {c_p}^{0.4} k^{0.6}}{\mu^{0.4}}^{a}$	$\left(\frac{\mathbf{V}^{0.8}}{D^{0.2}} \right) = \text{const.}$
b	Bonilla, 1957 [128] (Eq. 9-80)	$P = \frac{0.092 L \dot{Q}^{2.8}}{D^{1.2} A^{1.8} \left(T_{\text{o}} - T_{\text{i}}\right)^{2.8}} \left(\frac{\mu^{0.2}}{\rho^{2.0} {c_p}^{2.8}} \right)$	$\frac{\rho^{2.0} {c_p}^{2.8}}{\mu^{0.2}}^{b}$	$\left(\frac{L \dot{Q}^{2.8}}{D^{4.8} \left(T_{\text{o}} - T_{\text{i}}\right)^{2.8}} \right) = \text{const.}$
c	Bonilla, 1957 [128] (Eq. 9-82)	$P = \frac{49859 L \dot{Q}^{3.5}}{D^{0.5} A^{2.5} \left(T_{\text{w}} - T_f\right)^{3.5}} \left(\frac{\mu^{0.1833}}{\rho^{2.0} {c_p}^{1.167} k^{2.33}} \right)$	$\frac{\rho^{2.0} {c_p}^{1.167} k^{2.33}}{\mu^{1.833}}^{c}$	$\left(\frac{L \dot{Q}^{3.5}}{D^{6.0} \left(T_{\text{w}} - T_f\right)^{3.5}} \right) = \text{const.}$
d	Lenert et al., 2012 [129]	$\frac{P}{\dot{Q}} \propto \frac{\dot{q}^{2.4} L^{0.4}}{\left(T_{\text{w}} - T_{\text{i}}\right)^{3.4}} \left(\frac{\mu^{1.4}}{\rho^{2.0} {c_p}^{1.6} k^{1.8}} \right)$	$\frac{\rho^{2.0} {c_p}^{1.6} k^{1.8}}{\mu^{1.4}}^{d}$	$\left(\frac{\dot{q}^{2.4} L^{0.4}}{\left(T_{\text{w}} - T_{\text{i}}\right)^{3.4}} \right) = \text{const.}$

[a] This FOM was determined at specified velovity and tube size.
[b] This FOM was determined at specified heat rate ($\dot{Q}$), temperature difference between fluid inlet and outlet, and tube size.
[c] This FOM was determined at specified temperature difference between tube wall and the fluid, and tube size.
[d] This FOM was determined at specified heat flux ($\dot{q}$), tube length, temperature difference between external wall and fluid, and tube size.

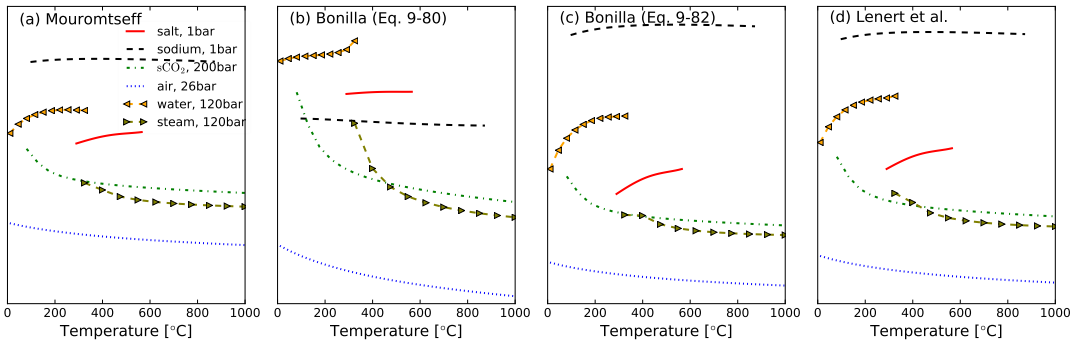

Fig. 2.4: FOM for different HTF, calculated by the different correlations as linked in Table 2.1. The vertical axis is in a logarithmic scale. Units of measurements and absolute magnitudes have been omitted because its only the relative magnitude that matters within each graph.

tube, exergy destruction, external losses, and tube wall conduction should also be considered. Proper evaluation of working fluids requires a more detailed model that brings in all of these phenomena, as discussed in the following sections.

2.4 Development of a comparative model

An approach to modelling and comparing CSP systems is to consider them as energy chains, consisting of a tubular receiver with fixed size of 100 m^2, a pump, a simplified TES, and a simplified PB with a fixed second-law efficiency ($\eta_{II,PB}$) of 75%[4] [85] for each working fluid. Co-optimising the PB and receivers together is beyond the scope of this work and therefore, a fixed second-law efficiency is included to account for some power block irreversibilities. The heat transfer correlations for internal convection for each fluid selected for this work are described. Pumping work and pressure stresses on the tubes are considered in the modelling. In addition, detailed receiver configurations and exergy accounting for each component of the whole system are developed.

2.4.1 Receiver integrated model

In this chapter, tubular receivers are composed of multiple tube banks in series, under an assumption of uniform flux. The impact of design parameters including the number of tubes per bank, passes, and flow direction, are several of the key receiver choices in the receiver optimisation process. The effect of varying flow direction (the fluid flows from the centre of the receiver to the edges or from one edge to the other edge) on the system performance is not discussed in this chapter, due to the assumption of uniform flux distribution on the receiver. A Gemasolar-style receiver [95] was

[4]It is also a rule of thumb that is approximately true across a wide temperature range, scale, and pressure, for commercially mature systems.

modelled, with several tube banks /passes connected in series, with several tubes connected in parallel in each bank, as shown in Fig. 2.5. The receiver was divided into n segments (where $n = 100$[5] in full flow path length), to accurately calculate heat and hydrodynamic transfers along the front half of the tube. The back half of the tube was assumed as an adiabatic wall, with no heat transfer in any form, as shown in Fig. 2.6. The receiver size was fixed at 100 m^2, with uniform G (1 kW/m^2) and the optical concentration ratio CR (800[6]), thus, the total incident energy, $\dot{Q}_{inc}$ was 80 MW. The tube lengths were fixed at 10 m. No spacing between tubes was assumed. Manifolds were used to redistribute the internal flow from one bank to the other. In this chapter, uniform flux was assumed, and the mass flow rate was evenly distributed to each tube in one bank, so that mixing effects in the manifold on the receiver can be ignored. Table 2.2 summarises all the fixed parameters considered in this chapter. The heat losses within non-irradiated portions of the receiver pipework, including the manifolds, have been ignored, on the assumption that good insulation will make such heat loss negligible compared to the losses from the exposed pipework. The pressure drops within the unexposed pipework and manifolds are also neglected since, as seen later, exergy destruction due to flow friction is rather negligible compared to other effects, for all cases except for some designs using air, which is anyway not found to be the preferred fluid. Nevertheless, the pressure drops in the manifolds are considered and modelled in Sec. 5.3.4.2 in the context of experimental results (Chapter 5).

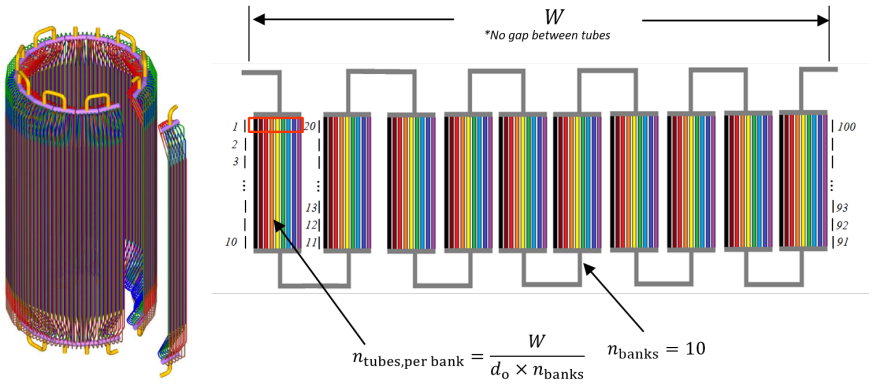

Fig. 2.5: Left: Configuration of a Gemasolar-style receiver modelling [95]. Note that in this study, we consider the receiver to be flat, not cylindrical. Right: the flow configuration considered in the present work, with a uniform incident flux. $n_{\text{tubes,receiver}} = \frac{W}{d_o}$. Manifolds are not considered. Sample flow segments are numbered as shown next to the tube banks.

[5]This number was selected to avoid exceeded computing cost, but not to affect the accuracy of the results. A mesh sensitivity study was conducted, but no details were included here. Note that this section uses uniform flux, which means that relatively limited mesh effects arising here. Section 3.3.5 includes a mesh sensitivity study due to the non-uniform flux used in Chapter 3.

[6]This CR has been adjusted for air case in Section 2.5.3, to study the effect of varying the CR on the exergy efficiency of the air system.

Table 2.2: Summary of the fixed parameters in this chapter.

A_{receiver} (m^2)	L_{receiver} (m)	G (kW/m^2)	CR	spacing between tubes	$\eta_{\text{II,PB}}$ (%)
100	10	1	800	0	75

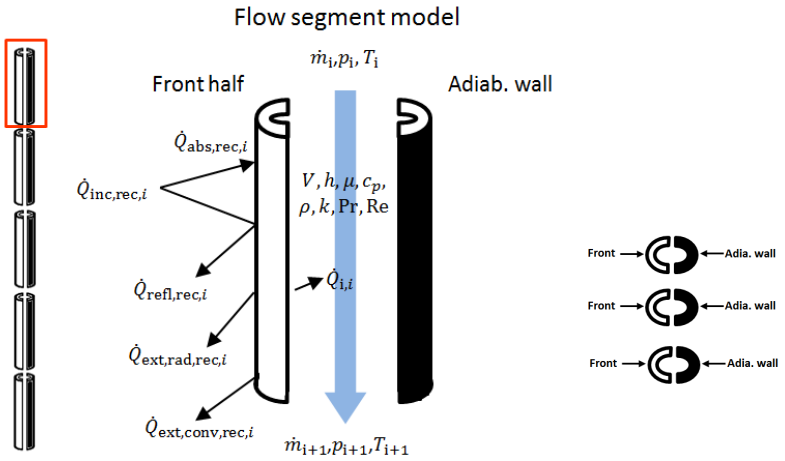

Fig. 2.6: Left: side view of an individual receiver tube. Middle: detailed energy balance, per segment. Right: top view.[130]

2.4.2 Energy and exergy accounting

Governing energy and exergy balance equations at steady state, used in this chapter, are described here. The incident energy per segment into a rectangular-shape billboard receiver is balanced by the reflection loss ($\dot{Q}_{\text{refl,rec},i}$) and the absorbed energy ($\dot{Q}_{\text{abs,rec},i}$).The absorbed energy is then balanced by segmental external losses by radiation ($\dot{Q}_{\text{ext,rad,rec},i}$) and convection ($\dot{Q}_{\text{ext,conv,rec},i}$), and net energy flow ($\dot{Q}_{\text{net,rec},i}$). Spillage losses were not considered in this chapter.

$$\dot{Q}_{\text{inc,rec},i} = \text{G} \cdot \text{CR} \cdot A_{\text{aper},i} = \dot{Q}_{\text{abs,rec},i} + \dot{Q}_{\text{refl,rec},i}, \tag{2.1}$$

$$\dot{Q}_{\text{refl,rec},i} = (1 - \alpha_{\text{eff}})\, \dot{Q}_{\text{inc,rec},i}, \tag{2.2}$$

$$\dot{Q}_{\text{abs,rec},i} = \dot{Q}_{\text{ext,rad,rec},i} + \dot{Q}_{\text{ext,conv,rec},i} + \dot{Q}_{\text{net,rec},i}, \tag{2.3}$$

$$\dot{Q}_{\text{ext,rad,rec},i} = \epsilon_i \sigma A_{\text{ext},i} \left(T_{\text{ext},i}^4 - T_{\text{amb}}^4 \right), \tag{2.4}$$

$$\dot{Q}_{\text{ext,conv,rec},i} = h_{\text{ext}} A_{\text{ext},i} \left(T_{\text{ext},i} - T_{\text{amb}} \right), \tag{2.5}$$

$$\dot{Q}_{\text{net,rec},i} = \frac{1}{2}\frac{2\pi k L_i \left(T_{\text{ext},i} - T_{\text{int},i}\right)}{\ln \frac{d_o}{d_i}}, \tag{2.6}$$

$$\dot{Q}_{\text{net,rec},i} = h_{\text{int},i} A_{\text{int},i} \left(T_{\text{int},i} - T_{\text{HTF},i}\right), \text{ and} \tag{2.7}$$

$$\dot{m}\left[(h_o - h_i) + \frac{1}{2}\left(\mathbf{V}_o^2 - \mathbf{V}_i^2\right)\right] = \dot{Q}_{\text{net,rec},i}. \tag{2.8}$$

where G is the direct normal irradiance in W/m^2, CR is the concentration ratio, $A_{\text{aper},i} = \frac{WL}{n}$. In total, there are n sequential segments in the receiver. The effective absorptivity, $\alpha_{\text{eff}} = \frac{\alpha}{\alpha + \frac{2(1-\alpha)}{\pi}} = 0.9676$, where $2/\pi$ compensates the cavity behaviour on a per-aperture-area basis at the front half of the tube to allow for the two-surface radiosity that will occur in the crevices between tubes. $A_{\text{ext},i} = \frac{1}{2}\pi d_{\text{ext}} L_{\text{ext},i}$ is the area of the front half external tube segment, $T_{\text{amb}} = 20°\text{C}$, and $k = 20$ W/(m·K) is an approximately average thermal conductivity value for the tube [131, 132, 133] (as shown in Fig. 2.7) and the conduction is assumed to occur only radially. $h_{\text{ext}} = 30$ W/(m^2 ·K) is an approximate mid-range mixed external convection coefficient value based on expected operational conditions [134]. The equivalent temperature of radiation of surrounding objects is assumed to be T_{amb} as the maximum temperature of the surroundings is quite low, and due to T^4 effects, it is not likely to have a strong effect. Eq. 2.6 is used to calculate tube wall conduction. Eq. 2.7 calculates internal convection.

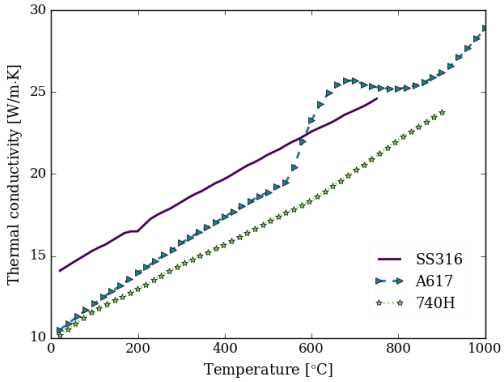

Fig. 2.7: Wall conductivities for a range of materials. Source: [131] (SS316), [132] (Alloy 617) and [133] (Alloy 740H).

The emissivity ϵ_i values, as a function of an absolute temperature in Kelvin, were determined by a curve-fit plot from Ho et al. [135]:

$$\epsilon_i = 0.1477 \log_e \left(T_{\text{ext},i} - 264.6\text{K}\right) - 5.671 \times 10^{-6} \left(T_{\text{ext},i} - 264.6\text{K}\right)^{1.3078} + 0.4988 \tag{2.9}$$

For a steady-state control volume, the total incident exergy in the receiver ($\dot{X}_{\text{inc,rec}}$)

is the sum of the exergy lost ($\dot{X}_{\text{loss,rec}}$), the exergy destruction ($\dot{X}_{\text{dest,rec}}$) and the net exergy ($\dot{X}_{\text{net,rec}}$) in each receiver segment. Hence, the exergy rate balance of the whole receiver is defined as:

$$\sum_{\text{rec},i} \dot{X}_{\text{inc,rec},i} = \sum_{\text{rec},i} \dot{X}_{\text{loss,rec},i} + \sum_{\text{rec},i} \dot{X}_{\text{dest,rec},i} + \sum_{\text{rec},i} \dot{X}_{\text{net,rec},i}, \tag{2.10}$$

where $\dot{X}_{\text{inc,rec},i}$ indicates the total exergy in incident sunlight and is calculated using Petela's formula [136], which ignores atmospheric scattering and absorption effects, and mirror imperfections, which would otherwise generally tend to reduce the exergy-to-energy ratio of the solar radiation:

$$\dot{X}_{\text{inc,rec},i} = \dot{Q}_{\text{inc,rec},i} \left(1 - \frac{4}{3}\frac{T_{\text{ref}}}{T_{\text{sun}}} + \frac{1}{3}\left(\frac{T_{\text{ref}}}{T_{\text{sun}}}\right)^4\right), \text{ and } \dot{X}_{\text{net,rec},i} = \dot{m}\left(\phi_{\text{i}} - \phi_{\text{o}}\right). \tag{2.11}$$

where T_{ref} is the reference temperature and is set to be 20°C.

A study by Asselineau et al. [93] examines the important effect of optical errors such as slope error, sun shape and mirror quality on the exergy performance of solar thermal concentrators. However, this effect was not considered in this chapter as the same energy input was used to make relative comparisons. ϕ denotes flow exergy, $\phi = h - h_{\text{ref}} - T_{\text{ref}}\left(s - s_{\text{ref}}\right) + \frac{1}{2}\boldsymbol{V}^2$.

$\dot{X}_{\text{loss,rec},i}$ indicates the exergy lost to the surroundings by heat transfer across the surface of receiver segment at $T_{\text{ext},i}$ and $\dot{X}_{\text{dest,rec},i}$ indicates internal irreversibilities in the receiver. The exergy losses and exergy destructions (internal irreversibilities) in the receiver segment are accounted as follows:

$$\dot{X}_{\text{loss,rec},i} = \dot{X}_{\text{loss,refl,rec},i} + \dot{X}_{\text{loss,ext,rad,rec},i} + \dot{X}_{\text{loss,ext,conv,rec},i}, \text{ and} \tag{2.12}$$

$$\dot{X}_{\text{dest,rec},i} = \dot{X}_{\text{dest,abs,rec},i} + \dot{X}_{\text{dest,wall,rec},i} + \dot{X}_{\text{dest,int,conv,rec},i} + \dot{X}_{\text{dest,flow,rec},i}. \tag{2.13}$$

More specifically, each exergy loss term in Eq. 2.12 is accounted as follows:

$$\dot{X}_{\text{loss,refl,rec},i} = \left(1 - \alpha_{\text{eff}}\right)\dot{X}_{\text{inc,rec},i}, \tag{2.14}$$

$$\dot{X}_{\text{loss,ext,rad,rec},i} = \dot{Q}_{\text{ext,rad,rec},i}\left(1 - \frac{T_{\text{ref}}}{T_{\text{ext},i}}\right), \text{ and} \tag{2.15}$$

$$\dot{X}_{\text{loss,ext,conv,rec},i} = \dot{Q}_{\text{ext,conv,rec},i}\left(1 - \frac{T_{\text{ref}}}{T_{\text{ext},i}}\right). \tag{2.16}$$

Each exergy destruction term in Eq. 2.13 is accounted as follows:

$$\dot{X}_{\text{dest,abs,rec},i} = \dot{X}_{\text{inc,rec},i} - \dot{X}_{\text{loss,refl,rec},i} - \dot{Q}_{\text{abs,rec},i}\left(1 - \frac{T_{\text{ref}}}{T_{\text{ext},i}}\right), \tag{2.17}$$

$$\dot{X}_{\text{dest,wall,rec},i} = \dot{Q}_{\text{net,rec},i}\left(\frac{T_{\text{ref}}}{T_{\text{int},i}} - \frac{T_{\text{ref}}}{T_{\text{ext},i}}\right), \tag{2.18}$$

$$\dot{X}_{\text{dest,int,conv,rec},i} = \dot{Q}_{\text{net,rec},i}\left(\frac{T_{\text{ref}}}{T_{\text{o},i}} - \frac{T_{\text{ref}}}{T_{\text{int},i}}\right), \text{ and} \tag{2.19}$$

$$\dot{X}_{\text{dest,flow,rec},i} = \dot{Q}_{\text{net,rec},i}\left(1 - \frac{T_{\text{ref}}}{T_{\text{o},i}}\right) + \dot{m}\left(\phi_{\text{i},i-1} - \phi_{\text{i},i}\right). \tag{2.20}$$

$\dot{X}_{\text{net,rec},i}$ indicates the net exergy gain with the working fluid, considering the pressure changes and kinetic energy.

$$\dot{X}_{\text{net,rec},i} = \dot{m}\left(\phi_{\text{o,rec}} - \phi_{\text{i,rec}}\right) \tag{2.21}$$

The second-law efficiency of the receiver (neglecting the pump and power block) is:

$$\eta_{\text{II}} = \frac{\sum \dot{X}_{\text{net,rec},i}}{\sum \dot{X}_{\text{inc,rec},i}} = \frac{\dot{X}_{\text{net,rec}}}{\dot{X}_{\text{inc,rec}}} \tag{2.22}$$

The exergy destruction in the pump is calculated as follows:

$$\dot{X}_{\text{dest,PU}} = \dot{W}_{\text{PU}} - \dot{m}\left(\phi_{\text{o,PU}} - \phi_{\text{i,PU}}\right) \tag{2.23}$$

where $\dot{W}_{\text{PU}}$ is the rate of the pump work, and is defined in Sec. 2.4.5.

The exergy destruction in the PB is calculated as follows:

$$\dot{X}_{\text{dest,PB}} = (1 - \eta_{\text{II,PB}})\dot{m}\left(\phi_{\text{o,rec}} - \phi_{\text{i,PU}}\right) \tag{2.24}$$

The second-law (exergy) efficiency of the Rankine power block (PB) $\eta_{\text{II,PB}}$, with a conventional Rankine cycle is assumed to be 75% [85].

The overall second-law efficiency of the system (including pump and power block) is the ratio of net work to the exergy of the sun reflected by the heliostat field,

$$\eta_{\text{II,sys}} = \frac{\dot{W}_{\text{net}}}{\dot{X}_{\text{inc,rec}}} = \frac{\dot{X}_{\text{net,rec}} - \dot{X}_{\text{dest,PU}} - \dot{X}_{\text{dest,PB}}}{\dot{X}_{\text{inc,rec}}} \tag{2.25}$$

As an example of these calculations, a Sankey diagram (in Fig. 2.8), demonstrates how the different exergy flows combine.

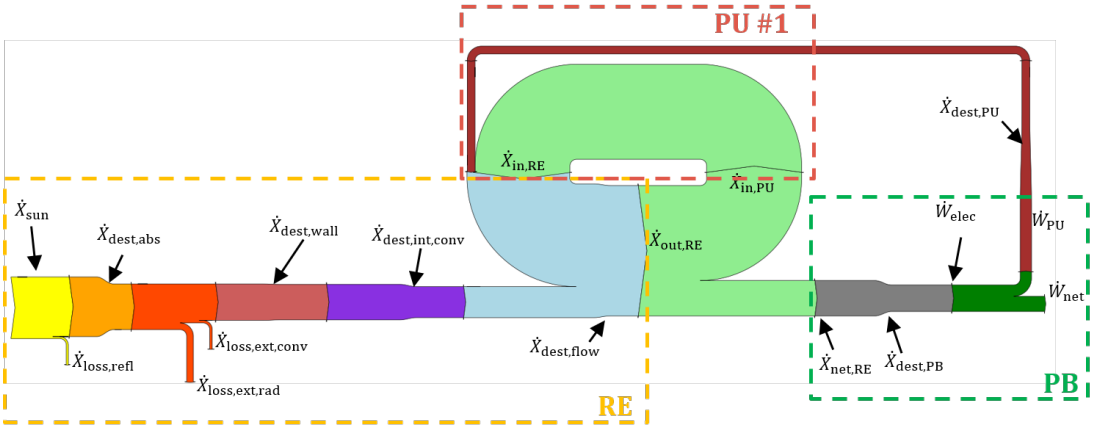

Fig. 2.8: A Sankey diagram to diagrammatically explain how the different exergy flows combine (add/remove, etc).

2.4.3 Pressure drop

The 1D momentum balance in the receiver, with no heat change, is:

$$\sum_{\text{rec},i} \left(p_{\text{o,rec},i} - p_{\text{i,rec},i}\right) = \sum_{\text{rec},i} \left[(\Delta p)_{\text{fric,rec},i} - \left(\rho_{\text{o,rec},i} \boldsymbol{V}^2_{\text{o,rec},i} - \rho_{\text{i,rec},i} \boldsymbol{V}^2_{\text{i,rec},i}\right)\right] \tag{2.26}$$

The pressure drop due to friction is calculated using the Darcy-Weisbach friction factor f_D, where friction factor f_D is assumed for turbulent, fully developed, smooth walls and ($3000 < \text{Re} < 5 \times 10^6$), as noted in Section 2.4.1.

$$(\Delta p)_{\text{fric}} = -f_D \frac{1}{2} \rho \mathbf{V}^2_{\text{i}} \frac{L}{d_{\text{i}}} \tag{2.27}$$

The exampled receiver model codes are included in Appendix A, which use molten salt as the working fluid.

2.4.4 The correlations for internal convection

The internal heat transfer coefficient is one of the main factors to examine the effectiveness of the working fluid. It is determined by the Nusselt number ($\text{Nu} = \frac{h_{\text{int}} d_{\text{i}}}{k}$), which is the function of Reynolds number ($\text{Re}_D = \frac{\rho \mathbf{V} d_{\text{i}}}{\mu}$) and Prandtl number ($\text{Pr} = \frac{c_p \mu}{k}$). For the range of working fluids, suitable internal convection correlations should be carefully considered to best represent the fluid. For molten salt, sCO_2 and air, the Gnielinski Correlation in [137] has been selected as it is widely used for fully developed turbulent flow in smooth tubes with uniform heat flux, or for gases, for $3000 \leq \text{Re}_D \leq 5 \times 10^6$ and $0.5 \leq \text{Pr} \leq 2000$. All properties are evaluated at bulk fluid

temperatures.

$$\mathrm{Nu} = \frac{\frac{f_\mathrm{D}}{8}\left(\mathrm{Re}_D - 1000\right)\mathrm{Pr}}{1 + 12.7\left(\frac{f_\mathrm{D}}{8}\right)^{0.5}\left(\mathrm{Pr}^{\frac{2}{3}} - 1\right)} \tag{2.28}$$

where f_D is Darcy friction factor and for smooth tubes:

$$f_\mathrm{D} = \left(0.79\ln\left(\mathrm{Re}_D\right) - 1.64\right)^{-2.0} \tag{2.29}$$

To simplify the modelling simulations, smooth tubes are assumed in this chapter. A comparison is made between smooth and rough wall assumptions as they relate to heat transfer and pressure drop. In general, the pressure loss due to friction is calculated using the Darcy friction factor f_D, as $f_\mathrm{D} = f\left(\mathrm{Re}_D, \frac{e}{d_\mathrm{i}}\right)$, where $\frac{e}{d_\mathrm{i}}$ is the relative roughness of the tube. For a turbulent flow with a Re value of 10^5 and $\mathbf{V}$ of 4 m/s, assuming relative roughness is approximated to be ($\frac{0.046\,\mathrm{mm}}{50\,\mathrm{mm}} = 9.2 \times 10^{-4}$) based on a common commercial steel tube, and with an inner diameter of 50 mm and a length of 10 m, it can be shown that friction factor f_D, the internal heat transfer coefficient and the pressure drop are accurate to within 25%, 10% and 12% respectively, under smooth tube assumption. Besides the accuracy, the smooth flow assumption may negatively influence the system efficiency by underestimating the pumping work required.

Liquid sodium requires different correlations due to its very low Prandtl number, typically in a range from 0.004 to 0.0075. Its high thermal conductivity and very low Prandtl number indicate that the thermal conduction is more significant compared to convection, so the thermal diffusivity is dominated by molecular conduction until Re > 2.14×10^5 [138]. Since the Gnielinski correlation is not valid for liquid sodium with such a low Prandtl number, four commonly-used correlations of heat transfer for liquid metal have been compared and described (Fig. 2.9).

For those liquid metals with slightly larger Prandtl number and Reynolds number, $0 < \mathrm{Pr} \leq 0.1$ and $10^4 \leq \mathrm{Re} \leq 5 \times 10^6$, Lyon and Martinelli, suggested the following correlation (as given by Foust [139]):

$$\mathrm{Nu} = 7.0 + 0.025\left(\frac{\mathrm{Re}_D\mathrm{Pr}}{0.85}\right)^{0.8} \tag{2.30}$$

Lubarsky and Kaufman [141] recommend the following correlation, for the case of the most of fully developed flows of fluids, $\mathrm{Re}_D\mathrm{Pr} < 200$:

$$\mathrm{Nu} = 0.625\left(\mathrm{Re}_D\mathrm{Pr}\right)^{0.4} \tag{2.31}$$

Skupinski et al. [140] recommended that the equation below could best represent sodium–potassium alloy (i.e. Nak) flow, for fully developed, turbulent, smooth tubes

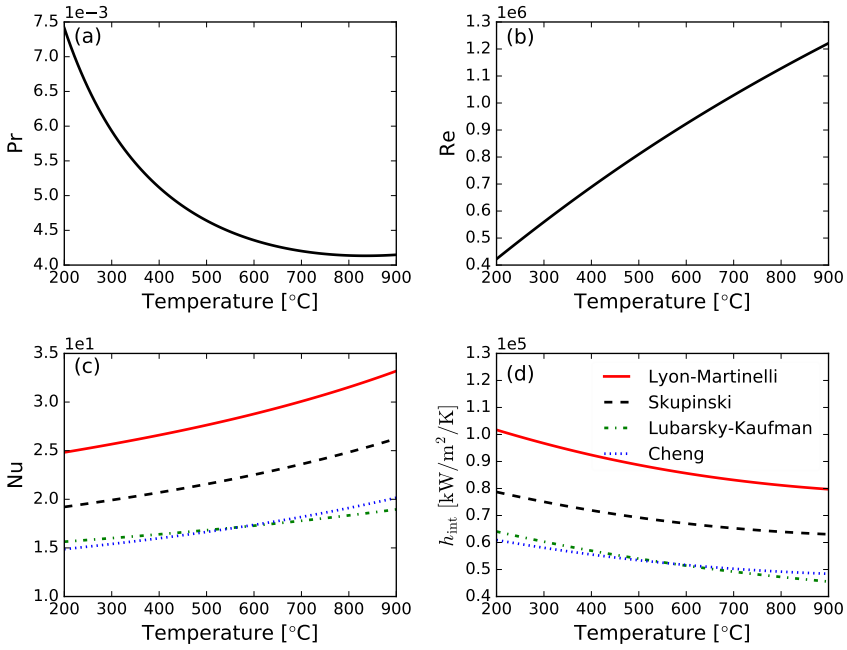

Fig. 2.9: Heat transfer performance of liquid sodium in the temperature range 200–900°C: (a) Prandtl number, (b) Reynolds number, (c) Nusselt number and (d) heat transfer coefficient, based on the correlations of Lyon and Martinelli (as given by Foust [139]) , Skupinski et al. [140], Lubarsky and Kaufman [141] and Cheng and Tak. [142], with flow parameters $d = 20$ mm and $\dot{m} = 3$ kg/s.

with uniform flux, $3 \times 10^{-3} \leq \mathrm{Pr} \leq 5 \times 10^{-2}$, $3.6 \times 10^{3} \leq \mathrm{Re} \leq 9.05 \times 10^{5}$:

$$\mathrm{Nu} = 4.82 + 0.0185 \left(\mathrm{Re}_D \mathrm{Pr}\right)^{0.827} \tag{2.32}$$

Using data from experiments with $\mathrm{Re}_D\mathrm{Pr} \geq 2000$ for Lead Bismuth Eutectic (LBE), Cheng and Tak[7] [142] gave that:

$$\mathrm{Nu} = 3.6 + 0.018 \left(\mathrm{Re}_D \mathrm{Pr}\right)^{0.8} \tag{2.33}$$

The Sodium-Nak Engineering Handbook [139] suggested that the correlation of Skupinski may be the best for sodium. On that basis, with the lack of further literature, and noting that it is the middle of the range compared to other correlations, this correlation has been selected for use in the present work.

Flow boiling of water/steam is a complex phenomenon due to the phase change, and requires special correlations. In this study, all tubes in a bank are assumed to experience the same flow rate and same incident flux distribution. The flow instabilities in two-phase flow that leads to unequal flows in parallel pipes can be mitigated through the use of orifice plates [143]. For the fluid in the single phase regions (either

[7]Referring to Cheng and Tak, there is a wide range of Nu values depending on the different experimental data set. Cheng mentions a range of reasons for the variation. There has not been, to our knowledge, any work that provides clarity on which is most accurate, especially as relates to sodium.

liquid water or super-heated steam), and for Re < 10^5, the Gnielinski correlation [137] (Eq. 2.28) is used. For Re$\geq 10^5$, a correlation suggested by Petukhov [144] is used as:

$$\mathrm{Nu} = \frac{\frac{f_D}{8}\left(\mathrm{Re}_D \mathrm{Pr}\right)}{1.07 + 12.7\left(\frac{f_D}{8}\right)^{0.5}\left(\mathrm{Pr}^{\frac{2}{3}} - 1\right)} \tag{2.34}$$

For the fluid in two-phase saturated mixtures with a steam quality in the range of $0 < x \leq 0.8$, the Kandlikar correlations [145] were used (see Appendix B), while in the range of $0.8 < x \leq 1$ and $0.88 \leq \mathrm{Pr} \leq 2.22$, the Groeneveld correlation [146] was used, similarly to the approach used by Zapata et al. [94].

2.4.5 Pump Work

The pressure drop across the receiver should be critically designed as it affects the pumping work required to supply the needed upstream inlet pressure. The large pump work and the extra costs for a larger pump should be avoided. In general, there is a trade-off between pressure drop and convection heat transfer.

In this work, liquids are treated as incompressible fluids. Pump work is defined to be negative when the system is doing work on the pump. Since it has been assumed that there is no heat transfer across the pump, if changes in potential energy are negligible, the energy balance of the pump and the isentropic pump efficiency (was set to 0.8) of a pump, assuming equal diameter pipes at inlet and outlet, are then reduced to:

$$0 = -\dot{W}_{\mathrm{PU}} + \dot{m}\left(h_i - h_o + \frac{\mathbf{V}_i^2 - \mathbf{V}_o^2}{2}\right) \tag{2.35}$$

$$\eta_{\mathrm{is}} = \begin{cases} \dfrac{\dot{m} v_o \left(p_o - p_i\right)}{-\dot{W}_{\mathrm{PU}}} \left(\text{incompressible}\right) \\ \dfrac{\dot{m}\left(h_{o,\mathrm{is}} - h_i\right)}{-\dot{W}_{\mathrm{PU}}} \left(\text{compressible}\right) \end{cases} \tag{2.36}$$

For the compressible gas like sCO_2 and air, the pump is working as a compressor which increases the pressure of the gas, by reducing the volume. The ideal gas equation ($pv = RT$) is applied to air. The work done on the pump increases the temperature of the gas, when the gas cannot be compressed to a smaller specific volume.

2.4.6 Pressure stresses on the tube

The tube dimensions (outer diameter and wall thickness) considered in this work are taken from ASME B36.10 [147]. For thin walled tubes ($\frac{r}{t} \geq 10$), the stresses in the

circumferential direction and axial direction are determined as :

$$\sigma_\theta = \frac{pr}{t} \; ; \; \sigma_z = \frac{pr}{2t} \tag{2.37}$$

For thick walled tubes ($\frac{r}{t} < 10$), the stresses at the inside surface considering only internal pressure, are calculated as the following [148]:

$$\sigma_\theta = p_\mathrm{i} \left[\frac{r_\mathrm{i}^2 + r_\mathrm{o}^2}{r_\mathrm{o}^2 - r_\mathrm{i}^2} \right] \; ; \; \sigma_z = \frac{p_\mathrm{i} r_\mathrm{i}^2}{r_\mathrm{o}^2 - r_\mathrm{i}^2} \; ; \; \sigma_r = -p_\mathrm{i} \tag{2.38}$$

Maximum distortion energy theory [149], also referred to as the von Mises yield criterion, is then applied. The equivalent stress is calculated as:

$$(\sigma_\theta - \sigma_z)^2 + (\sigma_z - \sigma_r)^2 + (\sigma_r - \sigma_\theta)^2 = 2\sigma_{Eq}^2 \tag{2.39}$$

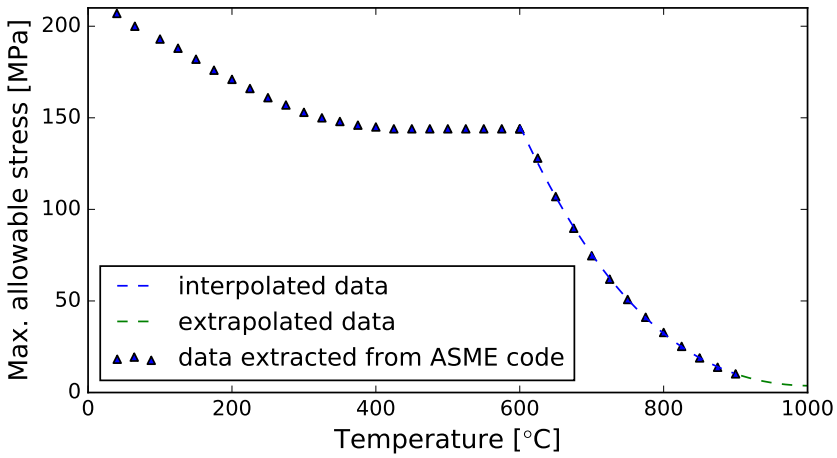

Fig. 2.10: Max. allowable stresses in MPa as a function of temperature for HAYNES® 230® [150]

The maximum allowable stress as a function of temperature for HAYNES® 230® is plotted in Fig. 2.10. A $F_{\text{safety,min}}$ of 1.2 ($F_{\text{safety}} = \frac{\sigma_{\text{allow}}}{\sigma_{Eq}}$) is preliminarily set to determine the minimum wall thicknesses by avoiding exceeding the yielding stress in the tubes. For the case of sCO_2 receivers which suffer from the high internal pressures, this minimum safety factor might be underestimated. HAYNES® 230® [151] is considered as the tube material in this chapter. It is a nickel-chromium-tungsten-molybdenum alloy, which has longer thermal stability and lower thermal expansion when compared to other high-temperature alloys. Alternative materials are studied in Chapter 6. The evaluation of alternative materials of construction is not included within the scope of the present chapter. Thermal stresses including creep and fatigue damage, are important considerations on tube material selection and appropriate tube wall thickness [72], but are not considered in the present work.

2.5 Results and Discussion

The thermal model is solved using the equation-based ASCEND modelling environment [152] with up to 10^4 nonlinear equations. Python codes, as a wrapper around the core model, are implemented to handle the parameter exploration. In the model, fixed parameters are receiver geometry (W and L), CR, n (i.e. i), $T_{\mathrm{i,PU}}$, $T_{\mathrm{o,rec}}$, $p_{\mathrm{o,rec}}$, h_{ext}, $\eta_{\mathrm{II,PB}}$ and η_{PU}. Free parameters are n_{banks}, d_{o}, and t. The second-law efficiency of the system $\eta\mathrm{II,sys}$ is the optimised parameter. The calculation procedure starts from setting fixed input parameters, $p_{\mathrm{o,PU}}$ and an initially guessed $\dot{m}$, but free $T_{\mathrm{o,rec}}$ and $p_{\mathrm{o,rec}}$. Once this initial procedure is converged, the $T_{\mathrm{o,rec}}$ and the $p_{\mathrm{o,rec}}$ are fixed and then the model is solved again using QRSLV non-linear equation solver [152] with $\dot{m}$ and $p_{\mathrm{o,PU}}$ being free variables. Once a robust solution has been found, a broad range of receiver configurations are analysed by varying some of the input parameters (i.e. n_{banks}, d_{o}, t) to examine the first and second law efficiencies of the receiver and the whole system (i.e. parametric studies). The optimal receiver designs are identified from the results of the parameter sweeps on the above-mentioned input variables.

2.5.1 Molten salt, liquid sodium and water/steam receivers

The effect of varying the tube diameter, wall thickness[8] and flow configurations for a molten salt receiver are studied, and shown in Fig. 2.11[9]. Fig. 2.11(a) shows the exergy efficiency for a molten salt receiver only, while Fig. 2.11(b) shows the exergy efficiency for molten salt system, including the effect of the receiver losses, pumping losses and PB losses. Overall results are shown later in Table 2.5. Reducing the tube diameter improves internal heat transfer, resulting in reduced exergy destruction in internal convection and external losses, due to lower inner and outer wall temperatures. A larger number of banks increases the tube friction due to increased fluid velocity, resulting in improved heat transfer enhancement and hence higher efficiency for the receiver. However, small-diameter tubes and a large number of banks increases the pressure drop across the receivers, consequently requiring increased pumping work. The trade-off between receiver efficiency and pumping losses leads to an optimum in system efficiency, which here is a molten salt receiver with fewer tube banks, dropping from five banks (i.e. the best case for the receiver only) to two banks (i.e. the best base for the whole system).

Without thinking about the costs or material limits, the best molten salt case ($d_o = 10.3\,\mathrm{mm}, n_{\mathrm{banks}} = 2, \Delta p_{\mathrm{rec}} = 16.93\,\mathrm{bar}, \eta_{\mathrm{II}} = 41.42\%$) has been found, as labelled on Fig. 2.11 (b). Pump isentropic efficiency and power block exergy efficiency were assumed to be 80% and 75%, respectively [85]. The regions with laminar or

[8] For each outer tube diameter, the corresponding wall thickness is determined based on the standard (STD) ASME B36.10 specifications.

[9] These figures require to be printed in colour, please consult the original pdf if you use the black-and-white copy.

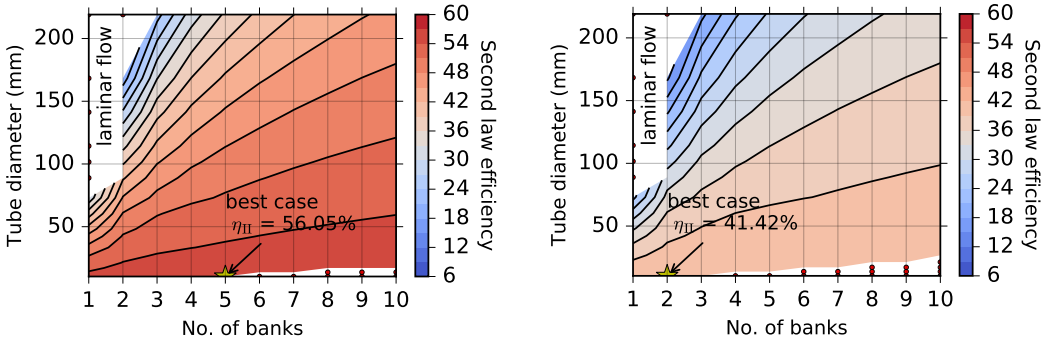

(a) $\eta_{II,rec}$ (b) $\eta_{II,sys}$

Fig. 2.11: The exergy efficiency for (a) molten salt receiver only, and (b) of the whole system (molten salt rec. + pump + Rankine cycle). The receiver is operating from operating from 290–565°C. Red dots on the bottom right of each figure indicate infeasible points where the pressure drops are over 100 bar. A laminar flow region appears as the simulation couldn't be converged if the Reynolds number was set more than 2000. In addition, the laminar flow only appears when the receivers have very few banks/bends. The lower bound on tube size is 10.3 mm, which is the smallest readily-available size under ASME B36.10 specifications. Solid efficiency lines clearly show the trend of the relationship between tube diameter and number of banks, that is, large-diameter tubes should configure with more banks in series to improve internal heat transfer when compare to small-diameter tubes if same second law efficiency is to be achieved.

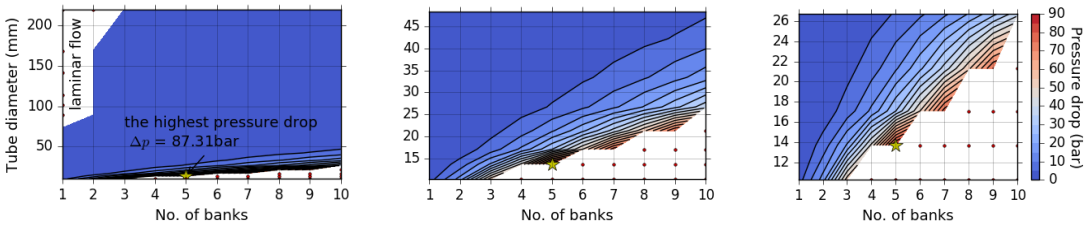

(a) 10.3 mm to 219.1 mm (b) 10.3 mm to 50 mm (c) 10.3 mm to 27 mm

Fig. 2.12: Localised pressure drops for studied molten salt receivers, as functions of varying tube size and flow configuration. The figure is divided into plots ((a): 10.3 mm to 219.1 mm; (b): 10.3 mm to 50 mm; (c): 10.3 mm to 27 mm) showing different ranges of tube sizes, for clarity. Red dots on the bottom right of each figure indicate that the pressure drops are over 100 bar.

transition flow (Re $<$ 3000) caused by a large-tube with one bank connected in series and the regions with large pressure drops ($>$ 100 bar) have been masked off.

Localised pressure drops for the studied molten salt receiver are shown in Fig. 2.12. Fig. 2.12(a) illustrates a complete picture of the pressure drop for a range of tube diameters and number of banks. The pressure drop increases rapidly for small tube sizes. The largest pressure drop occurs when $n_{\text{banks}} = 5$ and $d_{\text{o}} = 13.7$ mm. Fig. 2.12(b) provides a closer look at those tube diameters of interest commercially and Fig. 2.12(c) shows that with small-diameter tubes, pressure drop is very sensitive to the number of banks connected in series.

However, small tubes are costly to weld and the receiver should deploy a pump with high pressure drop which may increase the cost as well. Hence, from a cost point of view, it would be better to have larger tubes with fewer welds and simpler manufacturing. For example, for a specified configuration with larger tubes ($d_o = 48.3$ mm, $n_{\text{banks}} = 10$, $\Delta p_{\text{rec}} = 4.32$ bar, $\eta_{\text{II}} = 40.73\%$), the 0.7% drop in efficiency would be potentially paid off by a cheaper pump and a longer lifespan of tubes with less pressure stress. By way of example, it is noted that commercial salt receivers use tubes of approximate 23 mm in Solar Two [13] and 40.9 mm in Abengoa Solar [153].

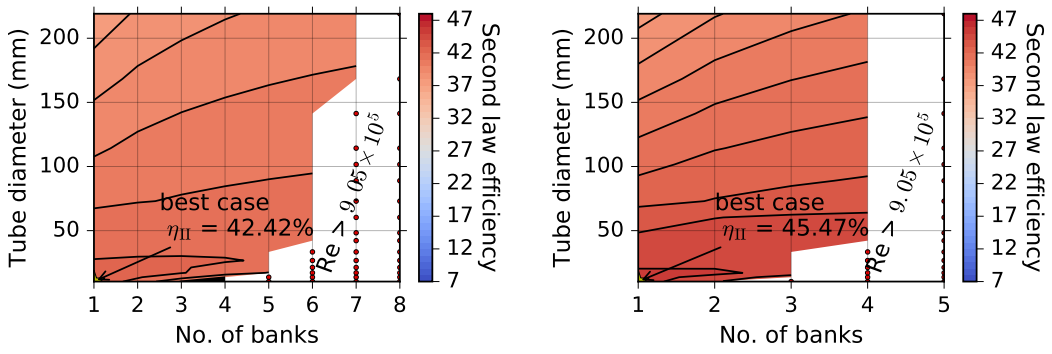

(a) sodium, operating from 310–585°C

(b) sodium, operating from 540–740°C

Fig. 2.13: Exergy efficiency $\eta_{\text{II,sys}}$, including the receiver and pump losses, for systems using sodium, as functions of varying tube size and flow configuration.

The optimal second-law efficiency for the whole system, including pumping and power block losses, is next examined for sodium, as shown in Fig. 2.13. The operating temperature range (310–585°C) of the sodium receiver (Fig. 2.13(a)) allows for a sodium-salt heat exchanger (Fig. 2.2(b)) and ensures that the comparison between sodium and molten salt systems is being done under the same power block conditions. Points with Re $> 9.05 \times 10^5$ are masked off due to the limits of the available heat transfer correlations. The results show that the sodium receiver was more efficient than that with molten salt. The sodium receiver is less sensitive to variations of

tube dimensions and flow configurations owing to its high thermal conductivity. Additionally, with fewer banks connected in series, sodium had better performance than molten salt. Referring to Mehos et al. [12], one way to improve the system efficiency was to improve the thermal-to-electricity efficiency by operating the sCO_2 Brayton cycle at high temperature (> 700°C). This could be achieved by using high temperature liquid sodium as the HTF in the receiver (Fig. 2.13(b)). The design case refers to Fig. 2.2(c). The receiver efficiency was increased due to low exergy destruction in absorption and in wall (Fig. 2.16). In order to store energy at high temperature, conventional molten salt cannot be used. Hence, other storage materials could be considered here, such as carbonate or chloride salts [154], PCM materials and molten glass as mentioned in Section 2.1.

However, an examination of exergy destruction in the heat exchanger is required for the best sodium case, in order to make a fair comparison with the best molten salt case. A simple calculation of the exergy destruction based on a 20°C pinch temperature is assumed for this heat exchanger, and gives exergy destruction of 0.8 MW, which is significant but not enough to erase the benefit of the sodium compared to the molten salt. Costs analysis will be conducted in Chapter 6. Full treatment of the receiver and heat exchanger will be conducted in Chapter 7.

Similar to molten salt, the most efficient water/steam receiver should have small-tubes with a few tube banks in series, as shown in Fig. 2.14. Gas flow can be treated as incompressible for low Mach number ($Ma = \boldsymbol{V}/c < 0.3$), as the compressibility effects are insignificant, less than about 3% [155]. The speed of sound of steam, c_{steam} at 545°C, 120 bar is 667.56 m/s. Therefore, those receiver designs with $\boldsymbol{V} > 200.268$ m/s were not shown on this figure. The exergy efficiency of the best water/steam system is 38.75%, which is 3% lower than the molten salt system, and 7% lower than the high-temperature sodium system. Further discussion on the differences between these fluids is provided in Section 2.5.4 further below.

2.5.2 sCO_2 receiver

The sCO_2 system should be treated carefully, as it was designed to operate at high temperature range and high pressure. The ideal-case scenario for sCO_2 would be a receiver with negligible pressure drop across the inlet and outlet (i.e. $p_i \approx p_o$) and negligible temperature difference cross the external wall and the fluid (i.e. $T_{\text{ext,rec}} \approx T_o$). Table 2.3 shows the minimum tube wall thickness required for this ideal-case scenario, as calculated using von Mises criterion. Tubes with DN greater than 80 have been crossed out due to the infeasibility of $F_{\text{safety,min}} = \frac{\sigma_{\text{allow}}}{\sigma_{\text{Eq}}} < 1.2$. σ_{Eq} is calculated using Eq. 2.38 and Eq. 2.39 by assuming an inlet pressure of p_{i} = 200 bar, while σ_{allow} is interpolated from Fig. 2.10 at 700°C.

Next, F_{safety} for each sCO_2 receiver using standard tubes, calculated $T_{\text{ext,rec}}$ and

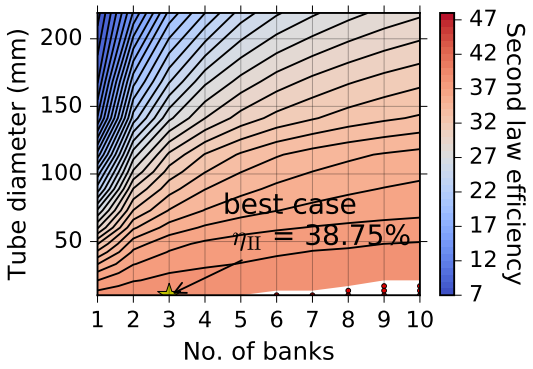

Fig. 2.14: Exergy efficiency $\eta_{II,sys}$, including receiver and pump losses, for systems using water/steam, as functions of varying tube size and flow configuration. The receiver is operating from 270–545°C. Red dots on the bottom right of the figure indicate that the pressure drops are over 80 bar.

Table 2.3: The minimum tube wall thicknesses for the ideal-case sCO_2 receivers, at 700°C and 200 bar.

DN	**DN6**	**DN8**	**DN10**	**DN15**	**DN20**	**DN25**	**DN32**	**DN40**
OD (mm)	10.3	13.7	17.1	21.3	26.7	33.4	42.2	48.3
t_{min} (mm)	1.65	2.20	2.75	3.42	4.29	5.37	6.78	7.76
DN	**DN50**	**DN65**	**DN80**	~~**DN90**~~	~~**DN100**~~	~~**DN125**~~	~~**DN150**~~	~~**DN200**~~
OD (mm)	60.3	73.0	88.9	~~101.6~~	~~114.3~~	~~141.3~~	~~168.3~~	~~219.1~~
t_{min} (mm)	9.69	11.73	14.28	~~16.32~~	~~18.63~~	~~22.70~~	~~27.04~~	~~35.20~~

calculated pressures is determined. With current receiver design points (80 MW on a receiver of 100 m^2, CR = 800), it appears impossible to obtain a feasible design for sCO_2 using standard tubes, in terms of finding appropriate tube size and wall thickness to meet the criterion of $F_{\text{safety}} > 1.2$. One possible solution to increase the safety factor is to lower the concentration ratio and increase the receiver size, while keeping the total energy on the receiver as same as 80 MW. The feasible cases were found with CR = 160, as shown in Fig. 2.15. All the red dots in the figure indicate that F_{safety} was smaller than 1.2. Reducing the CR results in low heat transfer in the receiver, consequently greatly reduces the system efficiency.

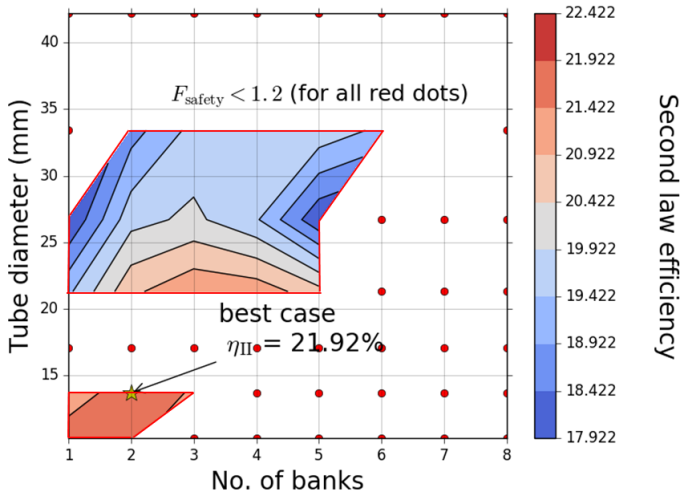

Fig. 2.15: Exergy efficiency $\eta_{\text{II,sys}}$, including receiver and pump losses, for systems using sCO_2, as functions of varying tube size and flow configuration. Only a limited set of were feasible for the sCO_2 system with CR = 160, as highlighted using red frames. The 17 mm tube is infeasible at its specified available thicknesses.

2.5.3 Air receiver

Under the assumptions in this study, the air system had uncompetitive performance due to poor heat transfer, which led to large exergy destruction in wall conduction and in internal convection. The trade-offs between external thermal radiation, internal convection and pumping losses for the air receiver were reflected in the system second-law efficiency, as shown in Fig. 2.16. A sensitivity study (in Table 2.4) was conducted to further evaluate the performance of the air system. For a given amount of $\dot{Q}_{\text{inc}}$ (here, 80 MW), the receiver aperture area was determined by the CR ($A_{\text{aper}} = \frac{\dot{Q}_{\text{inc}}}{\dot{G} \cdot CR}$). At each pressure and each CR, the most efficient system was chosen by varying the temperature range and n_{banks}. The results show that air operating in the lower pressure range was less efficient than in the elevated pressure range. A large consumption of pumping work resulted in a large amount of heat generation due to compression, since pressure and temperature were directly proportional, which reduced the system efficiency. An intercooler could be used to

reduce pumping work. At increased pressure (e.g. 100 bar), the pressure drop across the receiver would not cause as much pumping work as occurs at low pressure (e.g. 8 bar). Hence, with slightly larger $n_{banks} = 3$, better internal heat transfer occurred, and consequently the system efficiency was increased. The best-case $\eta_{II,sys}$ for the air receiver was identified as 36.43%.

Table 2.4: Exergy efficiency ($\eta_{II,sys}$) of the air system for varying pump inlet pressure and concentration ratio, all presenting the best-efficiency scenario after varying the operating temperature range, and n_{banks}.

	Exergy efficiency (%)		
Pressure (bar)	CR = 800	CR = 640	CR = 400
8	infeasible:$\dot{W}_{PU} > \dot{W}_{elec}$	infeasible:$\dot{W}_{PU} > \dot{W}_{elec}$	23.94
13	14.49	24.79	30.22
27	33.45	34.49	32.24
50	33.41	34.63	32.64
100	35.41	36.43	36.32

2.5.4 Overall comparison

Table 2.5 summaries the optimal configurations of flow for each fluid. It shows that sodium had the highest performance, followed by molten salt. Detailed exergy accounting is summarised in Fig. 2.17. Sodium performed the best among the selected fluids, especially in the higher temperature range. In contrast to salt, sodium is capable of supplying heat to a high-temperature sCO_2 Brayton cycle, which has higher thermal-to-electrical efficiency and may cost less than the steam Rankine cycle. The performance of the sodium receiver in the lower temperature range is only marginally better than salt due to the lower external wall temperature, before consideration of the exergy losses in the heat exchanger. Detailed exergetic consideration in the sodium receiver coupled with a heat exchanger will be investigated in Chapter 7. Molten salt is still a competitive source as a working fluid in the receiver, and together with its dual role as HTF and TES, and its low price, it is the most commonly used HTF in central tower CSP systems today. Water/steam can connect with the steam turbine directly, which saves cost on equipment such as the heat exchanger, but is difficult to integrate with storage. During the boiling process, exergy destruction in absorption was large due to the low external wall temperature, while exergy losses in external radiation was low. It seems that sCO_2 was not a promising HTF choice for the receiver. To deal with high working temperature and pressure in the receiver tubes causes greater exergy losses than the anticipated savings arising from

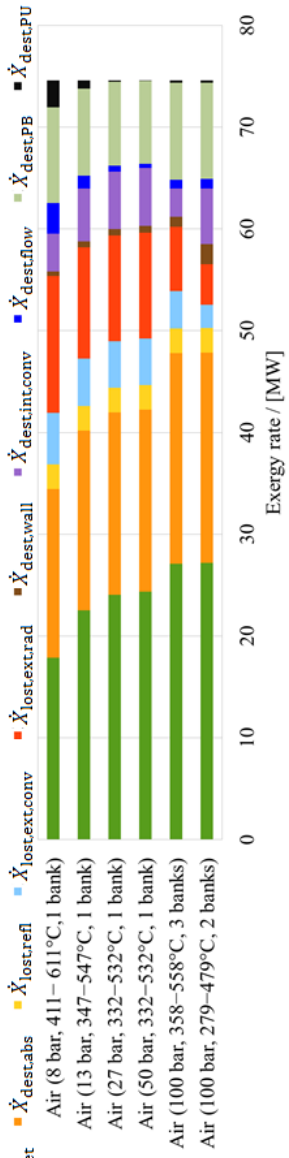

Fig. 2.16: Detailed exergy accounting for the air receivers with varied pressure, all presenting the best-efficiency scenario after varying the operating temperature range, and n_{banks}. For air, the greatest exergy efficiency is seen at higher pressures with a lower temperature range.

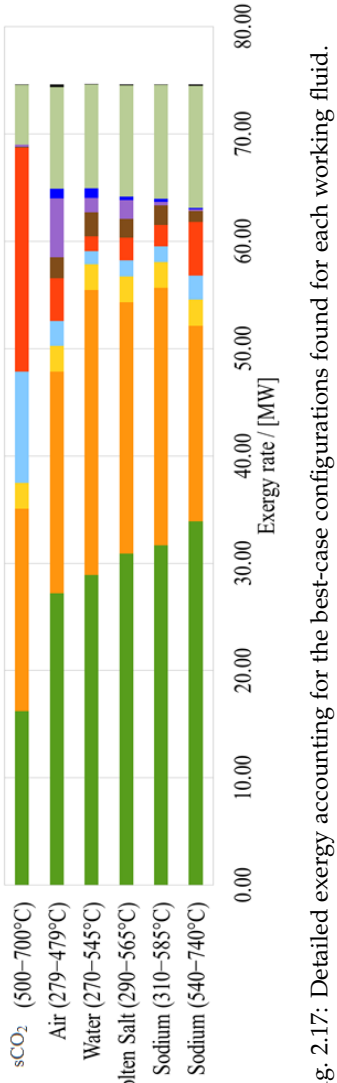

Fig. 2.17: Detailed exergy accounting for the best-case configurations found for each working fluid.

direct connection to an sCO_2 Brayton cycle. Air was not a strong HTF due to its poor thermophysical properties, which caused extremely high external wall temperatures. Air had the largest exergy destruction in internal convection and in pumping work, among all the fluids. It had to operate at lower temperature with low flux to avoid high external wall temperature, even though it had the ability to work at a high temperature range (e.g. 800-1000°C). Air receivers, if feasible, would need to make use of channels with some form of enhanced heat transfer, as earlier noted.

Table 2.5: Summary of the best-case receiver configurations identified for each HTF. It is noted that $T_{o,\mathrm{PU}} = T_{i,\mathrm{rec}}$.

	Molten Salt (290–565°C)	Sodium (310–585°C)	Sodium (540–740°C)	sCO_2 (500–700°C)	Air (279–479°C)	Water (270–545°C)
Case	#1	#2	#3	#4	#5	#6
$T_{\mathrm{ext,rec}}$ (°C)	642.97	639.16	789.58	718.56	680.39	653.57
$F_{safety,\mathrm{von\_Mises}}$	20.14	64.17	13.20	1.27	1.39	2.39
CR	800	800	800	160	640	800
$T_{i,\mathrm{PU}}$ (°C)	290	310	540	500	278.95	270
$T_{i,\mathrm{rec}}$ (°C)	290.74	310.52	540.93	503.46	282.42	270.77
$T_{o,\mathrm{rec}}$ (°C)	565	585	740	700	478.95	546.25
$p_{i,\mathrm{PU}}$ (bar)	1	1	1	200	100	120
$p_{i,\mathrm{rec}}$ (bar)	17.93	5.76	8.72	204.20	101.85	144
$p_{o,\mathrm{rec}}$ (bar)	1	1	1	200	100	119.60
$\mathbf{V}$ (m/s)	5.59	7.08	9.69	15.51	41.04	78.53
d_o (mm)/DN	10.3/DN6	10.3/DN6	10.3/DN6	13.7/DN8	48.3/DN40	10.3/DN6
t (mm)/Sch	1.73/Sch40	1.73/Sch40	1.73/Sch40	3.02/Sch80	3.68/Sch40	1.73/Sch40
n_{banks}	2	1	1	2	2	3
$n_{\mathrm{tubes,\,per\,bank}}$	485	970	970	364	103	323
Mach No.	-	-	-	-	0.075[a]	0.12
$\eta_{\mathrm{I,rec}}$ (%)	89.65	90.00	83.81	41.79	85.03	91.40
$\eta_{\mathrm{II,rec}}$ (%)	55.45	56.72	60.92	29.52	49.43	51.73
$\eta_{\mathrm{II,PU}}$ (%)	47.73	49.24	63.52	91.20	78.45	89.03
$\eta_{\mathrm{II,sys}}$ (%)	41.42	42.42	45.47	21.92	36.43	38.75
$\dot{W}_{\mathrm{PU}}$ (MW)	0.19	0.14	0.31	0.53	1.18	0.18
$\dot{W}_{\mathrm{net}}$ (MW)	30.90	31.79	33.92	16.35	27.18	28.91

[a] Speed of sound of air, C_{air}, at 478.95°C is 549.62 m/s

2.5.5 The effects of varying the temperature ranges, T_{sky} and h_{ext} on overall comparison

A sensitivity study was conducted, varying the temperature ranges (varying T_{i} but keeping T_{o}), varying T_{sky} (range: 0–90°C[10]) and varying h_{ext} (range: 10–40 W/(m^2·K)), relative to the base-case being the high-temperature sodium receiver case

[10]It is acknowledged that the sky temperature could even reach to –50°C, as discussed by Karn et al. [156]. However, our study emphasises that the effect of changing the sky temperature still be expected to be quite minor for these systems, due to the high CR.

in this chapter.

Regarding receiver inlet temperature, it is found that lowering the receiver inlet temperature leads to an increased thermal efficiency (Fig. 2.18a), but a decreased exergy efficiency (Fig. 2.18b). The decreased thermal efficiency at higher inlet temperature is due to larger convective and radiative losses at the higher temperatures. These increased energy losses are counteracted in the case of exergy efficiency by the decreased exergy destruction in absorption that occurs at higher temperatures (i.e. it is beneficial to collect heat at the highest possible temperatures). Further increasing the receiver inlet temperature beyond 540°C (with receiver outlet temperature held constant) would give further gains, however these gains have implications on the storage design, power block performance, and pumping flow rates, and a proper treatment of these is beyond the scope of the present work in this chapter. The follow-up works to look at performance-optimised receivers with varying temperature range including thermoelastic stress, tube material and cost analysis are addressed in Chapter 6.

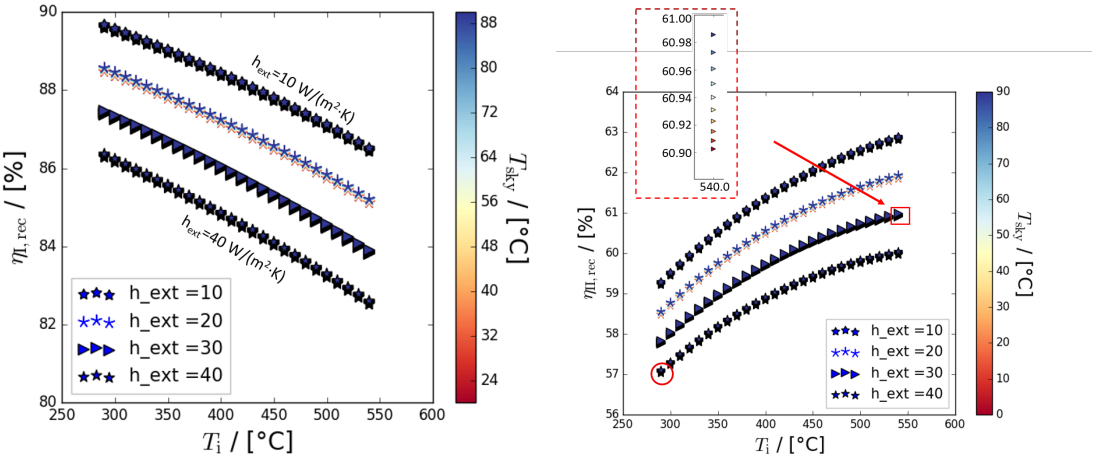

(a) Energy efficiency

(b) Exergy efficiency

Fig. 2.18: Sensitivity of (a) first- and (b) second-law efficiencies of the sodium receiver to varying inlet temperature (x axis), external convection coefficient (plot symbol), and sky temperature (plot colour). The receiver outlet temperature is held at 740°C. The inset in the right-hand plot highlights the small effect of sky temperature in the range 0 – 90°C on η_{II}. Top "star" line is the result when $h_{ext} = 10$ W/(m^2·K), while the bottom "star"line is when $h_{ext} = 40$ W/(m^2·K).

Regarding the external convection coefficient, it is found that an increase in its value from 10 to 40 W/(m^2·K) causes reduction of 3–4% in energy efficiency, or 2.5–3% in exergy efficiency.

Regarding the sky temperature, in contrast to what is seen in low-temperature solar-thermal systems, the sky temperature is shown here to have a negligible effect on receiver exergy efficiency (see Fig. 2.19). An increase to the sky temperature from 0 to 90°C only causes increase of only 0.08% in exergy efficiency.

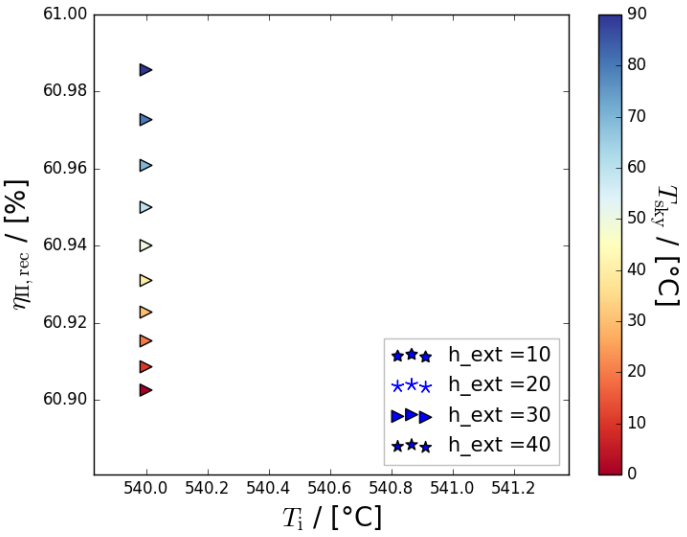

Fig. 2.19: Effective of sky temperature on the receiver second-law efficiency, for the best-case high temperature sodium receiver.

To further verify that our conclusions are valid for the rest of the working fluids, best-case molten salt and air receivers are also examined, as shown in Fig. 2.20. Studies show that varying the external convection coefficient for air receivers has a larger effect on the second-law efficiencies, when compared to the molten salt receiver due to the poor heat transfer of the air. However, again, this effect is still not significant enough to change our conclusions on the rankings of the performance of the working fluids in this chapter.

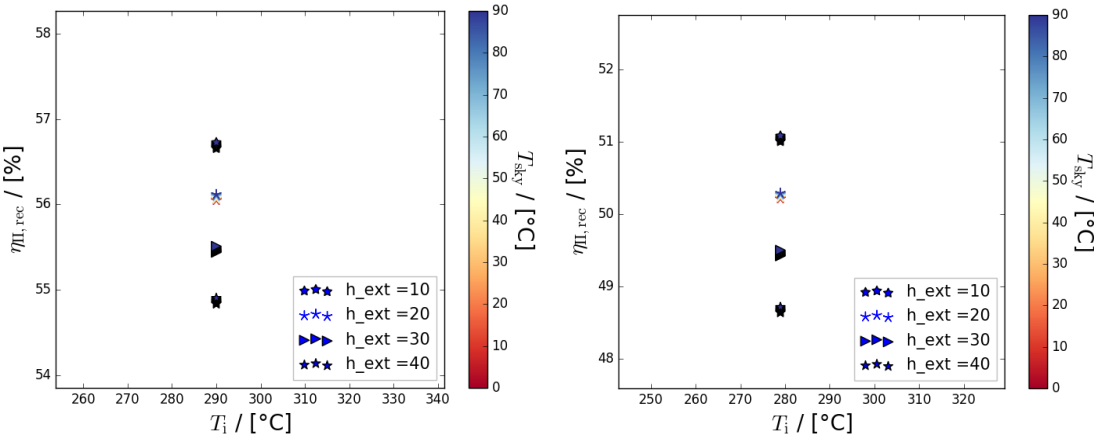

(a) molten salt

(b) air

Fig. 2.20: Sensitivity studies of (a) the molten salt and (b) the air receivers to varying external convection coefficient (plot symbol) and sky temperature (plot colour).

2.5.6 The effects of varying the external wall temperatures in the circumferential direction on overall comparison

Rodríguez-Sánchez et al. [95] found that radiation losses are higher if the variation in the tube wall temperature in the circumferential direction is considered. That study states that the tube wall temperature variation is a big concern: if the temperature of the rear or sides of the tubes is much lower than the front temperature, then $\overline{(T_{ext})^4}$ would be much greater than $\overline{T_{ext}}^4$ and it seems likely that approximating the tube as isothermal around its circumference could cause an underestimation of the radiative losses. In order to examine this question, further analysis relating to this effect has been conducted, by considering five model variations (Cases C1-C5) for each of the working fluids used in this chapter (i.e. molten salt, low temperature liquid sodium, high temperature liquid sodium, sCO_2, air and water/steam). All studies are conducted at the outlet conditions (i.e. one particular segment of the tube) of each fluid. Only the key parameters (Table 2.6) and the main results are summarised here. Detailed analyses refer to Appendix C.

Table 2.6: Summary of the key parameters made for Case C1 - C5.

Case No.	Key parameters
Case C1	Uniform flux across front half tube, and with effective absorptivity and surface emissivity being considered.
Case C2	In addition to Case C1, effective emissivity at the front half of the tube is considered.
Case C3	Non-uniform distribution of absorbed flux across the front half of the tube is considered, according to a cosine profile.
Case C4	View factor has been added to Case C3.
Case C5	View factor has been added to Case C1.

In the first Case C1, it has the same model and results that are provided in Section 2.4. This is the case of a tube supplied with heat uniformly across its front half, and with effective absorptivity and surface emissivity being considered.

In Case C2, it use the same model of Case C1, but consider effective emissivity at the front half of the tube, which makes an allowance for the cavity effect in the crevices between tubes, which acts to increase the radiative losses on an per-aperture-area basis.

In Case C3, a non-uniform distribution of absorbed flux across the front half of the tube is considered, according to a cosine profile ($\dot{Q}'_{abs,i} = \alpha_{eff} C G A_{ext,i} \cos(\theta)$,where $\theta = 0^\circ$ at the front of the tube), with scaling applied to ensure the same total absorbed

energy per tube section as in Case C1. The cosine profile shows a good match to the realistic flux profile for an irradiated tube-bank as provided in a report by Tilley et al. [153]. The effect of the circumferential variation in effective absorptivity is not considered, which will be higher in the crevices. This is considered to be a second-order effect, due to the small fractional increase arising due to this effect, whereas the cosine distribution is a first-order effect, varying the absorbed flux between zero at the base of the crevice and a peak value at the crest. The emissivity ϵ_i the receiver surface in Case C3 is considered the same as Case C1.

In Case C4, the same absorbed flux distribution as Case C3 is considered, but additional allowance for the view factors arising at different circumferential positions is made, and their impact on the local thermal emission heat loss from each part of the tube. In the crevice between adjacent tubes, the view factor from the tube surface to the surroundings is lower than at the crest of the tube. In this case, it made use of the basic surface emissivity. In addition, it assumes that the neighbouring tubes are experiencing identical HTF flow and irradiation conditions, such that they establish identical external surface temperature distributions as the present tube.

In Case C5, the same uniform absorbed flux distribution as Case C1 is considered, but view factors are added in this case.

The results from this study were that a cosine circumferential wall temperature profile with no consideration of view factors (Case C3) results in a reduction in the local first- and second-law receiver efficiencies of up to 0.4% and 0.29% (in the case of air) when compared to the case of uniform wall temperature (Case C1). If the most realistic case (Case C4) is compared to the case used in the manuscript (Case C1), the first- and second-law efficiencies, however, are increased by 1.81% and 1.19%, which means that the gain of considering view factors more than balances out the under-estimation on energy losses for the case of uniform circumferential wall temperatures.

This chapter emphasises a unified comparison between heat transfer fluids. The estimation of the heat loss applies to all the receivers, and based on the analysis of Cases C1–C5 above, the difference arising from a more detailed analysis of this effect at the local level would not be enough to change the relative rankings of our different fluids. Among all the heat transfer fluids, high temperature sodium has the highest external wall temperature, which means that the receiver efficiencies of the receiver would be even higher if the circumferential tube wall temperature variation and the view factor being considered. High temperature sodium is still the best candidate. sCO_2 still performs the worst. This is because that adding the effect of view factor is unlikely to increase the efficiencies of the sCO_2 receiver by more than 20%. The rest of the working fluids are very likely to remain their rankings, due to the similar external wall temperature ranges.

2.6 Conclusions

This chapter analysed the performance of a range of working fluids in tubular receivers. Subject to an assumption of uniform flux, and with sizes constrained to those available in ASME B36.10, a clear performance benefit from using sodium at high temperatures is seen; even at low temperatures, it is still better than molten nitrate salts, before allowing for the heat exchanger. Circumferential variation in the tube wall temperature is not considered throughout the whole receiver. Full analysis of the tube wall temperature variation in the circumferential direction is conducted in Chapter 6. An examination of exergy destruction in the heat exchanger (full details refer to Chapter 7) for the best low-temperature sodium case shows that the exergy destruction in the heat exchanger is very similar to the exergy destruction in the internal convection in the salt receiver. Thus, the efficiency gain at this lower temperature case is only very marginal for sodium. The reason that it is still beneficial is because the temperature differences between the internal wall and the working fluid are low, resulting in low exergy destruction in internal convection. sCO_2 ranks higher, as an HTF, than the air based on their thermophysical properties (Fig. 2.4). However, the studies on pressure and external losses conclude that the air receiver performs better than the sCO_2 receiver.

sCO_2 and air could be beneficial in other CSP approaches, but appear not to be applicable in simple tubular receivers with uniform flux based on efficiency. Water/steam is fairly reasonable from a receiver performance point of view, even though the relatively large exergy destruction in absorption makes it less efficient than sodium or molten salt. It is challenging to integrate with storage, but has clear appeal if process steam is the primary need.

To sum up, under assumed conditions of uniform flux, the most efficient CSP tower system, consisting of a tubular receiver, an appropriate TES and a simplified PB of fixed exergy efficiency, should have a receiver with small tubes, connected mostly in parallel. This conclusion is made without the consideration of thermal stress on the tubes or any techno-economic assessment. Relatively large tubes could reduce the material and fabrication costs on the receiver, due to reduced flow-path and less complexity, respectively. The trade-offs on the receiver efficiency, the total material cost on the receiver, and the cost of providing the necessary pumping work will affect the decision on the appropriate tube size and flow configuration. Another valuable conclusion from Fig. 2.13 is that multi-pass receiver should be considered to increase the system efficiency, if large diameter tubes are required due to cost considerations. For example, for a molten salt receiver, there was a 74.4% reduction in pressure drop if a 48.3 mm inside tube diameter would be selected instead of the 10.3 mm size, while there was only a 0.7% increase in exergetic efficacy.

Last but not the least, exergy analysis can be used along with cost data to estimate the impact on LCOE of different design configurations, even in the absence of a full

plant model that includes a power block. Thus if cost advantages of the sCO_2 Brayton cycle due to the more compact nature of the turbo-machinery can be realised, as well as the performance advantages indicated here by the exergy analysis, it follows that the sodium-sCO_2 Brayton system will result in lower LCOE than the salt-Rankine system.

Chapter 3

Parameter study for design of flat tubular molten salt receivers[1]

3.1 Introduction

An exergy analysis of a 'Billboard' style tubular receiver, as shown in Figure 3.1, with different heat transfer fluids (HTF) was studied in Chapter 2. It was shown that the performance of molten salt (with properties as per [157]) is highly competitive in its standard temperature range, but other fluids such as liquid sodium perform better if the temperature and solar flux concentration ratio can be increased. That study, however, considered only the case of uniform flux. This chapter, as a further development, examines how non-uniform flux impacts the thermal performance.

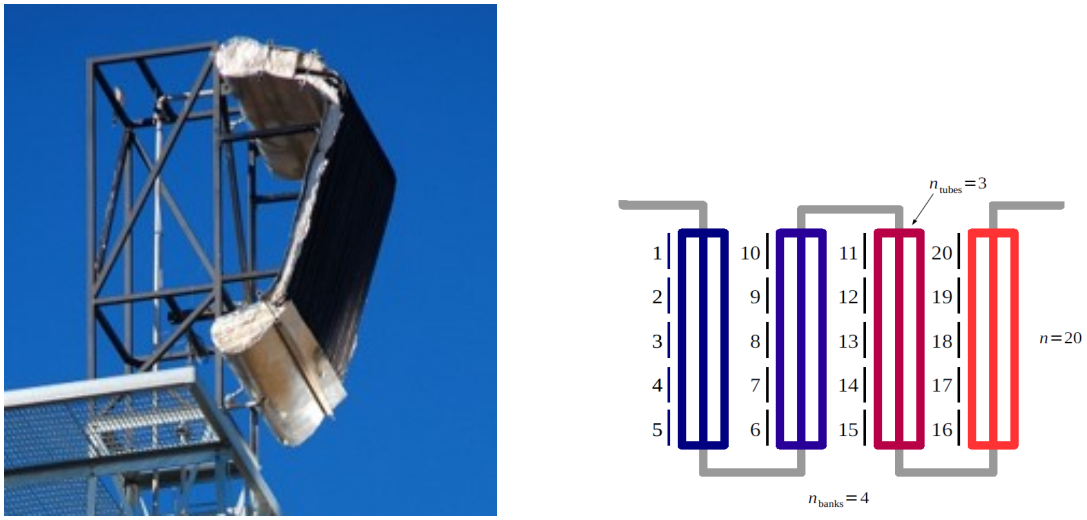

Fig. 3.1: Left, a billboard receiver (Source: Vast Solar); right, the receiver pipe flow model, with segment numbering and flow-path configuration.

[1]This chapter incorporates material from: Zheng, M. and Pye, J. Parameter study for design of flat tubular molten salt receivers. In *Proceeding of the Asia Pacific Solar Research Conference*, Canberra, 28-30 Nov 2016

The working temperatures of the molten salt are controlled within the range from 290°C to 565°C. The lower limit is to avoid freezing, and the upper limit is to avoid chemical degradation of the salt. The present model is limited to flat/convex receivers. The flow path is separated into n sequential segments, with n_{banks} banks of parallel tubes passing up and down the receiver surface, connected together in series, with number of parallel tubes (n_{tubes}) in each bank. The value of n_{banks} is calculated geometrically:

$$n_{\text{tubes}} = \frac{W}{d_{\text{o}} n_{\text{banks}}} \tag{3.1}$$

where W is the width of the receiver and d_{o} is the outer tube diameter.

3.2 Methodology

The net energy ($\dot{Q}_{\text{net,rec}}$) flow into a receiver from concentrated solar radiation ($\dot{Q}_{\text{sun,rec}}$) will be balanced by energy outflows from the flow of HTF or other energy conversion process, plus a range of energy losses ($Q_{\text{loss,rec}}$), due to spillage ($Q_{\text{spil,rec}}$), unwanted reflection ($\dot{Q}_{\text{refl,rec}}$), radiative emission ($\dot{Q}_{\text{ext,rad,rec}}$), convective ($\dot{Q}_{\text{ext,conv,rec}}$) or conductive processes (no conductive loss is considered here) [158]. Note that the spillage losses are considered in this chapter as an add-on to Chapter 2. Therefore, the total energy loss is the sum of these four contributions:

$$\dot{Q}_{\text{loss,rec}} = \dot{Q}_{\text{sun,rec}} - \dot{Q}_{\text{net,rec}} = \dot{Q}_{\text{spil,rec}} + \dot{Q}_{\text{refl,rec}} + \dot{Q}_{\text{ext,rad,rec}} + \dot{Q}_{\text{ext,conv,rec}}, \tag{3.2}$$

where the detailed expression for $\dot{Q}_{\text{refl,rec}}$, $\dot{Q}_{\text{ext,rad,rec}}$, and $\dot{Q}_{\text{ext,conv,rec}}$ are defined in Eq. 2.2, Eq. 2.4 and Eq. 2.5, respectively. The first-law efficiency of thermodynamics indicates how well an energy transfer process is accomplished and provides a sound basis for studying the various forms of energy. The overall first-law efficiency of the receiver ($\eta_{\text{I,rec}}$) as well as the receiver thermal efficiency ($\eta_{\text{th,rec}}$) are:

$$\eta_{\text{I,rec}} = \frac{\dot{Q}_{\text{net,rec}}}{\dot{Q}_{\text{sun,rec}}} = \frac{\dot{m}\left[(h_o - h_i) + \frac{1}{2}\left(\mathbf{V}_o^2 - \mathbf{V}_i^2\right)\right]}{\dot{Q}_{\text{sun,rec}}}, \text{and} \tag{3.3}$$

$$\eta_{\text{th,rec}} = \frac{\dot{Q}_{\text{net,rec}}}{\dot{Q}_{\text{inc,rec}}}, \text{where } \dot{Q}_{\text{inc,rec}} = \dot{Q}_{\text{sun,rec}} - \dot{Q}_{\text{spil,rec}} \tag{3.4}$$

where molten salt is assumed to be an incompressible fluid. No potential energy variation is considered. The maximum allowable stress is applied using the method mentioned in Sec 2.4.6. A more comprehensive allowable stress analysis is conducted later in Chapter 6, with the coding developed by Logie et al. [72].

Next, exergy accounting is considered in this chapter. The total exergy in the sun

is defined using Petela formula [136]:

$$\dot{X}_{\text{sun,rec}} = \dot{Q}_{\text{sun,rec}} \left(1 - \frac{4}{3}\frac{T_{\text{ref}}}{T_{\text{sun}}} + \frac{1}{3}\left(\frac{T_{\text{ref}}}{T_{\text{sun}}}\right)^4 \right), \text{ and } \dot{X}_{\text{net,rec}} = \dot{m}\left(\phi_{\text{i}} - \phi_{\text{o}}\right). \tag{3.5}$$

For a steady-state control volume, the exergy rate balance can be found as follows:

$$\dot{X}_{\text{sun,rec}} = \dot{X}_{\text{loss,spil,rec}} + \sum_{\text{rec,i}} \dot{X}_{\text{inc,rec},i} \tag{3.6}$$

$$\dot{X}_{\text{inc,rec},i} = \dot{X}_{\text{lost,rec},i} + \dot{X}_{\text{dest,rec},i} + \dot{X}_{\text{net,rec},i} \tag{3.7}$$

where a share of the exergy from the sun $\dot{X}_{\text{sun,rec}}$ is lost due to spillage ($\dot{X}_{\text{loss,spil,rec}}$). Therefore, the total incident exergy is $\sum_{\text{rec,i}} \dot{X}_{\text{inc,rec},i} = \dot{X}_{\text{sun,rec}} - \dot{X}_{\text{loss,spil,rec}}$.

The exergy losses and exergy destruction (internal irreversibilities) in the receiver are explained in detail in Eq. 2.12–2.21, and accounted as follows:

$$\dot{X}_{\text{loss,tot,rec}} = \dot{X}_{\text{loss,spil,rec}} + \dot{X}_{\text{loss,refl,rec}} + \dot{X}_{\text{loss,ext,rad,rec}} + \dot{X}_{\text{loss,ext,conv,rec}}, \tag{3.8}$$

$$\dot{X}_{\text{dest,tot,rec}} = \dot{X}_{\text{dest,abs,rec}} + \dot{X}_{\text{dest,wall,rec}} + \dot{X}_{\text{dest,int,conv,rec}} + \dot{X}_{\text{dest,flow,rec}}. \tag{3.9}$$

The overall second-law efficiency of the receiver ($\eta_{\text{II,rec}}$) is the ratio of the net increase in working fluid flow exergy ($\dot{X}_{\text{net,rec}} = \dot{X}_{\text{sun,rec}} - \dot{X}_{\text{loss,tot,rec}} - \dot{X}_{\text{dest,tot,rec}}$) to the exergy of the solar radiation reflected by the heliostat field:

$$\eta_{\text{II,rec}} = \frac{\dot{X}_{\text{net,rec}}}{\dot{X}_{\text{sun,rec}}} \tag{3.10}$$

The overall second-law efficiency of the system, including pump and power block, is defined as follows:

$$\eta_{\text{II,sys}} = \frac{\dot{W}_{\text{net}}}{\dot{X}_{\text{sun,rec}}} \tag{3.11}$$

where the second-law efficiency of the Rankine power block is assumed to be 75% [85]. Pressure drop due to friction is considered here, using Eq. 2.27. Eq. 2.35 and 2.36 are applied in this analysis to calculate the pumping loss. Also, it is assumed that there is no heat transfer across the pump. For detailed equations for energy and exergy balances, pump work calculations for incompressible-liquid assumptions, and $\dot{W}_{\text{net}}$ refer to Chapter 2.

Three flow configurations were established in this study, named "edge-to-edge", "edge-to-centre" and "centre-to-edge", as shown in Fig. 3.2.

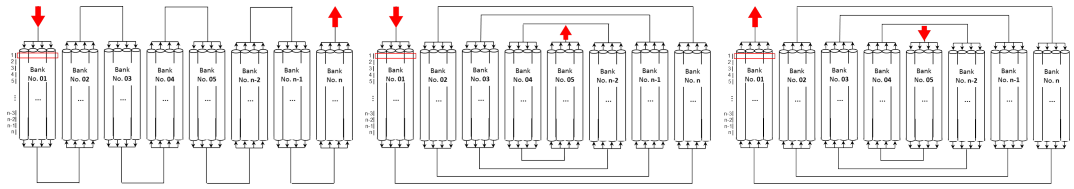

Fig. 3.2: Demonstrations of three flow configurations

3.3 Simulation and parametric studies

3.3.1 The effects of varying the flux on the receiver

The effects of varying the tube diameter, tube wall thickness, number of banks for a fixed-geometry receiver with uniform flux have been studied previously, in Chapter 2. However, the performance of the receiver is strongly constrained by material limits which in turn limit the allowable flux on the receiver. This section seeks to understand the benefits which arise at the receiver as a result of adjusting the flux profile, comparing a simple Gaussian 'spot' with a linear 'ramp' pattern, while respecting an upper limit on the peak flux of the molten salt working fluid.

3.3.1.1 Gaussian flux distribution

The distribution on the receiver, assumed here to be flat, has been firstly approximated by a bivariate Gaussian distribution. A Gaussian spot is physically based and arises naturally when effects due to the sun-shape, heliostat slope errors and tracking errors are combined with a single-point aiming strategy. The Gaussian spot is represented by:

$$G_{\text{rec}}(x,y) = \frac{\dot{Q}_{\text{sun}}}{2\pi\sigma^2} e^{\left[-\frac{1}{2}\left(\frac{r}{\sigma}\right)^2\right]}, \tag{3.12}$$

$$\text{where } r = \sqrt{\left(x - \frac{W}{2}\right)^2 + \left(y - \frac{L}{2}\right)^2}. \tag{3.13}$$

where G is the local flux (W/m^2) at position (x, y) on the receiver, x and y are horizontal and vertical coordinates on the receiver of width W and length L, measured from the bottom left (where the origin (0,0) is located). r is the distance between the coordinates (x, y) and the centre of the receiver.

For a given amount of energy, $\dot{Q}_{\text{sun}}$ (here, 20 MW), the flux density map is set by the spot size (σ) and the geometry of the receiver. Spot size is affected by mirror quality, heliostat shape and the circumsolar ratio. The effect of varying Gaussian spot size on the flux distribution on the receiver is shown in Fig. 3.3. Therefore, the parametric studies based on these factors have been presented in the following

sub-sections.

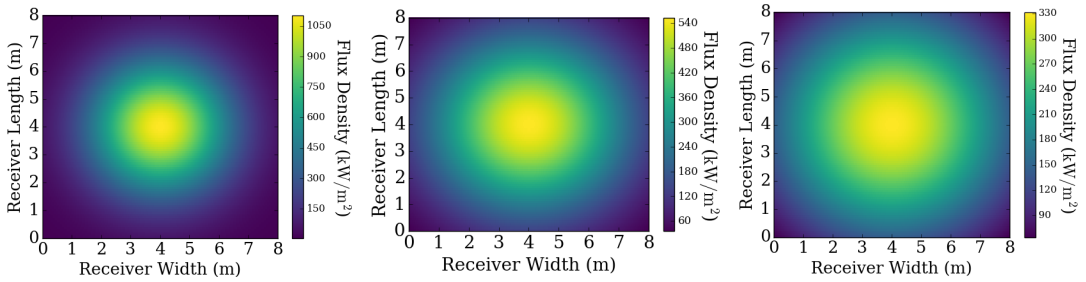

Fig. 3.3: Gaussian flux profiles on a square 64 m^2 receiver with varied Gaussian spot size σ: $\sigma = 1.7$ m (left), $\sigma = 2.4$ m (middle), $\sigma = 3.1$ m (right).

Firstly, the effect of varied spot size (σ) on the thermodynamic efficiencies was studied. The Gaussian distribution was incorporated into the model as described in Section 3.3.1.1. The fraction of solar flux incident on square targets of varying size, for varying σ, is shown in Fig. 3.4 below. Smaller spots allow the solar flux to be collected with a smaller aperture, as expected.

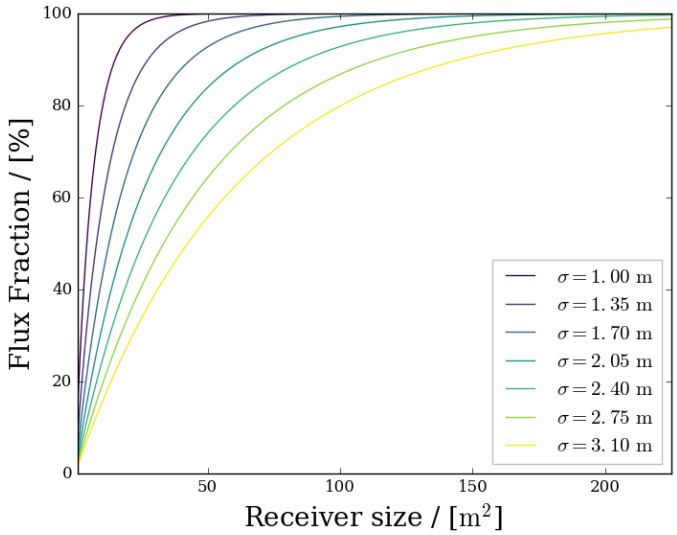

Fig. 3.4: Flux distribution fraction vs. Receiver size for different spot size, σ. The receiver aperture is a square. Flux distribution fraction = $\sum G_{\text{rec}}(x, y) \times (\frac{WL}{n})$.

Next, we studied the effect of the Gaussian spot size σ and the receiver aperture area A_{aper} on the peak flux $\dot{q}_{\text{peak}}$ (Fig. 3.5). For small spots, very large peak flux are seen, rendering the results above infeasible. The highest peak flux for molten salt is set to be 1.2 MW/m^2, which has been widely used in the similar research projects about the evaluation of the allowable stress [72, 90, 159, 160]. Therefore, the minimum σ value was selected to be 1.7 m for the remaining analysis, as a spot size that

gives a peak flux of only 1.09 MW/m^2.

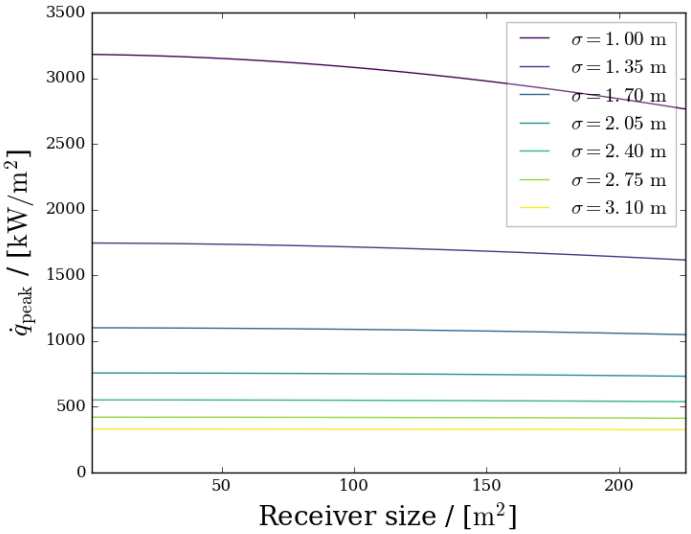

Fig. 3.5: Peak flux $\dot{q}_{\text{peak}}$ with varied spot size σ and receiver aperture area A_{aper}. In this study, n_{banks} = 20 and n_{seg} = 20, hence, the peak flux is changing with the receiver size.

A small spot area is capable of performing high first-law efficiency due to the high peak flux density and low effect of spillage, as shown in Fig. 3.6. The value of spillage fraction achieved in the case of optimal (maximum) first-law efficiency is ∼5–8%, showing the strong trade-off between the small area with high spillage versus a large area with high thermal losses. The "edge-to-centre" flow configuration gives the largest net work (see Fig. 3.7) due to the lowest external radiation loss from the elevated external wall temperatures due to the T^4 effect, followed by "edge-to-edge" (i.e. worse) and "centre-to-edge" (i.e. the worst), noting that exergetic efficiency can be inferred from the size of the green bar (net work) given that the exergy input is equal in all three cases. Exergy destruction in internal convection plays another important role here. The "edge-to-centre" flow configuration maximises the net energy to the fluid and minimises the overall temperature difference between the HTF and the inner wall, hence, leads to overall lowest exergy destruction in internal convection. Therefore, the best-case receiver size and flow configuration were selected to be 64 m^2 and "edge-to-centre" for the remaining analysis.

Detailed energy and exergy accounting for a molten salt receiver with variable σ and constant A_{aper} (64 m^2) are presented in Table 3.1 and Fig. 3.8. The dominant exergy destruction occurs in the absorption step, due to the large step-down in temperature between the sun and the external walls of the receiver (from 5800 K (refer to Eq. 3.5) to 903.15 K (= 630°C)), decreasing a little for the case of very small spots. Spot size σ has a strong effect on spillage, as well as internal convection. External radiation is sensitive to small areas of high external temperature, due to the T^4 effect at

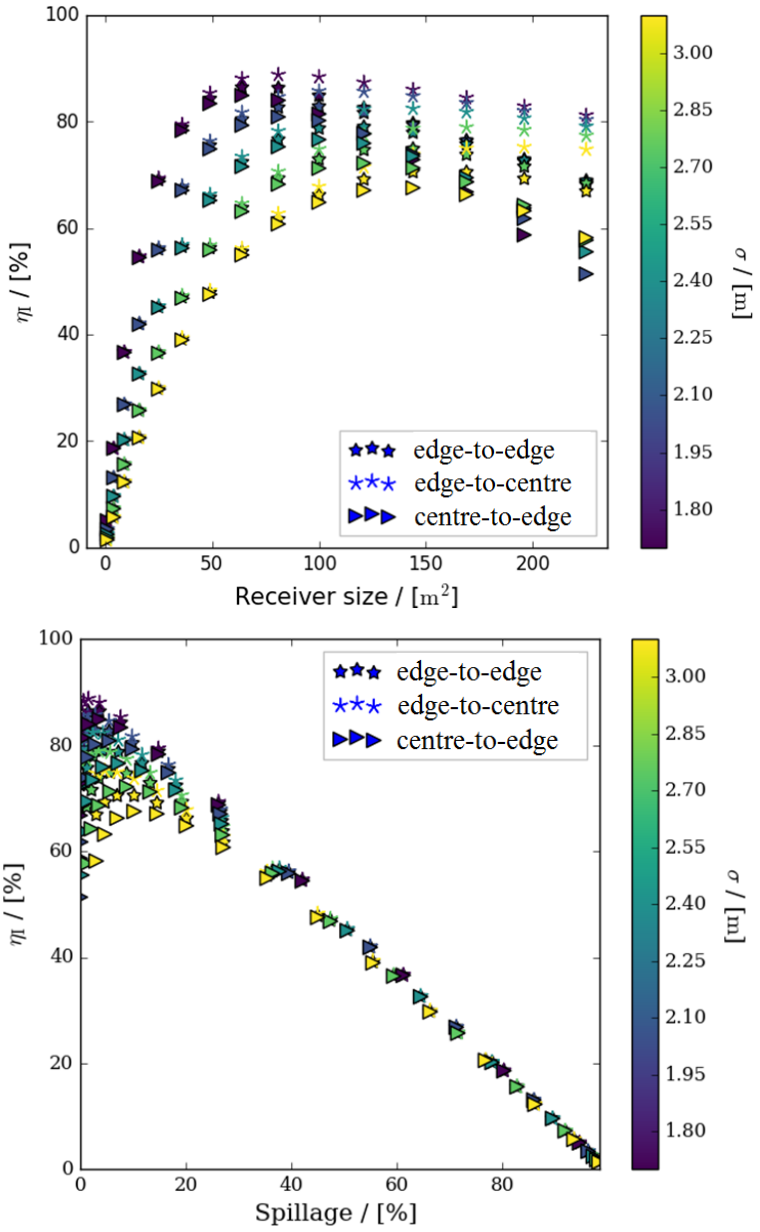

Fig. 3.6: The effect of variable receiver sizes (top) and the spillage on the first law efficiencies (bottom), with fixed number of banks (n_{banks}) and fixed outer tube diameter ($d_o = 32$ mm). This receiver model is as same as Case C1 in Chapter 2, but adds non-uniform flux, spillage and variable flow configuration into consideration. The receiver inlet and outlet temperatures are fixed at 290°C and 565°C, respectively. n=100; n_{banks} =10. Receiver sizes are varied from 1m^2 to 225 m^2 ($W = L$). Eq. 3.2, 3.2, and 3.12 are applied to obtain the energy balance. The top figure shows that the first-law efficiency is reducing when the receiver size is larger than ∼120 m^2 due to the larger thermal losses, even though the spillage is reducing (refer to Fig.3.4). The bottom figure shows that the optimal first-law efficiency achieves at ∼90% when the spillage is ∼5–8% (i.e. the receiver size is ∼80m^2). It shows that too small or too large in receiver size would results in large spillage loss or large thermal losses due to large surface area.

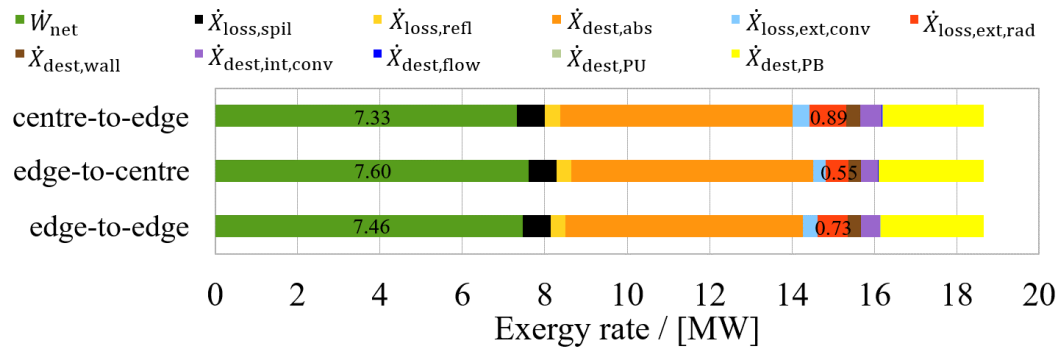

Fig. 3.7: Detailed exergy accounting for three flow configurations of the best-case receiver (64 m^2). The units of $\dot{W}_{net}$ and $\dot{X}_{loss,ext,rad}$ shown in this figure are in MW.

the wall (demonstrated in Fig. 3.9: solid lines). Internal convection losses arise from the large temperature difference between the HTF and the inner wall (demonstrated in Fig. 3.9: dash-dot lines and dash-dash lines). The trade-offs between spillage, external thermal radiation and internal convection lead to an optimal spot size with maximised total net exergy to the working fluid.

Table 3.1: Effect of the size of a Gaussian spot on receiver performance

Common parameters

$\dot{Q}_{sun}$ MW	T_{sun} K	P_{out} bar	k_{wall} W/(m·K)	h_{ext} W/(m^2·K)	T_{in} °C	T_{out} °C	G W/m^2	A_{aper} m^2	d_i mm	t mm	n_{banks}
20	5800	1	20	30	290	565	1000	64	30	2	20

Results

σ m	$\dot{Q}_{spil}$ MW	$\dot{Q}_{inc}$ MW	$\dot{Q}_{ref}$ MW	$\dot{Q}_{ext,conv}$ MW	$\dot{Q}_{ext,rad}$ MW	$\dot{Q}_{net}$ MW	η_{th} %	η_{I} %	$\eta_{II,sys}$ %	$T_{int,peak}$ °C
1.70	0.71	19.29	0.25	0.77	0.91	17.36	91.17	86.80	41.67	631.77
2.05	1.95	18.05	0.23	0.79	0.94	16.08	90.28	80.42	41.27	612.03
2.40	3.61	16.39	0.21	0.81	0.96	14.42	89.10	72.10	40.74	600.93
2.75	5.38	14.62	0.91	0.82	0.97	12.65	87.64	63.26	40.08	594.09
3.10	7.08	12.92	0.17	0.82	0.98	10.96	85.91	54.80	39.30	589.51

The receiver temperature profiles (Fig. 3.9) and the corresponding flux distributions (Fig. 3.3) for these cases show that, for this particular flow configuration (i.e. edge-to-centre), the maximum inner wall temperature ($T_{inc,peak}$) was 631.77°C, close to the maximum allowable film temperature for molten salt [71], is reached when the spot size σ is set to 1.7 m. The peak flux density in that case is 1.09 MW/m^2. A larger value of σ, for example 3.1 m, results in excessive spillage.

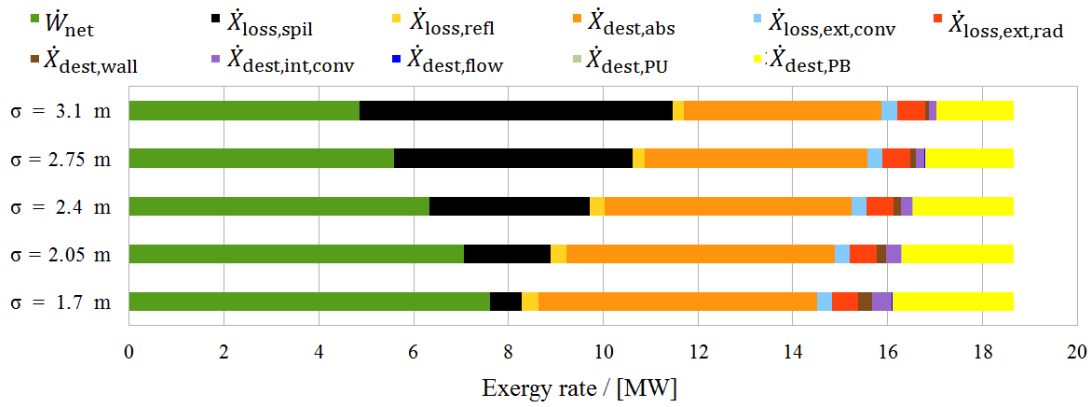

Fig. 3.8: Exergy accounting for the receiver with varying spot size, for fixed receiver size ($A_{aper} = 64 m^2$) and fixed total concentrated solar energy ($\dot{Q}_{sun} = 20$ MW). σ below 1.7 m leads to excessive peak flux greater than 1.2 MW/m^2. σ above 3.1 m leads to excessive spillage loss.

3.3.1.2 Linear ramp flux distribution

In the above study we found that with a Gaussian distribution, the maximum allowable flux is reached in only a small localised region, limiting the performance of the whole receiver. Therefore, it was proposed to examine whether a flux profile tailored to the rising fluid temperature could be shown to improve receiver performance. A simple linear ramp distribution in flux concentration was considered, with flux reducing from the left (inlet) to the right of the receiver surface, with the x-wise rate of reduction of flux (slope) being the variable parameter. Linear ramp may be physically impossible, but may give some ideas about upper bounds of performance. This very simplified profile is similar to those arising from more detailed study by Sánchez-González et al. [71], with the consideration of aiming strategy. A sinusoidal curve is applied at the edges of this idealised flux profile (see Fig. 3.10 (c)), to mimic modest spillage losses. We adjusted the size of the aperture and the Concentration Ratio (CR) in order to match the peak film temperature constraint. The total flux and spillage are constant at 20 MW, 3.6% respectively.

The width here is defined as the rate of change of aperture irradiance $G_{rec}(x, y)$ in the x-wise direction across the receiver. For the flat portion of distribution, excluding the sinusoid 'tails",

$$\text{slope} = \frac{\Delta G_{rec}(x, y)}{\Delta x} \tag{3.14}$$

The possible values of slope are from –120 to 120 kW/m^2/m, so that the maximum inner wall temperatures are below 630°C, when the lowest flux from that flat portion is set to be zero at the edge of the receiver, examples are shown in Fig. 3.10.

Results for the ramp flux profile study (Fig. 3.11) show that, the positive slope (higher flux at outlet) cases perform worse than negative slope cases (higher flux at

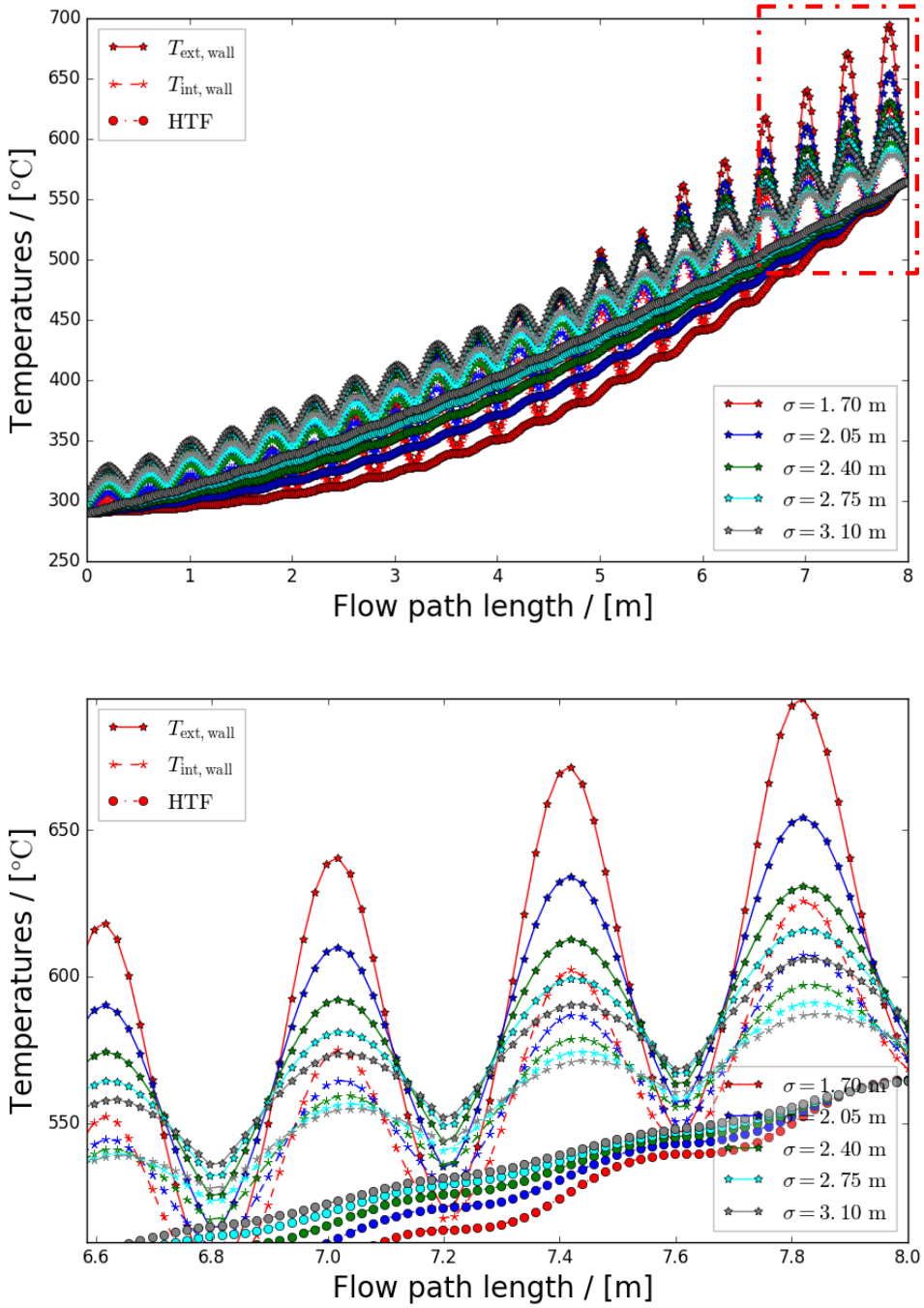

Fig. 3.9: Receiver temperature profiles, for a range of Gaussian spot sizes σ. The extracted details highlighted in red dashed-line box are shown at the bottom figure.

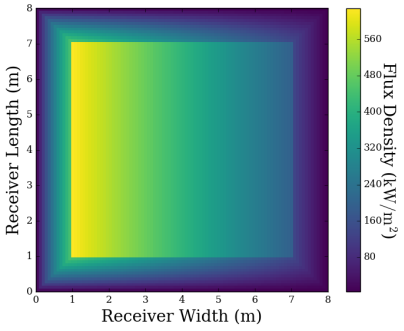

(a) slope –60 kW/m^2/m

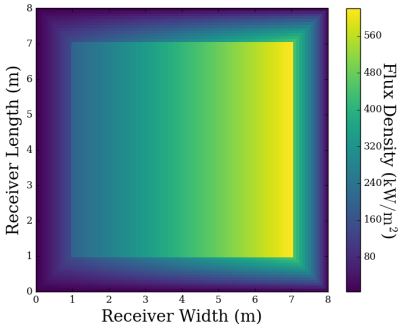

(b) slope +60 kW/m^2/m

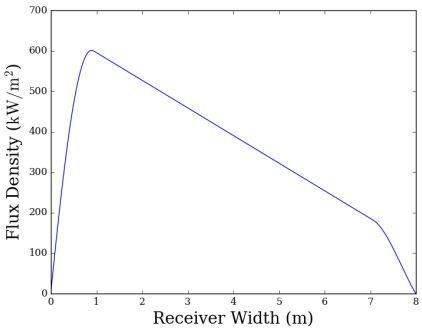

(c) slope –60 kW/m^2/m, one-dimensional plot

Fig. 3.10: Linear 'ramp' flux profiles: (a) slope –60 kW/m^2/m, (b) slope +60 kW/m^2/m, (c) one-dimensional plot with a slope of –60 kW/m^2/m

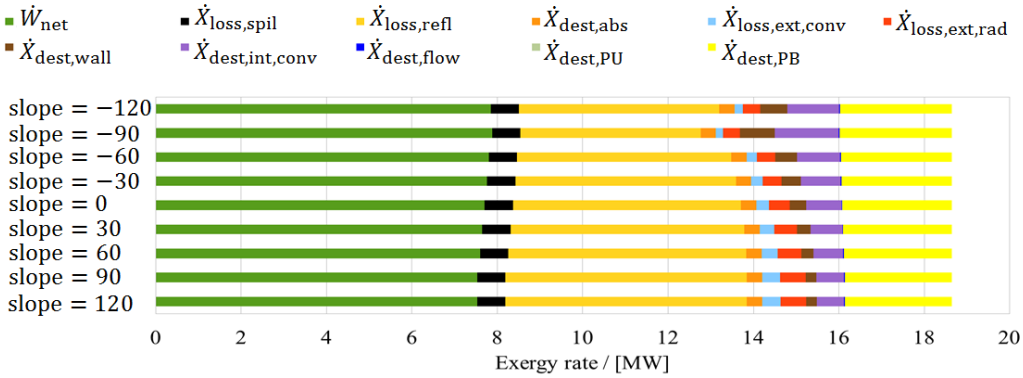

Fig. 3.11: Exergy accounting with variable slope (in kW/m^2/m). $T_{int,peak}$ were fixed at 630°C by varying the size of aperture and the CR. Flow configuration is "edge-to-edge" (left-to-right). With a slope of –90 kW/m^2/m, the smallest aperture was found and consequently, resulted in the best performance in exergy efficiency.

Table 3.2: Detailed exergy efficiency and receiver size with variable slope. Link to Fig. 3.11.

slope $kW/m^2/m$	peak flux kW/m^2	receiver size m^2	$\eta_{II,sys}$ %
–120	2030	16.42	43.64
–90	3119	12.25	43.81
–60	1389	21.77	43.33
–30	1136	25.00	43.14
0	872	30.25	42.83
30	836	36.00	42.52
60	811	40.96	42.25
90	837	49.00	41.86
120	798	49.00	41.83

inlet). When negative slope cases are used, and the aperture area is adjusted until the peak film temperature equals the maximum allowable value (630°C), smaller receivers with higher efficiency result (see Table 3.2). Even though the external surface temperatures are higher, the reduced area gives overall lower losses. The best case found was with a slope of –90 $kW/m^2/m$, since it had the smallest aperture of 12.25 m^2 which resulted in lowest exergy destroyed in absorption step.

The Gaussian flux represents a very non-linear flux distribution with a large area at much lower flux than the peak, while the ramp flux profile is linear. The non-linear flux distribution ends up causing high losses if hot fluid has to pass all the way through that large low-flux area. The heat-loss-per-area for the non-linear flux distribution is what drives the different behaviour. This study shows that aiming strategy is very important in defining what flow path is selected.

3.3.2 The effects of varying the tube diameter

We used the Gaussian flux distribution with "edge-to-edge" flow configuration as an example to study the effects of varying other major parameters on the thermodynamic efficiencies since the trends for these efficiencies are the same in the cases of Gaussian distribution and Linear distribution. The optimal spot size σ (1.7 m) and receiver size (64 m^2) were determined in Section 3.3.1.1.

To start with the tube inside diameter, decreasing tube diameter lowers the inner and outer wall temperatures, since a smaller tube gives higher fluid velocity, resulting in increased Reynolds number, and hence increased Nusselt number and improved internal heat transfer coefficient (Fig. 3.12). The result is reduced exergy destruction in internal convection and reduced external losses. Results for a Gaussian flux profile are shown in Fig. 3.13 and Table 3.3.

The optimal tube diameter has been identified by the model, which is 30 mm as

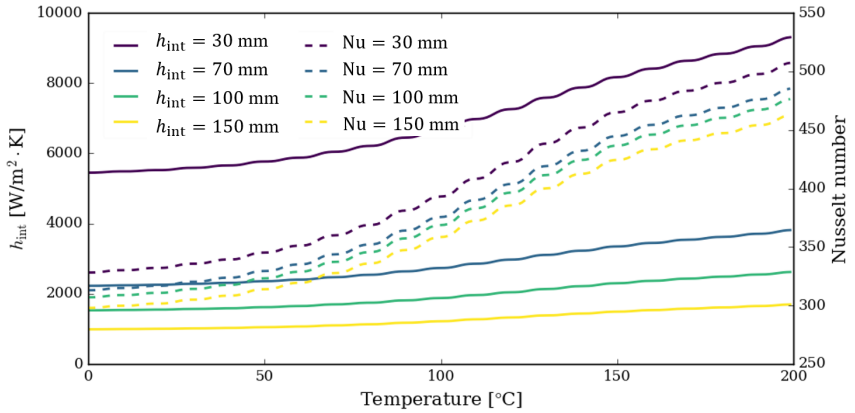

Fig. 3.12: Trends in internal heat transfer (h_{int}, Nu) with varied internal diameter d_i

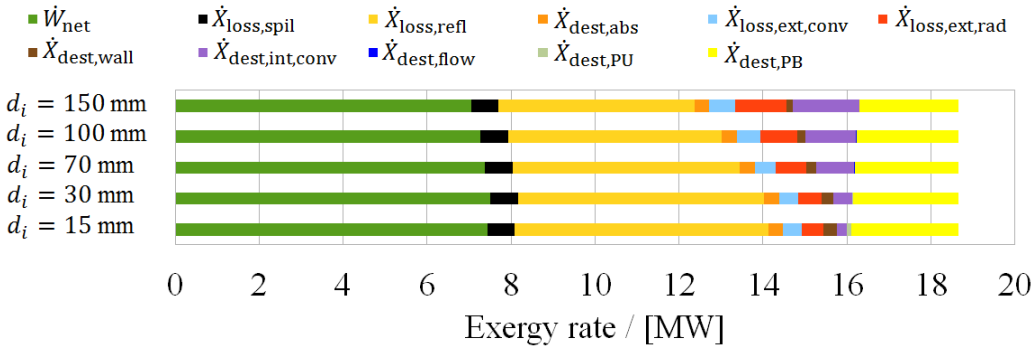

Fig. 3.13: Exergy accounting with variable d_i (Gaussian flux profile).

Table 3.3: Effect of tube diameter d_i with a Gaussian flux profile. Flow configuration is "edge-to-edge" (left-to-right)

Common parameters

$\dot{Q}_{sun}$ MW	T_{sun} K	P_{out} bar	k_{wall} W/(m·K)	h_{ext} W/(m^2·K)	T_{in} °C	T_{out} °C	G W/m^2	A_{aper} m^2	σ m	t mm	n_{banks}
20	5800	1	20	30	290	565	1000	64	1.9	2	20

Results

d_i mm	$\dot{Q}_{spil}$ MW	$\dot{Q}_{inc}$ MW	$\dot{Q}_{ref}$ MW	$\dot{Q}_{ext,conv}$ MW	$\dot{Q}_{ext,rad}$ MW	$\dot{Q}_{net}$ MW	η_I %	$\eta_{II,sys}$ %	Δ_p bar	$T_{int,peak}$ °C
15	0.71	19.29	0.25	0.76	0.84	17.44	87.21	41.31	70.91	594.98
30	0.71	19.29	0.25	0.77	0.91	17.36	86.80	41.67	7.10	631.77
70	0.71	19.29	0.25	0.83	1.14	17.06	85.32	41.01	0.48	727.85
100	0.71	19.29	0.25	0.88	1.36	16.80	84.01	40.39	0.16	798.08
150	0.71	19.29	0.25	0.96	1.79	16.29	81.45	39.16	0.04	910.59

shown in Table 3.3. If d_i becomes too small (e.g. 15 mm), it causes excessive pressure drops (Δp) and consequently, large exergy destruction in the pump.

3.3.3 The effects of varying the tube wall thickness

Reducing the tube wall thickness has the expected effect of improving receiver performance by reducing the thermal resistance of the wall and hence exergy destruction in the wall as well as lowering external temperatures and the corresponding thermal losses. A secondary effect is that a thinner tube length allow an increase in the total pipe length, allowing a slight increase in n_{tubes} per bank, even allowing non-integer (non-physical) values. Results are shown in Fig. 3.14 and Table 3.4.

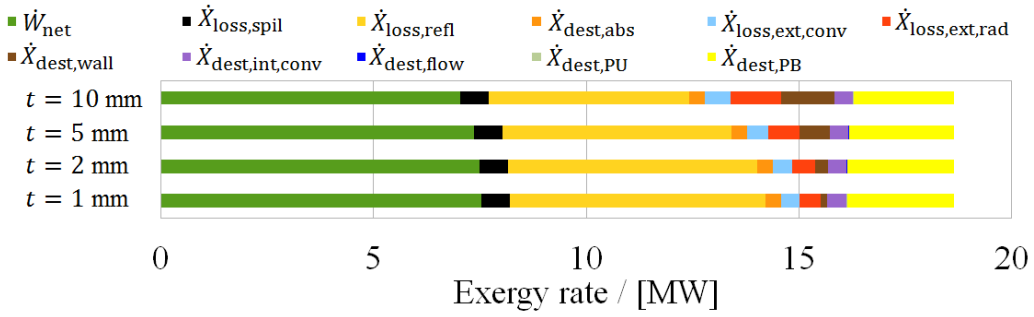

Fig. 3.14: Exergy accounting with the changing tube thickness t (Gaussian flux profile).

3.3.4 The effects of varying the n_{banks}

The number of banks (n_{banks}) shown in Fig. 3.1 allows varying degrees of flow in parallel or in series. By increasing n_{banks}, the flow path lengthens and there are less tubes in parallel. The important effects of tube friction and heat transfer enhancement, due to varying fluid velocities in the different configurations, are captured. Results (Fig. 3.15 and Table 3.5 for Gaussian profile; Fig. 3.16 and Table 3.6 for linear profile) show the effect of changing n_{banks}. Similar to the scenario of varying the tube diameter, a larger number of banks causes reduced external radiation and internal convection exergy destruction, resulting in higher overall efficiency, driven by improved internal convection. If n_{banks} were large, however, the tube wall thickness t would need to be increased to avoid excessive hoop stress in the tubes (this model requires a safety factor on hoop stress of at least one compared to an allowable stress fixed constant at 100 MPa), but at this stage t was kept constant and n_{banks} were less than 40 due to the allowable stress limit. Fig. 3.15 and Table 3.5 show that highest performance is obtained with highly in-series flow ($n_{\text{banks}} = 30$), when the flux profile is Gaussian. Next, we considered the same optimal linear flux distribution in Section 3.3.1.2 (slope, –90 kW/m^2/m) and again considered variables in n_{banks}. Results are presented in Fig. 3.16 and in Table 3.6. It shows that the $n_{\text{banks}} = 20$ gives

the best performance.

The above studies show that both decreased d_i and increased n_{banks} will increase the receiver pressure drop Δp, resulting in much increased pumping work.

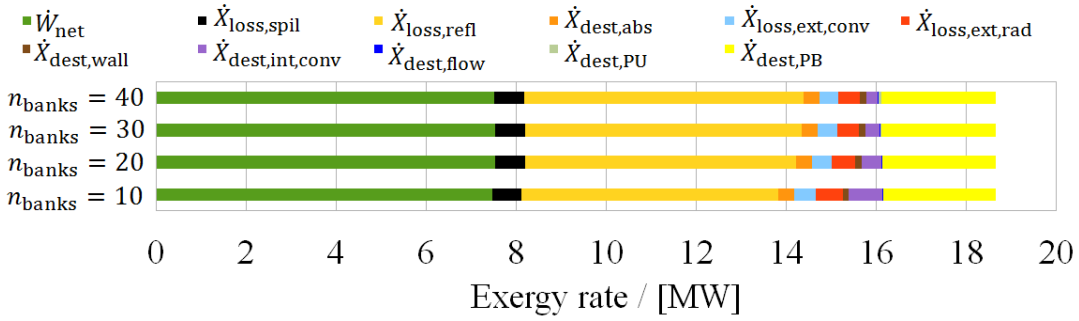

Fig. 3.15: Exergy accounting with the changing n_{banks} (Gaussian flux profile).

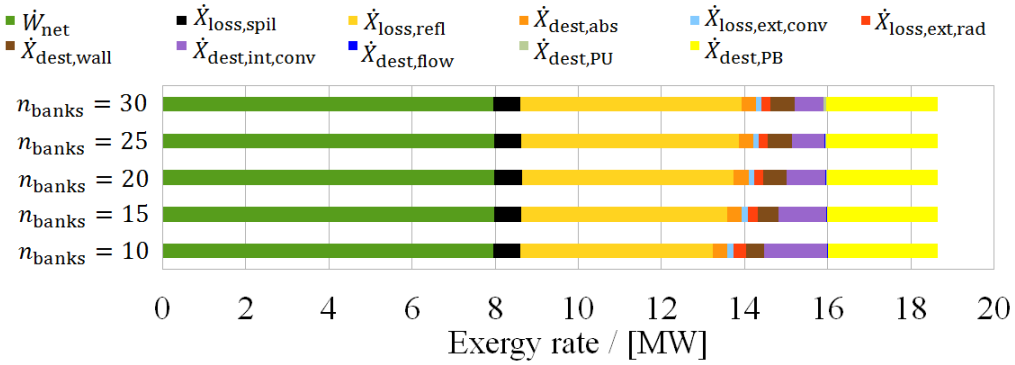

Fig. 3.16: Exergy accounting with effect of variable n_{banks} (Linear profile).

3.3.5 The effects of modelling inter-tube flux variation within a bank on the receiver performance

The number of inter-tube in one bank is defined here as the total number of flux variations within that one bank. Each inter-tube-per-bank has uniform flux distribution across the tubes horizontally, but not vertically. There is little effect on varying the inter-tube-per-bank on the receiver performance when the number of banks is larger (see Fig. 3.17). However, it would be of interest to study when the number of bank is less, as the varied wall temperatures would affect exergy destruction distributions. In addition, the model includes tube-end manifolds and minor losses to mimic a real case scenario. Optimal spot size σ = (1.7 m) and receiver size (64 m^2) were determined and used for the remaining analysis. One question of interest would be: "Designing a billboard receiver with odd or even numbers of panels (banks), which one is better?"

Table 3.4: Effect of tube wall thickness t with a Gaussian flux profile

Common parameters

$\dot{Q}_{sun}$ MW	T_{sun} K	P_{out} bar	k_{wall} W/(m·K)	h_{ext} W/(m²·K)	T_{in} °C	T_{out} °C	G W/m²	A_{aper} m²	σ m	d_i mm	n_{banks}
20	5800	1	20	30	290	565	1000	64	1.9	30	20

Results

t mm	$\dot{Q}_{spil}$ MW	$\dot{Q}_{inc}$ MW	$\dot{Q}_{ref}$ MW	$\dot{Q}_{ext,conv}$ MW	$\dot{Q}_{ext,rad}$ MW	$\dot{Q}_{net}$ MW	η_I %	$\eta_{II,sys}$ %	Δ_p bar	$T_{int,peak}$ °C
1	0.71	19.29	0.25	0.75	0.84	17.44	87.22	41.88	6.43	631.32
2	0.71	19.29	0.25	0.77	0.91	17.36	86.80	41.67	7.10	631.77
5	0.71	19.29	0.25	0.83	1.15	17.05	85.26	40.91	9.19	632.61
10	0.71	19.29	0.25	0.94	1.76	16.34	81.68	39.17	12.68	632.30

Table 3.5: Effect of varying n_{banks} with a Gaussian flux profile

Common parameters

$\dot{Q}_{sun}$ MW	T_{sun} K	P_{out} bar	k_{wall} W/(m·K)	h_{ext} W/(m²·K)	T_{in} °C	T_{out} °C	G W/m²	A_{aper} m²	σ m	d_i mm	t mm
20	5800	1	20	30	290	565	1000	64	1.9	30	1

Results

n_{banks}	$\dot{Q}_{spil}$ MW	$\dot{Q}_{inc}$ MW	$\dot{Q}_{ref}$ MW	$\dot{Q}_{ext,conv}$ MW	$\dot{Q}_{ext,rad}$ MW	$\dot{Q}_{net}$ MW	η_I %	$\eta_{II,sys}$ %	Δ_p bar	$T_{int,peak}$ °C
10	0.71	19.29	0.25	0.80	0.98	17.28	86.38	41.49	0.93	681.23
20	0.71	19.29	0.25	0.75	0.84	17.44	87.22	41.88	6.43	631.32
30	0.71	19.29	0.25	0.74	0.80	17.50	87.49	41.90	20.04	612.33
40	0.71	19.29	0.25	0.73	0.78	17.52	87.62	41.74	45.11	602.12

Table 3.6: Receiver performance for Linear flux profile with varynig n_{banks}.

Common parameters

$\dot{Q}_{sun}$ MW	T_{sun} K	P_{out} bar	k_{wall} W/(m·K)	h_{ext} W/(m²·K)	T_{in} °C	T_{out} °C	G W/m²	A_{aper} m²	d_i mm	t mm
20	5800	1	20	30	290	565	1000	12.25	30	1

Results

n_{banks}	$\dot{Q}_{spil}$ MW	$\dot{Q}_{inc}$ MW	$\dot{Q}_{ref}$ MW	$\dot{Q}_{ext,conv}$ MW	$\dot{Q}_{ext,rad}$ MW	$\dot{Q}_{net}$ MW	η_I %	$\eta_{II,sys}$ %	Δ_p bar	$T_{int,peak}$ °C
10	0.71	19.29	0.25	0.22	0.44	18.38	91.90	44.16	2.98	628.17
15	0.71	19.29	0.25	0.20	0.37	18.46	92.31	44.32	6.91	602.35
20	0.71	19.29	0.25	0.20	0.34	18.50	92.49	44.34	14.29	590.30
25	0.71	19.29	0.25	0.20	0.32	18.52	92.61	44.29	25.97	585.49
30	0.71	19.29	0.25	0.20	0.31	18.54	92.68	44.16	42.91	581.48

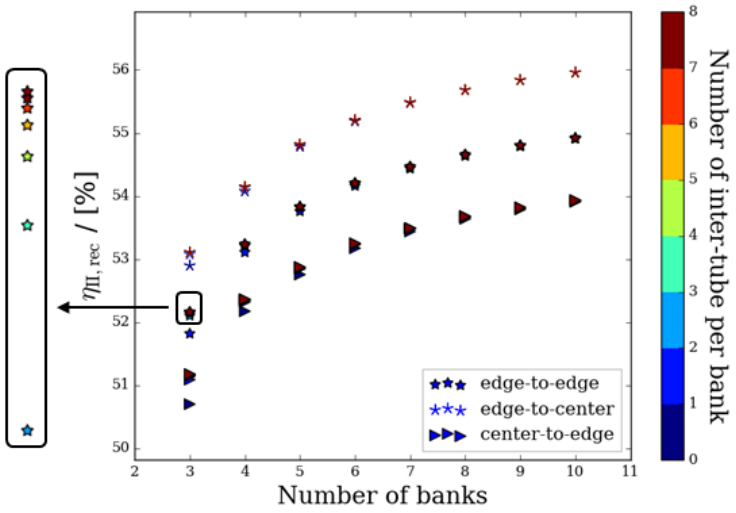

Fig. 3.17: The effect of varying number of inter-tube-per-bank on the second law efficiencies, with fixed receiver size ($A_{aper} = 64$ m^2), fixed total concentrated solar energy ($\dot{Q}_{sun} = 20$ MW), fixed spot size (σ =1.7 m) and fixed outer tube diameter ($d_o = 32$ mm).The inset highlights the small effect of varying inter-tube-per-bank in the range 1–8 on $\eta_{II,rec}$.

In the above study, we found a very marginal effect on varying number of inter-tube-per-bank on the receiver performance, when compare with the effect on varying number of banks and flow configurations. Fig. 3.18 shows that with one inter-tube-per-bank, the flux was coarsely averaged and hence, the receiver performance was highly affected. When the number of inter-tube-per-bank increased, the flux was gradually refined and hence, the receiver performance was gradually increased. However, when number of inter-tube-per-bank was larger than 3, the difference in receiver performance was no longer big enough to be observed. To summarise, the decision on the flow configuration affects the receiver performance the most, followed by the number of banks and lastly, the number of inter-tube-per-bank. The main reason is that to vary the flow configuration, external wall temperature distribution is much varied and consequently, the receiver performance is obviously differentiated.

3.4 Conclusions

From these case studies, the trends of first- and second-law efficiencies for individual conditions have been found. A comparison between best-case Gaussian and linear flux distributions is summarised in Table 3.7. Results show that the linear flux distribution (i.e. high flux at low temperature) is able to improve the efficiencies by ~6% due to the smallest receiver area required, when compared with Gaussian distribution. The "edge-to-centre" flow configuration performs the best with the Gaussian distribution, which is contrast to the reality. This is due to the reason that Gaus-

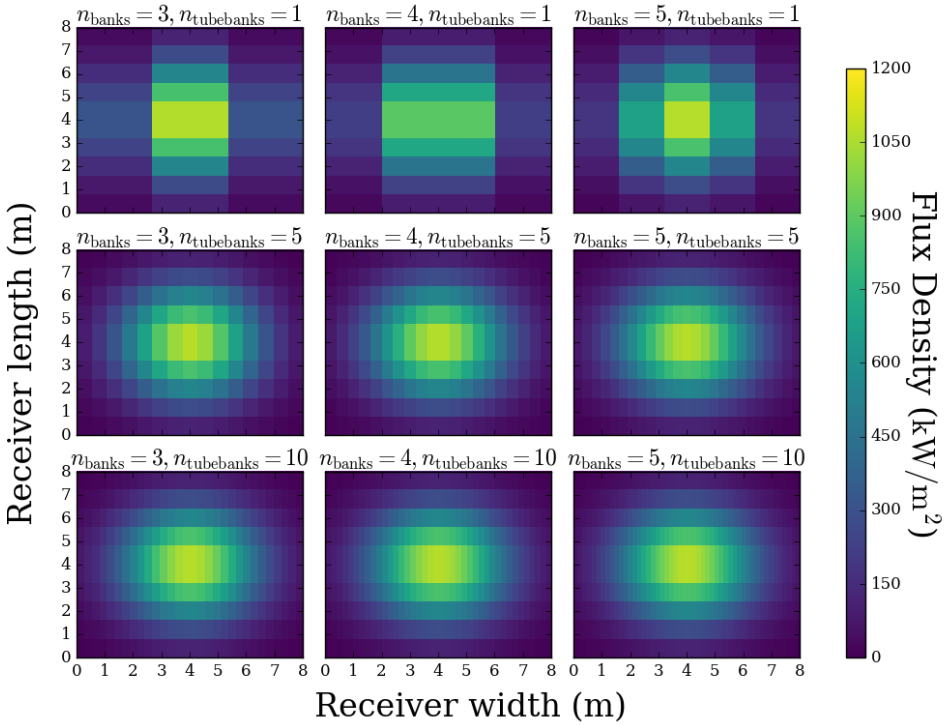

(a) Flux profiles

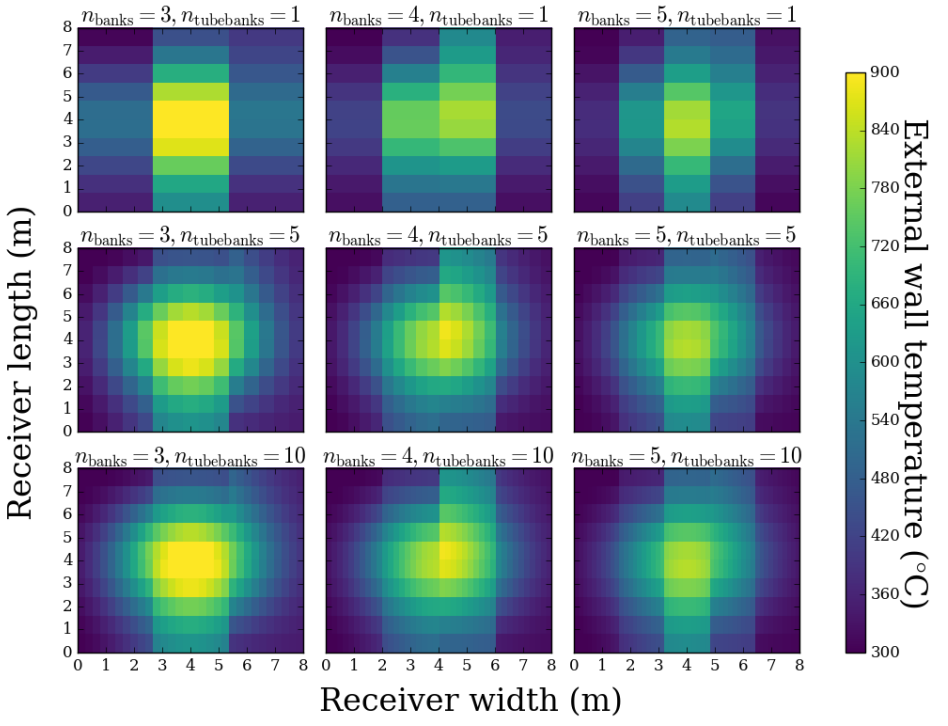

(b) External wall temperature profiles

Fig. 3.18: The effect of varying number of inter-tube-per-bank, with fixed receiver size ($A_{aper} = 64$ m^2), fixed total concentrated solar energy ($\dot{Q}_{sun} = 20$ MW), fixed spot size (σ =1.7 m) and fixed outer tube diameter ($d_o = 32$ mm). Flow configuration is "edge-to-edge" (left-to-right). (a): flux profiles; bottom; (b): external wall temperature profiles.

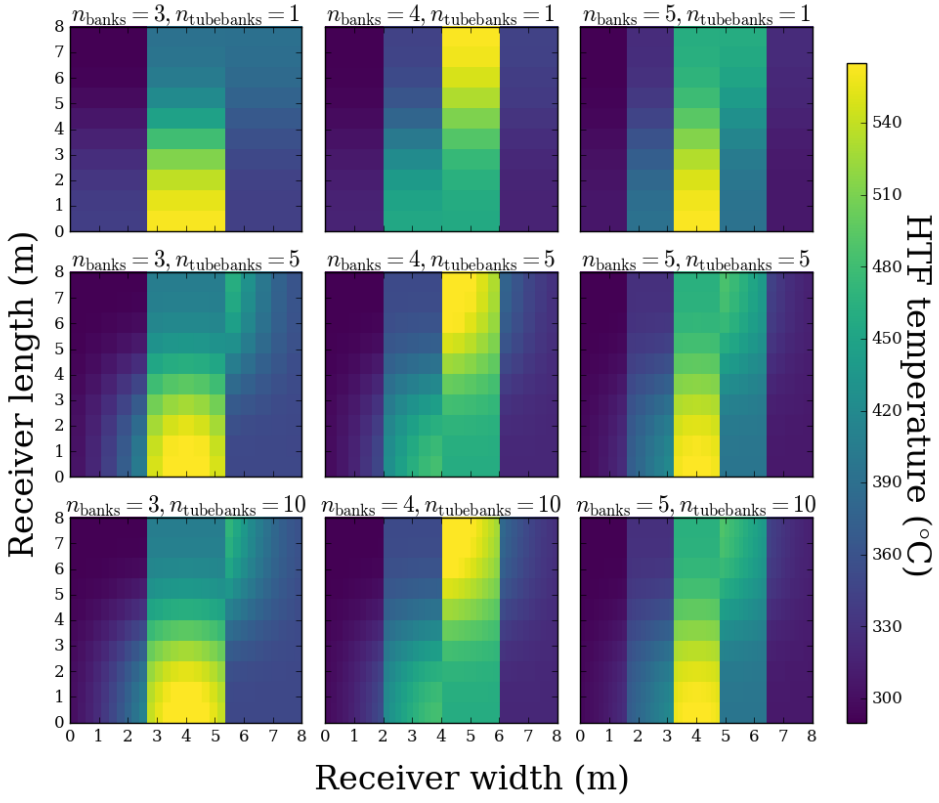

(c) HTF temperature profiles

Fig. 3.18: The effect of varying number of inter-tube-per-bank, with fixed receiver size ($A_{\text{aper}} = 64$ m^2), fixed total concentrated solar energy ($\dot{Q}_{\text{sun}} = 20$ MW), fixed spot size (σ =1.7 m) and fixed outer tube diameter ($d_{\text{o}} = 32$ mm). (c): HTF temperature profiles (cont.)

sian distribution has peaky flux in the centre of the receiver. It resulted in heating of the fluid entirely in the centralised concentrated spot, and it would encounter a large amount of heat loss at the outer area (i.e. edges) of the receiver. So, the best strategy in such case would be to heat the fluid up at the end to minimise the heat losses. With the Gaussian flux, the only alternative is to have extremely high spillage to achieve more uniform flux, but in this case, more spillage loss would occur. The "edge-to-centre" flow configuration is able to minimise the overall external losses. The ramp profile performed better, matching material limits more closely over the receiver surface, hence permitting a smaller receiver with lower losses. It evidently shows the benefits of linear flux distribution, especially in the context of restriction in elevated temperatures and being able to tolerate higher flux densities. The trade-off between spillage and peak flux density is a significant factor on affecting the first-law efficiency of the receiver, as studied in Section 3.3.1.1. However, the concept of linear ramp flux represents the upper bounds of the ideal flux distribution, which, in a way, is not physical to be achieved in reality. Spillage is caused by sun-shape, heliostat slope errors and tracking errors. These three factors have to be considered in modelling the optical performance, since they constrain the resolution of the flux distribution. The ideal flux distribution might not be achieved due to the limitations on the heliostat mirror quality. The concept of the bladed receiver (see Chapter 4) seeks the solution to overcome the flux limit on the flat receiver, so that at same energy level, the bladed receiver is able to reduce the spillage loss by absorbing more flux, without requiring infeasible mirror qualities.

In addition to the effect of flux profile, effects of tube diameter, thickness and flow configuration were examined, and it was shown that in the absence of more detailed models of material constraints, the most efficient molten salt receivers have a large number of thin small-diameter pipes running highly in series, with the consideration of the pumping losses. A detailed model on the material constraints, the receiver lifespan and the cost of the receiver is developed in Chapter 6.

Table 3.7: Summary comparison of best-case designs for Gaussian and Linear flux profiles

Common parameters

$\dot{Q}_{sun}$ MW	T_{sun} K	P_{out} bar	k_{wall} W/(m·K)	h_{ext} W/(m^2·K)	T_{in} °C	T_{out} °C	d_i mm	t mm
20	5800	1	20	30	290	565	30	1

Results

Flux	$\dot{Q}_{inc}$ MW	$\dot{Q}_{ref}$ MW	$\dot{Q}_{ext,conv}$ MW	$\dot{Q}_{ext,rad}$ MW	$\dot{Q}_{net}$ MW	η_I %	$\eta_{II,rec}$ %	A_{aper} m^2	n_{banks}
Gaussian	19.29	0.25	0.74	0.80	17.50	87.49	41.90	64.00	30
Linear	19.29	0.25	0.20	0.34	18.50	92.49	44.34	12.25	20

Chapter 4

Bladed Receivers with Active Airflow Control (BRAAC) Project: Hydrodynamic Modelling and on-sun testing[1]

4.1 Introduction

The previous two chapters (Chapter 2 and Chapter 3) have examined performance of receivers that are essentially flat, or at least convex, and it has been seen that high fluxes ultimately limit the performance of the receiver. In this chapter, a novel non-convex receiver configuration is considered, with the goal of improving the receiver performance.

4.1.1 Overview of bladed receiver concept

The bladed receiver (see Fig. 4.1), the novel design considered here, is based on a concept which was developed by Sandia National Laboratories (Sandia) and the Australian National University (ANU) [27, 28, 161]. This design uses a bladed or 'louvered' arrangement of tube banks to overcome the flux limits for state-of-the-art molten salt receivers and simultaneously to increase the light trapping effect via a cavity effect and a varied concentration ratio while respecting peak flux limits for tubes, especially considering molten salt. The blades are added to the high flux regions of the flat receiver to reduce the peak flux, and also to arrange the flow so that cooler surfaces are outwards as much as possible. However, the added blades may increase the surface area of the receiver, which result in larger thermal losses. The trade-off between optical and thermal performance on the bladed receiver leads to an optimal bladed receiver design. The objective of this chapter is to address the question of "Can the concept of the novel bladed receiver outperform the conventional

[1]The results before Section 4.5 had been presented by the author at the ASME Power & Energy Conference, in Lake Buena Vista, FL, USA, 24–28 Jun 2018, titled "Bladed or conventional flat receivers: which geometry is more efficient?"

flat receiver?".

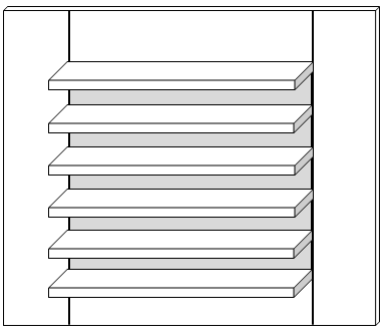

Fig. 4.1: The concept a bladed receiver.

4.1.2 Modelling approach and coordination

An integrated model was developed so that the optical performance and thermal performance could be examined simultaneously. A comprehensive flow chart of the calculation process is illustrated in Fig. 4.2.

The optical and thermal radiative performances of the receiver were examined using "Tracer", which is a Python-based Monte Carlo ray-tracing library. It uses an energy-partitioning approach that offers better convergence rates for complex geometries with multiple reflections. It was capable of simulating the light-trapping behaviour between the bladed structures in particular. The optical configuration consists of tiling of the receiver and adjustment of the length of the blades. Ray-tracing models were described and examined by Ye Wang in her PhD thesis [101]. In this way, her flux distribution maps were passed to the author's hydrodynamic model. Internal flow models were then developed by the author to evaluate the thermal performance on both conventional flat and bladed solar-thermal receivers.

The approach to examining the thermal performance on both flat and bladed receivers is to develop 1D hydrodynamic numerical models, which consider external radiative convection, heat conduction through the tube wall, internal convective heat transfer and pressure stresses as a function of incident flux distribution, receiver size, flow configuration, working fluid properties, tube size, tube wall thickness, and inlet and outlet conditions. Flat and bladed receiver models are established for large-scale reference case1s. The CSIRO facility in Newcastle, Australia was used for the small-scale experimental on-sun testing due to limited space offered. The plant layout (i.e. heliostat positions and tower geometry) of the Abengoa PS10 11 MW solar thermal tower plant [104] was used in this study, as the reference field layout, to compare the performance of the flat and the bladed cases. The receiver size, tube size, flow configuration and aiming strategy were thoroughly examined and a de-

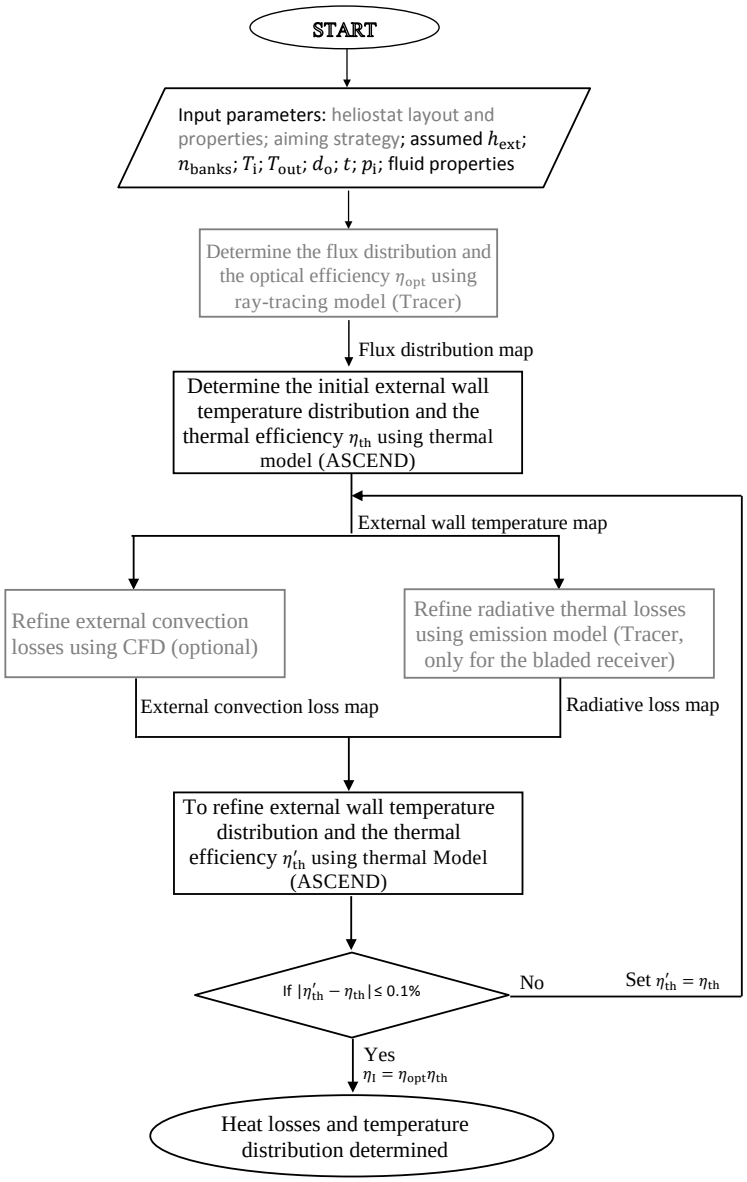

Fig. 4.2: The flow chart for the integration concept. The work, that the author was conducted, has been highlighted in black.

sign with optimal efficiency was determined for the flat case. Next, a bladed receiver design was sought, which was able to show a better performance for the same PS10 field, through several iterative refinements. The working fluid in the receivers is assumed to be conventional molten salt (60% $NaNO_3$, 40% KNO_3), heated from 290°C to 565°C, from receiver inlet to the outlet.

CFD (computational fluid dynamics) modelling was conducted by Felipe Torres in OpenFOAM with a steady-state RANS (Raynolds Average Navier-Stokes equations) turbulence model called SST k-ω (Shear-Stress Transport k-omega) [162, 163], to examine the external losses as a function of the receiver surface temperature. These simulations provided the average heat transfer coefficient for these receivers under various conditions such as receiver pitch angle, wind direction, wall temperature, and wind speed. The CFD simulations were validated with wind tunnel experiments by Torres et al. [164].

Apart from hydrodynamic models, Monte Carlo ray-tracing simulations and CFD models are involved in the ARENA Project 2014-RND010 "Bladed Receivers with Active Airflow Control". These two parts were assigned to other project team members, and hence are not included in this thesis.

Once the reference models were established, the next step was to test the on-sun performance of these two receivers at CSIRO. CSIRO, the Australian National Science Agency, has its energy centre in Newcastle which hosts solar field and energy research hub [165]. It has two facilities: Solar Field 1 and Solar Field 2 (see Fig. 4.3). The tower allows for mounting of different receivers for testing. There is a control system for aiming heliostats and maintaining a specified flux distribution. Water and compressed air pipework are available at the top of the receiver. There is a cooling tower and electricity supply for pumps and controls. Due to the limitations of the CSIRO facility, it was not possible to test the receivers with the same design points, for example, the designed receiver sizes and the chosen working fluid. Hence, alternatives were developed to test the receivers at a smaller scale with water and air instead of molten salt [166].

4.2 Hydrodynamic model description

The hydrodynamic model was solved using the equation-based ASCEND modelling environment, which was introduced in Chapter 2. The detailed energy balance and momentum balance expressions can be found in Section 2.4.2. An internal heat transfer correlation was suggested by Gnielinski for turbulent flow in smooth tubes for $1.5 < Pr < 500$ and $3000 < Re < 10^6$ [137]:

$$Nu = 0.012 \left(Re^{0.87} - 280\right) Pr^{0.4} \tag{4.1}$$

Fig. 4.3: CSIRO's heliostat field with two towers in Newcastle, NSW.

where $\mathrm{Re} = \frac{\rho \mathbf{V} d_i}{\mu}$ and $\mathrm{Pr} = \frac{c_p \mu}{k}$, all properties are evaluated at bulk temperatures.

The flow path was firstly separated into several banks of parallel tubes, as shown in Fig. 4.4. The flux variation in circumferential direction are ignored, so all tubes in the bank are assumed to experience the same flux. The backward-facing half of the tube was assumed to be an adiabatic wall. Three flow configurations were established in this project, which are as same as defined in Fig. 3.2.

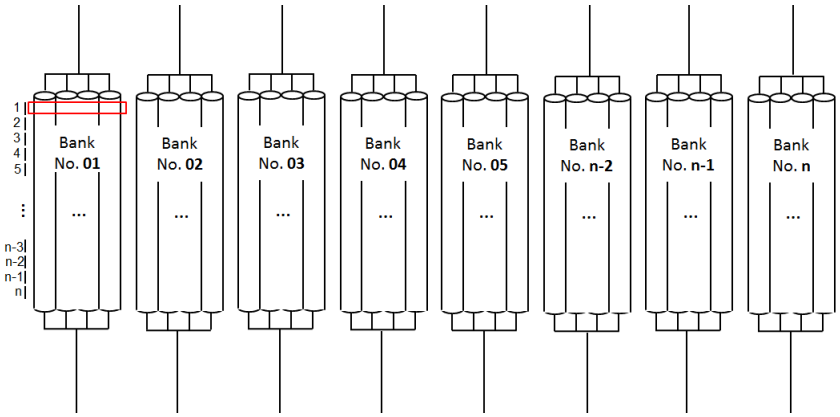

Fig. 4.4: The breakdown of the flow path

4.3 Methodology

In this analysis[2], the energy losses due to the spillage ($\dot{Q}_{\mathrm{spil,rec}}$), the reflection ($\dot{Q}_{\mathrm{refl,rec}}$), the external radiation ($\dot{Q}_{\mathrm{ext,rad,rec}}$) and the external convection ($\dot{Q}_{\mathrm{ext,conv,rec}}$) are considered. For the bladed receivers, the surfaces are divided into small meshes.

[2]The model used in this chapter is an extension of the model described in Chapter 2, and only the additional details are explained in the following section.

View factors are considered between each mesh element to capture the effect of tube tips, gaps between blades, by implementing the radiosity analysis. The total external radiation loss ($\dot{Q}_{\text{ext,rad,rec}}$) is calculated according to the radiosity balance. All of the radiative calculations are implemented in the ray-tracing model, which is conducted by Wang [101]. The total number of mesh elements on the receiver in the ray-tracing model is equivalent to the total number of segments in the thermal model, so that integration can be conducted. The detailed expressions for $\dot{Q}_{\text{ext,conv,rec}}$ and $\dot{Q}_{\text{net,rec}}$ have been defined in Eq. 2.5 and 2.6, respectively. The external convection coefficients (h_{ext}) are varied for different scenarios and have been labelled in each case. For the flat case, the external convection coefficient is assumed to be 16 W/m^2·K, while for the bladed receiver, this value is assumed to be 8 W/m^2·K. These two values used in this chapter are consistent with the conclusions made by Nock et al. [167] and by Torres et al. [168] for the large-scale receiver designs using CFD model, with an averaged wind speeds of 2.5 m/s, in headwind direction (yaw 0°). The wall conduction k is assumed to be 20 W/m·K throughout the whole analysis. It is an average value for the commonly used tube materials in the tubular receivers, such as SS316 at $\sim$ 400°C [131], Alloy 617 at $\sim$ 500°C [132], Haynes 230 at $\sim$ 600°C [151], and Alloy 740H at $\sim$ 800°C [133].

And therefore, the rate of energy balance for the steady-flow receiver becomes:

$$\dot{Q}_{\text{sun,rec}} = \dot{Q}_{\text{spil,rec}} + \dot{Q}_{\text{refl,rec}} + \sum_{\text{rec},i} \dot{Q}_{\text{abs,rec},i} \tag{4.2}$$

where $\dot{Q}_{\text{spil,rec}}$ and $\dot{Q}_{\text{refl,rec}}$ are calculated using optical modelling, which was implemented by another project member, Wang [101]. $\dot{Q}_{\text{abs,rec},i}$ is the total energy being absorbed in one segment, which is defined in Eq. 2.3.

The optical efficiency is then:

$$\eta_{\text{opt}} = 1 - \frac{\dot{Q}_{\text{spil,rec}} + \dot{Q}_{\text{refl,rec}}}{\dot{Q}_{\text{sun,rec}}} = \frac{\sum_{\text{rec,i}} \dot{Q}_{\text{abs,rec},i}}{\dot{Q}_{\text{sun,rec}}} \tag{4.3}$$

The thermal efficiency is defined as:

$$\eta_{\text{th}} = \frac{\sum_{\text{rec,i}} \dot{Q}_{\text{net,rec},i}}{\sum_{\text{rec,i}} \dot{Q}_{\text{abs,rec},i}} \tag{4.4}$$

It notes that the thermal efficiency defined in this chapter is different from Chapter 3, Eq. 3.4. And therefore, the overall system efficiency η_{tot} is:

$$\eta_{\text{tot}} = \eta_{\text{I}} = \frac{\sum_{\text{rec,i}} \dot{Q}_{\text{net,rec},i}}{\dot{Q}_{\text{sun,rec}}} = \eta_{\text{opt}} \cdot \eta_{\text{th}} \tag{4.5}$$

4.4 Finalised PS10 design cases

4.4.1 PS10 reference flat case

Having a larger receiver results in a higher optical efficiency due to lower level of spillage, but also a lower thermal efficiency due to larger external losses. A range of simulations were conducted in order to obtain a thorough analysis of a flat receiver with a PS10-like flux distribution. Monte Carlo ray-tracing simulations were implemented firstly to examine the flux distribution on the receiver, including the effects of heliostat slope error and aiming strategies, sun-shape error, and heliostat reflectivity, which are summarised in Table 4.1. Varying the heliostat field aiming strategy and the aperture area of the receiver varied spillage and reflection, and consequently led to an optimal optical performance. Then, the energy balance for the receiver with a number of segments was determined, by implementing the flux map generated by ray tracing simulation, and balancing the external convective and radiative losses, and internal heat transfer to the working fluid. The trade-offs on external convective, external radiative losses and pumping losses due to varying the flow configuration, the tube size, the tube wall thickness, and the flow length (i.e. number of tube banks) led to an optimal thermal performance. The effects of varying the tube diameter, the tube wall thickness and the number of banks on the thermal efficiencies were discussed in Chapter 2 (uniform flux distribution), and in Chapter 3 (non-uniform flux distribution), and hence, are not studied here again since the trends of the performance are the same. The effect of varying flow configuration on thermal performance of the receiver is shown in Fig. 4.5. The "edge-to-centre" candidate gives the highest overall thermal efficiency but also highest peak external wall temperature among these three options due to less hot spots.The combined effect of optical performance and thermal performance results in an optimal receiver design, as shown in Fig. 4.6. For the "edge-to-centre" flow configuration, higher peak flux gives fewer hot spots, and consequently, results in more efficient receiver. However, for the remaining two flow configurations, lower peak flux results in more efficient receiver due to less external losses at low fluid temperature regions. There is more detail in the Wang's PhD thesis [101].

Table 4.1: The key parameters used in the optical model for PS10 designs.

No. of heliostats	Heliostat size	Slope error	Mirror reflectivity	Sunshape	Aiming strategy
624	12.9 m (Width) × 9.6 m (Height)	0.9 mrad	0.95	Pillbox	the image size priority in SolarPILOT

Detailed energy and exergy breakdown for the finalised PS10 flat receiver is summarised in Table 4.2. It was found to be a 10-m length square receiver with 25 tube banks connected in "edge-to-centre" pattern, the outer tube diameter was 60 mm with a 1.5 mm tube wall thickness under peak flux of 1198 kW/m^2. The finalised

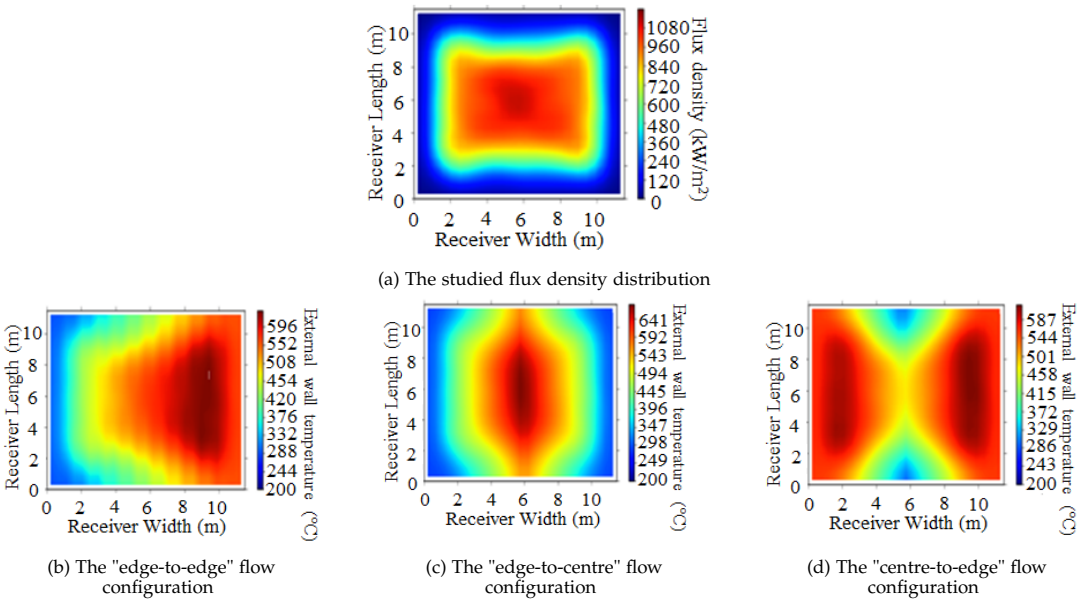

(a) The studied flux density distribution

(b) The "edge-to-edge" flow configuration

(c) The "edge-to-centre" flow configuration

(d) The "centre-to-edge" flow configuration

Fig. 4.5: The effect of varying flow configuration on thermal performance. (a) the flux distribution; (b)–(d) the external wall temperature distribution for different flow configurations, where (b) gives $\eta_{\text{th}} = 91.9\%$, (c) gives $\eta_{\text{th}} = 92.9\%$, and (d) gives $\eta_{\text{th}} = 91.5\%$.

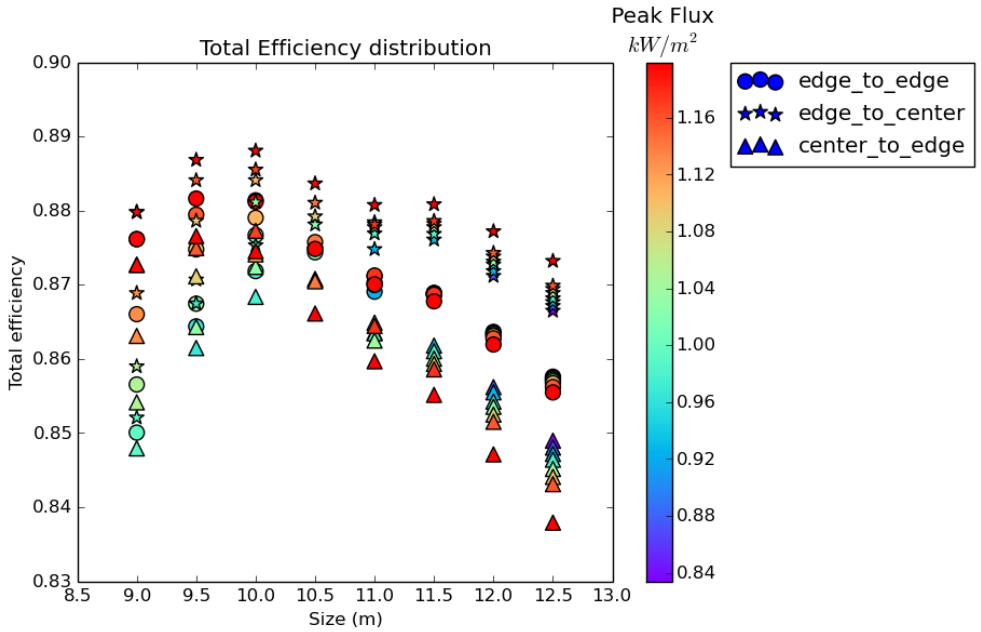

Fig. 4.6: Parametric study on the receiver efficiency for the flat receiver. This figure is owned by Wang in her PhD thesis [101]. The thermal model was that presented by the author.

flux distribution and the external wall temperature distribution are shown in Fig. 4.7. The minimum and maximum external wall temperatures are 289.5°C and 665.7°C, respectively.

The optimised PS10 flat receiver was calculated to have a total efficiency (η_{tot}) of 91.66%, consisting of 0.74% for spillage loss, 3.88% for reflection loss, 2.64% for external radiative loss and 1.09% for external convective loss. It was also calculated to have 56.67% for total exergy efficiency, consisting of 0.74% for spillage loss, 3.88% for reflection loss, 1.78% for exergy loss in external radiation, 0.71% for exergy loss in external convection, 1.95% for exergy destruction in wall, 2.69% for exergy destruction in internal convection and 0.02% for exergy destruction in flow.

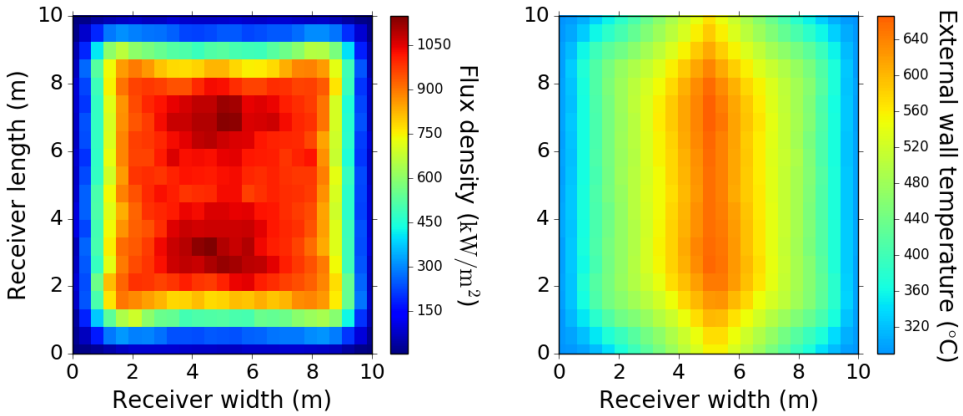

Fig. 4.7: Finalised flux and the external wall temperature distributions for PS10 flat case. Receiver layout: 10 m × 10 m.

4.4.2 PS10 bladed case

For the bladed receivers, the working fluid firstly runs through the edges, as marked "A, B, C, D" in Fig 4.8(a). By introducing the edges, the energy loss in spillage could be much reduced. In addition, as the flux and the working fluid temperature at these sections were both low, the calculated external wall temperatures were low, which resulted in a very small amount of external energy losses. The external radiation loss and the external convection loss were calculated using Eq. 2.4 and Eq. 2.5, respectively. There were no blades attached on the edges, as the low flux on the edges would eliminate the benefits of using blades to overcome the flux limits. In contrast, extra blades would increase the convective heat loss and the cost. The receiver is tilted down, to essentially line up with the centre of the heliostat field. The effect of varying the blade angles has been investigated by Wang et al. [169]. Then, the working fluid passed to the blades (flowing from the tips to the back wall, see Fig 4.8(b)), which were attached to the central part of the receiver. There were two reasons: firstly to minimise the temperature of the tips due to high flux, and secondly

Table 4.2: Detailed results of the finalised PS10 flat case

Inputs								
Receiver mesh	$\dot{Q}_{sun}$	p_{out}	k_{wall}	h_{ext}	T_{in}	T_{out}	T_{ref}	A_{aper}
20 ×10	65.79 MW	1 bar	20 W/m·K	16 W/m^2·K	290°C	565°C	20°C	100 m^2
Results: energy breakdown								
$\dot{Q}_{spil}$	$\dot{Q}_{ref}$	$\dot{Q}_{abs}$	$\dot{Q}_{ext,rad}$	$\dot{Q}_{ext,conv}$	η_{opt}	η_{th}	η_{I}	p_{in}
0.48 MW	2.55 MW	62.75 MW	1.74 MW	0.72 MW	–	–	–	14.02 bar
0.74%	3.88%	95.38%	2.64%	1.09%	95.38%	96.09%	91.66	
Results: exergy breakdown								
$\dot{X}_{sun}$	$\dot{X}_{loss,spil}$	$\dot{X}_{loss,ref}$	$\dot{X}_{dest,abs}$	$\dot{X}_{loss,ext,rad}$	$\dot{X}_{loss,ext,conv}$	$\dot{X}_{dest,wall}$	$\dot{X}_{dest,int,conv}$	$\dot{X}_{dest,flow}$	η_{II}
61.35 MW	0.45 MW	2.38 MW	19.37 MW	1.09 MW	0.44 MW	1.20 MW	1.65 MW	0.01 MW	–
100%	0.74%	3.88%	31.57%	1.78%	0.71%	1.95%	2.69%	0.02%	56.67%

to reduce the radiative losses from the hottest parts of the blades due to the T^4 effect. High flux was expected on the bladed area, so that the value of adding blades could be seen. It is necessary that a significant share of the total flux be absorbed on the blade surfaces, in order for the blades to be beneficial in the overall design. The front half tubes on the blades were discretised circumferentially, except the outside tube on each blade was considered as a 4-sector one (i.e. tip, top, bottom and adiabatic wall sections, see Fig 4.8(c)). Finally, the working fluid runs through the back wall (see Fig 4.8(d)), in an "edge-to-centre" flow configuration. The backwards-facing half of the tubes on the edges and the back wall were assumed to be adiabatic walls. It was assumed that the working fluid in the receiver would remain the same as the conventional molten salt. The temperature range of the working fluid was from 290°C at the inlet to 565°C at the outlet.

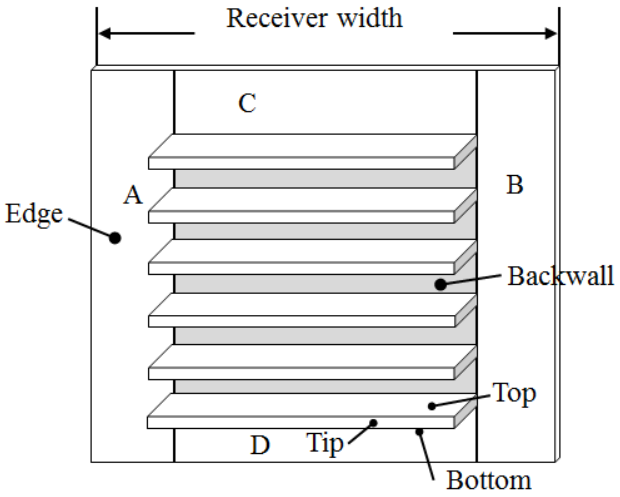

(a) Illustration of the numbering system

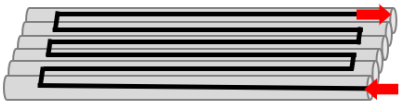

(b) Fluid flow configuration on the blade.

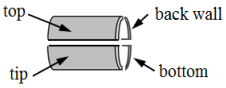

(c) Tube segments for the first tube on the blade.

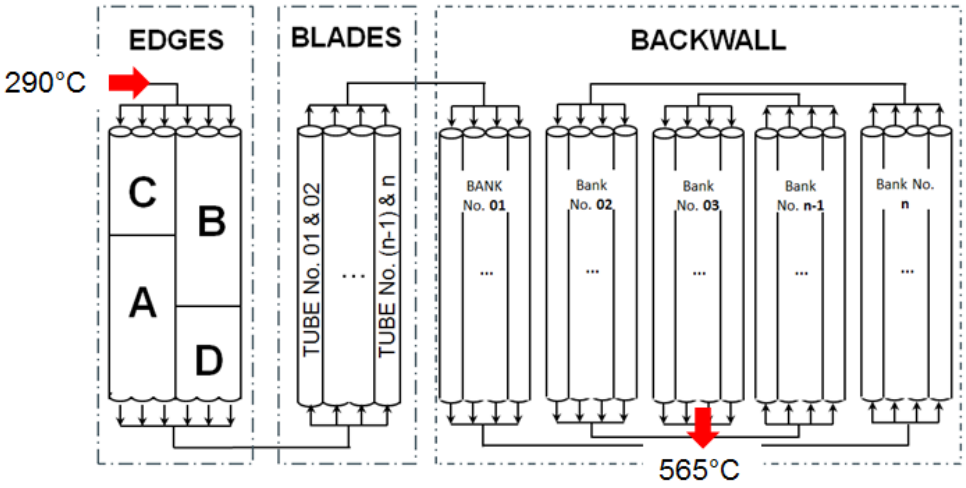

(d) Detailed flow configurations of the bladed receiver

Fig. 4.8: The break-down of the flow configuration for the bladed receiver.

The objective in design of a bladed receiver was to find a configuration that could show significantly better performance compared to a flat reference case. A series of bladed receiver designs were examined by varying the aiming strategies, the blades length, the space between blades, the number of blades, the size of the edges, but keeping the flow configurations the same. Examples are shown in Fig 4.9. Short and long blades were studied, as well as wide-spaced and narrow-spaced blades. The size of the 'edge' section was also studied. Results showed that longer blades would give higher optical efficiency due to light trapping enhancement, but lower thermal efficiency as external convection and radiation losses were increased due to larger surface area. It was concluded that a larger number of short blades was preferable. The finalised flux profiles and the external wall temperature profiles for PS10 bladed case is shown in Fig 4.10. The blades are much cooler than the back wall, due to the flow-pathing within the structure. In addition, the blade tips are cooler than the backs of the blades.

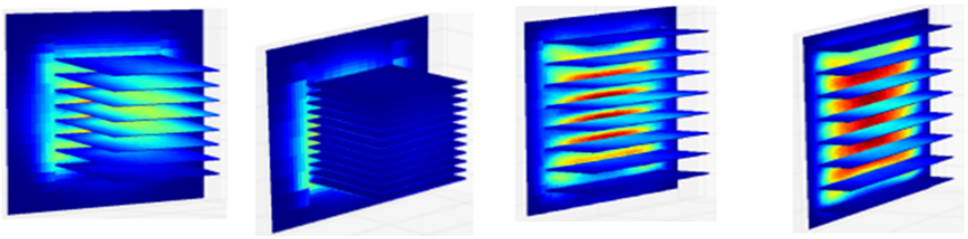

(a) Flux distribution

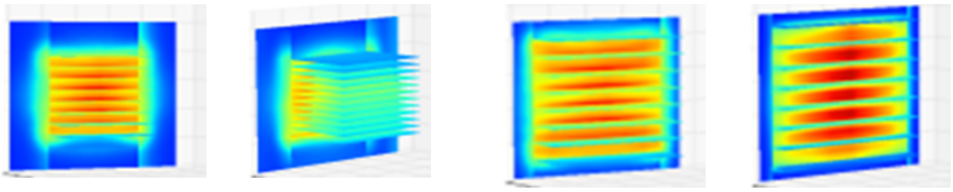

(b) The corresponding external wall temperature distribution

Fig. 4.9: Examples of a series of intuitive bladed receiver designs.

The detailed energy and exergy breakdown for the finalised PS10 bladed receiver is summarised in Table 4.3. It was calculated to have 94.15% for total energy efficiency, consisting of 0.76% for spillage loss, 1.95% for reflection loss [3], 2.00% for external radiative loss and 1.44% for external convective loss, where the external conditions are obtained from the referenced CFD models, stated in Section 4.3. It was also calculated to have 58.29% for total exergy efficiency, consisting of 0.75% for spillage loss, 1.96% for reflection loss, 1.37% for exergy loss in external radiation, 0.70% for exergy loss in external convection, 1.58% for exergy destruction in wall, 2.71% for exergy destruction in internal convection and 0.0082% for exergy destruction in flow.

[3]Detailed optical losses are studied in Wang's PhD thesis [101].

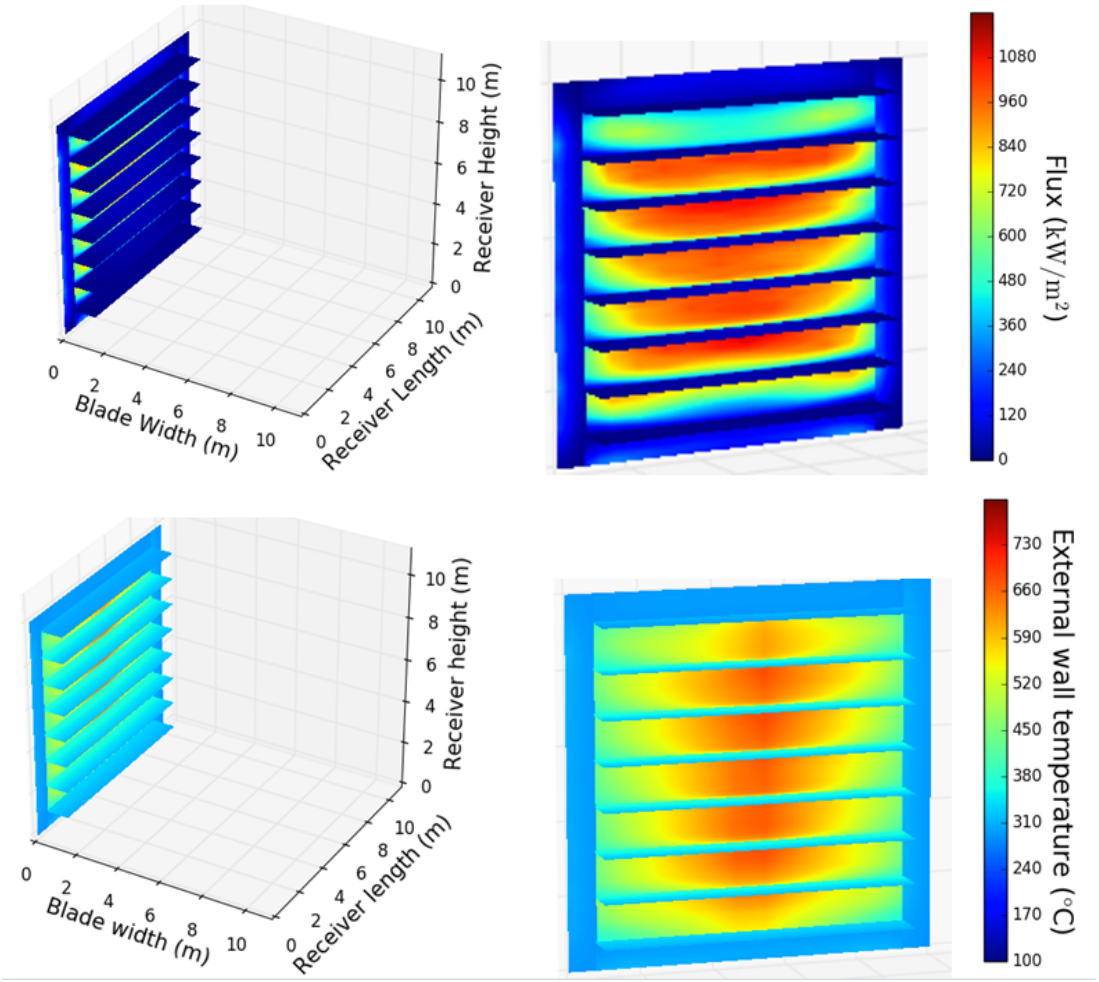

Fig. 4.10: Finalised flux profiles (Top) and the external wall temperature profiles (bottom) for PS10 bladed case. It was found to achieve a reasonable benefit, in the absence of a thorough optimisation process. Receiver layout: back wall: 10 m $\times$ 10 m; 8 blades: 8.5 m $\times$ 0.995 m each.

Table 4.3: Detailed results of the finalised PS10 bladed case

Inputs

$\dot{Q}_{sun}$	k_{wall}	h_{ext}	T_{in}	T_{out}	T_{sun}	d_i	t
65.80 MW	20 W/m·K	8 W/m^2·K	290°C	565.83°C	5800 K	47.8 mm	1.5 mm

Results: energy breakdown

	$\dot{Q}_{spil}$	$\dot{Q}_{refl}$	$\dot{Q}_{abs}$	$\dot{Q}_{ext,rad}$	$\dot{Q}_{ext,conv}$	mesh
Edges	–	–	2.93 MW	0.16 MW	0.06 MW	20 ×10
Blades			14.35 MW	-0.08 MW	0.39 MW	40 ×10
Backwall			46.70 MW	1.246 MW	0.30 MW	20 ×25
Total	0.50 MW	1.28 MW	63.98 MW	1.32 MW	0.75 MW	η_I
	0.76%	1.95%	–	2.00%	1.14%	94.15%

Results: exergy breakdown

	$\dot{X}_{sun}$	$\dot{X}_{loss,spil}$	$\dot{X}_{loss,refl}$	$\dot{X}_{dest,abs}$	$\dot{X}_{loss,ext,rad}$	$\dot{X}_{loss,ext,conv}$	$\dot{X}_{dest,wall}$	$\dot{X}_{dest,int,conv}$	$\dot{X}_{dest,flow}$	η_{II}
Edges	–	–	–	–	0.09 MW	0.03 MW	0.02 MW	0.04 MW	0.0003 MW	–
Blades					-0.05 MW	0.21 MW	0.18 MW	0.32 MW	0.001 MW	
Backwall					0.81 MW	0.19 MW	0.77 MW	1.3 MW	0.03 MW	
Total	61.33 MW	0.46 MW	1.20 MW	20.02 MW	0.84 MW	0.43 MW	0.97 MW	1.66 MW	0.005 MW	–
	100%	0.75%	1.96%	32.64%	1.37%	0.70%	1.58%	2.71%	0.0082%	58.29%

4.4.3 Conclusion

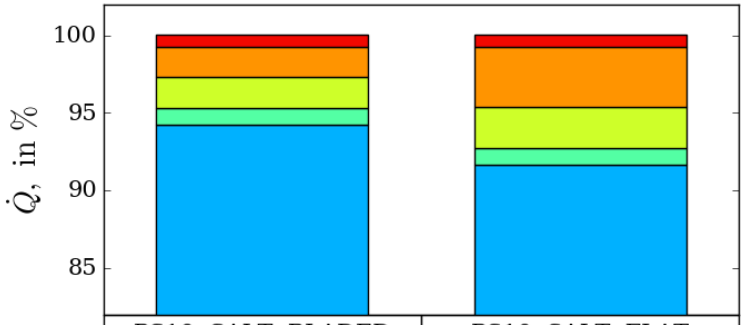

	PS10, SALT, BLADED	PS10, SALT, FLAT
$\dot{Q}_{\text{spil}}$	0.76	0.74
$\dot{Q}_{\text{refl}}$	1.95	3.88
$\dot{Q}_{\text{ext,rad}}$	2.00	2.64
$\dot{Q}_{\text{ext,conv}}$	1.12	1.09
$\dot{Q}_{\text{net}}$	94.20	91.66

Fig. 4.11: The summarised energy accounting for both PS10 flat and bladed receivers. These numbers can be found in Table 4.3 and Table 4.2 respectively, where obtain detailed results

As summarised in Fig. 4.11, for the bladed concept (receiver layout: back wall: 10 m $\times$ 10 m; 8 blades: 8.5 m $\times$ 0.995 m each), the reflective (1.95%) and the external radiative (2.00%) losses are much reduced due to the light trapping effect, unlike the flat case (receiver layout: 10 m $\times$ 10 m) where reflected rays are wasted. The reflective and the external radiative losses for the flat case are 3.88% and 2.64%. An example of the thermal radiation trapping effect is illustrated in Fig. 4.12. The results of this analysis suggests that a bladed receiver design has the potential to be more efficient than a conventional flat receiver. The results for this bladed receiver show at least a 2.49% improvement in efficiency relative to the flat case. In other words, the concept of a bladed receiver is able to achieve at least 30% of reduction in receiver optical and thermal losses. It is noted that while this receiver design was informed by the analysis, it has not been rigorously optimised (instead has relied on a degree of design intuition). Hence the 2.49% gain in efficiency does not necessarily represent the maximum possible improvement.

4.5 On-sun testing

The objective of on-sun tests is to attempt to confirm the predicted performance benefits for the bladed receiver, relative to the best flat receiver, can be demonstrated in a realistic experimental scenario. The receivers keep the same shape as the PS10 case but at smaller scales. Flux distributions and temperature distributions were matched to the PS10 case, to get the same optical losses (but scaled by area) and

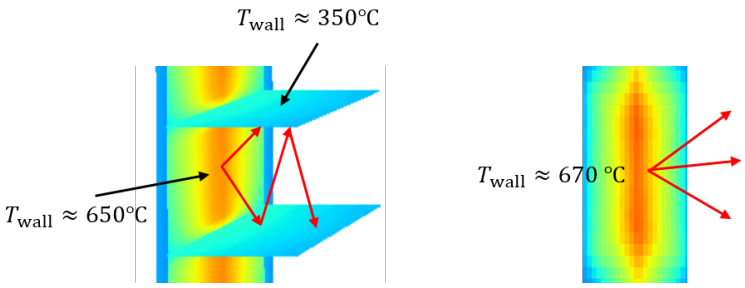

Fig. 4.12: Illustration of the thermal radiation trapping effect, refers to the red arrows.

the same thermal losses (but scalded by area). Firstly, the size of the receiver was determined by matching the available space upon the tower at the CSIRO facility. The available testing space was a 1.5 m $\times$ 1.5 m square. A 0.2 m margin on each side for fabrication and installation was considered and hence, the receiver size was initially fixed at a 1.3 m $\times$ 1.3 m square. Importantly, the intended working fluid, molten salt, was not available at CSIRO. Therefore, two alternative working fluids, water and air were chosen to access optical and thermal performance respectively and separately, as shown in 4.13. The optical efficiency could be tested with high flux and low temperature (i.e. to neglect thermal loss). Water was selected as the working fluid to apply strong receiver cooling. However, the thermal efficiency test required hot external surfaces, at temperature as close as possible to those expected with molten salt. These temperatures could not be achieved using CSIRO facility, and hence, air was adopted for this test. As a result, the overall performance could be tested as a combination of making use of these two fluids. The results of this 'virtual experiment' design were published by Pye et al. [166]. Detailed design strategies, receiver geometries and final simulation results on both small-scale flat and bladed receivers are described in Sec. 4.5.1. Actual experimental results are summarised and discussed in Sec. 4.5.2.

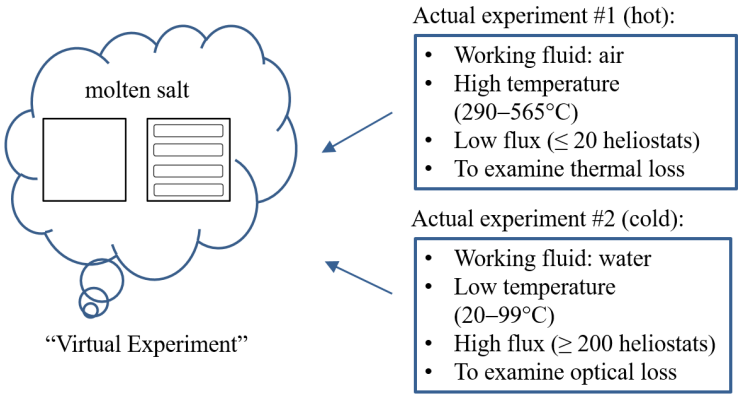

Fig. 4.13: The concept of the "virtual experiment".

4.5.1 Comprehensive design analyses

Small tubes were considered to enhance the internal heat transfer of the air receivers. The tube size was fixed at 12.7 mm with a 0.9 mm thickness. The spacing between tube centres was approximately 13.5 mm. As a result, the flat receiver size was eventually fixed at 1.296 m $\times$ 1.296 m square, consisting of 8 tube banks with 12 tubes in each bank. The bladed receiver footprint was fixed at a 1.281 m $\times$ 1.281 m square. The bladed receiver consists of three sections, namely the edge, blade and back-wall, as shown in Fig. 4.14. The edge section consists of four panels with 7 tubes on each panel. The blade section consists of four coiled single-pass loops (i.e. 8 blades) to minimise manufacturing and material costs, with 9 tubes on each blade. The flow configuration for blades was determined as the working fluid running from the tips (i.e. the outermost) to the back wall (i.e. the innermost). The back wall consists of 8 banks with 10 tubes per bank. The flow configuration for the back-wall was "edge-to-centre".

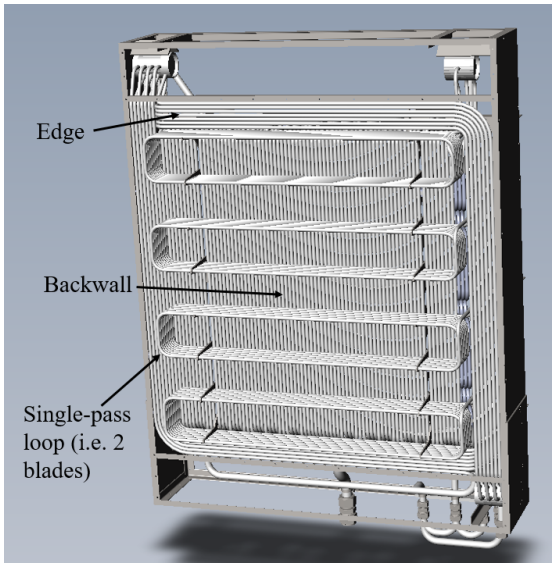

Fig. 4.14: The design concept of the bladed receiver.

The purpose of testing the receiver with air as the heat transfer fluid was to determine thermal performance by matching the external wall temperature distribution to that expected in a molten salt receiver as closely as possible. Air receivers were characterised by low-flux and high-temperature to reduce the optical losses to minimum. The thermal performance of the molten salt receivers was evaluated based on the external losses on the receivers, as functions of external wall temperatures. Therefore, by matching the external wall temperature distributions on the air receivers to those of the molten salt receivers, the external losses of the molten salt receiver could be mimicked and examined through air receivers, and consequently, the thermal performance could be determined, without examining the internal heat transfer features of the molten salt receivers.

Low-temperature water tests were established to determine the optical performance of the receiver. The receivers were designed under high-flux and high water flow rate conditions. The strategy was to keep the water temperature as low as possible (<100°C, the boiling point at the ambient pressure) to reduce the thermal losses (i.e. convective and radiative losses) to a minimum and to allow the optical losses to dominate. In this way, the quantity of the optical losses of the receiver would be directly measured using an experimental method. Ideally, the optical performance should be represented using the largest possible number of heliostats.

The final designs of the receiver mock-up proposed for on-sun testing are discussed in the following sections: Section 4.5.1.1 and Section 4.5.1.2.

4.5.1.1 CSIRO air receiver design cases

The aim of air receiver test is to quantify thermal losses without excessive optical losses (refer back to Fig. 4.13). It requires to achieve high temperature using low fluxes, which suits the use of air as a HTF. Hence, a small number of heliostats were used (i.e. 20 heliostats) to reduce the optical losses to the minimum, while to match the external wall temperature distribution to the maximum. Aiming points are manually determined, so that the external wall temperature profiles could be matched. The distribution of the external wall temperature (right figure in Fig. 4.15(a)) for the air case is very sensitive to the flux distribution, due to the poor heat transfer properties of the air. As a result, the design of the flux distribution (left figure in Fig. 4.15(a)) is of importance when matching minimum and maximum external wall temperatures is the goal. Compressed air (7 bar absolute) was pre-heated before entering the receiver, such that the inlet side of the receiver could be hot enough to allow matching of the operating temperature range for the molten salt receiver, and consequently, to match the distribution of the external wall temperature. In this way, the external heat loss could be obtained from a surface of "known" temperature distribution. Therefore, for the air tests, the number of heliostats, the flow rate and the inlet temperature of the air were adjusted to best match the temperature profiles of the large-scale molten salt receiver listed at the bottom row in Table 4.4. These case studies showed that the smaller the number of heliostats (a factor of 0.8, compared to the original estimate of 22), the better the maximum external wall temperature could be matched to the reference molten salt flat case. In addition, it was found that matching a couple more heliostats (e.g. 2 heliostats) on the edges to increase the inlet wall temperatures helped the overall temperature matching, even though this would increased the spillage loss a little. The finalised number of heliostats for the air tests was 20 (Case 7). This process of finding the best parameters was labour-intensive, and although it is acknowledged that the final max. external wall temperature was a little higher than desired, this was the best solution that could be obtained.

Table 4.4: Flat air receiver case study ($p_{in} = 7$ bar). For iterations # 2 to # 6, a factor of 0.8 was applied on the number of heliostats used to reduce the total energy on the receiver and consequently to better match the external wall temperature profiles, no ray tracing was done to reduce the computational cost.

Case #	No. of helios	$\dot{Q}_{abs}$ kW	$\dot{m}$ kg/s	T_{in} °C	T_{out} °C	p_{out} bar	$T_{ext,wall,min}$ °C	$T_{ext,wall,max}$ °C	η_{th} %
1	22	67.86	0.12	290	543.65	6.34	255.19	690.46	40.98
2	–	67.86×0.8	0.12	290	488.13	6.37	251.49	615.18	39.80
3	–	67.86×0.8	0.12	350	506.82	6.33	294.13	627.99	31.74
4	–	67.86×0.8	0.09	350	528.89	6.62	282.37	606.97	27.19
5	–	67.86×0.8	0.087	350	531.34	6.64	280.88	664.63	26.64
6	–	67.86×0.8	0.088	350	530.34	6.63	281.38	663.40	26.83
7	20	59.98	0.08	320	590.94	6.68	290.21	683.57	39.34
Ref. salt	–––	–	290	565	–	289.54	660.96	–	

The flux distribution and the external wall temperature profiles of the PS10 flat molten salt case were shrunk down and distored to match the 1.2 m × 1.2 m prototype scale, and through this modelling have been replicated on the small-scale CSIRO field, as shown in Fig. 4.15(b). with small interpolation error on the maximum external wall temperature, drops from 665.70°C to 660.96°C due to the different mesh sizes handled in the two cases. Spatial representations of the pressure drop and the localised temperature difference between small-scale air case and full-scale salt case have been plotted in Fig. 4.16. Larger pressure drops occur in the centre of the receiver due to the localised temperature increase of the HTF. The total thermal loss calculated for the small-scale flat air receiver is 36.38 kW (3.98%), consisting of 10.53 kW (1.15%) of external convective loss and 25.85 kW (2.83%) of external radiative loss.

Similar strategies were developed to obtain the finalised bladed air case, as shown in Table 4.5. The small number of heliostats were selected to minimise optical losses, so that the performance of the receiver was focused on thermal efficiency. As a result, both minimum and maximum external wall temperatures were matched well to the large-scale molten salt case, as the differences in both minimum and maximum wall temperatures were less than 1°C. The finalised flux profiles, the fluid temperatures, and the external wall temperatures are shown in Fig. 4.17. The blade temperatures reflect the mechanism of the flow path (i.e four coiled single-pass loops). The middle of the back wall has the highest fluid and external wall temperatures due to the design of the flow path. The total thermal loss calculated for the small-scale bladed air receiver is 34.81 kW (3.73%), consisting of 11.37 kW (1.22%) of external convective loss and 23.44 kW (2.51%) of external radiative loss.

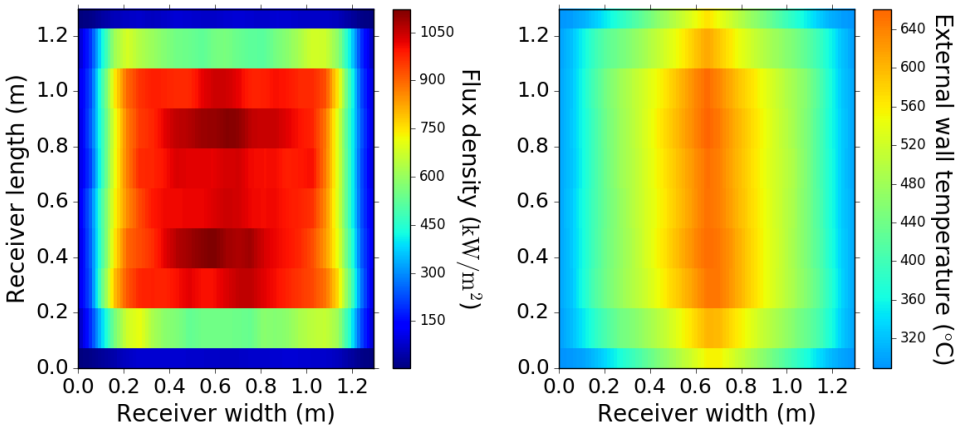

(a) Flux and temperature distributions of the PS10 full-scale case, shrunk and distorted to match the 1.2 m × 1.2 m prototype scale.

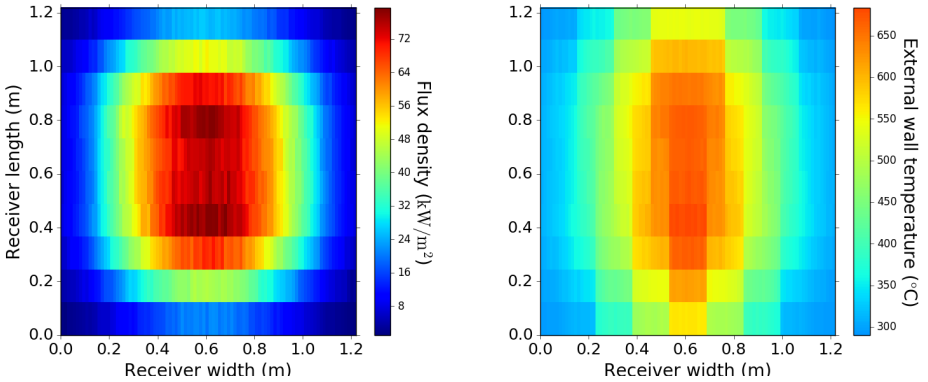

(b) Finalised flux distribution and external wall temperature profile on CSIRO small-scale flat air receiver, based on modelling using expected air inlet and flux conditions from 20 heliostats in the field.

Fig. 4.15: Flux and external wall temperature distribution comparisons between molten salt and air cases.

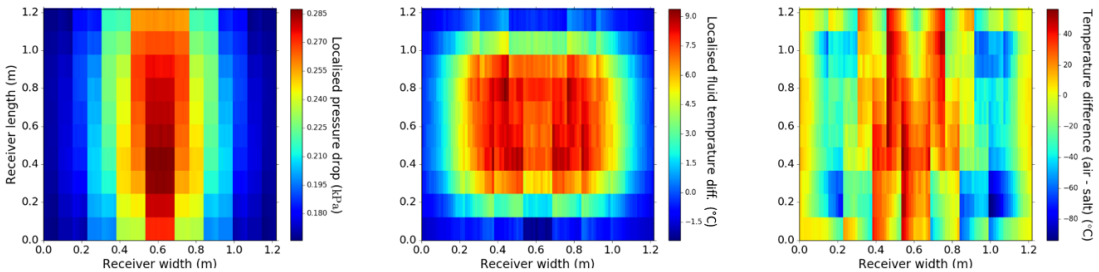

Fig. 4.16: Left: localised pressure drop; middle: localised HTF temperature difference; right: localised external wall temperature difference between the air and salt case.

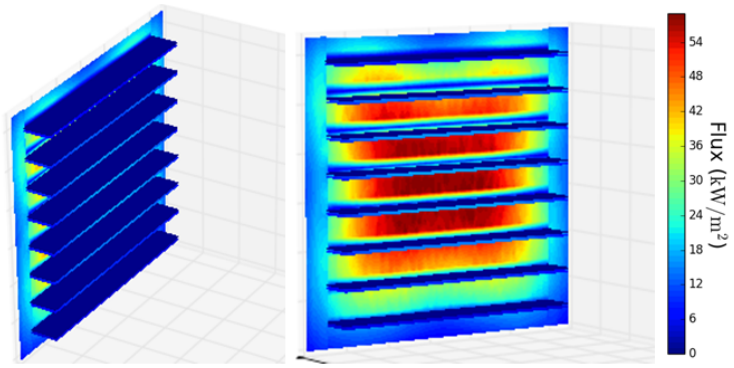

(a) Flux distribuion

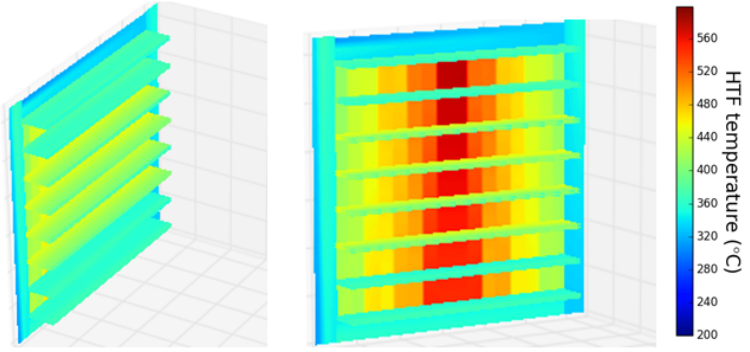

(b) Working fluid operating temperature

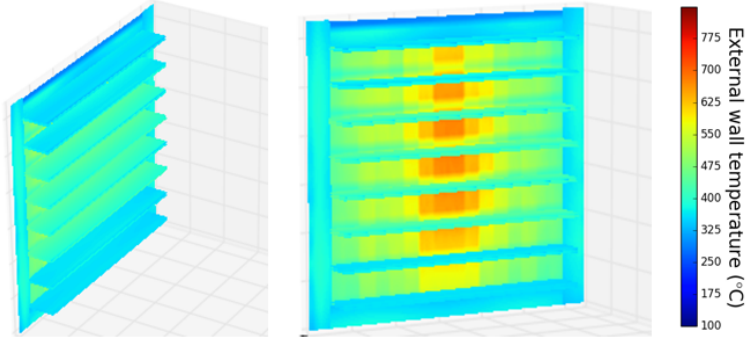

(c) External wall temperature distribution

Fig. 4.17: Finalised (a) flux distribution, (b) working fluid temperature and (c) the corresponding external wall temperature distribution for CSIRO small-scale bladed air receiver.

Table 4.5: Bladed air receiver case study ($p_{in} = 7$ bar)

Case #	No. of helios	$\dot{Q}_{abs}$ kW	$\dot{m}$ kg/s	T_{in} °C	T_{out} °C	p_{out} bar	$T_{ext,wall,min}$ °C	$T_{ext,wall,max}$ °C	η_{th} %
1	22	67.86	0.06	200	604.49	2.59	172.89	791.68	32.26
2	–	67.86×0.8	0.06	250	611.27	2.37	207.86	797.17	28.93
3	–	67.86×0.8	0.06	300	613.17	2.11	238.65	797.84	25.39
4	–	67.86×0.8	0.06	300	551.88	2.55	235.21	717.32	25.13
5	–	67.86×0.8	0.05	300	564.81	3.84	227.71	737.16	21.87
6	–	67.86×0.8	0.057	300	559.91	3.41	230.94	729.33	23.20
7	20	59.98	0.08	320	578.55	3.24	290.42	681.54	38.60
Ref. salt	–	–	–	290	565	–	289.21	682.31	–

4.5.1.2 CSIRO water receiver design cases

The aim of this low-temperature water test is to examine the optical performance of the receiver, and to neglect the thermal losses by running the receiver at low temperatures. From optical efficiency point of view, the bladed receiver would perform better than flat receiver due to the light-trapping effect. A study of Wang [101] found that a larger number of heliostats would be more beneficial to the bladed receiver, when the number of heliostats was greater than ∼50, as shown in Fig. 4.18. However, it would cause more thermal loss due to larger surface area, and consequently more convection loss. Therefore, a higher incident flux would result in an increased advantage for the optically superior bladed design, which means that testing with a high flux would show the greatest benefit. However, the following design constraints in this CSIRO water test limited the number of heliostats could be used:

- The peak flux was constrained at 1.2 MW/m^s.
- For the water test, the max. fluid temperature was set below 100°C (the boiling point at 1 atm).
- The pump power was limited (7 bar absolute) by the available installed equipment at CSIRO, which consequently limited the total heliostats we have used in this test.

20 heliostats (as used in the air test) were not sufficient for this test due to the pump limit and the numerical accuracy of the tests. A large δT (outlet T – inlet T) was aimed to maximise the accuracy of the absorbed flux measurement. But on the other hand, the external surface temperature was minimised to avoid thermal losses, and therefore, maximum pumping rate was required. The limitation on the pump capacity restrained the water flow rate and consequently, limited the number of heliostats being used, as adding more heliostats would require higher mass flow rate to achieve the same (fixed) upper limit of the water outlet temperature. More flow means more pressure drop through the receiver, and more pumping power required. Initially, 200 heliostats were selected to match the flux distribution of the

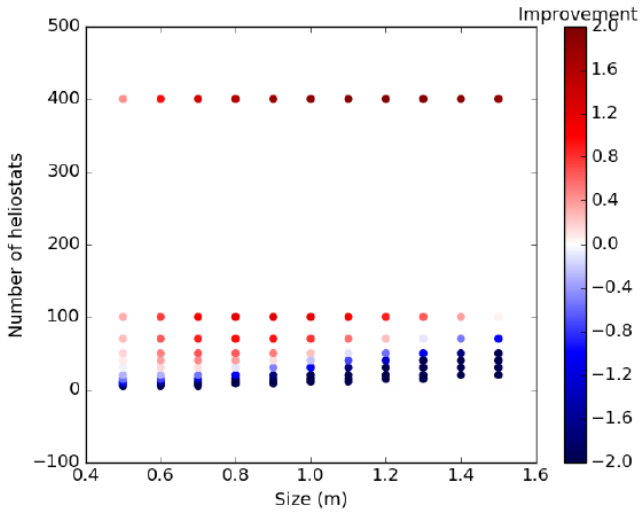

Fig. 4.18: The improvement in the total efficiency from the bladed receiver with different receiver sizes and number of heliostats, when compared to the flat receiver. This figure was extracted from the PhD thesis of Wang [101]. In this study, the external wall temperature distribution on the receiver was assumed to be unchanged. The bladed receiver would perform better than flat receiver optically due to the light-trapping effect. However, it would cause more thermal loss due to larger surface area, and consequently more convection loss. Therefore, a higher incident flux would result in an increased advantage for the optically superior bladed design, which means that testing with a high flux would show the greatest benefit. Study showed that the advantage of using bladed receiver (pink/red dots) could be seen when the number of heliostats was larger than 50.

reference PS10 flat case, followed by varying the mass flow rate and the internal flow configurations (i.e. n_{banks} and $n_{\text{tubes,perbank}}$) to keep the water temperature as low as possible. For example, for Case #1 and #2 in Table 4.6, the outlet temperature of the receiver was reduced by 27°C, by reducing the number of banks (n_{banks}) connected in series (i.e. more parallel tubes in one bank, less banks in series). The shorter the flow path, the smaller the pressure drop as well. Once the modelling mechanism was determined, the final step was to gradually increase the number of heliostats to virtually represent the reference case using the CSIRO facility, while keeping the water temperature low. The top four cases are listed in Table 4.6 below. From flat receiver point of view, a larger number of heliostats would cause more spillage and reflective loss, when comparing Case #3 and Case #4 in Table 4.6. The peak flux constraint (1.2 MW/m^2) caused that more heliostats had to aim to the edges to avoid excessive flux limitation at the central of the receiver, which resulted in more spillage. Reflective loss is proportional to the total incident energy, and hence, the more the energy, the more the reflective loss. Therefore, the finalised number of heliostats for the water tests was 255, without causing excessive pressure drop. The water case was expected to flow fast enough to keep low the external wall temperatures, as shown in Fig. 4.19, to neglect the external convective and radiative losses on the receiver, as the thermal efficiency of this proposed flat water receiver was 99.6%.

For the bladed water test, as the bladed part caused too much pressure drop,

Table 4.6: Flat water receiver case studies. The results showed that thermal losses are negligible due to the features of high-flux and low-temperature.

	Case #			
	1	2	3	4
No. of helios	200	200	200	255
$\dot{m}$ (kg/s)	1.80	2.50	4.00	4.00
n_{banks}	16	8	8	8
$n_{\text{tubes,perbank}}$	6	12	12	12
T_{in} (°C)	20.00	20.00	20.00	20.00
T_{out} (°C)	115.40	88.40	62.90	70.60
p_{in} (bar)	6.00	6.00	6.00	3.48
p_{out} (bar)	1.98	4.98	3.51	1.00
$\dot{Q}_{\text{sun}}$ (kW)	828.70	828.70	828.70	980.10
$\dot{Q}_{\text{spil}}$ (kW)	13.10	13.10	13.10	29.90
$\dot{Q}_{\text{refl}}$ (kW)	32.62	32.62	32.62	37.10
$\dot{Q}_{\text{ext,rad}}$ (kW)	1.21	1.23	0.81	0.99
$\dot{Q}_{\text{ext,conv}}$ (kW)	2.52	2.55	1.92	2.28
η_{opt} (%)	94.48	94.48	94.48	93.17
η_{th} (%)	99.52	99.52	99.65	99.64

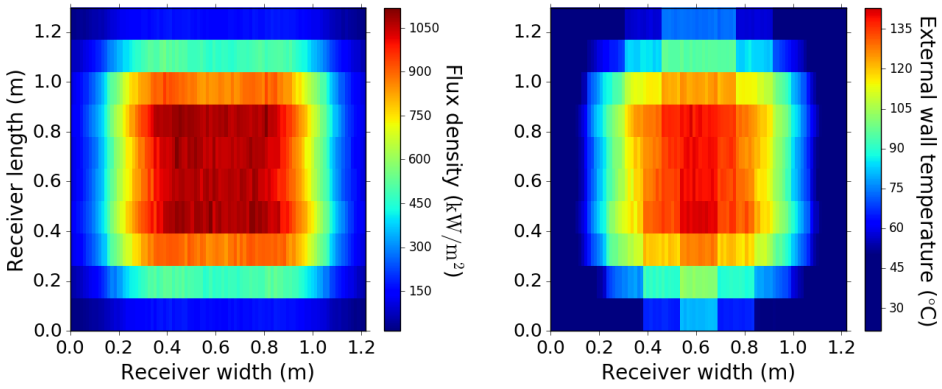

Fig. 4.19: The flux profile (left) and the external wall temperature profile (right) for CSIRO flat water case.

the water receiver was split into two flow streams (i.e. "blades" and "edges + back wall"). This parallel flow reduced pressure drop, and allowed operation within the pump capacity limit as per the CSIRO facility requirement. The flux profiles and the external wall temperature profiles are shown in Fig. 4.20.

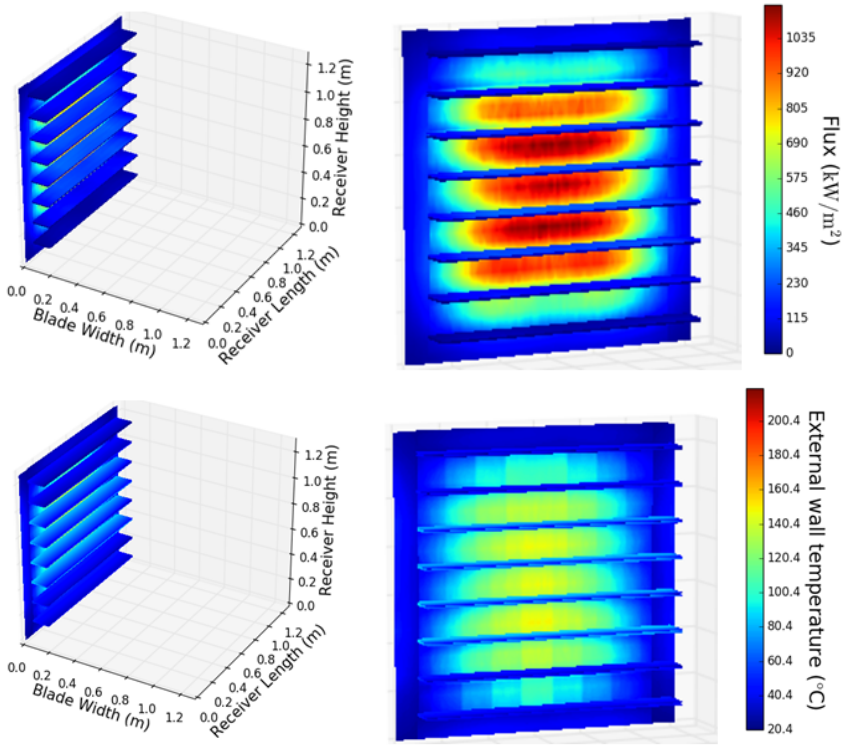

Fig. 4.20: Finalised flux profiles (Top) and the external wall temperature profiles (bottom) for CSIRO bladed water case.

4.5.1.3 Conclusion

The 'virtual experiment' testing strategy is summarised in Fig. 4.21[4]. As shown at the bottom of the figure, the optical losses from the water experiment are added to the thermal losses from the air experiment, and divided by the total incident energy from the water case. The efficiencies calculated using this method approximately examine the performance of the scaled-down molten salt receivers. Under these conditions, it is predicted that a bladed receiver achieves an efficiency of 91.77%, which is 2.32% higher than the optimised flat receiver design with an efficiency of 89.46%.

[4]This figure is seeking to explain the method of the virtual experiment itself, and not the issues of error propagation. Therefore, the number of significant digits in this figure does not indicate the "true values" of the experiments. The uncertainty in the experiments, as a topic, it is discussed extensively in Section 4.5.2.

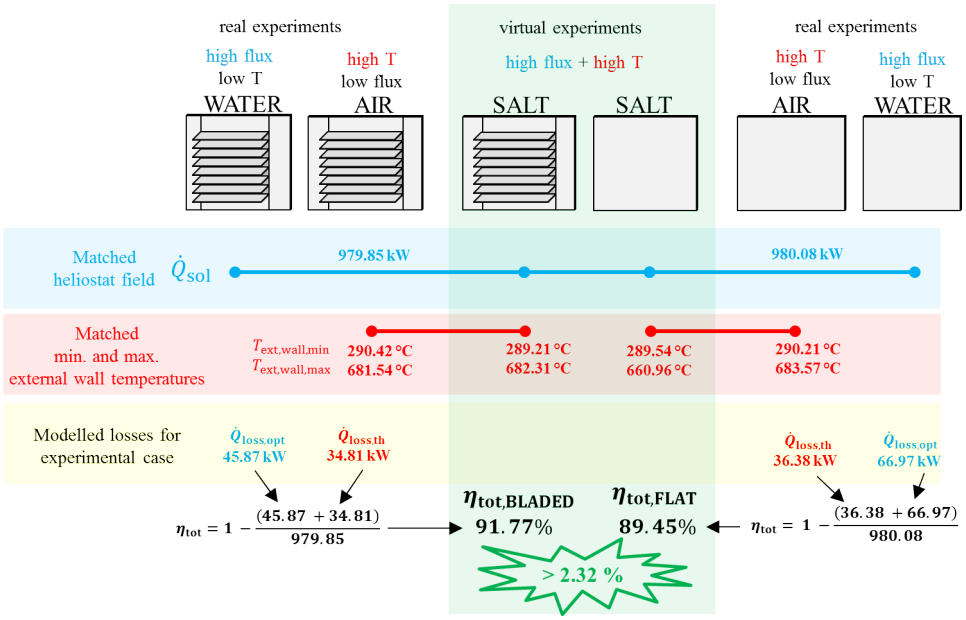

Fig. 4.21: Overall strategy for water and air testing to predict performance of the 'virtual' molten salt receivers.

This 'virtual experiment' testing of the scaled-down version of the large-scale PS10 systems was designed to provide evidence in support of those findings in Section 4.4. An efficiency gain of 2.32% was expected to be achieved in the on-sun testing, corresponding to an approximately 22% reduction in receiver losses.

4.5.2 Experimental results and discussions

4.5.2.1 Experimental setup and results

The manufactured receivers for the on-sun testing are shown in Fig. 4.22. Before the real tests, a sequence of trial tests was completed to ensure that the components were operating as expected, such as no leaking in tubes, bends or joints and no breakdown of the electrical components on the skid-frame assembly. Meanwhile, this sequence of preliminary tests could also help validate if the assumptions made regarding heat transfer and pressure drop processes were similar to those expected during on the on-sun testing. Then, the proposed on-sun testing was conducted at CSIRO, including four main tests, as planned:

1. Flat + air
2. Flat + water
3. Bladed + air
4. Bladed + water

(a) Flat receiver (b) Bladed receiver

Fig. 4.22: Full pictures of (a) flat and (b) bladed receivers with Pyromark coating.

Each test was conducted over a limited period of selected days in April–May 2019, where sun input was adequate and wind speed mild to maximise the stability of the testing. The collected quasi-steady data, as in the average values for a 30 s interval, have been plotted in Fig. 4.23.

And then these data have been post-processed and summarised, in Table 4.7, in the format of a final set of time-intervals, the DNI, the working fluid inlet temperature T_{in}, and outlet temperature T_{out}, the mass flow rate $\dot{m}$, the total incident energy $\dot{Q}_{\text{inc}}$, the net heat to the working fluid ($\dot{Q}_{\text{i}} = \dot{m}c_p(T_{\text{out}} - T_{\text{in}})$) and the resulting energy loss ($\dot{Q}_{\text{loss}} = \dot{Q}_{\text{inc}} - \dot{Q}_{\text{i}}$). For air, ideal gas assumptions and constant specific heat capacity of 1.07 kJ/(kg·K) were used in the calculation. For water, a constant specific heat capacity of 4.178 kJ/(kg·K) was used. The time-intervals selected correspond to periods of approximate steady-state conditions. The rest of the parameters were calculated as the average value over that time-interval.

Note that there was an unexpected in-line thermocouple failure during the bladed air receiver test. For the flat air receiver, FA4' and FA5' the results were measured using the external thermocouple directly, while FA4" and FA5" were calculated using the correlation determined from the regression process, as discussed in Sec. 4.5.2.3.

4.5.2.2 Uncertainty analysis

A Python uncertainties package [170] was implemented to analyse the uncertainty in the measurements, where the uncertainty determined how large the margin would be, between the experimental measurements and the "true values". Random errors cause different/random measurements in the experiments, which are unpredictable. The more repeated experiments conducted, the better estimate on the random error can get. Systematic errors give the same amount of the "error", if the experiments are conducted in same way of measurements. Therefore, repeated measurements are

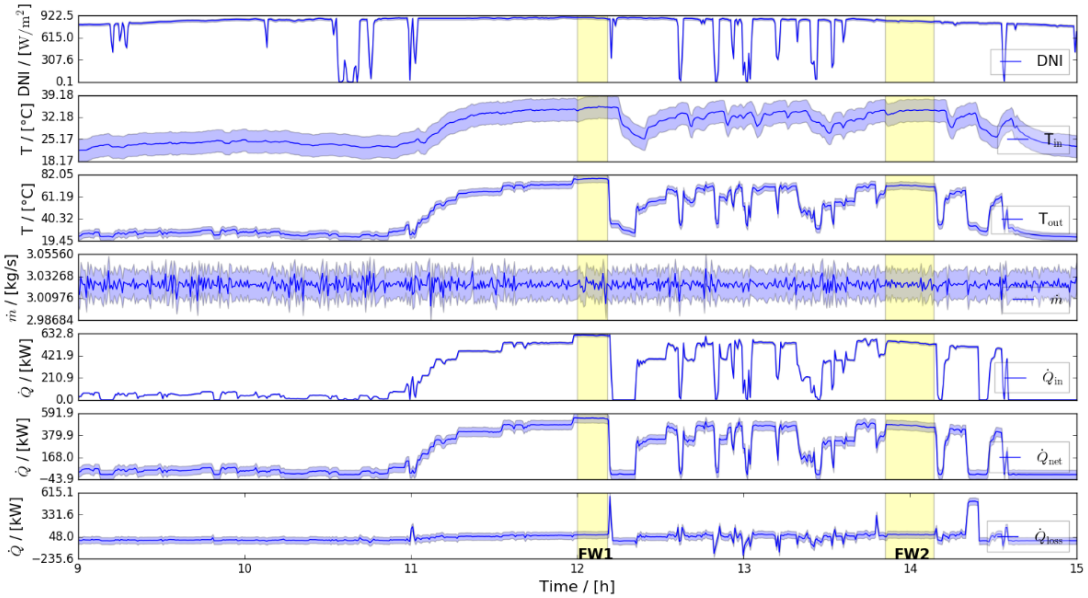

(a) Flat water test on 17 April 2019

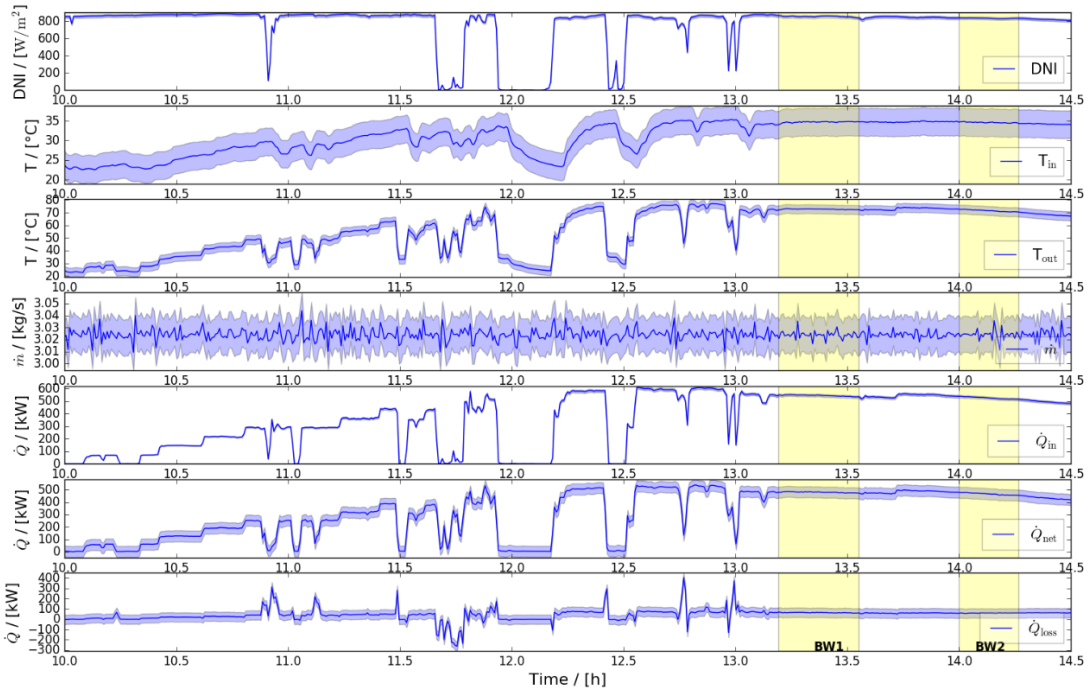

(b) Bladed water test on 18 April 2019

Fig. 4.23: Quasi-steady operational performance for (a) the flat water test on 17 April 2019, (b) the bladed water test on 18 April 2019, (c) the flat air test on 30 May 2019 and (d) the bladed air test on 30 May 2019

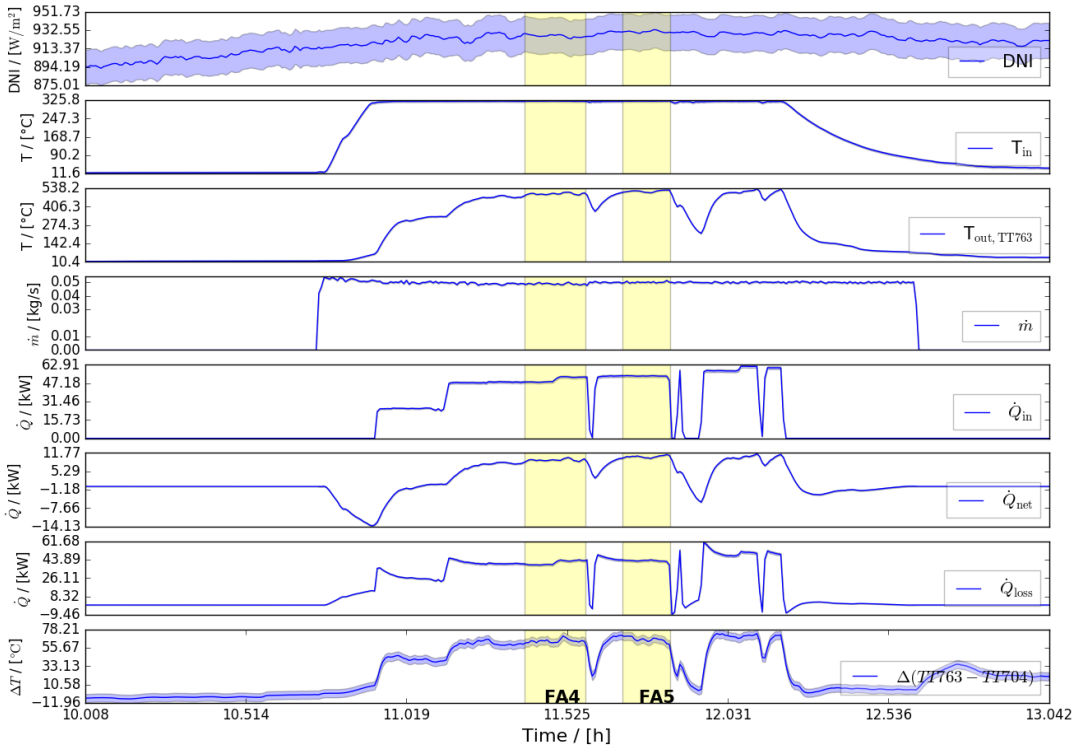

(c) Flat air test on 30 May 2019

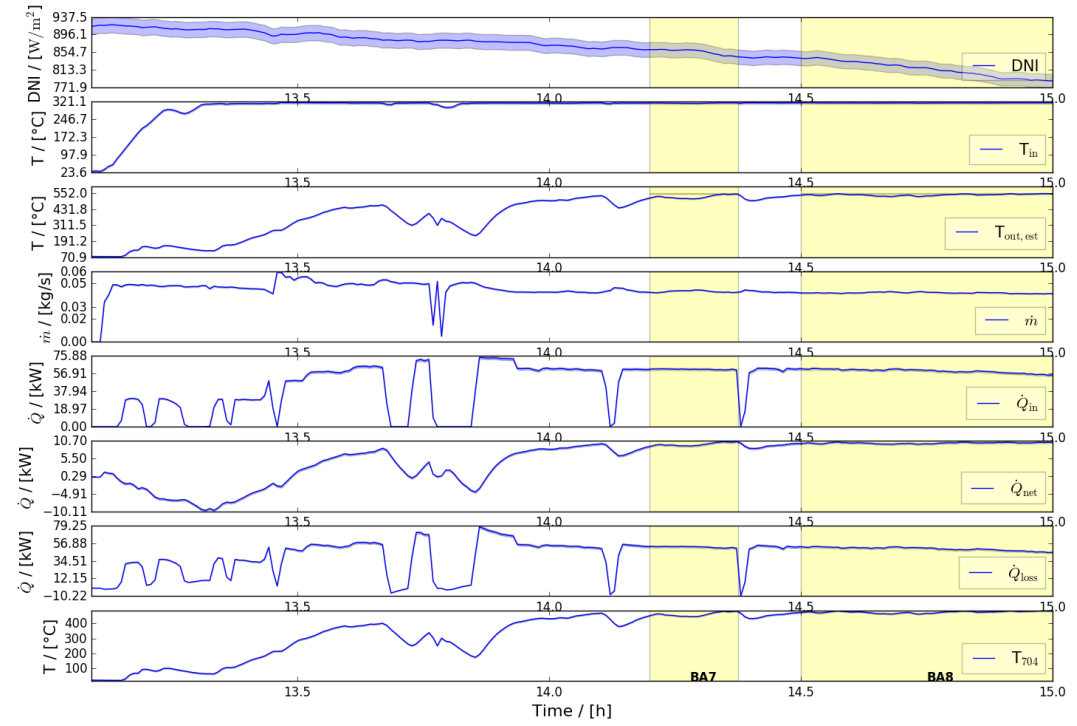

(d) Bladed air test on 30 May 2019

Fig. 4.23: Quasi-steady operational performance for (a) the flat water test on 17 April 2019, (b) the bladed water test on 18 April 2019, (c) the flat air test on 30 May 2019 and (d) the bladed air test on 30 May 2019

Table 4.7: Dates, times and key results from the on-sun testings of the flat and bladed receivers. Results used for final evaluations are highlighted in bold (i.e. FW2, BW1, FA5" and BA7).

Date	Interval	Clock time	DNI W/m^2	T_{in} °C	T_{out} °C	$\dot{m}$ Kg/s	$\dot{Q}_{inc}$ kW	$\dot{Q}_{net}$ kW	$\dot{Q}_{loss}$ kW
Flat water 17/04/19	FW1	12:00:00-12:11:00	890±18	35.1±3.5	78.1±3.5	3.024±0.015	618±12	543±45	75±46
	FW2	**13:51:00-14:08:30**	**845±17**	**34.1±3.5**	**71.4±3.5**	**3.024±0.015**	**548±11**	**471±45**	**76±46**
Bladed water 18/04/19	**BW1**	**13:11:30-13:33:00**	**854±17**	**34.7±3.5**	**72.7±3.5**	**3.024±0.015**	**543±11**	**481±45**	**63±46**
	BW2	14:00:00-14:16:00	835±17	34.6±3.5	71.3±3.5	3.024±0.015	523±10	464±45	58±46
Flat air 30/05/19	FA4'	11:23:30-11:35:00	927±19	321.2±3.5	499.5±3.5	0.0488±0.0005	50.3±1.0	9.3±0.2	41.0±1.0
	FA4''	11:23:30-11:35:00	927±19	321.2±3.5	500.1±3.6	0.0488±0.0005	50.3±1.0	9.4±0.3	41.0±1.0
	FA5'	11:42:00-11:51:00	931±19	321.5±3.5	517.5±3.5	0.0501±0.0005	53.1±1.1	10.5±0.2	42.6±1.1
	FA5''	**11:42:00-11:51:00**	**931±19**	**321.5±3.5**	**516.7±3.6**	**0.0501±0.0005**	**53.1±1.1**	**10.5±0.3**	**42.6±1.1**
Bladed air 30/05/19	**BA7**	**14:12:00-14:22:30**	**856±17**	**315.0±3.5**	**524.9±3.6**	**0.0430±0.0004**	**61.6±1.2**	**9.7±0.3**	**51.9±1.3**
	BA8	14:30:00-15:00:00	815±16	315.6±3.5	539.3±3.6	0.0419±0.0004	59.7±1.2	10.0±0.2	49.7±1.2

not able to tell the systematic effects. Different measurements are required to estimate the systematic errors. Uncertainty consists of random and systematic errors. Correlations between variables are automatically handled in the Python uncertainties package. This feature is of importance when, for example, two thermocouples are sharing one single cold junction compensation. Experimental results are summarised by Pye et al. [171]. Type K thermocouples with their accuracy (i.e. a systematic error) and the errors in the cold junction compensation were considered [172]. The thermocouple measurements were taken every one second over the time intervals of interest, and hence the random errors in thermocouple measurements were negligible. The accuracy of the mass flow meter for air (Manufacturer: Oval, coriolis type, Part Number: Sensor SN0250-SS-323R; Transmitter CT9401-R7MV31) was $\pm$ 1% [173] and for water (Manufacturer: Omega, turbine type, Part Number: FTB-1425) was $\pm$ 0.5% [174]. The accuracy of the DNI capture device was assumed to be $\pm$ 2% [175]. To summaries, Table 4.8 provides all instruments' uncertainties. A full uncertainty analysis for the flat air test on 30 May 2019, as an example, is attached in Appendix D. This analysis showed that water cases have large uncertainty due to the low temperatures in inlet and outlet.

Table 4.8: A summary of the detailed instruments' uncertainties.

	Air Test		Water Test	
	Instrument	Accuracy	Instrument	Accuracy
Thermocouple	Type K Class 2	$\pm$2.5°C ($\leq$ 333°C) $\pm$0.75°C (333°C–1200°C)	Type K Class 2	$\pm$2.5°C ($\leq$ 333°C) $\pm$0.75°C (333°C–1200°C)
Data acquisition	Schneider Electri TSXAEY1614 and ABE-7CPA12	No significant error	Schneider Electri TSXAEY1614 and ABE-7CPA12	No significant error
Mass flow meter	Manufacturer: Oval	$\pm$1%	Manufacturer: Omega	$\pm$0.5%
DNI	DNI capture device	$\pm$2%	DNI capture device	$\pm$2%

4.5.2.3 The regression process for the failure of a thermocouple

There was an unexpected in-line thermocouple failure during the bladed air receiver test. Unfortunately, it was an important in-line thermocouple, as it was supposed to measure the outlet temperature of the bladed receiver. Without it, it is very difficult to accurately calculate the net heat to the working fluid. Due to limited time and budgets and the complexity in replacing the broken thermocouple which was mounted within the receiver inner insulation, an alternative way to indirectly determine the outlet temperature of the bladed air receiver was conducted using an uninsulated thermocouple placed 1.5 m downstream from the broken in-line thermocouple. A regression process has been conducted using data from both the faulty thermocouple and the one downstream (see Fig. 4.24), as fortunately, both these

two thermocouples were operating normally during the early flat air tests on the same day. The predicted temperature difference between these two thermocouples was about 2°C, when compare Case FA4′ to Case FA4", Case FA5′ to Case FA5", as shown in Fig. 4.24(a). Case FA4′ and FA5′ were the original results using the in-line thermocouple, while Case FA4″ and FA5″ were the predicted results using the preferred results. This was a very unfortunate situation and clearly, more experiments after fixing the thermocouple would be preferable. It seems that there was no better choice but using these unsatisfactory data to fix the missing data. Therefore, the outlet temperatures for both flat and bladed air receiver tests on 30 May 2019 were calculated using the preferred curve-fit correlation in Fig. 4.24 b: $\left(T_{\text{original}} - T_{\text{alternate}}\right) = 51.62 + 0.03016 \times T_{\text{alternate}}$. In this way, reasonable predictions on the flat and the bladed air receivers could be made.

4.5.2.4 Discussions

The final evaluation for the flat and bladed receiver was determined using the experimental data. Optical losses were obtained from the heat loss from the high-flux water experiments, with negligible thermal losses. The heat loss from the high-temperature air experiments were then used to determine the thermal losses. Therefore, the nominal value of the total efficiency expression for each type of the receiver (flat or bladed) was calculated as the following:

$$\eta_{\text{tot}} = 1 - \left(\frac{\dot{Q}_{\text{loss,opt}} + \dot{Q}_{\text{loss,th}}}{\dot{Q}_{\text{inc}}} \right) \approx 1 - \left(\frac{\dot{Q}_{\text{loss,water}} + \dot{Q}_{\text{loss,air}}}{\dot{Q}_{\text{inc,water}}} \right) \tag{4.6}$$

Together with the derivative calculated using the same uncertainty method mentioned above, the total efficiency of the bladed receiver was $80 \pm 8\%$, while that of the flat receiver was $79 \pm 8\%$. The efficiency gain ($\eta_{\text{tot,bladed}} - \eta_{\text{tot,flat}}$) from this on-sun testing was $0.65 \pm 0.08\%$.

The uncertainty calculated (i.e. $\pm 0.08\%$) in the efficiency gain showed that, somehow, a consistent gain was expected to be achieved, with the consideration of the numerical correlation between input variables. However, it was likely to be a biased conclusion, since the uncertainty calculated here is only based on one set of flat and bladed receiver results. The random errors in the measurements were eliminated due to repeated measurements in every 30 seconds, which is reasonable. The way of calculating uncertainty with correlation being handled, turned out that the systematic errors were cancelled out due to the same thermocouples and same flow meters used, when examining the difference between variables, which is also reasonable. However, it assumed that all of the errors in the thermocouples is systematic error. In addition, no uncertainty in the reflectivity, flux distribution and wind condition were measured. The uncertainties in the flux measurement were of importance in approaching to the final comparison between flat and bladed receivers, which was unfortunately unknown. Wind was very likely a source of uncertainty, since it af-

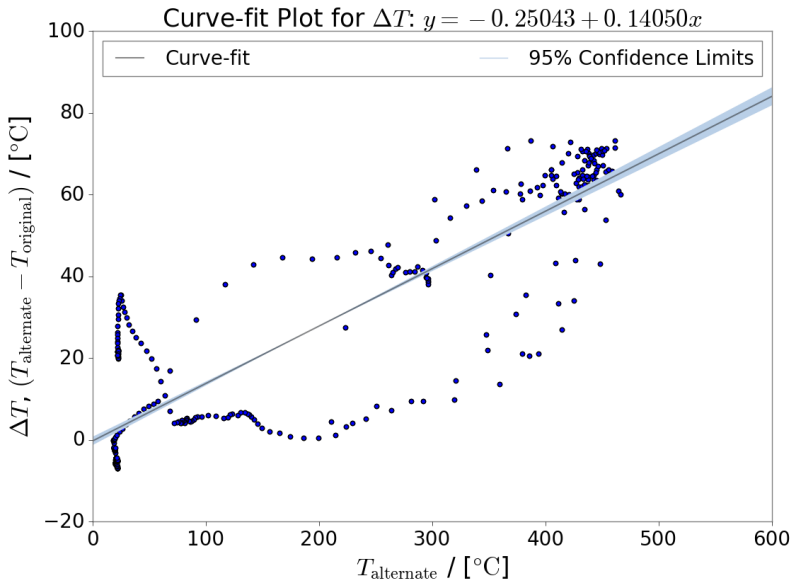

(a) The curve-fit plot for the whole day

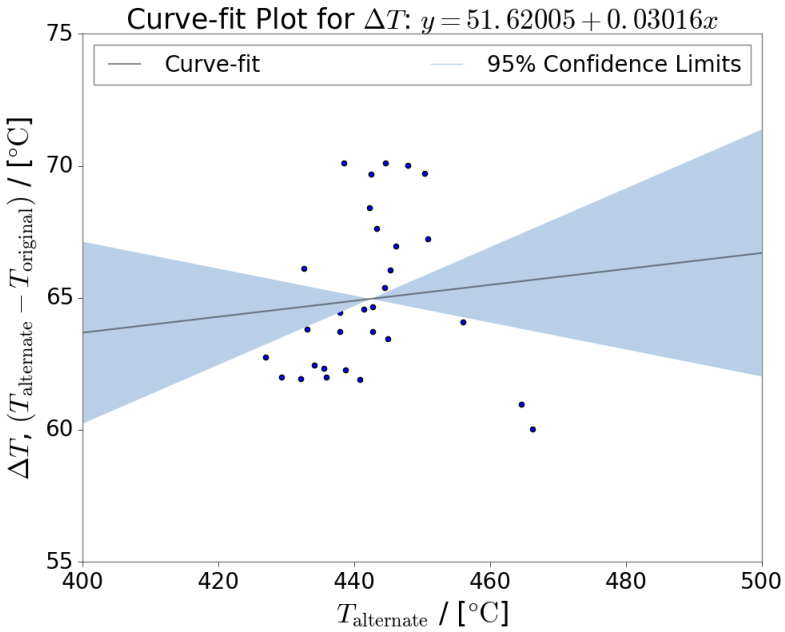

(b) The curve-fit plot only for two steady-state periods

Fig. 4.24: The correlations of temperature measurements between intended in-line thermocouple and alternative external thermocouple on 30 May 2019. Top: a curve-fit plot for the whole day; bottom: a curve-fit plot only for two steady-state periods on the same day. The impact of wind was not considered in this analysis, which might affect the accuracy of the predicted temperature measurements.

fected the total heat loss calculated on the certain receiver. Therefore, it was very challenging to quantify uncertainties due to unknown wind speed and wind direction. They could not be handled with the available data. The ambient conditions might not have been consistent throughout all the tests. In this study, the specific heat capacity of water and air were assumed to be constant at 4.18 kJ/(kg·K) and 1.07 kJ/(kg·K), respectively. The difference between $c_p(T)$ and $\overline{c_p}$ was not considered. The qualities of the water and the air were unknown (e.g. pure water or impure). All of these uncertainties and inconsistencies led to the question of "To what extent, could the uncertainty analysis in this study present the true performance of the receiver?".

4.6 Conclusions

The concept of the bladed receiver is examined, where the heliostat field and flux distribution are assumed to be PS10-like. It is found that the large-scale bladed molten salt receiver is capable of improving the efficiency by at least 2.49%, considering both optical and thermal losses, when compared to the optimised flat receiver. The light trapping enhancement between blades leads to the much reduced reflective and external radiation losses. Simultaneously, the mechanism of adding blades to overcome the flux limit on the conventional flat receiver is validated.

Next, the on-sun testing is conducted at CSIRO, Newcastle, Australia, to further test this concept in practice. A 'virtual experiment' is designed and evaluated, due to the lack of any ready access to testing infrastructure able to make use of high-temperature molten salts. It utilises water and air as alternative working fluids to indirectly but near-accurately test the performance of both large-scale flat and bladed molten salt receivers on the small-scale receivers. An efficiency gain of 2.32% is expected to be captured from the on-sun testing. This efficiency gain is very close to the large-scale results, which shows that the concept of the 'virtual experiment' is capable of replicating the performance of the large-scale receivers. The key conclusions of the large-scale PS10 receivers, virtual designs and experimental results are summarised in Table 4.9.

However, the experimental results show a modest improvement of 0.65% in receiver performance for the bladed receiver, when compared to the flat receiver. This improvement was slightly less that the result expected according to the model. The optimised design models are reconciled with experimental results next in Chapter 5. Nevertheless, this conclusion was made based on very limited experimental data. Unexpected weather conditions (e.g. windy or cloudy) could occur during the high-temperature testing on 30th of May 2019, as the DNI was relatively low. This might reduce the performance gain, since the advantage of the bladed receiver was more clear at higher DNI, when compared to the flat receiver. The assumptions about the slope error, reflectivity and wind conditions did not consider the systematic error

Table 4.9: Conclusions of the large-scale PS10 receivers, virtual designs and experimental results

	Large-scale PS10		Virtual designs		experimental results	
	Flat	Bladed	Flat	Bladed	Flat	Bladed
Footprint (m^2)	10×10	10×10	1.2×1.2	1.2×1.2	1.296×1.296	1.28×1.28
n_{blades}	–	8	–	8	–	8
T_{in} (°C)	290	290	320	320	321.5±3.5	315.6±3.5
T_{out} (°C)	565	565.83	590.94	578.55	516.7±3.6	524.9±3.6
$T_{ext,wall,max}$ (°C)	660.96	682.31	683.57	681.54	–	–
$T_{int,wall,min}$ (°C)	289.54	289.21	289.54	290.42	–	–
$\dot{Q}_{sun}$ (kW)	65.79×10^3	65.80×10^3	980.08	979.85	–	–
$\dot{Q}_{spil}$ (kW)	0.48×10^3	0.5×10^3	–	–	–	–
$\dot{Q}_{ref}$ (kW)	2.55×10^3	1.28×10^3	–	–	–	–
$\dot{Q}_{ext,rad}$ (kW)	1.74×10^3	1.32×10^3	25.85	23.44	–	–
$\dot{Q}_{ext,conv}$ (kW)	720	750	10.53	11.37	–	–
η_{opt} (%)	95.38	97.29	93.17	96.45	86	88
η_{th} (%)	96.09	96.76	96.02	95.15	90	89
η_{tot} (%)	91.66	94.15	89.45	91.77	79±8	80±8

analyses and might change the results. Under such circumstances, accuracy and precision of measurements subject to random errors could not be guaranteed, especially when there was one essential thermocouple (i.e. to measure the outlet temperature of the flat air receiver) not working during the testing. Repeated measurements under different testing conditions (e.g. various ambient conditions, various wind speeds) should be obtained to reduce random errors, however, such testing is very expensive.

Chapter 5

BRAAC Project: Experimental Reconciliation

5.1 Introduction

In Chapter 4, a bladed receiver design was described and modelled, with an expected 2.49% performance gain. Experimental results were also described, but they indicated an 0.65% percent gain, which was less than predicted. In this chapter, the differences are considered, and possible sources of experimental and modelling error are examined. Temperature and pressure were the sources of the uncertainties in both modelling and experiments, which could be responsible for these discrepancies. In addition, they are the most direct measurements encountered in engineering design situations, and hence these simulation results are targeting to be matched with the experimental results. The aim of this chapter is to develop a calibrated model, which can replicate the experimental outcomes by optimising the temperature and the pressure-related parameters in the model, so that (a) the accuracy of the model could be confirmed; (b) the experimental results could be aligned with the understanding of physics; (c) the flat receiver could be compared to the bladed receiver. The thermocouples designated across the flat and the bladed receivers are shown as the red dots in Fig. 5.1.

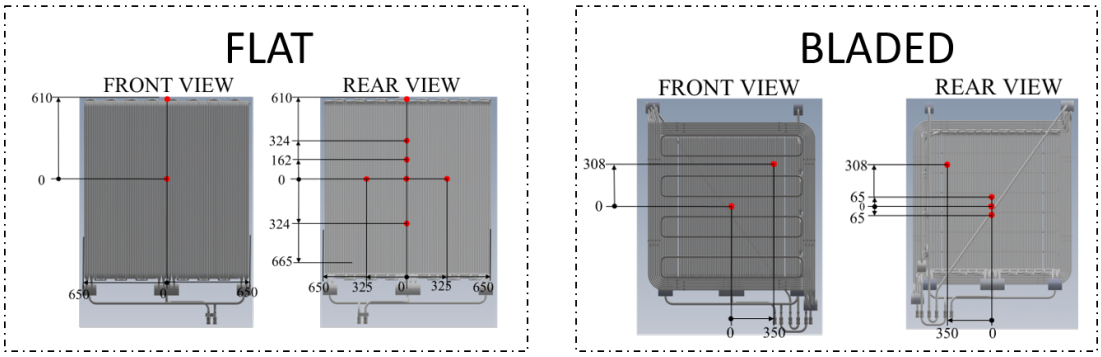

Fig. 5.1: Instructions on thermocouple location for flat and bladed receivers. Dimensions are in mm.

(a) The full picture of the bends from top of the receiver

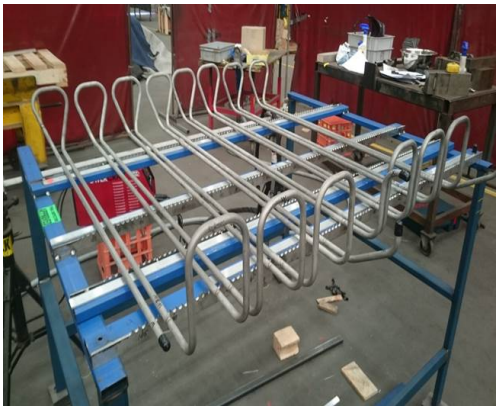

(b) Single tube path with bends

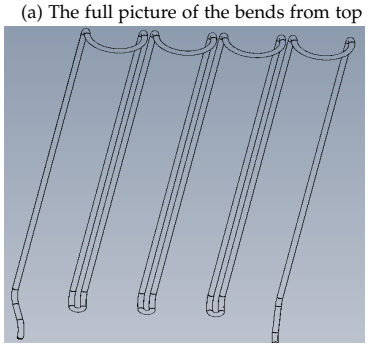

(c) Tube path #1

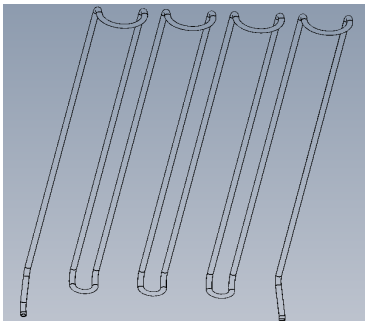

(d) Tube path #2

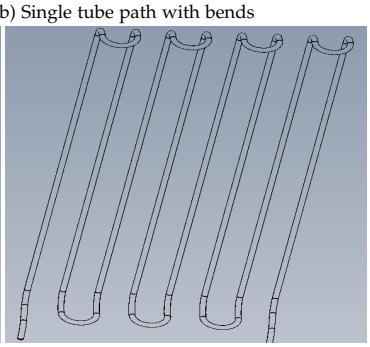

(e) Tube path #6

Fig. 5.2: Tube configuration of the flat receiver, including bends and manifolds, (a) full picture, (b)single tube path (c)–(e) individual tube bend configuration.

First of all, the simulation results were attempted to be matched with the experimental results for the steady-state flat water and the flat air cases. The real tube configuration of the flat receiver, including detailed demonstration of the bends and the manifolds, is illustrated in Fig. 5.2. The flat receiver consisted of 8 parallel tubes and each tube consisted of 16 90° bends, 7 return bends and 8 straight parts. In total, there were three headers connected at the ends of the tubes (i.e. two at the inlets and one at the outlet). A similar approach was conducted next for the bladed receivers.

5.2 Parameter estimation

The main uncertainties in the receiver model to matching with experimental results were external heat transfer coefficient h_{ext}, internal heat transfer coefficient $h_{\text{int}} = \frac{\text{Nu}k}{d_i}$, roughness of the tube e and nominal loss coefficient K (where $\Delta P = K\frac{1}{2}\rho\mathbf{V}^2$). The approach to calibrating the model with the experiments was to implement a Python constrained optimisation package "COBYLA" to minimise the difference between these two models caused by the four uncertainty parameters. Firstly, the optimisation method was applied to minimising the difference in temperatures at specific locations across the receiver, as indicated in Fig. 5.1, by varying the h_{ext} and the h_{int}, where h_{int} was represented by a multiplier $f_{\text{int,conv}}$ ($h_{\text{int}} = f_{\text{int,conv}}\frac{\text{Nu}k}{d_i}$). An iteration process was conducted next to minimise the difference in pressure drop by varying the K. Finally, the first step was repeated to obtain the optimised results. The objective function, using the flat receiver as an example, was defined as:

$$\min_{x_0,x_1,x_2,x_3}\left[f_{\text{FW1}}\left(x_0,x_1,x_3\right)+f_{\text{FW2}}\left(x_0,x_1,x_3\right)+f_{\text{FA4}}\left(x_0,x_2,x_3\right)+f_{\text{FA5}}\left(x_0,x_2,x_3\right)\right] \quad (5.1)$$

where FW1, FW2, FA4 and FA5 were the four flat cases summarised in Table 4.7, x_0 is the h_{ext}, in $\text{W}/(\text{m}^2{\cdot}\text{K})$, x_1 was the $f_{\text{int,conv,water}}$ for water cases, x_2 was for air cases ($f_{\text{int,conv,air}}$) and x_3 was the total nominal loss coefficients K in the manifolds and the bends.

Each term in Eq. 5.1 (e.g. $f_{\text{FW1}}\left(x_0,x_1,x_3\right)$) was determined using the least-squares method, which minimises the sum of the squares of the residuals (i.e. temperature difference between the experiment and the simulation at the same thermocouple location) made in the results of every single equation (i.e. each type of the receiver), as follows:

$$f=\sum_{i=1}^{i=n}\left(T_{i,\text{exp}}-T_{i,\text{min}}\right)^2 \quad (5.2)$$

where 1,2,...,n are the thermocouple locations, and there are a total of n thermocouples.

The optimisation processes were the same for both the flat and bladed receivers, except that only BW1 and BA7 (numbering was the same as labelled in Table 4.7) was calibrated and optimised due to the high computational costs, since these two cases were selected to conduct the final evaluation in Chapter 4.

5.3 Flat cases

Fig. 5.3 shows the locations of thermocouples, and the corresponding temperature measurements as averaged for each of the tests (FW1, FW2 FA4 and FA5). In each test, the top two sub-figures indicate the thermocouple measurements, while the bottom two are the corresponding simulation results. The model used in this study has been described in Chapter 2 and Chapter 4. The flow configuration has been modified to align with the manufactured model (refer back to Fig. 5.4). For example, the flow path was split into two inlets with serpentine flow configurations, where each inlet was coupled with a header. The fluids were merged into the outlet header. The flow pattern was "edge-to-centre". Effects such as the circumferential temperature variation were not considered in the current model.

5.3.1 Initial optimisation results

In this section, four flat cases (FW1, FW2 FA4 and FA5) were optimised in one single model, using Eq. 5.1, to reduce the overall discrepancy in all the cases to minimum. The flat cases were optimised using the method mentioned in Eq. 5.1. The optimised external wall temperatures have been shown in Fig. 5.5, where the optimised values were consistent with experimental observations. Note that the temperatures, 31°C for FA4 and 32°C for FA5 as indicated by $*$ on the figures, were not considered in the optimisation algorithm as the accuracy of these low measurements was in doubt. The original and the corrected parameters after optimisation were listed in Table 5.1. The optimised values of each parameter could only numerically describe the disparities between experimental results and simulations. Some results were questionable, such as 130.09 for K and 0.05 for $f_{\text{int,conv,water}}$. Therefore, questions arise as to the optimised values; what the physical significance behind these values were, as they were of significant practical interest to be discussed. The discussions were conducted in the following sections, consisting of three parts: incident flux distribution matching, external wall temperature matching and pressure matching. The first two parts were associated with external and internal heat transfer coefficients, while the third part was associated with a nominal loss coefficient.

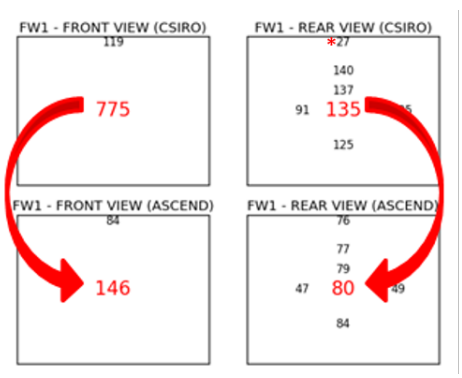

(a) FW1

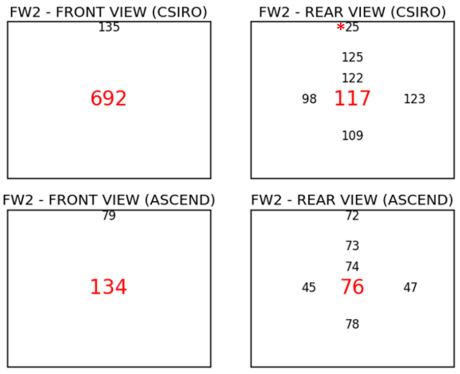

(b) FW2

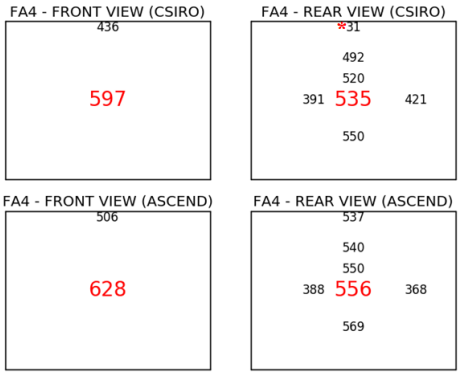

(c) FA4

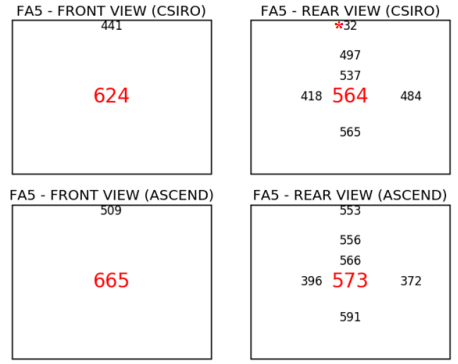

(d) FA5

Fig. 5.3: Experimental temperature results vs simulation temperature results for the receiver front and rear surface. For both flat water and air cases, $h_{\text{ext}} = 16$ W/(m^2·K), $K = 32.71$, $e = 0.046$ mm and $f_{\text{int,conv}} = 1$. Numbers in red are the temperature measurements in °C. The location of the numbers in the figure indicates the thermocouple locations on the receiver, aligning with Fig. 5.1. Red arrows are the examples, showing that those two temperatures should be compared. Red $*$ indicates certain measurement was not considered in the optimisation process.

Table 5.1: Design points for each optimised receiver.

	Original parameter		Corrected parameter	
	Water	Air	Water	Air
h_{ext} (x_0), W/(m^2·K)	16	16	21.12	21.12
$f_{\text{int,conv,water}}$ (x_1)	1	–	0.051	–
$f_{\text{int,conv,air}}$ (x_2)	–	1	–	1.49
K (x_3)	32.71	32.71	130.09	130.09

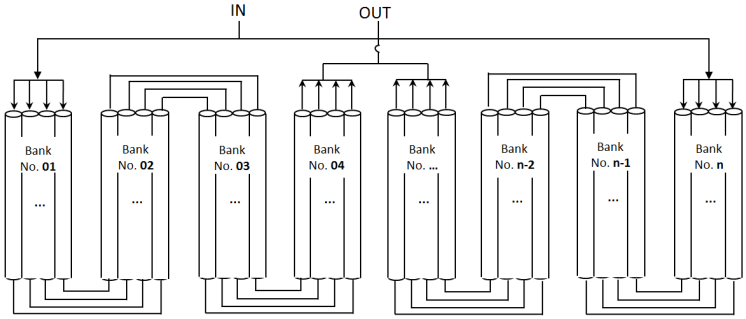

Fig. 5.4: Flow configuration of the flat receiver.

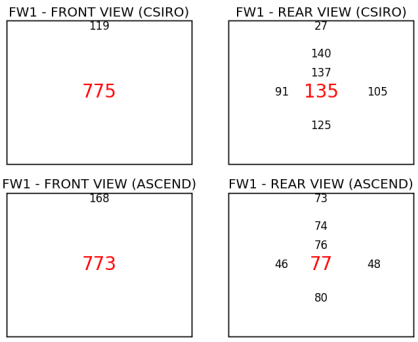

(a) FW1

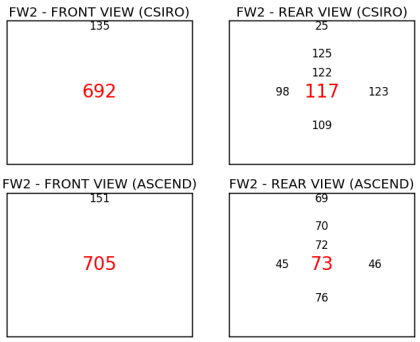

(b) FW2

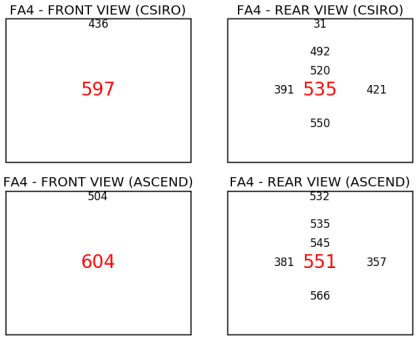

(c) FA4

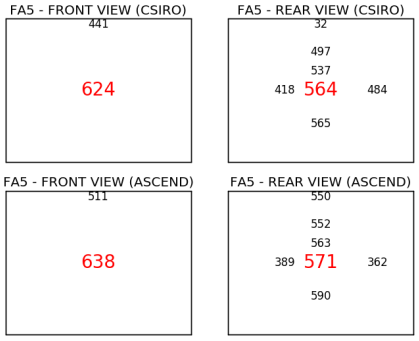

(d) FA5

Fig. 5.5: Results for the initial optimisation. For the flat water cases, $h_{\text{ext}} = 21.12$ W/(m^2·K), $K = 130.09$, $e = 0.046$ mm and $f_{\text{int,conv}} = 0.051$ For the flat air cases, $h_{\text{ext}} = 21.12$ W/(m^2·K), $K = 130.09$, $e = 0.046$ mm and $f_{\text{int,conv}} = 1.49$

5.3.2 Incident energy matching[1]

The total incident energy and the flux distribution generated from the experiment were obtained using the CSIRO live ray-tracing program, where the ray resolution was set quite low to allow for rapid evaluation. The optical performance, as recommended by CSIRO colleagues, was obtained by rebuilding the state of the heliostat field from the log files written by the control system and simulating it using Tracer (more details see Wang's PhD thesis [101]), a preferred ray tracing tool, as it is also capable of handling the case of the multi-reflection and light-trapping effects that arise in the later case of the bladed receiver. Shading and blocking effects were considered in Tracer. CSIRO also suggested that a Buie sunshape with circumsolar ratio (CSR) of 0.10 could be appropriate, slope error of 1.64 mrad and reflectivity of 0.90 could be applied to the heliostat surfaces. The centroids based on the surveyed receiver positions were[2]: 3 033 mm, 4.17 mm, 27 195 mm for the air case with a tilted angle of 15.51°, and 3 033 mm, 55.08 mm, 27 079 mm for the water case with a tilted angle of 38.62°. The effective absorptivity of the planar receiver was assumed to be 0.96, considering the light-trapping effects between adjacent tubes. The blocking ends of two adjacent blades that consisted of coils of tubes were modelled as planar surfaces with sharp turns to simulate the blocking effect, which was conducted by Wang [101] in her PhD thesis (see Fig 5.6). However, the energy absorbed on the blocking ends was not included in the total absorbed energy for the bladed receiver.

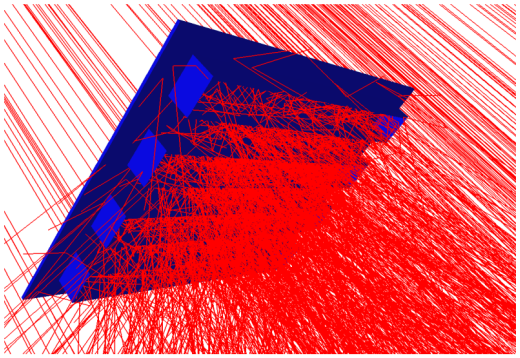

Fig. 5.6: An illustration on how the blocking effect was simulated in the coiled blades, by Wang [101].

For the simulation of each test case, the DNI was taken to be the average value within the testing period labelled in Table 4.7, in AEST, UTC +10. The sun position was calculated based on the starting time of each testing period, while solar noon was estimated at 11:50 am for all the cases. The comparison of the heliostat fields (the PS10 and the CSIRO) and the kay parameters of these two fields are extracted from Wang's PhD thesis [101] and shown in Fig. 5.7 and Table. 5.2.

[1]This optical matching was conducted by Wang, as she was involved in the BRAAC project to deal with optical analysis.

[2]A half-space is used for the thousands separator.

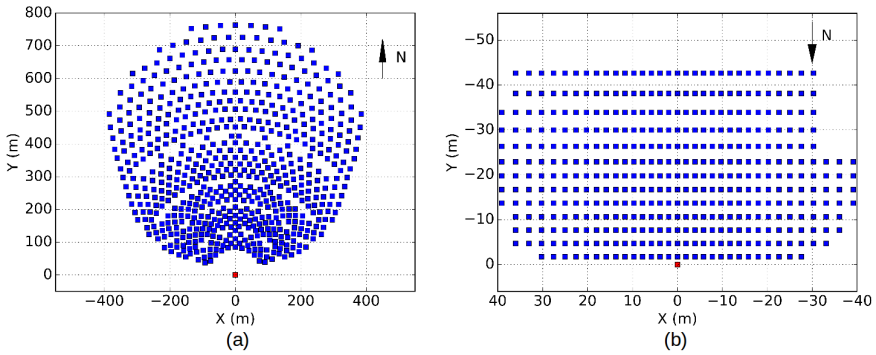

Fig. 5.7: The heliostat fields of (a) PS10 and (b) CSIRO. Extracted from Wang's PhD thesis [101]

Table 5.2: The key parameters of the PS10 and the CSRIO heliostat fields. Extracted from Wang's PhD thesis [101]

	PS10	CSIRO
Tower height (m)	115	30
Field land scale (m)	780	45
Tower to land ratio	0.147	0.667
Facing direction	North	South
Heliostat width (m)	12.9	1.85
Heliostat height (m)	9.6	2.44
Tracking Mechanism	Azimuth-elevation	Pitch-roll
Slope error (mrad)	0.9	1.64
Reflectivity	0.95	0.94

The calculation of the incident energy was performed initially by the CSIRO control system and reported in the experimental data files. A later off-line simulation was conducted using Tracer. Very good agreement was obtained between the two tools. After re-simulating the flux map using the data from the log files, the total incident energy rate of the flat water case calculated using Tracer was 1.60% higher than that calculated by CSIRO, while the flat air case was 2.05% lower. These differences, although relatively small, are of the same magnitude as the differences in receiver performance, and as such it is important to consider their source. Possible sources are as below:

- The sun position in each case was fixed at the starting point within the testing period. This assumption, however, would not cause a large difference in the results due to the short time interval of interest. The change in sun position would be less than 7.50°, if the time duration was less than half an hour.
- Solar noon was assumed to be at 11.50 am, since the solar noon was 11:52 am on 17th and 18th of April, and was 11:50 am on 30th of May (source: [176]).
- Air attenuation was not considered, since the heliostat field was relatively small. The distance between the furthest heliostat and the receiver was less than 100 m. Therefore, the effect of air attenuation was nearly negligible.
- All the unused heliostats were set in the vertical position in Tracer, while some of the unused heliostats were set in the standby position at CSIRO. This would make the most difference in the results. Difference poses of heliostats would have different blocking and shading effects with respect to the surrounding heliostats. However, the actual poses of the unused heliostats were hard to reproduce, outside the CSIRO control system. Therefore, they were simplified in the vertical position in Tracer.

The flux distributions for all four cases (FW1, FW2, FA4 and FA5), with the comparison between simulated results from CSIRO (top) and Tracer (bottom) were plotted in Fig. 5.8 and Fig. 5.9. Overall, the results from the Tracer model were consistent with the optical model used by CSIRO. However, there were no flux measurements involved in the experiments. Therefore, the assumptions made in the optical models[3] could not be evaluated in this thesis. The distributions of external wall temperature were studied next, based on the flux distributions that were obtained from the optical model introduced above.

5.3.3 Temperature matching

Dominant parameters that affected the external wall temperatures were the external and internal heat convection coefficient. These coefficients could be validated

[3]Optical models were carried out by Wang [101]. The overall optical analysis was not the research scope of this thesis and therefore, was not included in this thesis.

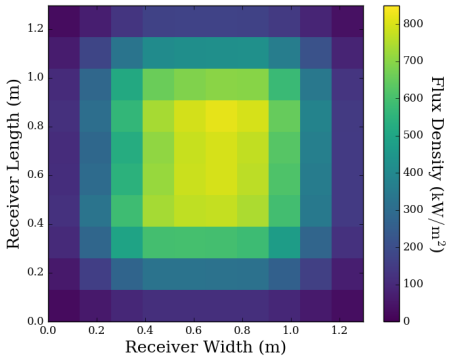

(a) CSIRO: FW1, min. flux = 24.35 kW/m^2, max. flux = 817.58 kW/m^2

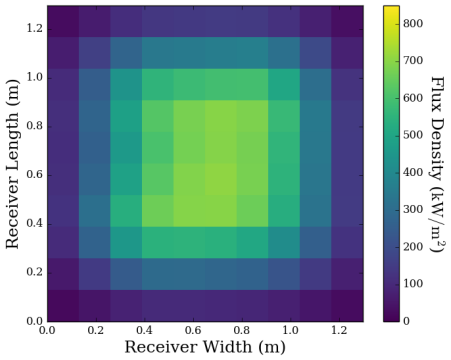

(b) CSIRO: FW2, min. flux = 21.40 kW/m^2, max. flux = 709.08 kW/m^2

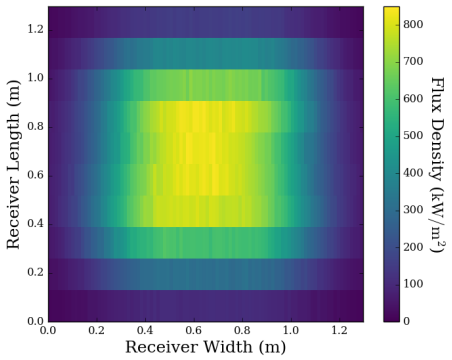

(c) Tracer: FW1, min. flux = 13.81 kW/m^2, max. flux = 844.25 kW/m^2

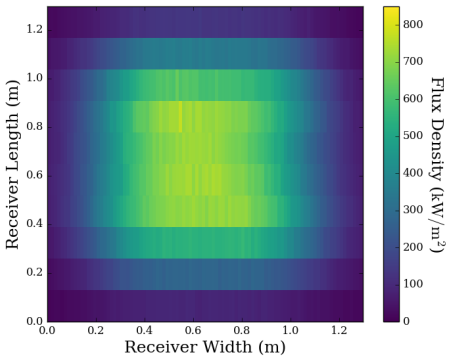

(d) Tracer: FW2, min. flux = 12.63 kW/m^2, max. flux = 775.47 kW/m^2

Fig. 5.8: Flux distribution, water cases. 10×10 flux maps were provided by CSIRO, as shown in (a) and (b), while 10×96 flux maps were developed in Tracer using the same specified aim-points as reconciled by the CSIRO control system, and then implemented in ASCEND. There were 96 tubes in the receivers. The flux map was not interpolated in y-axis direction to reduce the the computational costs, when calculating the thermal performance of the receiver based on the mesh size of the flux map.

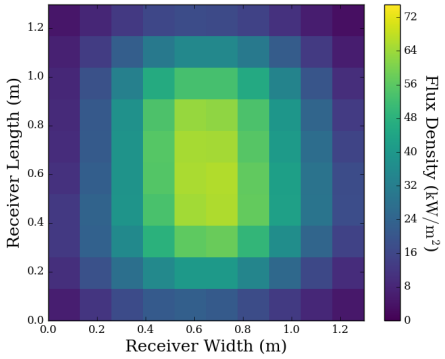

(a) CSIRO: FA4, min. flux = 3.06 kW/m^2, max. flux = 66.30 kW/m^2

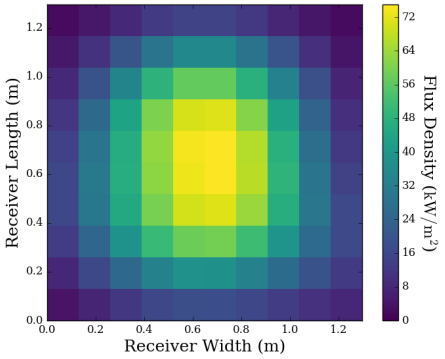

(b) CSIRO: FA5, min. flux = 2.13 kW/m^2, max. flux = 75.63 kW/m^2

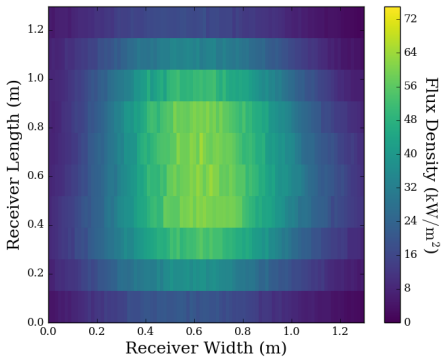

(c) Tracer: FA4, min. flux = 1.37 kW/m^2, max. flux = 64.94 kW/m^2

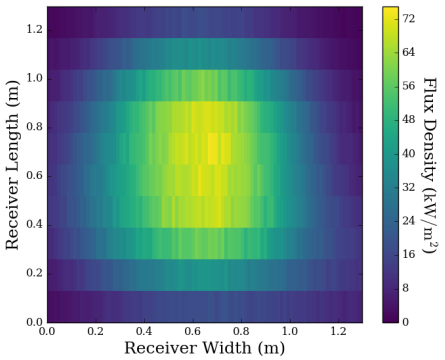

(d) Tracer: FA5, min. flux = 1.07 kW/m^2, max. flux = 74.04 kW/m^2

Fig. 5.9: Flux distribution, air cases (similarly to Fig. 5.8).

using experimental results.

Comparing the temperatures of flat air tests of experimental results to those of the simulation results, we can confidently state that the optimised parameters were well matched with the assumed parameters in the simulation—the external heat transfer coefficient (16 W/(m^2·K) [167]) and the internal convection correlations (suggested by Gnielinski [137]). It was noted that the temperature variation might be caused by the difference in the flux distribution, shown in Fig. 5.9. The slightly higher maximum flux in the centre of the receiver might result in a higher external wall temperature, where the front thermocouple was located.

For the flat water case (flux distributions shown in Fig. 5.8, however, the explicit comparison in Fig. 5.3 showed a large variation occurred in external wall temperatures, which resulted in extremely poor internal heat transfer in the optimisation afterwards (i.e. 95% worse than experiments). However, the empirical relation used for calculating internal convection heat transfer was very unlikely to be so inaccurate, considering the Reynolds numbers calculated for the water cases (i.e. 4×10^4 – 8×10^4) were in turbulent flow range. A number of possible causes were then discussed in the following sections, in sequence from minor to major effects.

5.3.3.1 Coarse mesh smoothing effect in flux distribution

There would be some discrepancies occurring at the peak-flux matching as shown in Fig. 5.8 and Fig. 5.9, even though the total incident energy could be matched well (as discussed in Section 5.3.2). The simulation results were obtained based on a 10×10 flux map provided by CSIRO. This coarse mesh might dilute the realistic flux in the centre of the receiver to a lower averaged value in order to maintain identical total energy in one single grid when compared to a 10×96 mesh, where the peak flux and the peak external wall temperature were expected to be captured in the centre of the receiver.

5.3.3.2 Tube wall temperature variation in the circumferential direction

One assumption made in the receiver models was that the tube was supplied with heat uniformly across its front half (a flat external surface was assumed ($A_{\text{ext,tube}} = Ld_o$)), and with effective absorptivity and surface emissivity being considered (named as "Case C1"). A very relevant study has been conducted in Chapter 2 (refer to Section 2.5.6 for summarised results, and Appendix B for model details), and shows that this assumption caused an under-estimation of the peak tube wall temperature, assuming the peak tube wall temperature was on the centre of the tube.

In order to examine this question, one modified model was conducted relating

to this effect. Here, a non-uniform distribution of absorbed flux across its front half was considered (named as "Case C2"), according to the cosine profile ($\dot{Q}_{\text{abs,tube}} = \alpha_{\text{eff}} \dot{q}^{'} A_{\text{tube}} \cos(\theta)$), where the absorbed flux was symmetrical about the angular coordinate $\theta = 0°, 180°$), with scaling applied to ensure the same total absorbed energy per tube section as in Case C1. The cosine profile was applied to estimate the reduction of the absorbed energy due to cosine effect. The emissivity ϵ_i of the receiver surface in Case C2 was considered the same as Case C1.

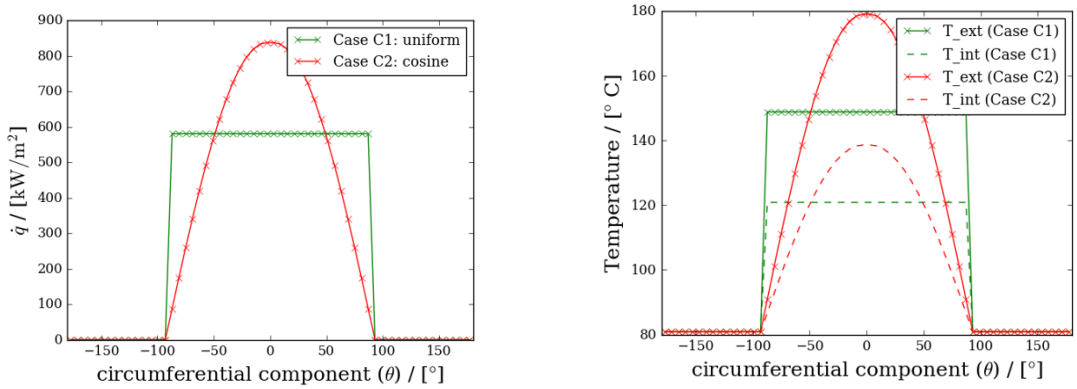

(a) Flux profiles

(b) Temperature profiles

Fig. 5.10: "FW1" is selected in this study, with $T_{\text{HTF}} = 80°$C. (a) flux profiles in the circumferential direction of the tube and (b) the corresponding inner and outer wall temperature profiles, where thermocouple is supposed to measure the external wall temperature at $\theta = 0°$. The peak flux ($\dot{q}_{\text{abs}}$) of Case C1 is 576.5 kW/m^2 on the unfolded surface, and of Case C2 is 836.0 kW/m^2.

To summarise, a cosine circumferential wall temperature profile with no consideration of view factors (Case C2) would result in an increase in the peak circumferential wall temperature when compared to the case of uniform wall temperature (Case C1), as shown in Fig 5.10. However, this effect did not fully explain the large variation between thermocouple measurements and model simulations, as the temperature at the front centre of the receiver could only be increased from 146°C (which was the same as the temperature calculated in Fig. 5.3(a)) to 179°C in this approach. Therefore, other effects which may also be at play were expected and examined next.

5.3.3.3 Effect of thermocouple configuration

A 27 mm (length) × 17 mm (width) × 3 mm (thickness) plate was used to protect the thermocouple, which was mounted on top of the tube surface, as shown in Fig 5.11. The temperature measured by the thermocouple could be directly affected by the irradiance transmitting, plate temperature and the hot air trapped between the plate and the tube. In this section, the effects of the wall conduction of the plate, the

[4]The photo was taken several months later, after the receiver was returned to ANU from CSIRO, and there had been rain and dust in the meantime. The emissivity from this photo cannot be inferred.

(a) Before testing (b) After testing

Fig. 5.11: The welding of the thermocouple on the receiver (a) before and (b) after on-sun testing. The surface appearance after on-sun testing (b) indicates a significant difference in surface emissivity from before testing (a)[4].

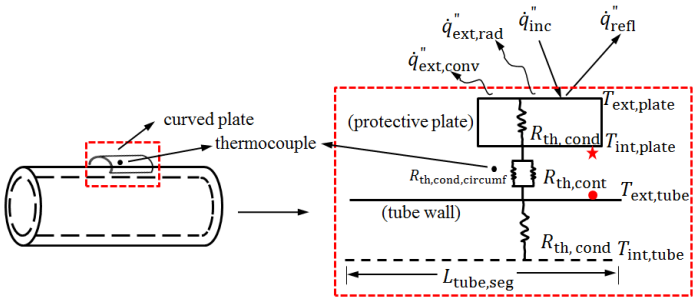

Fig. 5.12: The schematic diagram of the thermocouple (black dot) with a protective plate on top. The breakdown of the thermal resistance was circled in red dotted lines. Temperatures at the internal plate (red star) and external tube (red dot) were of interest to investigate the noise on thermocouple measurement.

temperature difference between the plate and the external wall, and the temperature variation in the circumferential direction of the tube have been conducted. Imagining the thermocouple and the external tube wall brought into contact as indicated in Fig. 5.12, there might be a temperature difference between the two materials due to the result of a thermal contact resistance. Assuming the flux density on the plate was constant, the total absorbed energy on the plate was:

$$\dot{Q}_{\text{abs,plate}} = \alpha_{\text{eff}} \dot{q} A_{\text{plate}} \tag{5.3}$$

where α_{eff} was set in a range from 0.7–0.99 to study the effect of varying α_{eff} on external wall temperature. The heat flux $\dot{q}$ is 836.0 kW/m^2.

External radiation and external convection losses were considered as:

$$\dot{Q}_{\text{ext,rad}} = \epsilon \sigma_c A_{\text{plate}} \left(T^4_{\text{ext,plate}} - T^4_{\text{amb}} \right) \tag{5.4}$$

$$\dot{Q}_{\text{ext,conv}} = h_{\text{ext}} A_{\text{plate}} \left(T_{\text{ext,plate}} - T_{\text{amb}} \right) \tag{5.5}$$

where $h_{\text{ext}} = 16$ W/m^2·K, ϵ has been defined as Eq. 2.9.

Therefore, the net energy on the plate was defined as:

$$\begin{aligned} \dot{Q}_{\text{i,plate}} &= \dot{Q}_{\text{abs,plate}} - \dot{Q}_{\text{ext,rad}} - \dot{Q}_{\text{ext,conv}} \\ &= \frac{k_{\text{plate}} A_{\text{plate}} \left(T_{\text{ext,plate}} - T_{\text{int,plate}} \right)}{t_{\text{plate}}} \\ &= \frac{A_{\text{plate}} \left(T_{\text{int,plate}} - T_{\text{ext,tube}} \right)}{\frac{1}{h_{\text{cont}}}} \end{aligned} \tag{5.6}$$

In this study, a wide range of plate wall conduction values were used, from 10–40 W/m·K. The range of the thermal contact resistance $\frac{1}{h_{\text{cont}}}$ values were 0–0.2$\times 10^{-3}$ m^{2}K/W [177].

From the energy equation (Eq. 5.6), it is shown that the temperature measured by the thermocouple was not the true external wall temperature but some radiation-conduction-contact equilibrium temperature. A large error could result in temperature measurement if this energy balance is not properly considered. Therefore, a sensitivity study was conducted to examine the effect of varying the wall conductivity of the plate, the thermal contact resistant between hot plate and tube, and the surface reflectivity α_{eff} of the tube on the thermocouple measurement. The inner wall temperature of the plate was the temperature of interest in this study as the thermocouple measurement was supposed to be a value between the inner wall temperature of the plate and the external wall temperature of the tube.

First of all, the effect of varying the wall conductivity of the plate on the temperature for water case FW1 with varied $\frac{1}{h_{\text{cont}}}$ was examined. Results in Fig. 5.13 showed that the wall conductivity of the plate would not affect its inner wall temperatures significantly, when compared to the $\frac{1}{h_{\text{cont}}}$. Then, the effects of varying the thermal contact resistance and the effective reflectivity on the temperatures was examined. The intention of this analysis is to figure out one single set of values for the thermal contact resistance and the effective reflectivity that could make thermocouple measurements and simulations well matched for all four cases.

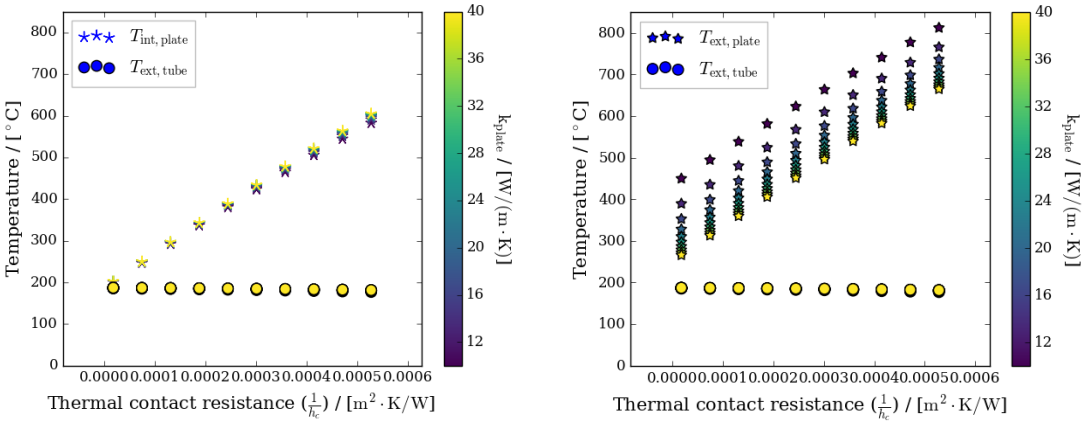

Fig. 5.13: The effect of varying the wall conductivity of the plate on the temperatures for the water case "FW1", for a range of $\frac{1}{h_{\text{cont}}}$. Left: stars indicate the internal temperature of the protective plate. Right: stars indicate the external temperature of the protective plate.

After conducting a series of studies on air case FA4, the results in Fig. 5.14 showed that the effect of α_{eff} seemed to be stronger than the effect of $\frac{1}{h_{\text{cont}}}$. In addition, the result for a reasonable effective reflectivity was dominated by h_{ext}, as Fig 5.14(b) showed that the $f_{\text{int,conv}}$ did not improve the α_{eff} obviously. Fig 5.14(a) and (c) indicated that either the Pyromark was very damaged to cause a rather low α_{eff}, or a higher h_{ext} was required to have a more reasonable α_{eff} (e.g. in a range of 0.86–0.9, as shown in Fig 5.14(c)). The overall study showed that the effect of thermal contact resistance would not be significant for the air cases as the given incident flux on top of the plate was low and the external wall temperature of the tube was high. These findings could also validate that the external wall temperatures for the initial simulation air cases in Fig. 5.3 were matched well with the experimental measurements, since the interference factor of thermal contact resistance was low.

Next, the appropriate thermal contact resistance $\frac{1}{h_{\text{cont}}}$ was examined. Results were shown in Fig. 5.15. The initially optimised h_{ext} (i.e. 21.20 W/(m^2·K)) was applied on the rest of the three cases, FA5, FW1 and FW2, but remaining $f_{\text{int,conv}} = 1$. A wide range of thermal contact resistances were observed to be possible from water cases, FW1 and FW2, as the thermocouple measurements could be any temperature value between the internal plate and the external tube wall. A large uncertainty would

exist if the thermocouple was not be adhered to the external tube.

5.3.3.4 Failure of thermocouple insulation

One unlikely but possible error could occur if two wires made contact with each other before the end of the connection head, due to the insulation failure. A hint could be observed from Fig. 5.11(b). The characteristics of the thermocouple metal could be changed if they were exposed to the high flux and high temperature atmosphere, where overheating might happen.

5.3.3.5 An airlock in the tube

Another issue could be an airlock in the tube. It might happen when the air was trapped by the flow of the water, preventing the free flow of water. However, this phenomenon was considered before the water test and steps were taken to attempt to avoid it. For example, high flow rate pumping was applied before starting the water tests, which made this experimental failure unlikely happen.

5.3.3.6 Discussion

A series of studies have been conducted to comprehensively analyse the possible reasons why simulation results were different from the experimental measurements in three aspects. Studies show that the effect of thermocouple configuration was very likely the leading cause. However, a wide range of possible $\frac{1}{h_{\text{cont}}}$ were detected due to the uncertainty in thermocouple welding circumstance. It seems that the previous section provides a compelling explanation for the high measurements. What is not possible, though, is to correct those measurements, since there is too much uncertainty. Unfortunately, with very limited experimental data, there was no clear-cut answer to the understanding of the reason for the high temperature measurements at the front centre of the water receiver. Suggestions for future experiments of this type, could be:

- mounting the thermocouples inside the tube wall to make direct contact, if possible;
- using insulated protection if mounting the thermocouple externally;
- using an infrared camera to measure the receiver surface temperature distributions;
- repeating experiments under different testing conditions, such as variable ambient conditions, variable sunlight conditions and variable wind speeds.

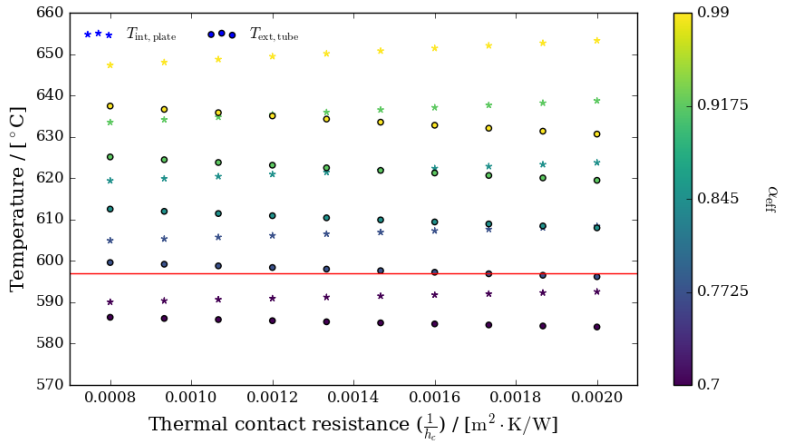

(a) FA4: $f_{\text{int,conv}} = 1$, $h_{\text{ext}} = 16.00$ W/(m^2·K)

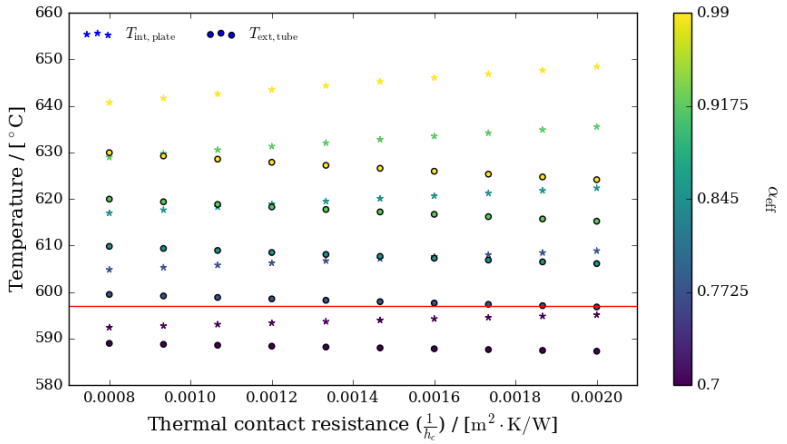

(b) FA4: $f_{\text{int,conv}} = 1.49$, $h_{\text{ext}} = 16.00$ W/(m^2·K)

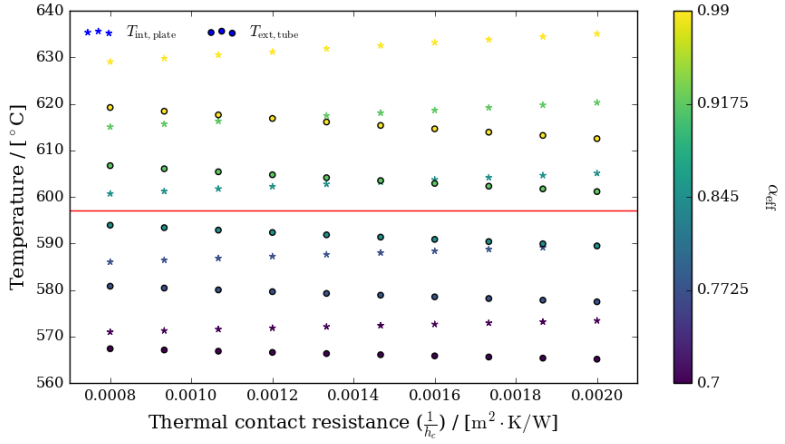

(c) FA4: $f_{\text{int,conv}} = 1$, $h_{\text{ext}} = 21.20$ W/(m^2·K)

Fig. 5.14: Sensitivity studies on thermal contact resistance and effective reflectivity of tube for Case FA4. Red lines indicated the thermocouple measurements.

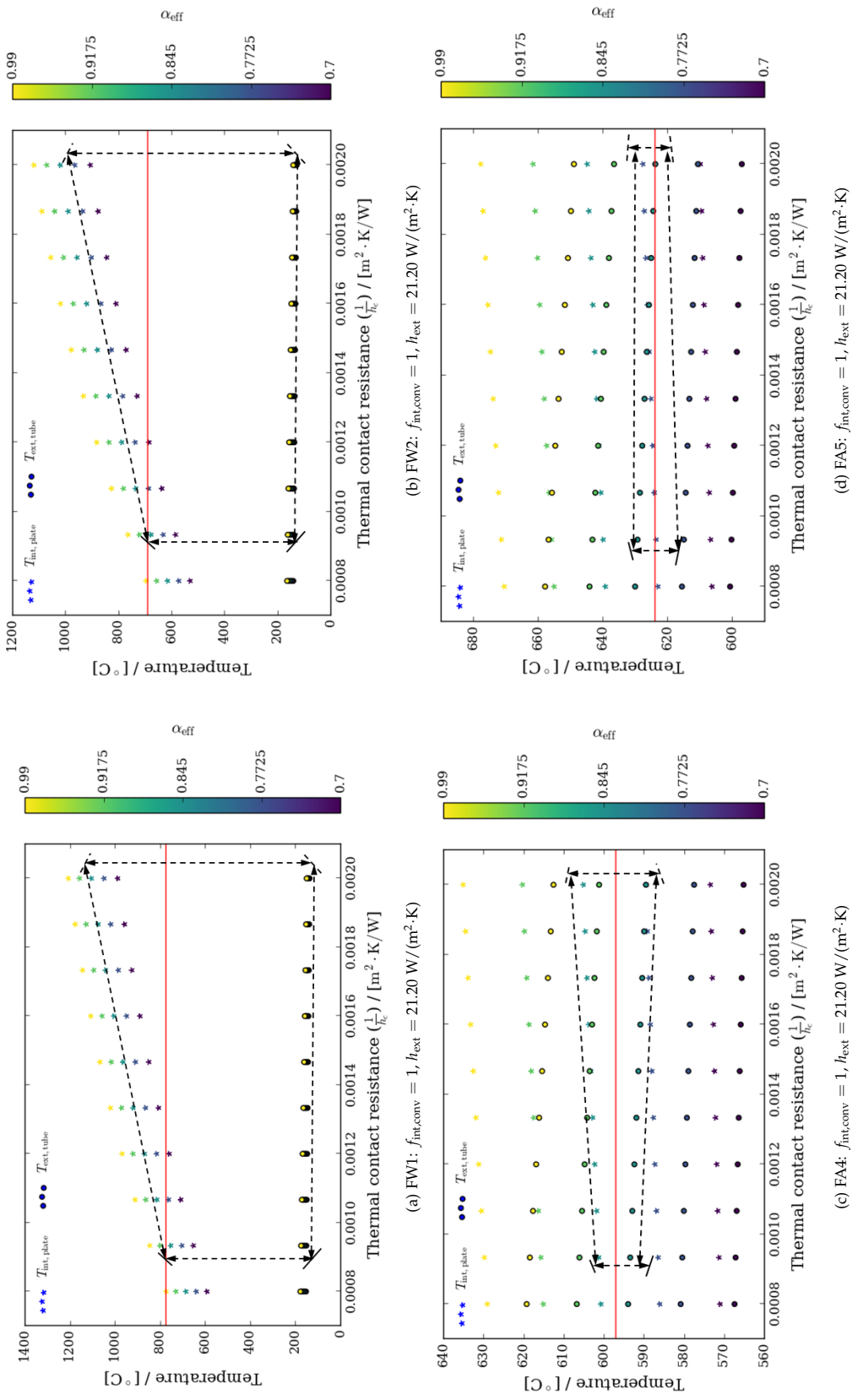

(a) FW1: $f_{\text{int,conv}} = 1$, $h_{\text{ext}} = 21.20$ W/(m^2·K)

(b) FW2: $f_{\text{int,conv}} = 1$, $h_{\text{ext}} = 21.20$ W/(m^2·K)

(c) FA4: $f_{\text{int,conv}} = 1$, $h_{\text{ext}} = 21.20$ W/(m^2·K)

(d) FA5: $f_{\text{int,conv}} = 1$, $h_{\text{ext}} = 21.20$ W/(m^2·K)

Fig. 5.15: Sensitivity studies on thermal contact resistance and effective reflectivity of tube for all four cases: FW1, FW2, FA4 and FA5, with $h_{\text{ext}} = 21.20$ W/(m^2·K). The possible range for $\frac{1}{h_{\text{cont}}}$ was circled in each case, using dotted lines with arrows.

5.3.4 Pressure drop matching

Besides the temperature, the pressure drop across the receiver was also valuable to be reconciled with the flow meter measurement, so that a better understanding about the hydraulic performance of the receiver could be made. The analysis of pressure drop has been split into two parts: the major losses due to the friction in the tubes, and the minor losses due to the tube bends and the headers.

5.3.4.1 Major loss

The major loss in a developed flow is related to the friction, where the friction is a function of the roughness of the tube e. Therefore, this section examined if the roughness of the tube was the dominant cause of the pressure drop. The Darcy-Weisbach equation (Eq. 2.27) is used here.

Hence, if the roughness of the tube wall is known, we can find the friction factor ($f = f\left(\frac{\rho \mathbf{V} D}{\mu}, \frac{e}{D}\right)$) and then the pressure drop. Unfortunately, the roughness of the tube used in this experiment was unknown. Therefore, a sensitivity study on the flat and the bladed cases has been carried out to show that varying the roughness of the tube would not cause a large difference in pressure drop. In this sensitivity study, a wide range of roughness values were selected, 0.0015 mm (e.g. drawn tubing), 0.046 mm (e.g. wrought iron) and 0.15 mm (e.g. galvanised iron) [155].

Table 5.3: The effect on varying the roughness of the tube on the flat water and the flat air cases on the pressure drop (i.e. Δp in bar), with $K = 32.71$ (refers to Sec. 5.3.4.2).

	Δp (bar)			
e (mm)	0.0015	0.046	0.15	CSIRO exp. result
flat water (FW1)	1.89	2.22	2.64	5.48
flat water (FW2)	1.89	2.23	2.64	5.49
flat air (FA4)	0.11	0.13	0.14	0.50
flat air (FA5)	0.16	0.17	0.14	0.53

5.3.4.2 Minor losses

The above study showed that the uncertainty in the roughness of the tube was not the main cause of the difference between theory and experiment. The minor losses refer to the pressure losses in the tube fittings (e.g. bends K_b, contractions K_{con} and enlargements K_{enl}) and within the headers. The friction pressure drops in the elbows were not considered due to the relatively short lengths. All of the minor pressure

drops in the tube fittings could be calculated by:

$$\Delta p_{\text{fittings}} = -\left(\sum_{\text{bend}} K_{\text{b}} + K_{\text{con}} + K_{\text{enl}}\right)\frac{1}{2}\rho \mathbf{V}^2, \tag{5.7}$$

as proved by Crane Co. Technical paper [178]. For one return bend, $K_{\text{b}} = 50 f_{\text{D}}$ and for one 90° bend, $K_{\text{b}} = 30 f_{\text{D}}$ [178]. The friction factor f_{D} was obtained using the Moody diagram. If $\frac{e}{D} = \frac{0.046\text{ mm}}{10\text{ mm}} = 0.0046$ and $\text{Re} = 10^4 \sim 6 \times 10^4$, then $f_{\text{D}} = 0.037 \sim 0.032$.

The total resistance coefficient K_{b} of the flat receiver was 30.71, referring to 7 return bends plus 16 90° bends. $K_{\text{con}} = 1$ and $K_{\text{enl}} = 1$. Pressure drop within headers was not considered in this chapter.

The above analyses show that local losses were likely the major cause of the pressure difference between the experimental results and the simulation results. For the bends and headers with specific angles and shapes used in the experiments, there was unlikely a way to accurately calculate the pressure drops without conducting experimental tests, since it was difficult to predict the real behaviour in the bends and headers using simulation models due to the three-dimensional motions. One possible circumstance that could occur in the bends is the swirling effect. Swirl flow happens through two consecutive out-of-plane bends, which was summarised by Islek [179]. It causes high pressure drop, and the nominal loss coefficient K values suggested by Crane Co. [178] did not consider the swirl effect. Turiso et al. [180] indicated that the velocity in the double bend would increase, and the pressure drop would also increase. The unlikely but possible airlock in the tube, mentioned in Sec 5.3.3.5, may increase the pressure drop due to fewer tubes with flow (i.e. no flow through tubes with airlock), and consequently may lower the receiver efficiency. The optimisation result shows a similar trend with their conclusion. The result shows that the minor loss in the out-of-plane bends could be (130.09/32.71)×100=398% larger than on-the-plane bends. Suggestions for future experiments of this type are:

- conducting more experiments to determine the roughness of the tube, using the straight part of the tube to avoid the uncertainties in bends.
- studying the pressure drop in one similar single out-of-plane bend to have a better understanding of the hydraulic performance.
- building a CFD model to simulate the internal flow of the experimental setup. One out-of-plane bend could also be simulated.

(a) Blades

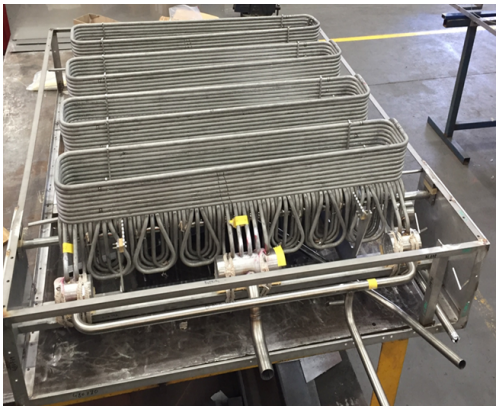

(b) Bladed receiver with bends, heaters and framing

Fig. 5.16: Bladed receiver assembling.

5.4 Bladed cases

A few photos of the bladed receiver are displayed in Fig. 5.16. First of all, the flux maps for the bladed water and air receivers were re-simulated using Tracer[5]. The external wall temperature comparison between experiments and simulations for the bladed air case (BA7) and bladed water case (BW1) have been shown in Fig. 5.17. Due to the very similar behaviour and very high computation costs, only one time interval for each fluid was studied. These two selected cases (i.e. BA7 and BW1) were also used in Chapter 4 for the final experimental evaluations.

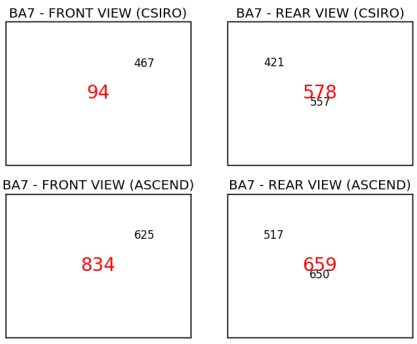

(a) BA7

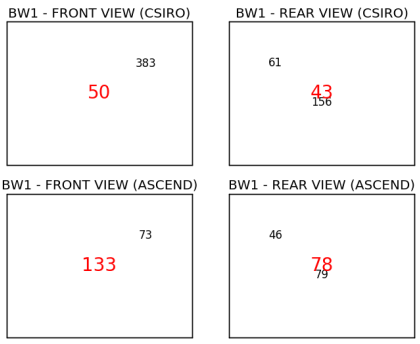

(b) BW1

Fig. 5.17: The temperature distributions for the bladed cases, before matching. Key results from the on-sun tests for these two cases were highlighted in Table 4.7. Parameters were $f_{\text{int,conv}} = 1$, $h_{\text{ext}} = 8.00$ W/(m^2·K) and $K = 39.33$.

The initial parameters used in the simulations were h_{ext} =8 W/(m^2·K), $f_{\text{int,conv,water}} = 1$, $f_{\text{int,conv,air}} = 1$ and $K = 39.33$ (consists of $K_{\text{blade}} = 4$, $K_{\text{edge}} = 2.62$, $K_{\text{bkW}} = 32.71$).

[5]Optical related studies were conducted by Wang.

The initial K value was obtained using the same approach as mentioned in Section 5.3.4.2 and in [178]. The comparison between experimental measurements and the initial simulation results have been summarised in Table 5.5. Inputs of simulations were aligned with the experimental measurements, highlighted in bold. It is worth noting that the pressure drop in the "blade" section of case BW1 in the simulation (i.e. $\Delta p = 4.97 - 1 = 3.97$ bar) was well matched with the measurements (i.e. $\Delta p = 5.11 - 1 = 4.11$ bar). The difference was only 3.4%. The disparity in pressure drop in the edge and the back wall sections of case BW1 was expected to be large due to the uncertainty in the "out-of-plane" bends in the back wall, as discussed in Section 5.3.4.2. The parameter corrections for the bladed cases are investigated in the following section.

5.5 Overall comparison between flat and bladed cases

Both flat and bladed receiver models were updated again to make a final comparison of the receiver performance, according to the optimised corrections on the internal and external convection coefficient, and the nominal loss coefficient. The initial optimisation results showed that, for the water cases, the thermocouple measurements on external wall temperatures at the front surface of the receivers were unreliable as the reduction in internal convection coefficient (95% worse than the initial value) was not likely to truly happen, according to the studies in Section 5.3.3. Therefore, the updated optimisation procedures were based on the air cases only, where in those cases the external wall temperatures were supposed to be high but the flux on the tubes were relatively low, so that there would be fewer issues with the thermocouple behaving abnormally. The corrected parameters using air cases were updated and shown in Fig. 5.18 below. Table 5.4 summarised the experimental results, and the simulation results for the flat receivers, after implementing re-simulated flux map using Tracer, inlet temperature of the working fluid and the mass flow rate as indicated in the experiments, together with the final optimisation results. These final results were used later for the comparison between flat and bladed receivers.

The approach to attaining the final corrected parameters for the temperature related parameters (i.e. h_{ext}, $f_{\text{int,conv,air}}$) in the bladed receivers was to conduct the least-squares optimisation method mentioned in Section 5.2. No optimisation process was conducted on the pressure matching due to high computational costs. The ratio for the corrected K in the flat case was used here, $\text{ratio}_K = \frac{130.09}{32.71} = 3.98$. Note that this correction ratio was only applied to the "back-wall" section in the bladed receivers, since the "blade" section was already matched well before the correction.

After applying all the correction parameters into bladed case BA7 and case BW1, a good agreement could be seen in the bladed air case between experimental measurements and the updated modelling. Consequently, the thermal losses calculated

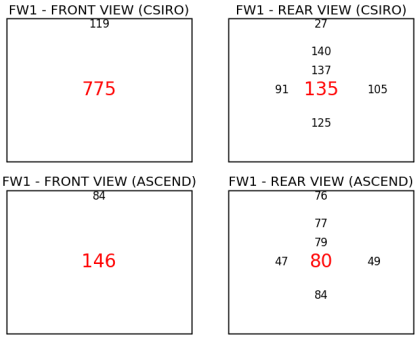

(a) FW1

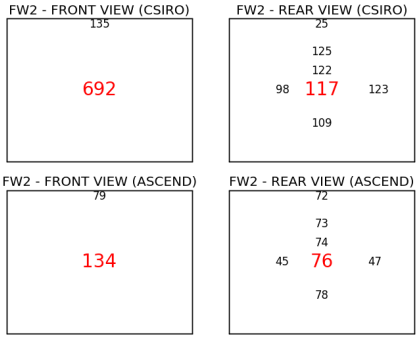

(b) FW2

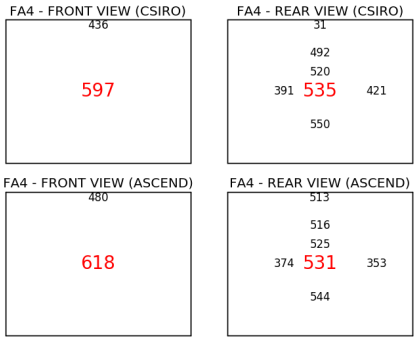

(c) FA4

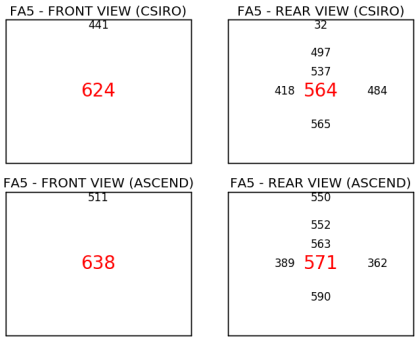

(d) FA5

Fig. 5.18: Final results after corrections. For the flat water cases, $h_{ext} = 20.32$ W/(m^2·K), $K = 130.09$, $e = 0.046$ mm and $f_{int,conv,water} = 1$ For the flat air cases, $h_{ext} = 20.32$ W/(m^2·K), $K = 130.09$, $e = 0.046$ mm and $f_{int,conv,air} = 0.8$

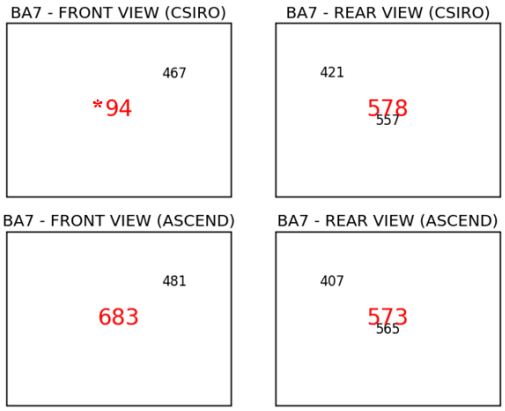

(a) BA7

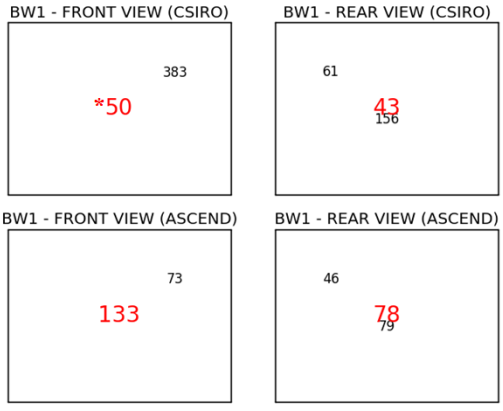

(b) BW1

Fig. 5.19: The temperature distributions for the bladed cases, after applying the ratio of the parameters. Parameters are $f_{int,conv,water} = 1$, $f_{int,conv,air} = 1.50$, $h_{ext} = 20.72$ W/(m^2·K) and $K = 4 + 2.67 + 3.98 \times 32.71 = 136.71$. Numbers labelled in $*$ were not considered in the optimisation due to the improper measurements.

Table 5.4: Detailed results of the experiment, the simulation before and after parameter corrections for the flat cases. Inputs of simulations were highlighted in bold. Cases FW2 and FA5 were used for final evaluations, to align with earlier analyses in Table 4.7. $\eta_{\text{th}} = \frac{\dot{Q}_{\text{net}}}{\dot{Q}_{\text{inc}} - \dot{Q}_{\text{refl}}}$.

	Experiments				Simulations (before)				Simulations (after)			
	FW1	FW2	FA4	FA5	FW1	FW2	FA4	FA5	FW1	FW2	FA4	FA5
h_{ext} (W/m^2/K)	–	–	–	–	16	16	16	16	20.32	20.32	20.32	20.32
$f_{\text{int,conv}}$	–	–	–	–	1	1	1	1	1	1	0.8[a]	0.8
K	–	–	–	–	32.71	32.71	32.71	32.71	130.09	130.09	130.09	130.09
$\dot{m}$ (kg/s)	3.024±0.015	3.024±0.015	0.0488±0.0005	0.0501±0.0005	**3.024**	**3.024**	**0.0488**	**0.0501**	**3.024**	**3.024**	**0.0488**	**0.0501**
T_{in} (°C)	35.1±3.5	34.1±3.5	321.2±3.5	321.5±3.5	**35.1**	**34.1**	**321.2**	**321.5**	**35.1**	**34.1**	**321.2**	**321.5**
T_{out} (°C)	78.1±3.5	71.4±3.5	500.1±3.5	516.7±3.5	82.3	76.7	544.2	568.7	82.2	74.2	519.4	565.8
p_{in} (bar)	6.5±0.1	6.5±0.1	6.3±0.1	6.4±0.1	3.23	3.23	**6.3**	**6.4**	6.78	6.80	**6.3**	**6.4**
p_{out} (bar)	1±0.05	1±0.05	5.8±0.1	5.8±0.1	**1**	**1**	6.20	6.23	**1**	**1**	6.00	6.01
$\dot{Q}_{\text{inc}}$ (kW)	618±12	548±11	50.3±1.0	53.1±1.1	621.8	562.2	48.4	53.0	621.8	562.2	48.4	53.0
$\dot{Q}_{\text{refl}}$ (kW)	–	–	–	–	24.3	22.0	1.9	2.1	24.3	22.0	1.9	2.1
$\dot{Q}_{\text{ext,rad}}$ (kW)	–	–	–	–	0.6	0.6	23.7	26.1	0.06	0.6	22.4	23.2
$\dot{Q}_{\text{ext,conv}}$ (kW)	–	–	–	–	1.5	1.4	11.1	11.4	1.9	1.8	13.7	14.5
$\dot{Q}_{\text{loss,tot}}$ (kW)	75±46	76±46	41.0±1.0	42.6±1.1	26.4	24.0	36.7	39.6	26.8	24.4	38.0	39.8
$\dot{Q}_{\text{net}}$ (kW)	543±45	471±45	9.4±0.3	10.5±0.3	595.4	538.3	11.7	13.4	595.0	537.8	10.4	13.2
η_{th} (%)	–				99.6%	99.6%	25.2%	26.3%	99.6%	99.6%	22.4%	25.9
η_{tot} (%)	$1 - \frac{76+42.6}{548} \times 100\% = 79 \pm 8\%$				$1 - \frac{24.0+39.6}{562.2} \times 100\% = 88.7\%$				$1 - \frac{24.4+39.8}{562.2} \times 100\% = 88.6\%$			

[a] The increase in the pressure drop is mainly due to the increase in the minor loss (i.e. the K value). The decrease in internal heat transfer would decrease the outlet temperature of the receiver, which could better match with the experimental results.

in the air model could be confidently used in the final energy comparison between flat and bladed cases. Note that, the improbably low measurements at the centre of the front surface for both cases (as labelled in $*$ in Fig. 5.19) were not considered in the analysis. The large temperature difference in the BW1 case was due to the low temperature measurements at the back wall; the temperature difference, for example, was 81.40% at the centre of the back surface (i.e. $\frac{78-43}{43} \times 100 = 81.40\%$). However, it was believed that the thermal losses in the bladed water receiver should be marginal, as it was designed to have high flux but low heat transfer fluid temperature (<100°C) and hence, very low external wall temperature on the receiver. The detailed results, after correcting those parameters, are listed in Table 5.5. The differences between simulated results and experimental results (flat receivers: 88.6% vs 79 $\pm$ 8%; bladed receivers: 89.0% vs 80 $\pm$ 8%) were due to limitations in experimental conditions that could be achieved in practice, in particular due to limits in pressure drop and pump capacity. A water boost pump had to be installed as part of the receiver test system since the pressure from the CSIRO feedwater system was low at the top of the tower. In addition, the uncertainty about the flux levels could not be measured. The difference in the thermal efficiencies, between calculated simulation results before and after the parameter corrections, were only 2.8% (i.e. $(25.2 - 22.4)\%$), 0.4% (i.e. $(26.3 - 25.9)\%$) and 2.2% (i.e. $(28.5 - 26.3)\%$) in the flat air cases (FA4 and FA5) and the bladed air case (BA7) respectively, which showed that the h_{ext} and internal convection correlations in the low-flux high-temperature air cases were appropriately used. The final results for the bladed receiver showed an improvement of 0.5% in receiver performance (refer to Table 5.4 and Table 5.5) when compared to the flat receiver, which showed a good agreement with the experimental measurements (was 0.65 $\pm$ 0.08% as concluded in Section. 4.5.2).

5.6 Conclusions

The 0.5% improvement in the updated bladed receiver, when compared to the updated flat receiver, was consistent with the conclusion made in Chapter 4. The analysis highlighted that the pressure drops in the flat receiver and in the back wall of the bladed receiver were likely significantly higher than the original models. The K values were 400% higher than the values expected, which was associated with the presence of out-of-plane bends. The pressure drop in the "blade" section could be well matched without optimisations, which showed that the pressure drop in the straight tubes and in the regular 90° bends could be well predicted using the literature. The difference of the pressure drop in the "blade" section between experimental measurements and the simulation was only 3.4%. The front-surface thermocouple appeared to be measuring very high temperatures for the high-flux low-temperature water cases, which were not consistent with the original models. Those measurements on the front surface were not credible in any of the high flux cases. Therefore, those high flux water cases were removed from any of the parameter corrections.

Table 5.5: Detailed results of the experiment, the simulation before and after parameter corrections for the bladed cases. Inputs of simulations were highlighted in bold. Cases BW1 and BA7 were used for final evaluations, to align with earlier analyses in Table 4.7. $\eta_{\text{th}} = \frac{\dot{Q}_{\text{net}}}{\dot{Q}_{\text{inc}} - \dot{Q}_{\text{refl}}}$.

	Experiments			Simulations (before)			Simulations (after)		
	BW1		BA7	BW1		BA7	BW1		BA7
	blade	edge + bkW		blade	edge + bkW		blade	edge + bkW	
h_{ext} (W/(m^2·K))	–	–	–	8	8	8	10.16	10.16	10.16
$f_{\text{int,conv}}$	–	–	–	1	1	1	1	1	0.8
K	–	–	–	39.33	39.33	39.33	136.71	136.71	136.71
$\dot{m}$ (kg/s)	0.98	2.05	0.043±0.0004	**0.98**	**2.05**	**0.043**	**0.98**	**2.05**	**0.043**
T_{in} (°C)	34.7±3.5	34.7±3.5	315.0±3.5	**34.7**	**34.7**	**315.0**	**34.7**	**34.7**	**315.0**
T_{out} (°C)	72.7±3.5		524.9±3.6	74.1		687.4	74.5		647.3
p_{in} (bar)	5.11±0.10	5.11±0.10	7.66±0.38	4.97±0.10	2.47±0.024	**7.66**	4.13	4.85	**7.66**
p_{out} (bar)	1±0.02	1±0.02	5.82±0.1	**1**	**1**	6.57	**1**	**1**	5.78
$\dot{Q}_{\text{inc}}$ (kW)	543±11		61.6±1.2	546.0		67.4	546.0		67.4
$\dot{Q}_{\text{refl}}$ (kW)	–		–	8.4		1.2	8.4		1.2
$\dot{Q}_{\text{ext,rad}}$ (kW)	–		–	1.0		35.3	1.0		19.7
$\dot{Q}_{\text{ext,conv}}$ (kW)	–		–	1.3		13.5	3.3		27.6
$\dot{Q}_{\text{loss,tot}}$ (kW)	63±46		51.9±1.3	10.7		59.0	12.7		47.3
$\dot{Q}_{\text{net}}$ (kW)	481±40		9.7±0.3	535.3		17.4	533.3		21.2
η_{th} (%)	–			99.6%		26.3%	99.2%		28.5%
η_{tot} (%)	$1 - \frac{63+51.9}{543} \times 100\% = 80 \pm 8\%$			$1 - \frac{10.7+59.0}{546.0} \times 100\% = 87.2\%$			$1 - \frac{12.7+47.3}{546.0} \times 100\% = 89.0\%$		

Better understanding between experimental data and receiver models was obtained through the optimisation process, not only the temperature and the pressure matching, but the use of additional instruments which were not available using the tests. The optimisation results showed the thermal performance of both flat and bladed receivers was appropriately calculated using the simulation model before correcting h_{ext} and internal convection, as the differences in the thermal efficiency performance were <3.0% in all cases. Overall, both flat and bladed models had better function when compared to the experimental measurements, especially on the effects of pressure drop, internal and external convection coefficients.

However, this conclusion could not fully reflect the realistic performance of the receivers due to very limited experimental data. Nonetheless, this chapter provided valuable literature for future experiments. Future experiments which could overcome the limitations of the reconciliation could be: repeated experiments under a wide range of conditions (ambient conditions, wind conditions, flux conditions); improved method of mounting the front surface thermocouples; addition of an infrared camera for realistic temperature measurements, and realistic flux distribution measurements.

It is worth nothing that a relatively small gain, whether it is 2.5% or 0.5%, for a receiver that is basically the same aperture area for both flat and bladed, is unlikely to be worth the effort. The concept of the bladed receiver is demonstrated as far as performance, but there are serious doubts over its potential as a commercially-viable concept, due to the likely higher cost of such a design.

Chapter 6

Durability, cost and efficiency trade-offs in tubular receivers with a range of working fluids for CSP[1]

6.1 Introduction

The performance gains due to novel geometries (Chapter 4) were not so promising as the gains that were found with a 'ramp' flux profile (Chapter 3). In this chapter, more parameters (e.g. the operating temperatures, the working fluid and the tube material choices) are considered to better understand how well different options perform, when used with the more conventional convex receiver designs. In addition, noting the concerns of Chapter 5 , the question of cost-versus-performance is essential to be considered, not just performance. The main metric for justifying the economic feasibility of Concentrating Solar Power (CSP) systems is typically the levelised cost of energy (LCOE). Improvements can be made broadly through either reductions in capital costs or improvements to the efficiency of components in the energy chain for the entire system. In Chapter 2, high temperature sodium was found to be the best working fluid candidate, when compared to other candidates (e.g. molten salt[2], air, water/steam and sCO_2), under the uniform flux distribution assumption. It was also assumed that no external wall temperature variation was considered across the front half of the tube, throughout the whole receiver. Chapter 3 studied the effects of varying the flux distribution and the flow configuration on the tubular molten salt receiver. Again, external wall temperature variation was not considered due to the computational limitations of the models. In addition, both studies had no considerations of the material damage or the costs of the receiver. In Chapter 2, there was a superficial analysis of one single tube-section, which established that it was not too critical for performance estimation. However this chapter relates to the tube failure, for which the peak temperature is much more important. That is the reason that

[1]The preliminary results had been presented by the author at the ASME Power & Energy Conference, in Bellevue, WA, USA, 14–17 Jul 2019, titled "Durability, cost and efficiency trade-offs in tubular receivers with a range of working fluids for CSP"

[2]Molten salt in this thesis refers to solar nitrate salt, a mixture of 60% $NaNO_3$, 40% KNO_3.

more focus was given to considering the temperature variation in the circumferential direction of the tube. Therefore, this chapter focuses on the impact of the receiver component, specifically a tubular receiver in a point-focus CSP system, and considers the relationships between material costs, receiver efficiency, and system-level design for a range of working fluids (i.e. molten salt (60% $NaNO_3$, 40% KNO_3), chloride salt (46.0wt% $MgCl_2$–38.9wt% KCl–15.1wt% NaCl) and sodium). The aim is to develop a unified analysis incorporating these different working fluids, tube materials, non-uniform flux distribution and flow paths, so that a globally optimal choice can be made. Although numerous studies on receiver design have been conducted (Section 1.9), few studies undertake this type of broad comparison. In addition, this study focuses on the thermal direction in the receiver, which is in contrast with assuming fixed operating temperatures in other studies. The study of Li et al. [80], for example, examines the optical performance of receivers as a function of the receiver temperature (average blackbody cavity temperature), which goes further in the optical direction.

High-temperature receivers ($\geq$ 700°C) have been proposed in third-generation (Gen3) CSP technology [12] to align with high-temperature sCO_2 Brayton cycle to achieve high efficiencies ($\geq$ 50%). Conventional molten salt (maximum temperature is 565°C) is not able to be used at those elevated temperatures due to chemical degradation and corrosion [40]. However, it has been considered as a working fluid in the receiver due to low cost. An appropriate alternative is chloride salt, which is capable of being operated at high temperatures (i.e. 700°C) (see Section 1.4.2 for literature). Hence, chloride salt is considered in this study.

For this chapter, a numerical one-dimensional flow model takes a selection of working fluids, temperature ranges and operating pressure ranges that reflect the current and next-generation concepts for tubular receivers for CSP. The model consists of a range of tube banks connected in series, with several parallel tubes in each bank. External convection, internal convection, thermal resistance of the pipe and radiative losses are studied, with non-uniform incident flux distributions. The tube wall temperature variation is considered by applying the cosine effect to the circumferential incident flux. The model examines the relationship between the second-law efficiencies of receivers and the costs of the receiver including any necessary receiver replacement over an operating lifetime of 30 years, for three selected working fluids (molten nitrate salt, chloride salt and liquid sodium) using three selected materials (Stainless Steel 316 (SS316) [131], nickel-chromium-cobalt-molybdenum alloy Alloy 617 [132] and nickel-base superalloy Alloy 740H [133]), by optimising the flux distribution, operating temperature range of the HTF, the receiver size, the flow configuration and the tube size using a multi-objective genetic algorithm.

The alternative fluids have a wide range of temperatures and pressures which, impact the thermal and mechanical stresses that some receivers experience. Creep-fatigue damage dominates the lifetime of the receiver, where creep is a time-dependent

deformation, and fatigue occurs when a material is subjected to repeated loading and unloading. This thermoelastic material model also considers a simplified analysis of allowable stress (developed by Logie et al. [72]) at the temperatures in question together with the recommended cycling design life.

6.2 Methodology

6.2.1 Receiver layout

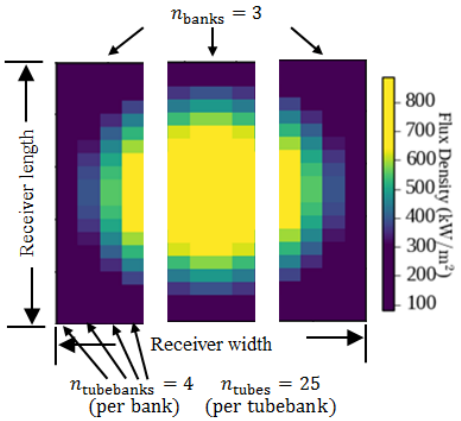

(a) A Gaussian flux distribution, $\sigma = 3$ m.

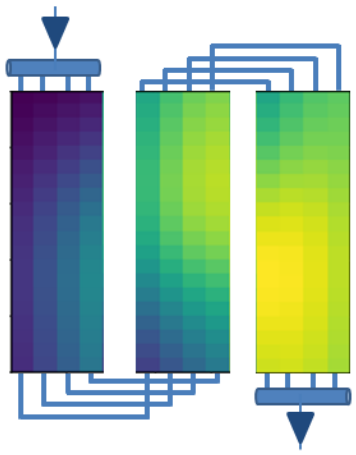

(b) The corresponding HTF temperature distribution, with serpentine "edge-to-edge" flow configuration.

Fig. 6.1: The demonstration of a 10 m $\times$10 m receiver layout, with three banks and four sub-banks in each bank. The flux has been varied into four meshes horizontally in each bank, since there are four sub-banks. Flow configuration: edge-to-edge. Manifolds are coupled at the receiver inlet and outlet to regulate fluid flow.

The foundation of the receiver model has been separately addressed in Chapter 2, 3 and 4. In this chapter, an advanced model is built by merging all the previous features together into one model. In addition, one new feature is added, which is the ability to examine the effect of varying the circumferential tube wall temperature. There are several parallel sub-banks in each bank being considered, and in each sub-bank, there are several parallel tubes, which have identical flux in the horizontal direction.

For each segment, a non-uniform distribution of incident flux across its front half is considered, according to the cosine profile ($\dot{Q}_{inc,i,\theta} = \alpha C G A_{ext} \cos\theta$), where the incident flux is symmetrical about the angular coordinate $\theta = 0°$ and 180°. The cosine profile is applied to estimate the reduction of the incident energy due to the cosine effect. In this study, a Gaussian flux distribution was assumed for the model to approximately simulate the flux profile on the aperture of the receiver, as described in

Section 3.3.1.1. The flux distribution has been varied horizontally along the width of the receiver, and vertically along the tube into a series of segments. An example of the receiver layout is demonstrated in Fig. 6.1. This is a model artifact rather than a physical implementation (i.e. 100 tubes per bank, approximated as four sub-banks of identical parallel tubes). In this particular case, three banks with four sub-banks in each bank and 25 tubes in each sub-bank is shown. The flux is assumed the same horizontally for the 25 tubes in each sub-bank. The receiver size is 10 m $\times$ 10 m with a Gaussian spot size σ of 3 m. Fig. 6.1(a) shows the Gaussian flux distribution on the receiver and (b) shows the resulting HTF temperature distribution with an "edge-to-edge" flow configuration. Three flow configurations are considered in this study, namely "edge-to-edge", "edge-to-centre", and "centre-to-edge", as elaborated in Figure 3.2. Entry and exit headers are considered to regulate the pressure drop in each flow path. Heat and pressure losses in the headers are not considered in this analysis.

6.2.2 Energy and exergy accounting

The total incident energy $\dot{Q}_{\text{inc,rec}}$ on the receiver is equivalent to the total area under the bell curve of a Gaussian distribution, and it is the sum-up of the incident energy ($\dot{Q}_{\text{inc,rec},i}$) in all segments ($i$) of the receiver. In each segment, $\dot{Q}_{\text{inc,rec},i}$ is the sum-up of the incident energy $\dot{Q}_{\text{inc},i,\theta}$ in the circumferential directions. The remainder energy from $\dot{Q}_{\text{sun,rec}}$ is considered as the spillage, as follows:

$$\dot{Q}_{\text{sun,rec}} = \dot{Q}_{\text{spil,rec}} + \sum_{\text{rec},i} \dot{Q}_{\text{inc,rec},i} \tag{6.1}$$

where $\dot{Q}_{\text{inc,rec}}$ is defined in Eq. 3.4.

Detailed energy and exergy equations are defined in Section 3.2. In this chapter, the external convection coefficient is assumed to be $h_{\text{ext}} = 20$ W/m^2·K, which is based on mixed external convection for receivers of realistic size (See Fig 6.2), and is a sensible mid-range value based on expected operational conditions (wind speed range: 0–16 m/s) studied by Siebers and Kraabel [134]. The value used in this study is reasonably consistent with their findings. However, it notes that the external convection coefficient would change, if the scale of the receiver size is changed. The wall conductivities (Fig. 2.7) used in this study and the allowable stresses (Fig. 6.3) for design condition calculations are aligned with the data recommended in the material codes, as a function of the temperature. Materials selected are: SS316 [131], Alloy 617 [132] and Alloy 740H [133].

The internal convection correlations considered here are distinguished for different working fluids to best represent their thermophysical properties. All properties in the correlations are evaluated at bulk fluid temperatures. For molten salt and chloride salt, the Gnielinski correlation [137] (Eq. 2.28) has been applied. For liquid sodium, Skupinski correlation [140] (eq. 2.32) has been applied. et al. All working

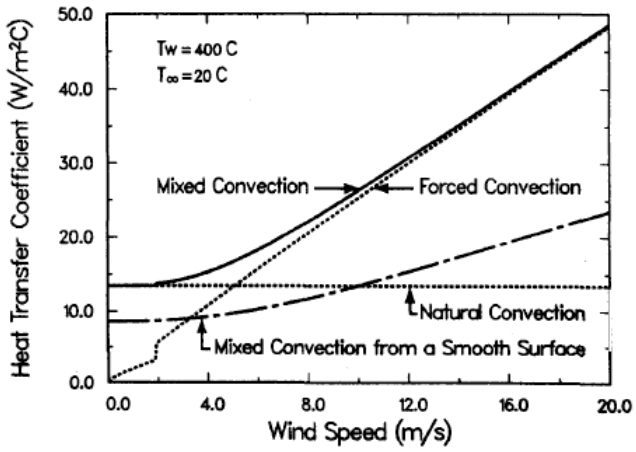

Fig. 6.2: External convection coefficient h_{ext} versus wind speed for the 10 MW_e Barstow Receiver at $T_{\text{wall}} = 400°C$. Receiver size: 7.01 m diameter and 13.71 m height [134].

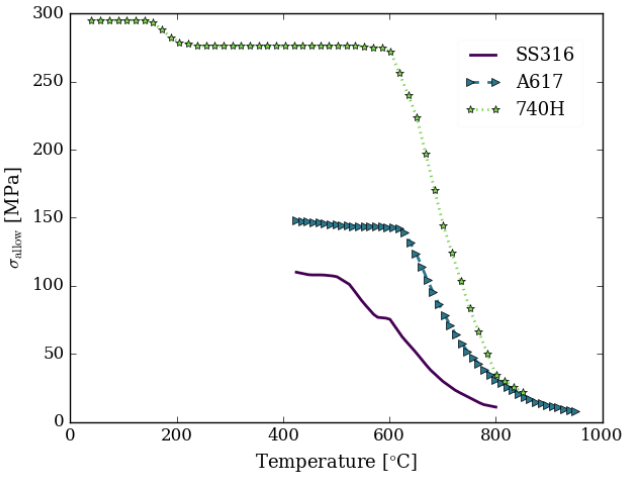

Fig. 6.3: The allowable stress for the selected materials. Source: [131] (SS316), [132] (Alloy 617) and [133] (Alloy 740H).

fluids in this chapter are assumed to be incompressible fluids.

6.2.3 Temperature profile

After solving the external and the internal tube wall temperatures by using the rate of energy balance equation (Eq. 3.2), the rate of external convection equation (Eq. 2.5) and the rate of net energy equations (Eq. 2.6–2.8), the average surface temperatures $\bar{T}_i$ and $\bar{T}_o$ are found by:

$$\bar{T}_i = \frac{1}{2\pi}\int_0^{2\pi} T(r_\mathrm{i},\theta)d\theta \tag{6.2}$$

$$\bar{T}_o = \frac{1}{2\pi}\int_0^{2\pi} T(r_\mathrm{o},\theta)d\theta \tag{6.3}$$

where r_i is the internal radius, and r_o is the external radius. θ is the circumferential component. The internal ($T(r_\mathrm{i},\theta)$) and the external ($T(r_\mathrm{o},\theta)$) temperature fields in the circumferential direction are obtained by solving the energy rate equations in the circumferential direction.

Finally, Logie et al. [72] employ a least-squares fitting algorithm to determine the coefficients in Eq. 6.4 and seeks the Fourier series of Eq. 6.4 at the inner (Eq. 6.5) and outer (Eq. 6.6) surfaces to reduce the effort required to minimise the (integral) sum of the squares of the differences over the entire cross-sectional area of the tube:

$$T_\theta = \sum_{n=1}^{\infty}\left(A_n r^n + B_n r^{-1}\right)\cos(n\theta) + \left(C_n r^n + D_n r^{-1}\right)\sin(n\theta) \tag{6.4}$$

$$T(r_\mathrm{i},\theta) = \bar{T}_i + \sum_{n=1}^{\infty}\left[B'_n\cos(n\theta) + D'_n\sin(n\theta)\right] \tag{6.5}$$

$$T(r_\mathrm{o},\theta) = \bar{T}_o + \sum_{n=1}^{\infty}\left[B''_n\cos(n\theta) + D''_n\sin(n\theta)\right] \tag{6.6}$$

where B' and B'' represent the coefficient B in Eq. 6.4 at inner tube and outer tube, respectively. It notes that the rear of each tube is assumed to be adiabatic. An example of the inner and outer wall temperature profiles around the whole circumference is shown in Fig. 5.10.

6.2.4 Thermoelastic stress

The approach to examining the thermal stress in this study is to only consider the elastic deformation. Yield stress, which causes the plastic deformation, is not considered. After solving the temperature $T(r,\theta)$, thermoelastic stresses are calculated by using the non-axisymmetrically heated tube stress and the dominant axial thermal

stress model [72]:

$$\sigma_{r,\mathrm{th},i} = K_i \frac{\alpha E}{2(1-\nu)} \left[-\ln\frac{r_\mathrm{o}}{r} - \frac{r_\mathrm{i}^2}{r_\mathrm{o}^2 - r_\mathrm{i}^2} \left(1 - \frac{r_\mathrm{o}^2}{r^2}\right) \ln\frac{r_\mathrm{o}}{r_\mathrm{i}} \right] + K_{\theta,i} \frac{\alpha E}{2(1-\nu)} \left(1 - \frac{r_\mathrm{i}^2}{r^2}\right) \left(1 - \frac{r_\mathrm{o}^2}{r^2}\right) \tag{6.7}$$

$$\sigma_{\theta,\mathrm{th},i} = K_i \frac{\alpha E}{2(1-\nu)} \left[1 - \ln\frac{r_\mathrm{o}}{r} - \frac{r_\mathrm{i}^2}{r_\mathrm{o}^2 - r_\mathrm{i}^2} \left(1 + \frac{r_\mathrm{o}^2}{r^2}\right) \ln\frac{r_\mathrm{o}}{r_\mathrm{i}} \right] + K_{\theta,i} \frac{\alpha E}{2(1-\nu)} \left(3 - \frac{r_\mathrm{i}^2 + r_\mathrm{o}^2}{r^2} - \frac{r_\mathrm{i}^2 r_\mathrm{o}^2}{r^4}\right) \tag{6.8}$$

$$\sigma_{z,\mathrm{th},i} = K_i \frac{\alpha E}{2(1-\nu)} \left[1 - 2\ln\frac{r_\mathrm{o}}{r_\mathrm{i}} \right] + K_{\theta,i} \frac{\alpha E \nu}{1-\nu} \left(2 - \frac{r_\mathrm{i}^2 + r_\mathrm{o}^2}{r^2}\right) \tag{6.9}$$

where subscripts r and z are the radial and the axial components, respectively. th notates thermal stress. i is the segment number. E is the Young's modulus in Pa, α is the linear thermal expansion coefficient in K^{-1}, ν is Poisson's ratio. K and K_θ are the axisymmetric and non-axisymmetric geometrical temperature contributions:

$$K_i = \frac{\bar{T}_i - \bar{T}_o}{\ln\frac{r_\mathrm{i}}{r_\mathrm{o}}} \tag{6.10}$$

$$K_{\theta,i} = \frac{r r_\mathrm{i} r_\mathrm{o}}{r_\mathrm{o}^2 - r_\mathrm{i}^2} \left[\left(\frac{B_1^{'} b - B_1^{''} r_\mathrm{i}}{r_\mathrm{i}^2 + r_\mathrm{o}^2} \right) \cos\theta + \left(\frac{D_1^{'} r_\mathrm{o} - D_1^{''} r_\mathrm{i}}{r_\mathrm{i}^2 + r_\mathrm{o}^2} \right) \sin\theta \right] \tag{6.11}$$

where the solution of this equation assumes that only the first two terms are needed.

For thick walled tubes ($\frac{r}{t} < 10$), the stresses due to internal tube pressure $\sigma_{r,\mathrm{pres},i}$, $\sigma_{\theta,\mathrm{pres},i}$ and $\sigma_{z,\mathrm{pres},i}$ are defined as:

$$\sigma_{r,\mathrm{pres},i} = \frac{p r_\mathrm{i}^2}{r_\mathrm{o}^2 - r_\mathrm{i}^2} \left(1 - \frac{r_\mathrm{o}^2}{r_\mathrm{i}^2}\right) \tag{6.12}$$

$$\sigma_{\theta,\mathrm{pres},i} = \frac{p r_\mathrm{i}^2}{r_\mathrm{o}^2 - r_\mathrm{i}^2} \left(1 + \frac{r_\mathrm{o}^2}{r_\mathrm{i}^2}\right) \tag{6.13}$$

$$\sigma_{z,\mathrm{pres},i} = \frac{p r_\mathrm{i}^2}{r_\mathrm{o}^2 - r_\mathrm{i}^2} \tag{6.14}$$

where pr notates pressure stress.

Finally, the equivalent Von Mises stress ($\sigma_{\mathrm{VM},i}$) is calculated as:

$$\sigma_{\mathrm{VM},i} = \sqrt{\frac{(\sigma_{r,i} - \sigma_{\theta,i})^2 + (\sigma_{\theta,i} - \sigma_{z,i})^2 + (\sigma_{z,i} - \sigma_{r,i})^2}{2}} \tag{6.15}$$

$$\sigma_{r,i} = \sigma_{r,\mathrm{th},i} + \sigma_{r,\mathrm{pres},i} \tag{6.16}$$

$$\sigma_{\theta,i} = \sigma_{\theta,\mathrm{th},i} + \sigma_{\theta,\mathrm{pres},i} \tag{6.17}$$

$$\sigma_{z,i} = \sigma_{z,\mathrm{th},i} + \sigma_{z,\mathrm{pres},i} \tag{6.18}$$

Logie et al. [72] showed that the maximum equivalent stress ($\sigma_{\mathrm{VM},i}$) takes place at the crown of each section (where $\theta = 0^\circ$ is defined). Figure 6.4 depicts the local concentrated solar flux distribution in the circumferential direction and the distribution of the inner and outer wall temperature, stress components $\sigma_{r,i}$, $\sigma_{\theta,i}$, $\sigma_{z,i}$ and $\sigma_{\mathrm{VM},i}$ on a section of the tube. Molten salt is considered as the HTF. To validate the stress calculations, stresses determined by Logie et al. [72] are plotted accordingly, labelled as dashed lines. The results from the model used in this study are in good agreement with the results from Logie et al. [72].

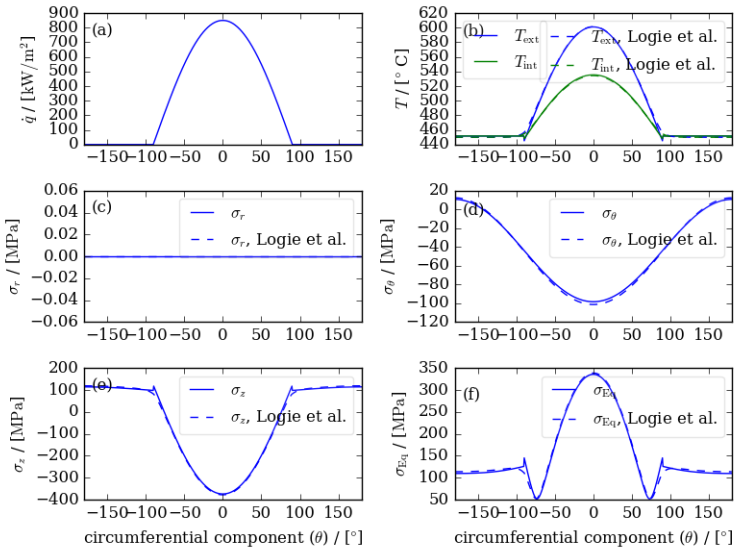

Fig. 6.4: The local circumferential flux distribution (cosine curve) and the corresponding inner and outer wall temperature distributions, thermal stress components $\sigma_{r,i}$, $\sigma_{\theta,i}$, $\sigma_{z,i}$ and $\sigma_{\mathrm{VM},i}$ on the tube with $d_o = 33.4$ mm and $t = 1.65$ mm. DNI = 850 W/m^2, CR=1000.

6.2.5 Creep-Fatigue damage

The total damage on the tubes, D, is calculated as the summation of individual fatigue and creep life fractions (i.e. Linear Damage Summation [181, 182, 183]):

$$D = \sum_{i=1}^{n} \frac{1}{N_d} + \sum_{i=1}^{n} \frac{\Delta t_i}{T_d} \approx \frac{n}{N_d} + \frac{\Delta t}{T_d} \tag{6.19}$$

where the number of on-off cycles to failure per year for fatigue tests n = (365 days − the days where DNIs are too low to operate the receiver) = 317 and the holding time per year in high temperature cycling, Δt = 2624, is the sum of the total hours that receiver operated in 317 days. The number of cycles per year and the total holding hours per year were assumed to be constant over 30 years of operation. These two values (n and Δt) are calculated using the System Advisor Model (SAM) under the solar and meteorological conditions of Alice Springs, Australia [76] (see Fig. 6.5). The minimum $\dot{Q}_{\text{inc}}$ considered in calculating n and Δt was set to 200 MW_t, which means that the operating conditions were not taken into account if the incident power was less than 200 MW_t. N_d is interpolated from the design fatigue strain range data (see Fig. 6.6(a)) for each material (SS316 [131], Alloy 617 [132] and Alloy 740H [133]), and T_d is interpolated from the minimum stress-to-rupture data (see Fig. 6.6(b)) in the same sources. Finally, according to the ASME boiler and pressure vessel code, the total damage D has to be included in the safe region from Fig. 6.6(c) [183] to avoid receiver failure. Therefore, the lifespan is calculated as $\frac{x_2}{x_1}$. The mechanical damage values are based on the creep-fatigue failure data and the mechanical properties of the following alloys: SS316 [131], Alloy 617 [132] and Alloy 740H [133].

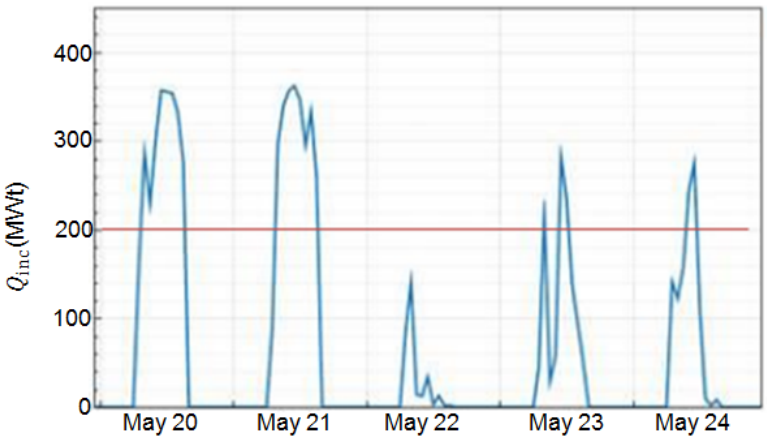

Fig. 6.5: Example of the meteorological conditions in Alice Springs, Australia. Data as supplied by System Advisor Model (SAM) [76]. Red line indicates the minimum Q_{inc} considered to calculate n and Δt.

It is assumed that the material behaviour lies on the elastic region only. No material behaviour in the elastic-plastic region or the stress relaxation is being con-

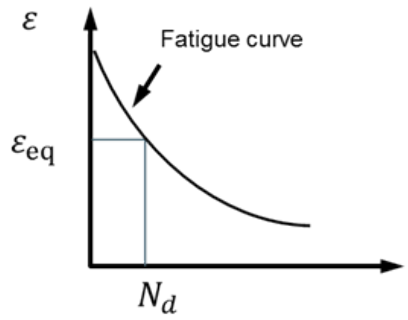

(a) Fatigue damage

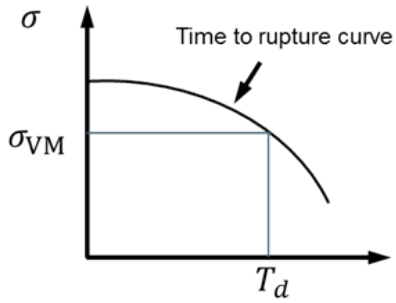

(b) Creep damage

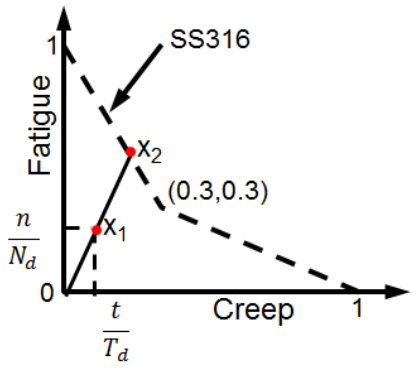

(c) Creep-fatigue interaction damage envelope, as proposed for SS316 [183].

Fig. 6.6: Creep and fatigue lifespan calculation

sidered in this study. However, a study by González-Gómez et al. [74] showed that the damage would be overestimated if only the elastic behaviour is considered, and consequently caused the receiver to have a shorter lifetime and more costs. Nevertheless, the elastic-only damage provides a conservative analysis on the lifetime, which makes it worthwhile in this study. In addition, the emphasis of this study is to compare the performance of variable HTFs on variable materials, using one single model under unified assumptions. Eq. 6.20 is used to calculate the strain components (ϵ_r, ϵ_θ and ϵ_z) from the thermoelastic stress components (σ_r, σ_θ and σ_z) calculated in Section 6.2.4 and the material properties under the assumption of elastic behaviour [133]. The number of cycles to failure (N_d) is a function of temperature and the equivalent strain. T_d is the time to rupture for a pure creep test at the same stress as the hold period. The ASME boiler and pressure vessel code, section III, Division 1 – subsection NH[3] is employed to calculate the T_d for the particular temperature and the equivalent stress (σ_{eq}).

$$\begin{pmatrix} \sigma_r \\ \sigma_\theta \\ \sigma_z \end{pmatrix} = \begin{pmatrix} \lambda+2\mu & \lambda & \lambda \\ \lambda & \lambda+2\mu & \lambda \\ \lambda & \lambda & \lambda+2\mu \end{pmatrix} \begin{pmatrix} \epsilon_r \\ \epsilon_\theta \\ \epsilon_z \end{pmatrix} \tag{6.20}$$

where λ is the Lamé's constant and μ is the shear modulus. More detailed explana-

[3]This table cannot be reproduced here due to copyright restrictions from ASME.

tions can be found in [184]. The properties λ and μ are obtained from the Young's modulus E and the Poisson ratio ν by solving Eqs. 6.21 and 6.22.

$$\lambda = \frac{E\nu}{(1+\nu)(1-2\nu)} \tag{6.21}$$

$$\mu = \frac{E}{2(1+\nu)} \tag{6.22}$$

The equivalent strain (ϵ_{eq}) is used to determine the number of cycles to failure (N_d) for the studied materials. It is obtained from Eq. 6.23 by using the components of the strain found from Eq. 6.20:

$$\epsilon_{\text{eq}} = \frac{\sqrt{2}}{2(1+\nu)}\sqrt{(\epsilon_r - \epsilon_\theta)^2 + (\epsilon_r - \epsilon_z)^2 + (\epsilon_\theta - \epsilon_z)^2} \tag{6.23}$$

And the strain range for each cycle is obtained as:

$$\Delta\epsilon_{\text{eq}} = \epsilon_{\text{eq,max}} - \epsilon_{\text{eq,min}} \tag{6.24}$$

where $\epsilon_{\text{eq,min}}$ is zero when the receiver is under off-sun condition and the stress components are zero.

6.2.6 Component costing

The approach of calculating the capital cost of a receiver is similar to the method adopted by Abengoa Solar [185]. In this study, the capital cost of a receiver (C) is defined in three terms, as follows:

$$C = mc_{\text{m}} + n_{\text{tubes}}c_{\text{F}} + C_{\text{A}}, \text{ where } C_{\text{A}} = A_{\text{ref}}c_{\text{A}} + C_{\text{o}} \tag{6.25}$$

where c_{m} is the cost of the tubes based on the tube material and mass, in USD/kg; c_{F} is the panel fabrication cost in USD/tube; C_{A} is other costs of the receiver in USD, including the cost of design, manufacturing and supplying, while c_{A} is in USD/m^2; and C_{o} is the design point cost.

The Abengoa 910 MW_{th} molten salt receiver has been referred to as a baseline to estimate the cost of the receiver. This 20 m (diameter) $\times$ 25 m (height) receiver had a cost of 51.55 M $\cdot$ USD (i.e. C) in 2008. The Abengoa report indicates that the total cost of the tube material (i.e. mc_{m}) and that of the tube fabrication (i.e. $n_{\text{tubes}}c_{\text{F}}$) was 1.89 M $\cdot$ USD and 1.42 M $\cdot$ USD in 2008, respectively. The fabrication cost consists of the costs for welds, nozzle and tube clips. This large-scale receiver consists of 1120 tubes. Therefore, the cost of fabrication for each tube was 1,268 USD in 2008, which is equivalent to 1,748 USD in 2021 with the consideration of an assumed indexation

rate of 2.5%p.a. [186]:

$$C_{2021} = C_{2008}(1 + 2.5\%)^{(2021-2008)} \tag{6.26}$$

Therefore, C_{A} =$(51.55 - 1.89 - 1.42 = 48.24)$ M $\cdot$ USD in 2008, which is equivalent to 66.50 M $\cdot$ USD in 2021.

The cost of this large-scale baseline receiver is then scaled down to that of a 100 m^2 receiver, in order to match an average receiver size in the study.

The function of cost in SAM (C_{SAM}) is applied here [76]:

$$C_{\mathrm{SAM}} = C_{\mathrm{ref}} \left(\frac{A}{A_{\mathrm{ref}}} \right)^{\mathrm{SE}} \tag{6.27}$$

where C_{ref} is the receiver reference cost (i.e. C_{ref} = C_{A}); the scaling exponent of the receiver cost (SE) is 0.7 [76]. Substituting $A = 100$ m^2 into the above equation (Eq. 6.27), then $C_{\mathrm{SAM}} = 9.67$ M $\cdot$ USD. This equation, however, indicates that the cost of the receiver is nil if the receiver size is approaching to 0 m^2, as shown in Fig. 6.7, which might not be accurate as some other costs still exist. Hence, the equation of the tangent at (100, 9.67) on the curve of C_{SAM} is applied to find the C_{o} at $A = 0$ m^2:

$$y = 0.068x + 2.90 \tag{6.28}$$

Hence,

$$C = (2.90\mathrm{M} \cdot \mathrm{USD}) + \left(\frac{0.068\mathrm{M} \cdot \mathrm{USD}}{m^2} A \right) + mc_{\mathrm{m}} + n_{\mathrm{tubes}} c_{\mathrm{F}} \tag{6.29}$$

where m denotes the mass of tubes in kg, and the term mc_{m}, is calculated as:

$$mc_{\mathrm{m}} = \left(\rho \frac{\pi}{4} \left(d_o^2 - d_i^2 \right) L \right) n_{\mathrm{tubes,total}} c_{\mathrm{m}} \tag{6.30}$$

where the density ρ and the cost of the materials c_{m} [187] are listed in Table 6.1[4].

Table 6.1: The density and the cost of the materials.

	Alloy 740H	Alloy 617	SS316
density ρ (kg/m^3)	8,050	8,360	7,750
material cost (USD/kg)	85.7	76.1	6.5

[4]The material costs are provided by the team member in the project of "CSP Gen 3: Liquid-Phase Pathway to SunShot [188]. Even though the data is not in that report, but rather was also used in the calculations that report reports.

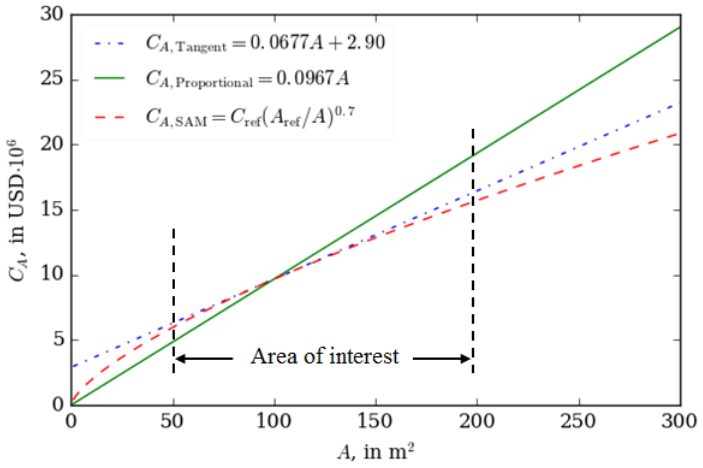

Fig. 6.7: The function of cost defined using three analytical methods.The area of interest in this study is 50–200 m^2.

6.3 Optimisation method

Genetic Algorithms (GAs) are optimisation techniques used to solve nonlinear optimisation problems. They have been applied to a range of fields, such as medicine, geotechnics, industrial chemical process and solar fuel plants [189, 190, 191, 192]. These random-based evolutionary algorithms are inspired by the theory of biological evolution developed by Charles Darwin and then formulated by Prof. John Holland in 1975 [193].

First of all, a population of "individuals" are determined randomly, where one individual (represented by 'chromosome') is one set of design parameters. Each individual is able to provide a solution to the problem, where in this study, the solution refers to one set of efficiency and cost. One population consists of a number of individuals (i.e. N) and it is called one generation. From the next generation onward, the combinations of two individuals are selected from the previous generation and then have an opportunity to do crossover and mutation to produce offspring. The fitness of all the offspring is evaluated (i.e. efficiency and cost are obtained). In the crossover process, most of the features from the selected designs are taken, depending on the probability of the crossover set. In the mutation process, if a randomly generated number is less than the probability of the mutation, the gene is replaced by this random number in the chromosomes, otherwise the gene (i.e. design parameter) is left. A multi-objective (minimum cost and maximum efficiency) optimisation (i.e. Pareto-frontier) using DEAP [194] is obtained after each generation, where N points have fallen on the Pareto-front curve. Pareto-front is a set of optimised points where no other points in the pool are more superior. In other words, the Pareto-front represents the most efficient designs at their corresponding cost levels in this study. In this way, over a number of generations, an optimised set of offspring, with good features that are inherited from previous generations, is obtained. In this analysis, the

population size N is 40, the number of generations is 200, the percentage of crossover is 0.95 while of mutation is 0.05. The optimised values are discrete.

As a summary to the method of this chapter, the receiver is optimised from the efficiency point of view, by varying the receiver size, flow configuration, tube diameter, and tube wall thickness, for a range of working fluids and tube materials. The performance of a receiver is also estimated based on number of hours per year at design point and damage (cycles per year and creep damage), and hence, the lifetime costs of the receiver can be calculated. Therefore, a Pareto-front relationship between the cost of the receiver for a 30-year lifespan and the second-law efficiency could be obtained.

6.4 Results

The Pareto-front relationship between minimum cost over 30 years and second-law (exergy) efficiency including the pumping losses, has been conducted for the selected fluids with multiple tube materials after optimising the receiver aperture area, the Gaussian spot size, the inlet and outlet fluid temperatures, the tube diameter, the wall thickness, the number of banks and the flow configuration. Only material damage in the elastic region is considered in this study, to provide a conservative damage analysis of the material. The selected tube materials are SS316, Alloy 617 and Alloy 740H. All these variables and their ranges considered in this study have been summarised in Table 6.2.

Table 6.2: The variables and their ranges considered in this study.

Variables	Range
aperture area (m^2)	50–200
Gaussian spot size σ (m)	0.5–10
number of banks	1–10
tube diameter	17 standard tube sizes from 10.3 mm to 273.1 mm, in ASME B36.10 [147]
wall thickness	"STD", "EXTRA STRONG" and "XX STRONG" corresponding to each tube size used, in ASME B35.10 [147]
flow configuration	"edge-to-edge", "edge-to-centre" and "centre-to-edge"
tube materials	SS316, Alloy 617 and Alloy 740H
fluid temperature range	molten salt: 290–565°C; sodium: 150–750°C; chloride salt: 400-800°C

The Pareto-front relationships, shown in Fig. 6.8 indicates the important impacts of material selection on the efficiency and cost of the receiver over 30 years. From the HTF selection point of view, the Pareto-front diagrams showed that liquid sodium outperformed other HTFs due to its better internal heat transfer, which obtained

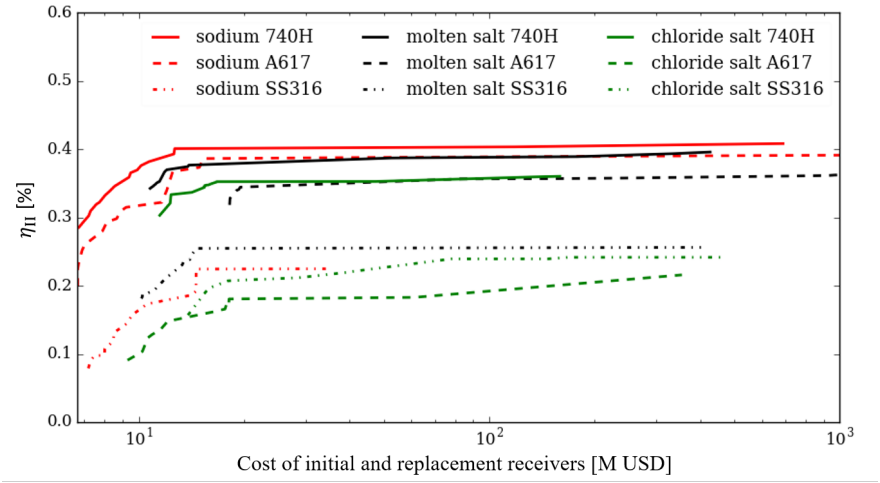

Fig. 6.8: The Pareto-front relationship between the cost of the receiver and the second-law efficiency for the selected fluids and the tube materials. The cost is for a 30-year operational life, and includes the original as well as any needed replacement receivers. All three HTFs have been examined for each tube material.

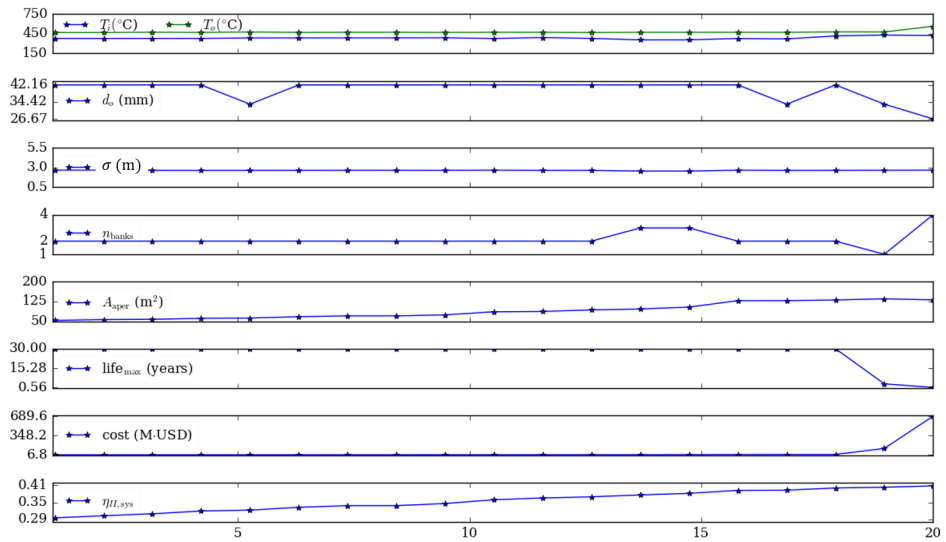

Fig. 6.9: The details of the Pareto-front points for a sodium receiver using Alloy 740. Only the first 19 points are plotted here, as the remaining 21 points (i.e. in total there are 40 points) result in a very low lifespan and consequently, excessively high costs. The tube wall thickness was not included in this figure as the result showed a consistent value of 1.65 mm for all the cases. For the same reason, the flow configuration was not included, "edge-to-centre" was indicated to be the consistent flow configuration choice for all the cases.

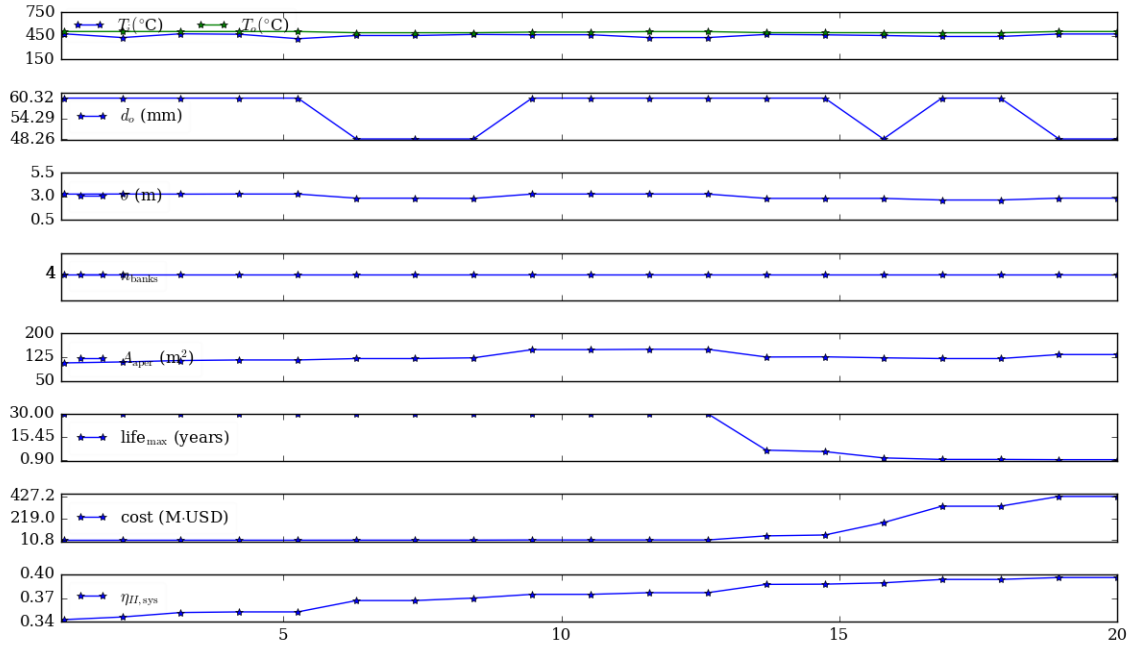

Fig. 6.10: The details of the Pareto-front points for a molten salt receiver using Alloy 740. Only the first 20 points are plotted here. The tube wall thicknesses were always shown to be 1.65 mm. The "edge-to-edge" flow configuration was the result of the flow configuration for all the cases.

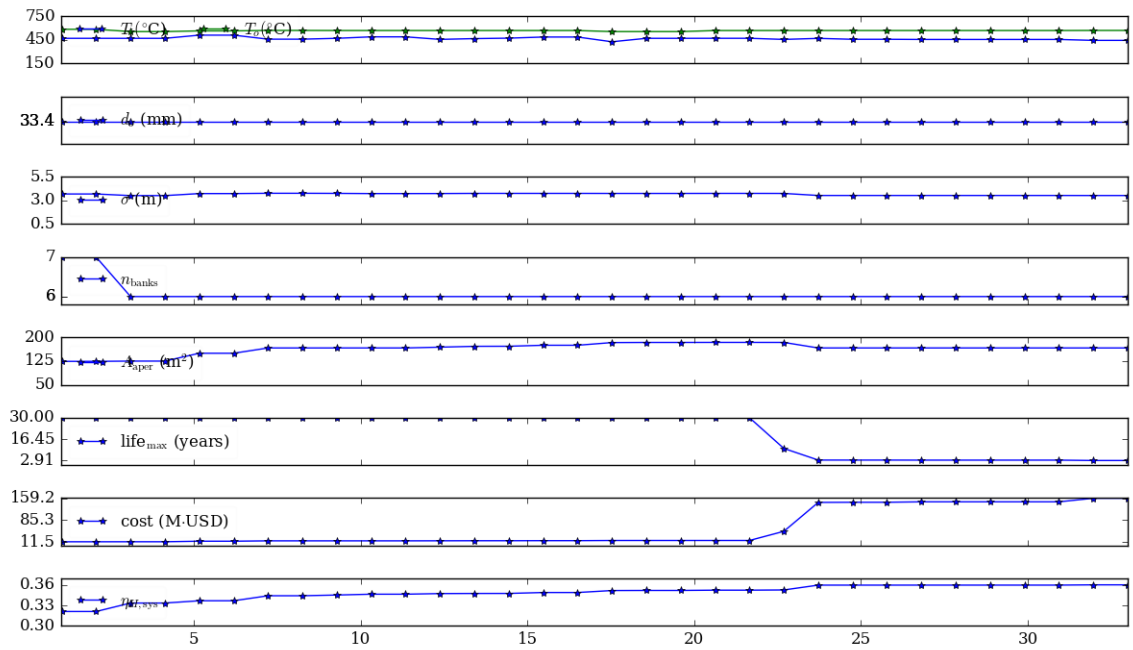

Fig. 6.11: The details of the Pareto-front points for a chloride salt receiver using Alloy 740. Only the first 33 points are plotted here. The tube wall thicknesses were always shown to be 1.65 mm. The "edge-to-edge" flow configuration was the result of the flow configuration for the first 11 points, while the "centre-to-edge" flow configuration was the result for the remaining 22 points.

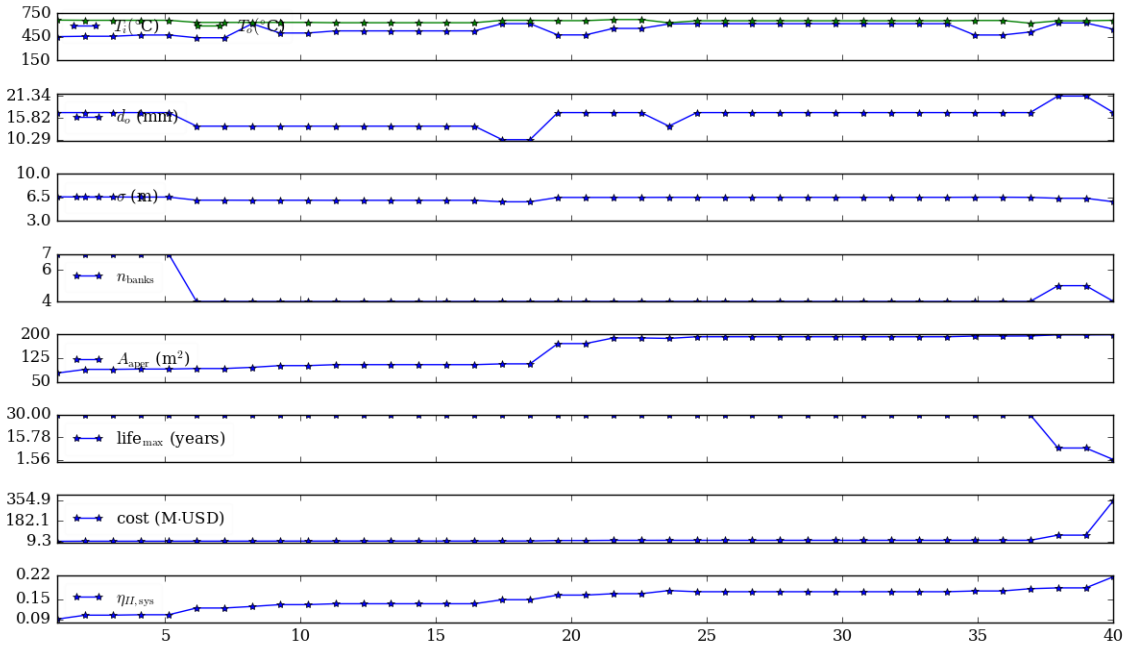

Fig. 6.12: The details of the Pareto-front points for a chloride salt receiver using Alloy 617. The tube wall thicknesses were always shown to be 1.65 mm. "centre-to-edge" was the result of the flow configuration for all the points.

a consistent conclusion as Chapter 2. One exception spotted was when SS316 was selected as the tube material. The results showed that molten salt could result in slightly higher second-law efficiency than sodium. From the tube material selection point of view, Alloy 740H improved the Pareto curve by at least 5% for all three working fluids, subject to the current assumed costs.

The detailed results for all the studied parameters on the Pareto-front curves for each fluid are shown in Fig. 6.9 (sodium), Fig. 6.10 (molten salt) and Fig. 6.11 (chloride salt), using Alloy 740H as an example for the material. The results show that longer paths (i.e. more n_{banks}) arose in optimised receiver designs for molten salt and chloride salt, as compared to sodium, to compensate their poorer internal heat transfer. Fig. 6.13(a) shows that the thermal conductivities of molten salt and chloride salt were very close and they were two orders of magnitude lower than sodium, which results in a large temperature difference between the HTF and the wall. Hence, boosting the mass flow rates was necessary to improve the internal heat transfer for these two fluids. For chloride salt, even smaller tubes were required to increase the flow velocity. The minimum available tube wall thickness (i.e. 1.65 mm) from ASME B36.10 [147] was indicated as the best choice for all the fluids in all Pareto-front points, due to the reason that the temperature difference between inner and outer walls was minimised with thinner tubes, and consequently resulted in longer receiver lifespan due to lower external wall temperatures. It was also found that the optimal temperature ranges for all three fluids, using Alloy 740H as the tube

material, were below 550°C, with small ΔT (less than 100°C) between inlet and outlet. It was subjected to the peaky Gaussian-like flux distribution, which ended up pushing the optimal temperatures down on Alloy 740H receivers, without sacrificing too much on spillage loss by reducing the peak flux. When it came to Alloy 617, the optimal temperature ranges for chloride salt receivers (450°C–700°C) were much higher than that of Alloy 740H (see Fig 6.12), since the optimal Gaussian spot sizes were much larger than that of Alloy 740H, which resulted in reduced peak fluxes but larger spillage losses, and consequently caused less efficient receivers. As a result, the trade-offs between spillage and working temperature ranges were identified through the optimisation process for different materials and fluids.

From an efficiency point of view, the ranking for the flow configurations on a receiver with a Gaussian-like flux distribution (i.e. peak flux in the centre of the receiver) was "edge-to-centre" (i.e. the most efficient), followed by "edge-to-edge", and lastly was "centre-to-edge" (i.e. the least efficient), as concluded in Chapter 3 (see Fig. 3.7). However, that chapter did not consider the effects of thermal stress and material constraints. The "edge-to-centre" flow configuration caused the highest external wall temperatures when compared to others due to the combined effect of hot fluid and peak flux at the centre of the receiver. The optimisation approach in this study was to figure out the most efficient but cheapest receiver configuration. Due to the better internal heat transfer characteristic of sodium, the "edge-to-centre" flow configuration could always be chosen to achieve high second-law efficiency and low cost on sodium receivers, as the higher external wall temperatures would not affect the material lifespan that much. "edge-to-edge" should be applied on molten salt receivers to moderate the external wall temperatures without reducing the second-law efficiencies too much. However, it seemed that the "centre-to-edge" flow configuration had to be considered for the chloride salt receivers to avoid excessively high external wall temperatures, due to worst heat transfer (refer to Fig. 6.13(a)). This was one of the reasons that chloride salt performed the worst among all three fluids.

The results in Fig. 6.8 also show that only Alloy 740H was an appropriate material for the chloride salt receivers in this study, as Alloy 617 and SS316 resulted in very low second-law efficiencies (below 25%). Low thermal conductivities might not be an issue for molten salt in relation to finding a relatively suitable tube material with reasonable performance in efficiency, as it is subjected to operating at low temperature range (i.e. 290–565°C). However, when it comes to chloride salt, which is supposed to operate at high temperature range (i.e. 400–800°C), even higher temperatures on the wall result due to low thermal conductivity. In addition, the viscosity of chloride salt is the highest in comparison to the other two HTFs, as shown in Fig. 6.13(b), which leads to a large pressure drop and consequently, a large von Mises stress. Fig. 6.12 shows that larger Gaussian spot size σ had to be considered, in order to reduce the peak flux on the chloride salt receiver and to make Alloy 617 a feasible material. The detailed study on the trade-offs between σ and efficiency η_{I} have been conducted in Section 3.3.1.1 and shown that larger σ resulted in lower

first-law efficiency due to larger spillage. The optimised results in this chapter validated this conclusion as Alloy 617 resulted in very low efficiencies due to the large σ, which resulted in large spillage loss. All these factors make Alloy 617 and SS316 inappropriate to co-operate with chloride salt due to lower stress-to-rupture values at elevated temperatures when compared to Alloy 740H. In addition, Alloy 617 is more expensive than SS316, which makes it least favoured to be applied on chloride salt receivers. It is worth noting that the replacement of the full receiver was considered over 30 years (i.e. $C_{\text{tot,30yrs}} = \frac{30}{\text{life}_{\text{max}}} C$), not only of the receiver panels. It would over-estimate the total receiver cost, especially for the cheaper material such as SS316, due to some unnecessary replacements on structural framing, stairways, engineering management, etc. This approach would weaken the price advantages of those cheap materials, since the panel cost would only consist of less than 20% of the total receiver cost. Nevertheless, this study provided numerous valuable findings on the trade-offs between different parameters through the extensive optimisation process for different working fluids with different tube materials, including the optimal Gaussian flux distribution, the optimal working fluid temperature ranges, the optimal tube size, the optimal flow configuration, receiver lifespan due to material limits, and so on.

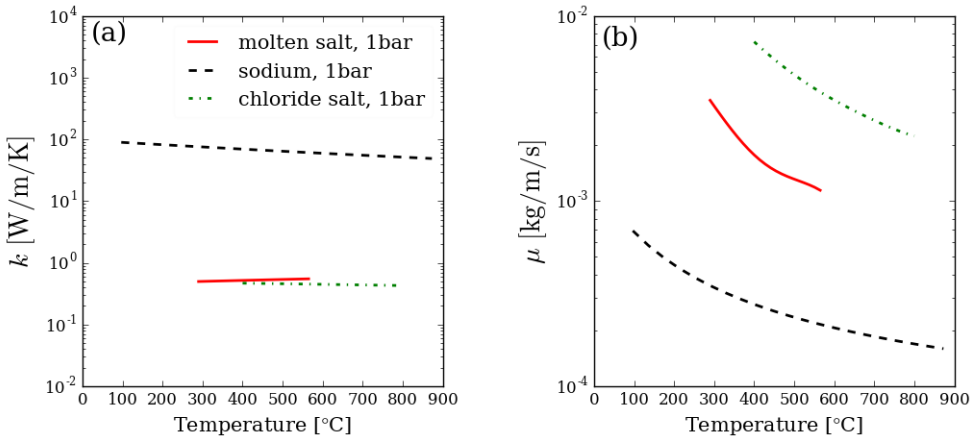

Fig. 6.13: Thermophysical properties of three selected HTFs as functions of temperature. (a) thermal conductivity; (b) viscosity. Source for the chloride salt was obtained in personal communications [195], where the date was very similar to, and consistent with other published sources [196].

The lifespan is likely to be very sensitive to the receiver design as a small change in the receiver design may cause a big difference in lifespan, as spotted from the second last two points in Fig. 6.9. A closer study on this finding is conducted, using Alloy 740H as an example. In order to figure out the causes of the difference in the resulting lifespan, first of all, the input parameters for two cases (i.e. the second last two points in Fig. 6.9: (S) lifespan = 3.32 years; (L) lifespan = 30 years) are listed in Table 6.3. In general, larger spot size would result in more spillage loss, as concluded in Section 3.3.1.1. However, the trade-off between a much larger receiver and slightly larger spot size results in less spillage loss in Case S, when compared to Case L. The

minimum lifespan occurs on the right centre of the receiver (where the red star is located) due to the highest flux falling on that segment, which results in the highest external wall temperature (see Fig. 6.14). Fig. 6.15 demonstrates the detailed flux profiles, temperature profiles, von Mises stresses and the resulting lifespan of that particular tube segment, location of the lowest lifespan across the whole receiver for each case. The maximum von Mises stress occurs on the crest of the tube ($\theta = 0°$), which is consistent with the study by Logie et al. [72].

Table 6.3: Detailed analysis on the selected two cases that result in different lifespan (i.e. (S) lifespan = 3.32 years; (L) lifespan = 30 years) . HTF: sodium; tube material: Alloy 740H; $\dot{Q}_{inc} = 80$ MW.

Input parameters

	T_{in} °C	T_{out} °C	ΔT °C	d_o mm	t mm	σ m	n_{banks} –	A_{aper} m^2	flow conf. –
S	429.34	476.28	46.94	33.4	1.65	2.66	1	135.20	edge to centre
L	356.19	471.00	114.81	42.16	1.65	2.56	3	96.40	centre to edge

Results

	$\dot{q}_{max}$ kW/m^2	$\dot{Q}_{spil}$ MW	$\dot{Q}_{inc}$ MW	$\dot{Q}_{abs}$ MW	$\dot{Q}_{net}$ MW	$\dot{X}_{sun}$ MW	$\dot{X}_{spil}$ MW	$\dot{X}_{inc}$ MW	$\dot{W}_{net}$ MW	$\dot{m}$ kg/s	$\eta_{II,sys}$ %
S	1633.12	4.39	75.61	73.16	67.48	74.61	4.10	70.51	30.11	446.44	40.36
L	1797.58	8.40	71.60	69.28	65.53	74.60	7.83	66.78	28.06	1132.26	37.61

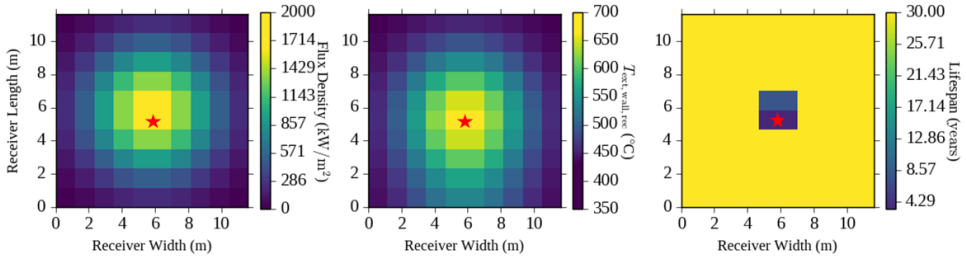

(a) Case S: life$_{max}$ =3.31 years. $\dot{q}_{max} = 1633.12$ kW/m^2

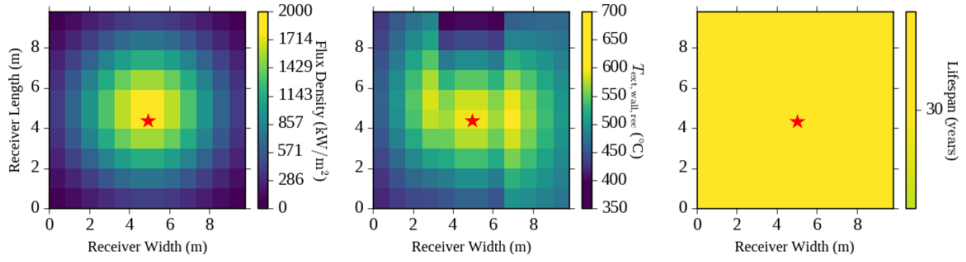

(b) Case L: life$_{max}$ =30.0 years. $\dot{q}_{max} = 1797.58$ kW/m^2

Fig. 6.14: The flux distribution (left), the external wall temperature on the crest (middle) and the localised life$_{max}$ (right) for the two cases (S and L) listed in Table 6.3. Red stars indicate the location where the lowest lifespan occurred in the receiver. The yellow-only colour bar on the bottom right figure indicates the minimum lifespan was 30 years in this scenario.

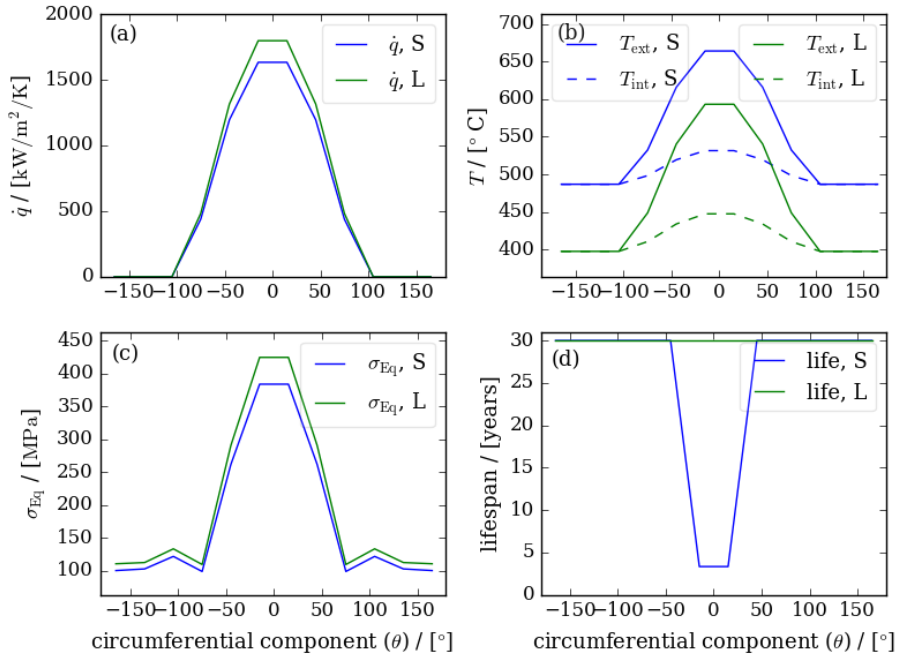

Fig. 6.15: The analyses of the stress and the lifespan on the particular tube segment in the circumferential direction, where the lowest lifespan is occurred (refers to the location of red stars labelled in Fig. 6.14).

From the tube material point of view, the results in Fig. 6.8 show that Alloy 740H performs better than other materials, for every HTF considered. It is found that, in this study, creep damage dominates the failure mechanism, when compared to the fatigue damage, which has also been verified by Barua et al. [133]. A case study has been conducted here to compare the intrinsic difference for different materials, where Case L in Table 6.3 was selected for this study. In Case L, it was found that Alloy 740H was capable of providing a 30-year lifespan for the receiver. By using the same inputs as Case L in Table 6.3, except replacing Alloy 740H with Alloy 617, it was found that Alloy 617 could only offer a receiver lifespan of 0.48 year, which was significantly lower. Key results for the particular receiver segment which offered the lowest lifespan, are summarised in Table 6.4 and the corresponding minimum stress-to-rupture curves at 593.35°C, as a function of time-to-rupture in hours are plotted in Fig. 6.16. The values are interpolated using tables of minimum stress-to-rupture values in Source [132] and [133] for Alloy 617 and Alloy 740H respectively. The black dot on the red curve indicates the time to rupture of Alloy 617 when $\sigma_{VM} = 382.12$ MPa, which provides a total holding time of 1261.81 hours. For Alloy 740H, however, the creep damage would not play a role in limiting the receiver lifespan to a value smaller than 30 years, as the most critical stress (i.e. 424.62 MPa) was even lower than the stress-to-rupture value (i.e. 590.68 MPa) at 30,000 hours, nor the fatigue damage as it is the second-order effect.

Table 6.4: Detailed results for comparing the difference between Alloy 617 and Alloy 740H. The assumed holding time per year in high temperature cycling $\Delta T = 2624$.

	$T_{ext,wall}$ °C	σ_{VM} MPa	time to rupture hours	lifespan years
Alloy 617	593.35	382.12	1261.81	0.48
Alloy 740H	593.35	424.62	>30,000	30

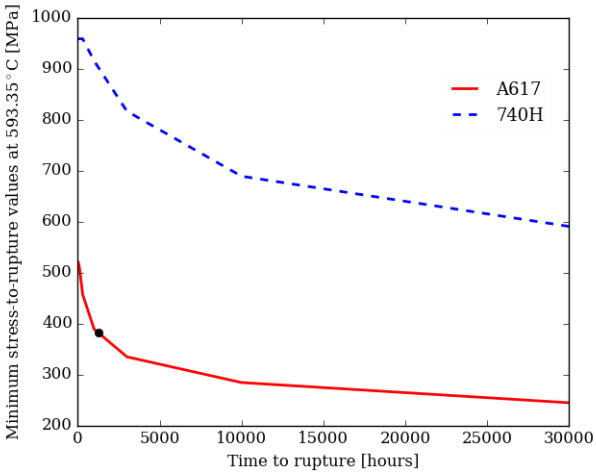

Fig. 6.16: Expected minimum stress-to-rupture values at 593.35°C, as a function of time-to-rupture in hours for Alloy 617 and Alloy 740H.

6.5 Conclusions

An extensive optimisation process has been conducted to examine the relationship between the performance of the receiver and the corresponding costs for a range of working fluids and tube materials. First of all, the approach to modelling a receiver was to establish a 1D model to calculate the efficiencies of a tubular receiver, where the performance of the tube has been considered axially and circumferentially. Inputs were the flux map determined using Gaussian distribution approach, the receiver size, the inlet and the outlet fluid temperatures, the tube diameter and thickness, the number of banks and flow configuration. These variables were then optimised using a genetic algorithm method to obtain a Pareto-front relationship between the performance of the receiver and the cost, where the cost is the total amount of the expenses over 30 years with the replacements in relation to the receiver lifespan.

Sodium performed the best due to its prominent internal heat transfer characteristic, when compared to molten salt and chloride salt. For molten salt and chloride salt, longer flow paths were required to improve internal heat transfer and, consequently, to reduce thermal losses. The trade-offs between the operating temperatures of the working fluid and the Gaussian spot sizes of the flux profile led to an optimised receiver (from the receiver efficiency point of view) that should have relatively low operating temperatures (400–600°C), otherwise, the flux density has to be reduced in order to lower the external wall temperature, which however would increase the spillage loss and consequently, reduce the efficiency. "edge-to-edge" and "centre-to-edge" flow configurations have to be employed on the molten salt and chloride salt receivers respectively to avoid excessively high external wall temperatures, even though they resulted in lower second-law efficiencies when compared to the "edge-to-centre" flow pattern. This is a meaningful result as in discussions on the optimisation of systems, they often assume certain power block or certain temperature requirements. This work pointed out that perhaps a lower working fluid temperature range, would get more out the receiver than the gain from the high temperature power block.

Without considering the material damage in the elastic-plastic region or the stress relaxation, Alloy 740H was the best material choice among the selected options (i.e. Alloy 740H, Alloy 617 and SS316), practically to align with the Gaussian flux distribution and the costs assumed in this study. The drawback of adopting Gaussian-like flux distribution was the localised hot spot, limiting the performance of the receiver, and more importantly, causing the failure of the tube in a short-time period. One approach to releasing tension at the hot spots was to consider a fully realistic flux distribution from Monte-Carlo ray-tracing and the aiming strategy. The idea of a linear ramp distribution was a good demonstration of showing the benefits of avoiding hot spots on the receiver, even though it was not a realistic flux pattern, which has already been discussed in Chapter 3. Another approach to extend the lifespan of the tube is to consider using thicker tubes or different materials in the highest flux cen-

tral region of the receiver [70]. Alloy 740H was capable of withstanding high stress before rupturing, especially at elevated temperatures. Such a characteristic makes it suitable for all HTFs, and more durable to be used on the tubular receivers. SS316 was cheap but very unlikely to be able to be employed under current circumstance (e.g. Gaussian-like flux distribution). These conclusions, however, were based on the costs which assumed that the total receiver cost over 30 years of service was the multiplier (i.e. $\frac{30}{\text{life}_{\text{max}}}$) of the total receiver cost with certain lifespan. For future work, only the necessary parts of the receiver (e.g. receiver panels) should be considered for replacement, so that cheaper materials would be given more chance to be re-evaluated, such as SS316. An appropriate cost model should be applied for deciding the best working fluid and the best tube material, since the cost of the fluid, cost of the heat exchanger and cost of the storage would all affect the final decisions.

Chapter 7

Exergy analysis of the impact of a heat exchanger on performance of an integrated sodium–salt CSP plant[1]

7.1 Introduction

The conclusions in Chapter 2 and Chapter 6 all showed that sodium was the best working fluid candidate. However, the sodium receiver has to be deployed with a heat exchanger, since it is not an appropriate TES medium, due to its high cost and low volumetric heat capacity, when compared to salt. Two options considered here for reaching higher temperatures are direct heating of a high-temperature chloride salt (46.0wt% MgCl2–38.9 wt% KCl–15.1 wt% NaCl), and indirect heating via sodium and an associated sodium–salt heat exchanger. The aim of this chapter is to examine the exergy performance of these two alternatives, and to identify which configuration is more effective in the final supply of heat to the power block, and to gain some insight into the reasons of why one performs better than the other in terms of exergy. The conceptual designs for the CSP tower system with sodium and salt as the receiver working fluid are illustrated in Fig. 7.1. A sodium–salt heat exchanger is required for the indirect case (Fig. 7.1(a)). However, high-temperature chloride salt (500–720°C) is suitable to be used both as the receiver working fluid and as the sensible thermal energy storage (TES) medium (Fig. 7.1(b)). Finally, the sCO_2 Brayton cycle is coupled in both cases, to achieve a high thermal-to-electricity efficiency at elevated temperature [197].

[1]This chapter incorporates material from: Zheng, M. Guccione, S. Fontalvo, A. Coventry, J. and Pye, J. Exergy analysis of the impact of a heat exchanger on performance of an integrated sodium–salt CSP plant. In *Proceeding of the 26th SolarPACES Conference*, Albuquerque, New Mexico, USA. 28 Sep - 2 Nov 2020.

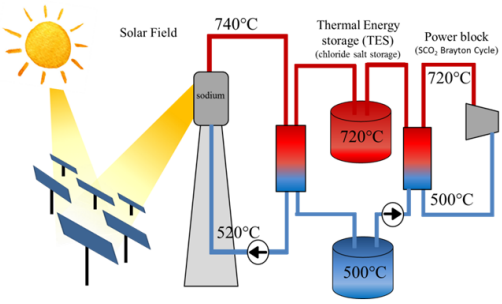

(a) sodium

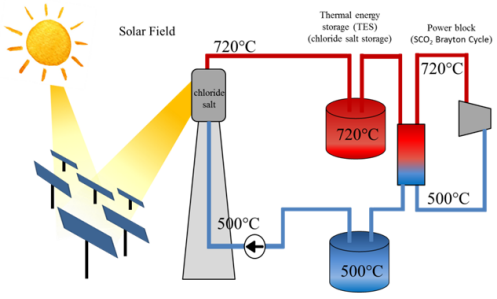

(b) chloride salt

Fig. 7.1: Conceptual designs for Gen3 tower systems with (a) sodium and (b) chloride salt as the receiver working fluid. Sodium receiver consists of 8 flow paths, with two panels (one north-facing and one diagonal south-facing are connected in series) in each path (i.e. in total 16 panels). Chloride salt receiver consists of two flow paths, with 6 panels connected in series (i.e. in total 12 panels).

7.2 Receiver and pump model

The present work takes as its input the designs of the optimised sodium receiver (designed by the Australian National University, ANU [198]) and the optimised salt receiver (designed by the National Renewable Energy Laboratory, NREL [195]), and an optimised sodium–salt heat exchanger design [199]. The design points for each of the specified receivers are summarised in Table 7.1 and Fig. 7.2. To summarise, the sodium receiver is much smaller than the salt one, but it uses larger tubes, 60.3 mm with a thickness of 1.2 mm. The salt receiver has two inlets and two outlets, while the sodium receiver has 8 inlets and 8 outlets and hence, the sodium receiver has a shorter flow path than the salt one. Each bank consists of a number of parallel tubes n_{tubes}, as indicated in Table 7.1.

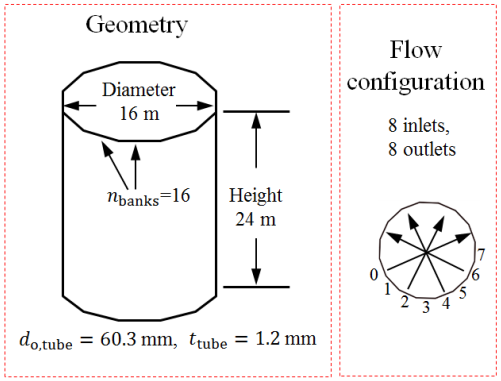

(a) sodium

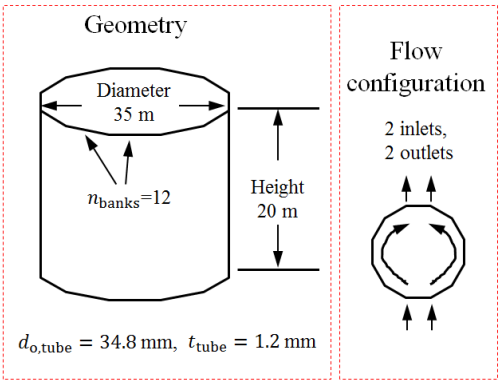

(b) chloride salt

Fig. 7.2: Detailed geometries of the receivers (a) sodium and (b) chloride salt.

The flux distributions on the 'unwrapped' cylindrical sodium and salt receivers are illustrated in Fig. 7.4. The flux that the sodium receiver can withstand, up to 1153.7 kW/m^2, is significantly higher than that for the salt receiver (up to 506.7

Table 7.1: Input parameters of each optimised receiver.

HTF	d_{rec} m	h_{rec} m	$T_{in,rec}$ °C	$T_{out,rec}$ °C	DNI W/m^2	$\dot{Q}_{inc}$ MW	n_{banks}	n_{tubes} per bank	d_o mm	t mm
Sodium	16	24	520	740	980	626	16	52	60.3	1.2
Salt	20	35	500	720	980	713	12	263	34.8	1.2

kW/m^2), by approximately a factor of two, since the high thermal conductivity of sodium increases the internal convection heat-transfer coefficient and consequently reduces the wall-fluid temperature difference, thereby reducing the circumferential temperature difference and allowing us to remain within allowable tube stresses (not covered by this study, though), considering the effects of creep and fatigue [133].

The cylindrical receiver surface was formed by multiple banks of tubes, with several parallel tubes connected in series per bank. The receiver model was solved using the equation-based ASCEND modelling environment with up to 10^4 non-linear equations [152]. It is a steady-state one-dimensional thermal model with discretised flow elements connected in parallel or in series. External radiation, external convection, wall conduction, internal convection and flow friction were considered. Detailed exergy accounting for a receiver with pumping loss was summarised in [197] and is also applied in this study. The flux boundary conditions are taken from Monte-Carlo Ray Tracing calculations from other work (from ANU [198] and NREL [195]). The solar field layout and the main characteristics of these two receivers are fully described by Fontalvo et al. [200]. The detailed exergy accounting was defined in Section 3.2.

Constants used in this study were: surface emissivity $\epsilon = 0.91$; external heat convection coefficients $h_{ext,sodium,rec} = 13$ W/(m^2·K) on tube aperture basis, and $h_{ext,salt,rec} = 10.3$ W/(m^2·K) and wall conductivity, $k_{wall} = 20$ W/(m·K) for a typical tube material, such as Haynes 230 [151]. The difference in external heat convection coefficients were due to different design assumptions made by ANU [198] and NREL [195], respectively. The internal convection correlation suggested by Skupinski [140] was applied on the sodium receiver, while the correlation suggested by Gnielinski [137] was applied on for salt, as explained in [197].

The pressure drop due to friction is considered using Eq. 2.27 and the Darcy friction factor $f_D = (0.79 \ln(\mathrm{Re}_D) - 1.64)^{-2.0}$ is for the turbulent, fully developed and smooth tube.

The momentum balance in each element of the receiver is defined as:

$$p_{o,rec,i} - p_{i,rec,i} = (\Delta p)_{fric,rec,i} - \left(\rho_{o,rec,i} V^2_{o,rec,i} - \rho_{i,rec,i} V^2_{i,rec,i}\right) \tag{7.1}$$

The energy balance of the pump (neglecting the potential energy) is reduced to:

$$0 = -\dot{W}_{\mathrm{PU}} + \dot{m}\left(h_i - h_o + \frac{\mathbf{V}_{\mathrm{i}}^2 - \mathbf{V}_{\mathrm{o}}^2}{2}\right) \tag{7.2}$$

where the pump work $\eta_{\mathrm{is}} = \frac{\dot{m}v_{\mathrm{o}}(p_{\mathrm{o}} - p_{\mathrm{i}})}{-\dot{W}_{\mathrm{PU}}}$ is calculated using an assumed isentropic pump efficiency of 80%; incompressible fluid assumptions are used in this analysis.

The temperatures of hot and cold well-insulated storage tanks are assumed to have constant values. A system-level optimisation for a sodium-salt-sCO_2 system was conducted by Fontalvo et al. [201] to find the lowest levelised cost of energy (LCOE).

7.3 Shell and tube heat exchanger (STHE)

A single-pass shell and tube heat exchanger (STHE) (see Fig. 7.3) was assumed in this study, with an assumed approach temperature of 20°C. It was deployed to take the sodium from the receiver and to heat up the salt that would be stored. The heat exchanger is separately optimised for lowest total annualised cost using TEMA guidelines, in the work by Guccione [199].

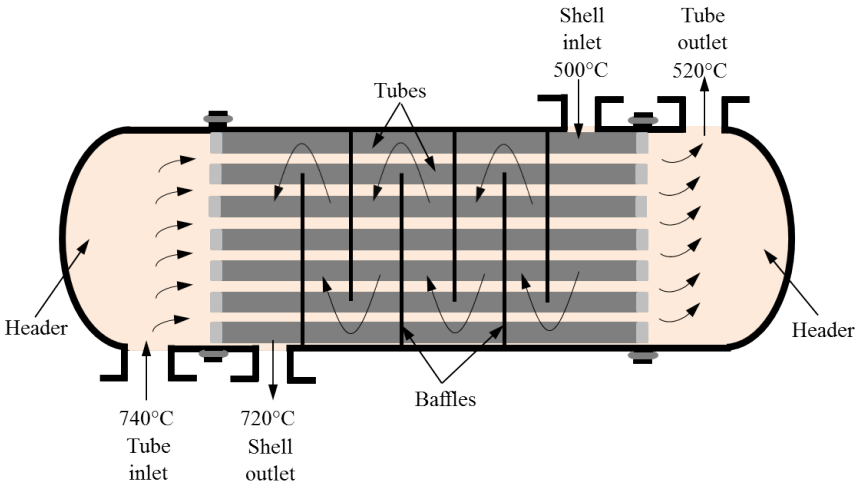

Fig. 7.3: Conceptual design of a single pass STHE. Corresponding shell and tube temperatures are labelled.

The chloride salt is designed as the working fluid on the shell side. The rate of heat in the shell side ($\dot{Q}_{\mathrm{shell}}$) is defined as:

$$\dot{Q}_{\mathrm{shell}} = \dot{m}_{\mathrm{shell}}\left(h_{\mathrm{out,shell}} - h_{\mathrm{in,shell}}\right) \tag{7.3}$$

The convection correlation for the shell side, $h_{conv,shell}$ [202] is applied as:

$$Nu = 0.273 Re^{0.635} Pr^{0.34} \tag{7.4}$$

The outer diameter of the tube is assumed as 22.23 mm, with a wall thickness of 1.1 mm. The velocity of the sodium in the tubes is fixed at 1.3 m/s. The internal convection correlation ($Nu = \frac{h_{int,tube} d_i}{k}$) suggested by Skupinski [140] is applied on the sodium, following the rationale given in [197]:

$$Nu = 4.82 + 0.0185 \left(RePr\right)^{0.827} \tag{7.5}$$

The rate of heat in the heat exchanger ($\dot{Q}_{HX}$) is calculated as:

$$\dot{Q}_{HX} = U A_{tube,tot} F \Delta T_{in} \tag{7.6}$$

where $A_{tube,tot} = n_{tubes} \pi d_o L$, $F = 1$ for single pass and the heat transfer correction factor.

For the counter-flow heat exchanger, the log mean temperature difference is defined as:

$$\Delta T_{in} = \frac{\Delta T_1 - \Delta T_2}{\ln\left(\Delta T_1 / \Delta T_2\right)} \tag{7.7}$$

where $\Delta T_1 = T_{h,i} - T_{c,o}$ and $\Delta T_2 = T_{h,o} - T_{c,i}$.

The overall heat transfer coefficient U (assuming negligible fouling effects) is calculated as:

$$U = \frac{1}{\frac{1}{h_{int,tube}} \frac{d_i}{d_i} + \frac{1}{h_{conv,shell}} J_{tot} + \frac{d_o \ln(d_o/d_i)}{2k}} \tag{7.8}$$

where the heat transfer correction factor, J_{tot} due to the combined effect for baffle cut and spacing, baffle leakage effects and the bundle bypass flow is 0.6 [203].

The rate of exergy destruction for STHE can be calculated from:

$$\dot{X}_{dest,HX} = \left[\dot{m}_{tube} \left(\phi_{i,tube} - \phi_{o,tube}\right) - \dot{m}_{shell} \left(\phi_{o,shell} - \phi_{i,shell}\right)\right] \tag{7.9}$$

where $\dot{m}$ is the mass flow rate, in kg/s. Subscripts i and o represent inlet and outlet states. Subscripts tube and shell represent tube stream and shell stream of the STHE. ϕ denotes the flow exergy as given above and the subscript 0 represents the reference state.

7.4 Results

After integrating the flux map into the thermal model, the corresponding fluid and external wall temperature are shown in Fig. 7.4. Due to the better heat transfer for the sodium, that receiver can withstand at a much higher flux [198]. Fig. 7.5 demonstrates detailed exergy accounting for a sodium–salt system integrated with an sCO_2 Brayton Cycle. The exergetic efficiency for this simplified power block is assumed to be 75% [85]. This Sankey diagram highlights the extra heat exchanger and extra fluid being recirculated in this system. A large amount of exergy is moved through the pumps and the heat exchanger, although the pumping work required is relatively minor. In this particular case, we can obtain 277 MW of electricity output, without considering the time-shifting effect of the storage.

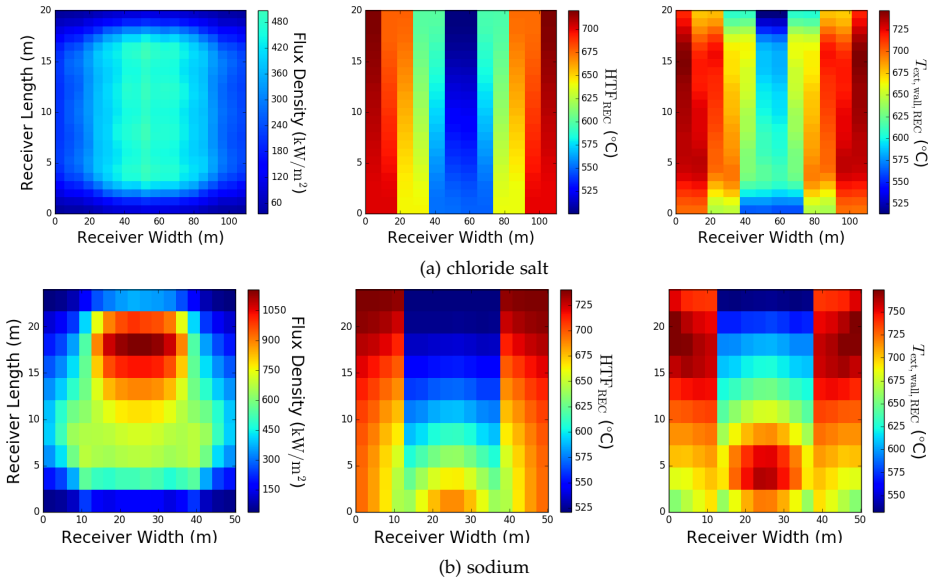

Fig. 7.4: Unwrapped flux and temperature profiles for (a) chloride salt and (b) sodium receivers. The range of the color bar for the flux distribution is 0–1200 kW/m^2; while for the rest of the temperature-related plots are 450–800°C.

The results of the exergy analysis of an integrated sodium-salt receiver and a salt receiver are summarised in Fig. 7.6. The denominators for all equations applied in Fig. 7.6(a) are the total exergy in absorbed energy ($\dot{X}_{\text{abs,sodium}} = 428.73$ MW;$\dot{X}_{\text{abs,salt}} = 484.49$ MW). Owing to the better thermophysical properties of sodium compared to those of salt, the exergy losses in external radiation and external convection from the sodium receiver are higher per area (Fig. 7.6(b)) due to higher surface temperature, but lower in terms of total exergy loss due to the smaller size. Fig. 7.7 allocates the absorbed energy of each receiver element into the corresponding binned external surface temperature ranges. At elevated temperature range (e.g. 750–800°C), 19.81% of energy is absorbed into the sodium receiver, while none is absorbed into the salt receiver. Due to a better internal heat transfer, sodium is capable of absorbing

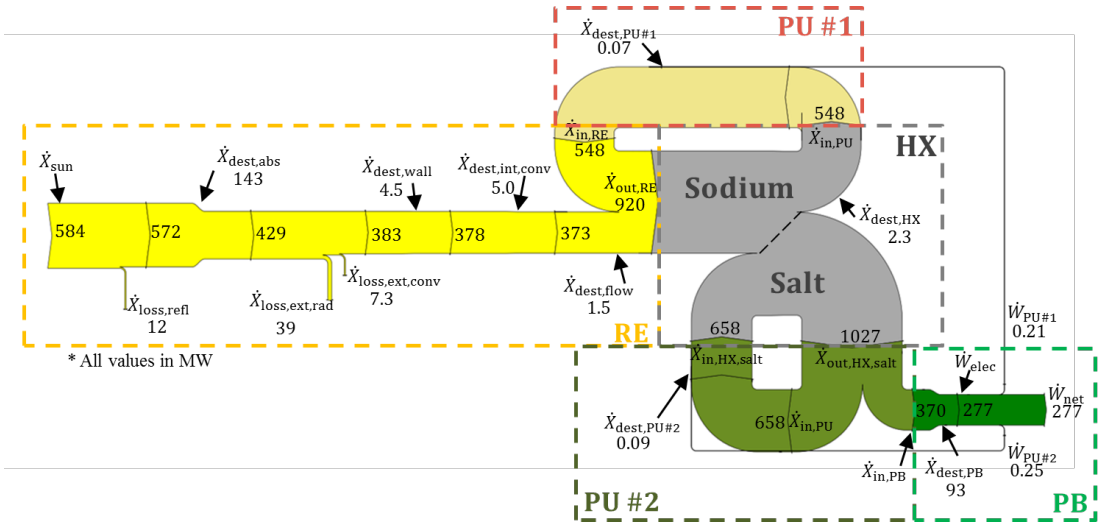

Fig. 7.5: Exergy Sankey diagram for a sodium–salt system integrated with a sCO_2 Brayton cycle with 75% exergetic efficiency.

more flux without causing excessively high temperatures on the tube surface. On the contrary, the flux on a chloride salt receiver has to be limited to avoid tube damages. As a result, sodium has lower heat loss due to higher flux and higher external wall temperature, and lower internal resistance due to high conductivity of sodium. It is worth noting that the exergy destruction in the heat exchanger for sodium–salt system is only 0.54%, which is a relatively small exergy consumption when compared to other components in the receiver. Exergy destructions in pumping due to mass flow across the receiver and the heat exchanger are negligible. The last column in Fig. 7.6(a) summarises that a sodium receiver deployed with a heat exchanger could achieve a 4.37% higher exergy efficiency than a salt receiver. It demonstrates that the system impact of the added heat-exchanger is not nearly large enough to erase the benefits of using sodium in the receiver, when compared to the salt receiver.

7.4.1 Sensitivity to varying DNI

A sensitivity study is carried out to study the effect of varying DNI on receiver performance, and to examine if the receivers perform consistently. As the design point, the DNI is set to be 980 W/m^2. The value of 980 W/m^2 is a close value for good clear sky approximation. In this study, various DNIs are scaled by factors of 1.0, 0.8, 0.6 and 0.4, without further ray tracing or aiming strategy adjustments. The key findings are summarised in Table 7.2 below, with design points highlighted in blue. Exergy loss in external radiation is listed in the table, as it is the main cause to the exergy difference between chloride salt and liquid sodium receivers. Exergy loss in percentage in external radiation is increased for each fluid. In order to maintain the temperature range in the receiver, lower DNI lowers the mass flow ($\dot{Q} = \dot{m} c_p \Delta T$), which results in poor heat transfer in the receiver and consequently relative high

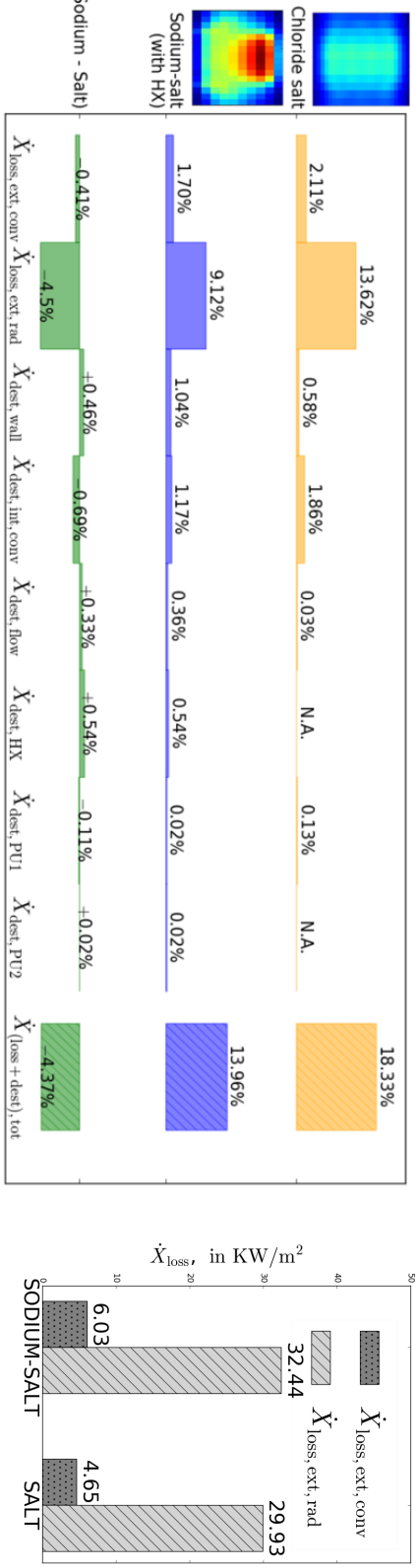

Fig. 7.6: Exergy destruction or loss. Each value is given as a fraction of the exergy of absorbed heat $\dot{X}_{abs,rec}$ for that receiver. (a) Units are in %; while (b) Units are in kW/m^2.

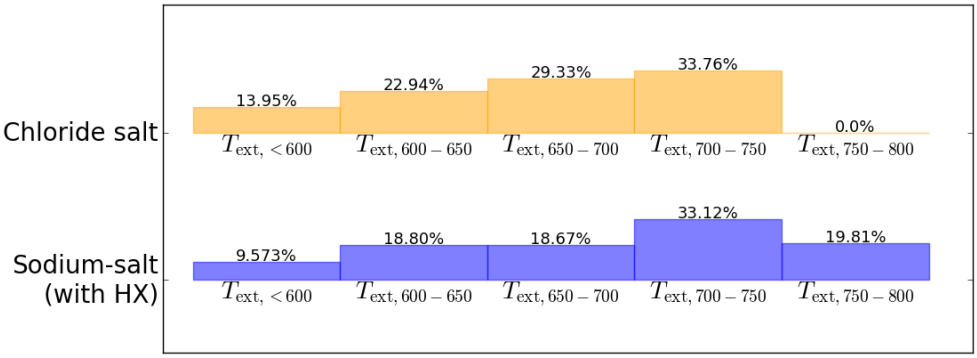

Fig. 7.7: Absorbed energy presented in different binned external surface temperature ranges, in %.

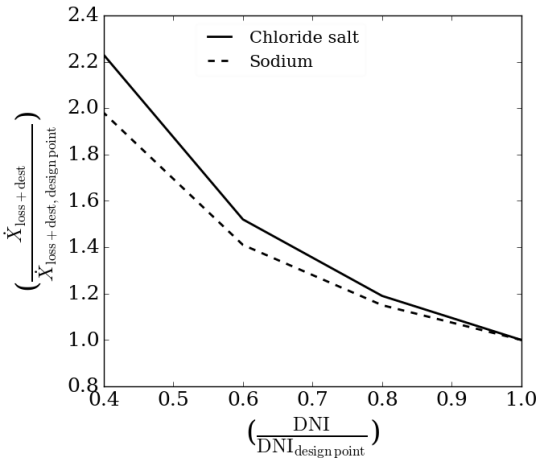

Fig. 7.8: Exergy loss and destruction when conducting the sensitivity study. The values in y axis are the ratios of the total exergy losses at specific DNI to the total exergy losses at design point, where DNI = 980 W/m^2.

external wall temperatures. The non-linear exergy loss in external radiation is due to T^4 effect, as shown in Fig. 7.8. The results in the table consistently show that sodium operates more efficiently than salt, with the performance even higher at lower DNI.

Table 7.2: Varying DNI. $\dot{X}$ losses are in %, where the denominators are the $\dot{X}_{\text{abs,rec}}$ at specific DNI.

HTF	DNI factor	DNI MW	$\dot{Q}_{\text{inc}}$ MW	$\dot{X}_{\text{abs,rec}}$ %	$\dot{X}_{\text{loss,ext,rad,rec}}$ %	$\dot{X}_{\text{loss+dest,rec}}$ %	$\dot{X}_{\text{dest,HX}}$ %	$\dot{X}_{\text{dest,PU,tot}}$ %	$\dot{X}_{\text{loss+dest,tot}}$ %
Salt	1.0	980	712.50	483.23	13.62	18.20	N.A	0.13	18.33
	0.8	784	570.00	368.10	16.87	21.73	N.A	0.08	21.81
	0.6	588	427.50	298.40	22.39	27.84	N.A	0.04	27.88
	0.4	392	285.00	193.30	33.99	40.85	N.A	0.01	40.86
Sodium	1.0	980	625.91	429.12	9.12	13.39	0.54	0.04	13.96
	0.8	784	500.73	342.23	11.17	15.50	0.52	0.04	16.06
	0.6	588	375.55	255.87	14.61	19.21	0.50	0.04	19.75
	0.4	392	250.36	170.14	21.63	27.12	0.45	0.04	27.62

7.5 Conclusion

To conclude, the exergy analysis in this study shows that a sodium receiver with an integrated heat exchanger is 4.37% more exergetic efficient, when compared to a direct chloride salt receiver. The comparison provided here is made after the two designs were optimised in other work, but provides a mechanistic explanation of the relative performance, and a single-model comparison of the two designs. Even more so at lower DNIs, the sodium receiver is more efficient due to its better heat internal transfer and smaller receiver aperture, and the additional exergy destruction in the sodium-salt heat exchanger is not enough to undermine those receiver benefits. Sodium is flammable, and reacts with water, and its safe handling and appropriate design in CSP have been discussed in prior works [204, 205]. The techno-economic analysis for these two receivers was further conducted by Guccione et al. [202]. From an economy point of view, a LCOE of 68.50 USD/MWh was expected to be achieved for the sodium system, against that of 72.7 USD/MWh for the salt system. It was expected that the higher efficiency combined with smaller size will enable sodium–salt systems to achieve lower LCOEs and greater commercialised competitiveness.

7.6 Acknowledgements

This chapter was conducted with funding support from ASTRI, the Australian Solar Thermal Research Institute. Help and support from Craig Turchi, Janna Mar-

tinek, Charles-Alexis Asselineau and Shuang Wang for providing the design points of the receivers are acknowledged.

Chapter 8

Summary and future work

8.1 Summary

This thesis has considered the design and performance of tubular receivers with a range of different working fluids, flux profiles, flow configurations and tube materials, using both numerical modelling and experimental measurement.

In Chapter 2, a range of heat transfer fluids have been compared, using energy and exergy analysis, and varying the tube diameter, tube wall thickness, and tube-bank flow configuration, with the assumption of uniform flux distribution. It was also assumed that there was no external wall temperature variation in the tube circumferential direction. The model has optimised exergy efficiency including pumping work, assuming uniform flux, and neglecting the effects of thermal stresses, circumferential tube temperature variations and cost. Suitable temperature and pressure conditions have been chosen for each fluid, based on a realistic configuration of an applicable thermal energy storage (TES) and power block (PB). The examined heat transfer fluids are molten salt (60% $NaNO_3$, 40% KNO_3), liquid sodium, supercritical carbon dioxide (sCO_2), air, and water/steam. Results showed that liquid sodium at an elevated (540–740°C) temperature range performs best, with a solar-to-fluid exergy efficiency of 60.92%. At a low temperature range (290–565°C), sodium was still marginally superior to molten salt, even after allowing for some exergy destruction in a sodium-to-salt heat exchanger. Water/steam also performs relatively well in the receiver, although the difficulties of integrating it with large-scale storage make it a challenging heat transfer fluid for an integrated system. Using sCO_2 as the heat transfer fluid appears infeasible due to excessively-high pressure stresses on the tubes. Air also appears unsuitable for simple tubular receivers, since poor heat internal transfer results in high losses due to much hotter external surfaces.

The performance of the receiver is strongly constrained by material limits which in turn limit the allowable flux on the receiver. Chapter 3 seeked to understand the benefits which arise at the receiver as a result of adjusting the flux profile, comparing a simple Gaussian 'spot' with a linear 'ramp' pattern, while respecting the upper limit on the allowable peak flux of the molten salt working fluid and the peak fluid

temperature at the wall. The ramp profile performs better, matching material limits more closely over the receiver surface, hence permitting a smaller receiver with lower losses. A $\sim$6% improvement on the receiver efficiency is shown in the linear 'ramp' distribution, when compared to the Gaussian distribution. The concept of the ramp profile releases a meaningful guide to what the upper bound of receiver performance and the flux profile would be, subject to the constraints considered.

The bladed receiver concept has been evaluated in Chapter 4, together with the performance comparison to the flat receiver. This study was involved in the project named "Bladed Receivers with Active Airflow Control (BRAAC)". The optimal performance of a conventional flat receiver was determined first, by varying the flux distributions, receiver sizes, tube diameters, wall thickness and the flow configurations. A fixed heliostat field layout matching the 'PS10' plant in Andalusia was assumed. The best-case first-law efficiency, including optical and thermal losses, is found to be 91.66% for an optimal flat molten salt receiver design. Next, a series of parametric studies were conducted on the bladed receiver, with varying the number of blades, the geometries of the blades, the geometries of the flat section, and the flow configurations. It has been found that larger blades give higher optical efficiency due to light trapping enhancement, but higher external convection loss due to larger area, and consequently, lower thermal efficiency. The internal heat transfer and the pressure drops were comprehensively examined. In addition, the trade-off between spillage losses and thermal losses was investigated, by adjusting the size and the number of the bladed and flat sections. With the bladed concept, the reflective and the external radiation losses are much reduced and as the results, at least a 2.49% improvement in efficiency is seen, when compared to the flat receiver.

Next, a novel 'virtual experimental' approach was utilised to test the large-scale flat and bladed molten salt receivers on the small-scale receivers due to the facility limitation at CSIRO, Australia. In addition, water and air are used as the substitutes of molten salt. Water cases with high flux but low temperature were designed to test the optical performance, while air cases with low flux but high temperature were designed to test the thermal performance. Small-scale water and air receivers were then built and tested at CSIRO, Australia. The experimental data have been collected and analysed. A 0.65 ± 0.008% efficiency gain is found from this on-sun testing. It is acknowledged that this uncertainty is controversial. However, this low uncertainty reflects the fact that a common set of thermocouples were used and subtracted the different, cancelling out the systematic error. In addition, the experimental data were the averaged values over an extended period, cancelling out the random error.

As the final study in relation to the BRAAC project, the simulation results have been reconciled with experimental data in Chapter 4. The nominal loss coefficient K signifying the combined effect of minor pressure losses in the pipe network, and the internal and the external heat transfer coefficients in the models were adjusted, so that the pressure drop and the temperature performance could be matched with

the experimental data to the greatest extent. Further detailed reconciliations were constrained by the limited experimental data. Suggestions to the future experiments of this type have been proposed, regarding to the need for the extra instruments and more extensive testing. The efficiency changes in the updated models are small and consistent with the earlier experimental results. The reliability of the model was validated using experimental data and the result in the updated bladed model shows a 0.40% higher efficiency than of the flat case.

An analysis of alternative tube materials and working fluids on a thermoelastic creep-fatigue model that considers receiver lifetime and replacement has been examined in Chapter 6. The preferred operating temperature ranges considering multiple fluids and tubes have been found to be 400–600°C, through an extensive optimisation process. This study went further in the thermal direction, which was different from assuming fixed operating temperatures in other studies. SS316, Alloy 617 and Alloy 740H were selected in this study, to examine the effects of varying the tube materials on the receiver performance due to the difference in material characteristics. The effects of varying flux distributions, receiver sizes, inlet and outlet fluid temperatures, tube diameters, wall thickness and flow configurations were optimised for a range of working fluids and tube materials. The circumferential tube wall variations were considered as well. Results show that sodium performs the best among all the fluid candidates due to its better internal heat transfer characterises. Alloy 740H has the ability to withstand higher stress at elevated temperatures, while SS316 is unlikely an appropriate material being used in this study, especially under current flux limitation that the Gaussian distribution has a peaky flux in the centre, which results in high external wall temperature, so that the material has to be strong enough to avoid the creep-fatigue failures.

High-temperature receivers are critical for third-generation (Gen3) Concentrating Solar Power (CSP) technology to achieve high system efficiencies, and play the role of converting concentrated sunlight into heat. In Chapter 7, two CSP systems with different working fluids in the receiver have been examined in order to achieve identical supply of heat to the power block: a direct high-temperature chloride salt system and an indirect high-temperature sodium receiver with an associated heat exchanger to heat the same chloride salt. The presented numerical model indicates that the indirect sodium–salt system has a 4.37% higher exergy efficiency than the direct chloride salt system. The exergy destruction in the added sodium-salt heat exchanger is only 0.54%, which does not outweigh the benefits gained due to other phenomena in the sodium receiver, when compared to the direct salt case with no heat exchanger requirement. Even at lower DNIs, the better heat-transfer characteristics of the sodium are responsible for its improved performance compared to salt in the receivers.

Table 8.1: A summary of the key findings in each chapter.

	Key features	Results
Chapter 2	Uniform flux, variable tube sizes and wall thicknesses, variable No. of banks, various working fluids	High-temperature sodium performed the best, $\eta_{sys} = 60.92\%$. It was 5.47% higher than molten salt.
Chapter 3	Non-uniform flux, molten salt, various flow-configurations	The linear "ramp" performed the best, with a 6% improvement on the receiver efficiency.
Chapter 4 and Chapter 5	Novel receiver design – bladed receiver concept, on-sun test, and experimental reconciliation	The bladed receiver obtained 2.49% performance gain, when compared to the flat receiver. Experimentally, The bladed receiver obtained $0.65\% \pm 0.008\% gain$.
Chapter 6	Non-uniform flux, various working fluids, variable tube sizes and wall thicknesses, various tube materials, tube creep-fatigue, receiver cost.	Low-temperature Alloy 740H sodium performed the best, with the Gaussian flux distribution.
Chapter 7	Integrated sodium–salt system vs direct chloride salt system	The sodium–salt system performed 4.37% better than the chloride salt system.

8.2 Future work

Generally, it can be expected that models with more accurate flux profiles will give more accurate estimates of the efficiencies of receivers in operation, and therefore, flux profiles with detailed ray-tracing and aiming strategy should be integrated with the model. In reality, especially for air receivers, rough tubes or tubes with fins [57] could be be considered to improve the heat transfer, as mentioned in Section 1.4.5, due to the poor conductivity of air. In the water-steam receiver, with the associated phase change, the benefit of using more than one tube size can be evaluated. The issue of flow velocity limits due to erosion and corrosion are the major factors in commercial designs, and should be considered in the future.

Minor pressure losses due to bends, valves, losses in headers and/or flow splitters should also be considered practically. The effect of swirl generated in the out-of-plane bends could be incorporated more carefully, as it might be possible that this effect is a benefit, since it is capable of improving the internal heat transfer. This effect reduces the front-to-back temperature difference in tubes and hence, reducing thermal stress and improving receiver life. To what extent it does this, however, is not yet known, and could be further studied. Some experimental tests or a CFD model to simulate one out-of-plane bend, for example, should be involved, in order to accurately examine the hydraulic performance.

Materials and their relative costs are important considerations for comparing a range of working fluids in a more holistic analysis. Material damage in elastic-plastic region and stress relaxation should be considered, in order to accurately examine the lifespan. Costs over 30 years should be considered in a more thorough way, by omitting any unnecessary replacement such as the design costs, the framing costs and other equipment costs, and/or by considering even the panel 'rotation', where panels in high flux regions are 'semi-retired' to the low-flux regions before eventually being worn out. It remains interesting to see if cheap materials like SS316 could perhaps find a role in CSP if they could be more strategically used. Owning to the better stress tolerance, Alloy 740H is expensive, but performs better in the Pareto-front relationship between receiver second-law efficiency and the cost. SS316 is cheap but is not capable of withstanding high external wall temperatures. The cost-performance trade-off is quite complex once these aspects are considered in more detail.

Bibliography

1. Clifford K. Ho and Brian D. Iverson. Review of high-temperature central receiver designs for concentrating solar power. *Renewable & Sustainable Energy Reviews*, 29:835–846, 2014. (cited on pages xv, 1, 3, 4, 5, and 9)

2. J. Coventry, C. Andraka, J. Pye, M. Blanco, and J. Fisher. A review of sodium receiver technologies for central receiver solar power plants. *Solar Energy*, 122: 749–762, 2015. (cited on pages 1 and 8)

3. A Fernández-García, Eduardo Zarza, Loreto Valenzuela, and Manuel Pérez. Parabolic-trough solar collectors and their applications. *Renewable and Sustainable Energy Reviews*, 14(7):1695–1721, 2010. (cited on pages 1 and 10)

4. B Bierman, C Treynor, J O'donnell, M Lawrence, M Chandra, A Farver, P Von Behrens, and W Lindsay. Performance of an enclosed trough eor system in south oman. *Energy Procedia*, 49:1269–1278, 2014. (cited on page 1)

5. Nishith B Desai and Santanu Bandyopadhyay. Line-focusing concentrating solar collector-based power plants: a review. *Clean Technologies and Environmental Policy*, 19(1):9–35, 2017. (cited on page 1)

6. Md Tasbirul Islam, Nazmul Huda, AB Abdullah, and R Saidur. A comprehensive review of state-of-the-art concentrating solar power (CSP) technologies: Current status and research trends. *Renewable and Sustainable Energy Reviews*, 91: 987–1018, 2018. (cited on page 2)

7. Keith Lovegrove, Gregory Burgess, and John Pye. A new 500 m^2 paraboloidal dish solar concentrator. *Solar Energy*, 85(4):620–626, 2011. (cited on pages 2 and 10)

8. Joachim Gretz. Solar thermal electricity generation EURELIOS, the 1 MW_e helioelectric power plant of the european communities. *International Journal of Solar Energy*, 1(1):3–19, 1982. (cited on pages 2 and 9)

9. Chris Dalitz. Australian historic engineering plaquing program: A historic engineering marker (HEM) for White Cliffs solar power station (1981). Technical report, For the Heritage Committee - Sydney Division, 2006. (cited on pages 2 and 9)

10. Juan Ignacio Burgaleta, Santiago Arias, and Diego Ramirez. Gemasolar, the first tower thermosolar commercial plant with molten salt storage. In *Proceedings of*

the SolarPACES 2011 Conference on Concentrating Solar Power and Chemical Energy Systems, Granada, Spain, 2011. (cited on pages 2, 3, and 7)

11. NREL. Concentrating solar power projects: Crescent Dunes solar energy project. https://solarpaces.nrel.gov/crescent-dunes-solar-energy-project/, 2016. Accessed: 2018-09-24. (cited on pages 2 and 7)

12. Mark Mehos, Craig Turchi, Judith Vidal, Michael Wagner, Zhiwen Ma, Clifford Ho, William Kolb, Charles Andraka, and Alan Kruizenga. Concentrating solar power gen3 demonstration roadmap. Technical report, National Renewable Energy Lab.(NREL), Golden, CO (United States), 2017. (cited on pages 2, 21, 22, 41, and 138)

13. Craig E Tyner, J Paul Sutherland, and William R Gould Jr. Solar Two: A molten salt power tower demonstration. Technical report, Sandia National Labs., Albuquerque, NM (United States), 1995. (cited on pages 3 and 40)

14. Manuel Romero, Reiner Buck, and James E Pacheco. An update on solar central receiver systems, projects, and technologies. *J. Sol. Energy Eng.*, 124(2):98–108, 2002. (cited on pages 3 and 10)

15. Sun Lab. Solar Two demonstrates clean power for the future. https://www.nrel.gov/docs/legosti/fy97/22835.pdf/, 2000. SAND2000-0613 Accessed: 2016-11-11. (cited on page 3)

16. NREL. Shouhang Dunhuang 100 MW Phase II. https://solarpaces.nrel.gov/shouhang-dunhuang-100-mw-phase-ii, 2019. Accessed: 2019-08-29. (cited on pages 3 and 7)

17. Antonio L Avila-Marin. Volumetric receivers in solar thermal power plants with central receiver system technology: a review. *Solar energy*, 85(5):891–910, 2011. (cited on pages 3 and 4)

18. Prashant Karhade. Concentrated solar thermal technology - Part II. http://prashantkarhade.com/concentrated-solar-thermal-technology-part-ii/, 2015. Accessed: 2016-10-03. (cited on page 3)

19. Avi Kribus, P Doron, R Rubin, R Reuven, E Taragan, S Duchan, and J Karni. Performance of the directly-irradiated annular pressurized receiver (DIAPR) operating at 20 bar and 1,200°C. *J. Sol. Energy Eng.*, 123(1):10–17, 2001. (cited on page 4)

20. Peter Heller, Markus Pfänder, Thorsten Denk, Felix Tellez, Antonio Valverde, Jesús Fernandez, and Arik Ring. Test and evaluation of a solar powered gas turbine system. *Solar energy*, 80(10):1225–1230, 2006. (cited on page 4)

21. C Ho, J Christian, D Gill, A Moya, Sheldon Jeter, S Abdel-Khalik, D Sadowski, N Siegel, Hany Al-Ansary, Lars Amsbeck, et al. Technology advancements for

next generation falling particle receivers. *Energy Procedia*, 49(0):398–407, 2014. (cited on page 4)

22. Clifford Ho, Jeremy Sment, Kevin Albrecht, Brantley Mills, and Nathaniel Schroeder. Gen 3 particle pilot plant (G3P3): High-temperature particle system for concentrating solar power (phases 1 and 2). Technical report, Sandia National Lab.(SNL-NM), Albuquerque, NM (United States), 2021. (cited on page 4)

23. Steve Schell. Design and evaluation of eSolar's heliostat fields. *Solar Energy*, 85 (4):614–619, 2011. (cited on pages xv, 4, and 5)

24. Matti Lubkoll, DJ Erasmus, TM Harms, TW Von Backström, and DG Kröger. Performance characteristics of the spiky central receiver air pre-heater (SCRAP). *Solar Energy*, 201:773–786, 2020. (cited on page 6)

25. L Vant-Hull and C R Easton. Solar thermal power systems based on optical transmission (a feasibility study). final report, june 15, 1973–september 30, 1975. URL https://www.osti.gov/biblio/7154323. (cited on page 6)

26. Michael Wagner, Zhiwen Ma, Janna Martinek, Ty Neises, and Craig Turchi. Systems and methods for direct thermal receivers using near blackbody configurations, May 12 2020. US Patent 10,648,697. (cited on page 6)

27. Joshua M Christian, Jesus D Ortega, Clifford K Ho, and Julius Yellowhair. Design and modeling of light-trapping tubular receiver panels. In *Energy Sustainability*, volume 50220, page V001T04A005. American Society of Mechanical Engineers, 2016. (cited on pages 6 and 73)

28. Joshua M Christian, Jesus D Ortega, and Clifford K Ho. Novel tubular receiver panel configurations for increased efficiency of high-temperature solar receivers. In *Energy Sustainability*, volume 56840, page V001T05A014. American Society of Mechanical Engineers, 2015. (cited on pages 6 and 73)

29. John Pye, Joe Coventry, Clifford Ho, Julius Yellowhair, Ian Nock, Ye Wang, Ehsan Abbasi, Joshua Christian, Jesus Ortega, and Graham Hughes. Optical and thermal performance of bladed receivers. In *AIP Conference Proceedings*, volume 1850, page 030040. AIP Publishing LLC, 2017. (cited on page 6)

30. LL Vant-Hull and Alvin F Hildebrandt. Solar thermal power system based on optical transmission. *Solar Energy*, 18(1):31–39, 1976. (cited on page 6)

31. Lukas Heller. Literature review on heat transfer fluids and thermal energy storage systems in CSP plants. *STERG Report, May*, 31, 2013. (cited on page 6)

32. J Pacio and Th Wetzel. Assessment of liquid metal technology status and research paths for their use as efficient heat transfer fluids in solar central receiver systems. *Solar Energy*, 93:11–22, 2013. (cited on pages 6 and 8)

33. Alejandro Calderón, Anabel Palacios, Camila Barreneche, Mercè Segarra, Cristina Prieto, Alfonso Rodriguez-Sanchez, and A Inés Fernández. High-temperature systems using solid particles as tes and htf material: a review. *Applied Energy*, 213:100–111, 2018. (cited on page 6)

34. K Vignarooban, Xinhai Xu, A Arvay, Keng Hsu, and Arunachala Mada Kannan. Heat transfer fluids for concentrating solar power systems–a review. *Applied Energy*, 146:383–396, 2015. (cited on pages 6 and 9)

35. Edouard González-Roubaud, David Pérez-Osorio, and Cristina Prieto. Review of commercial thermal energy storage in concentrated solar power plants: Steam vs. molten salts. *Renewable and sustainable energy reviews*, 80:133–148, 2017. (cited on pages 7 and 20)

36. L.P. Drouot and M.J. Hillairet. The THEMIS program and the 2500 KW THEMIS solar power station at Targasonne. *ASME Transactions Journal of Solar Energy and Engineering*, 106:83–89, 1984. (cited on page 7)

37. F Donatini, C Zamparelli, A Maccari, and M Vignolini. High efficency integration of thermodynamic solar plant with natural gas combined cycle. In *2007 International Conference on Clean Electrical Power*, pages 770–776. IEEE, 2007. (cited on page 7)

38. EcoWatch. World's first 24/7 solar power plant powers 75,000 homes. https://www.ecowatch.com/worlds-first-24-7-solar-power-plant-powers-75-000-homes-1891177555.html, 2016. Accessed: 2020-09-02. (cited on page 7)

39. SolarPACES. Final testing for 150 MW Noor III tower CSP. https://www.solarpaces.org/final-testing-for-150-mw-noor-iii-tower-csp/, 2018. Accessed: 2019-08-29. (cited on page 7)

40. James E Pacheco, Robert W Bradshaw, Daniel B Dawson, Wilfredo De la Rosa, Rockwell Gilbert, and Steven H Goods. Final test and evaluation results from the Solar Two project. *SAND2002-0120*, 2002. (cited on pages 7 and 138)

41. Daniel S Codd, Antoni Gil, Muhammad Taha Manzoor, and Melanie Tetreault-Friend. Concentrating solar power (CSP)—thermal energy storage (TES) advanced concept development and demonstrations. *Current Sustainable/Renewable Energy Reports*, 7(2):17–27, 2020. (cited on page 7)

42. Philip D Myers Jr and D Yogi Goswami. Thermal energy storage using chloride salts and their eutectics. *Applied Thermal Engineering*, 109:889–900, 2016. (cited on page 7)

43. Gowtham Mohan, Mahesh Venkataraman, Judith Gomez-Vidal, and Joe Coventry. Assessment of a novel ternary eutectic chloride salt for next generation high-temperature sensible heat storage. *Energy Conversion and Management*, 167: 156–164, 2018. (cited on page 7)

44. Wenjin Ding, Judith Gomez-Vidal, Alexander Bonk, and Thomas Bauer. Molten chloride salts for next generation CSP plants: electrolytical salt purification for reducing corrosive impurity level. *Solar Energy Materials and Solar Cells*, 199: 8–15, 2019. (cited on page 8)

45. Angel G Fernández and Luisa F Cabeza. Corrosion evaluation of eutectic chloride molten salt for new generation of CSP plants. Part 1: Thermal treatment assessment. *Journal of Energy Storage*, 27:101125, 2020. (cited on page 8)

46. Nicholas Boerema, Graham Morrison, Robert Taylor, and Gary Rosengarten. Liquid sodium versus hitec as a heat transfer fluid in solar thermal central receiver systems. *Solar Energy*, 86(9):2293–2305, 2012. (cited on page 8)

47. Orrington E Dwyer. Power generation from liquid metal nuclear fuel, December 23 1958. US Patent 2,865,827. (cited on page 8)

48. Vast Solar. Project description: Jemalong solar station pilot - 1.1 mw_e. http://vastsolar.com/portfolio-items/jemalong-solar-station-pilot-1-1mwe/, 2017. Accessed: 2019-01-02. (cited on page 8)

49. Craig Wood and Kurt Drewes. Vast solar: Improving performance and reducing cost and risk using high- temperature modular arrays and sodium heat transfer fluid. In *Proceedings of the SolarPaces Conference, Daegu, South Korea*, pages 1–4, 2019. (cited on page 8)

50. J Pacio, Andreas Fritsch, Csaba Singer, and Ralf Uhlig. Liquid metals as efficient coolants for high-intensity point-focus receivers: implications to the design and performance of next-generation csp systems. *Energy Procedia*, 49:647–655, 2014. (cited on page 8)

51. Nikola Lorenzin and Alberto Abanades. A review on the application of liquid metals as heat transfer fluid in concentrated solar power technologies. *International journal of hydrogen energy*, 41(17):6990–6995, 2016. (cited on page 8)

52. ASTRI. Astri milestone 12 report — for public dissemination. *Program Number 1-SRI002*, 2017. (cited on page 8)

53. Craig S Turchi, Z Ma, and J Dyreby. Supercritical co_2 for application in concentrating solar power systems. In *Proceedings of SCCO2 power cycle symposium*, pages 29–30, 2009. (cited on page 8)

54. Stephen E Zitney. Steady-state design and dynamic analysis of a supercritical co_2 recompression brayton power cycle. Technical report, NETL, 2017. (cited on page 8)

55. Advanced regulatory control of a 10 MW_e supercritical CO_2 recompression Brayton cycle towards improving power ramp rates, author=Mahapatra, Priyadarshi and Zitney, Stephen E and Albright, Jacob and Liese, Eric A,

year=2018, institution=National Energy Technology Lab.(NETL), Pittsburgh, PA, and Morgantown, WV .... Technical report. (cited on page 8)

56. Brayton Energy. High-efficiency receivers for supercritical carbon dioxide cycles. https://www.nrel.gov/docs/fy12osti/55449.pdf, 2012. (cited on page 9)

57. SK Saini and RP Saini. Development of correlations for nusselt number and friction factor for solar air heater with roughened duct having arc-shaped wire as artificial roughness. *Solar Energy*, 82(12):1118–1130, 2008. (cited on pages 9 and 177)

58. Klaus Hennecke, Peter Schwarzbözl, G Koll, M Beuter, B Hoffschmidt, J Göttsche, and Thomas Hartz. The solar power tower jülich—a solar thermal power plant for test and demonstration of air receiver technology. In *Proceedings of ISES World Congress 2007 (Vol. I–Vol. V)*, pages 1749–1753. Springer, 2008. (cited on pages 9 and 20)

59. Roman Korzynietz, JA Brioso, A Del Río, M Quero, M Gallas, Ralf Uhlig, Miriam Ebert, Reiner Buck, and D Teraji. Solugas–comprehensive analysis of the solar hybrid brayton plant. *Solar Energy*, 135:578–589, 2016. (cited on page 9)

60. B Grange, A Ferrière, D Bellard, M Vrinat, R Couturier, F Pra, and Y Fan. Thermal performances of a high-temperature air solar absorber based on compact heat exchange technology. *Journal of solar energy engineering*, 133(3), 2011. (cited on page 9)

61. Eduardo Zarza, Loreto Valenzuela, Javier Leon, Klaus Hennecke, Markus Eck, H-Dieter Weyers, and Martin Eickhoff. Direct steam generation in parabolic troughs: Final results and conclusions of the diss project. *Energy*, 29(5-6):635–644, 2004. (cited on page 10)

62. Dirk Krüger, Joachim Krüger, Juvaraj Pandian, Fabian Feldhoff, Markus Eck, Martin Eickhoff, and Klaus Hennecke. Kanchanaburi solar thermal power plant with direct steam generation. In *Proceedings*, 2010. (cited on page 10)

63. Clifford K Ho. Advances in central receivers for concentrating solar applications. *Solar energy*, 152:38–56, 2017. (cited on page 10)

64. U.S. Department of Energy (DOE). Ivanpah project summary. https://www.energy.gov/lpo/ivanpah, 2019. Accessed: 2019-08-29. (cited on page 10)

65. HELIOSCSP. Solar receiver successfully set atopping israel 121 mw ashalim concentrated solar power tower. http://helioscsp.com/solar-receiver-successfully-set-atopping-israel-121-mw-ashalim-concentrated-solar-power-tower/, 2017. Accessed: 2019-08-29. (cited on page 10)

66. Joe Coventry and John Pye. Coupling supercritical and superheated direct steam generation with thermal energy storage. *SolarPACES 2009, 15-18 Sept 2009*, 2009. (cited on page 10)

67. Reyhaneh Loni, E Askari Asli-Ardeh, B Ghobadian, Evangelos Bellos, and Willem Gabriel Le Roux. Numerical comparison of a solar dish concentrator with different cavity receivers and working fluids. *Journal of Cleaner Production*, 198:1013–1030, 2018. (cited on page 10)

68. Zineb Aqachmar, Amine Allouhi, Abdelmajid Jamil, Belgacem Gagouch, and Tarik Kousksou. Parabolic trough solar thermal power plant noor i in morocco. *Energy*, 178:572–584, 2019. (cited on page 10)

69. Wolfgang JC Schiel and Michael A Geyer. Testing an external sodium receiver up to heat fluxes of 2.5 mw/m^2: Results and conclusions from the IEA-SSPS high flux experiment conducted at the central receiver system of the Plataforma Solar de Almeria (Spain). *Solar energy*, 41(3):255–265, 1988. (cited on pages xv and 11)

70. Nicholas Boerema, Graham Morrison, Robert Taylor, and Gary Rosengarten. High temperature solar thermal central-receiver billboard design. *Solar Energy*, 97:356–368, 2013. (cited on pages xv, 11, 14, and 160)

71. Alberto Sánchez-González, María Reyes Rodríguez-Sánchez, and Domingo Santana. Aiming strategy model based on allowable flux densities for molten salt central receivers. *Solar Energy*, 157:1130–1144, 2017. (cited on pages 12, 60, and 61)

72. William R Logie, John D Pye, and Joe Coventry. Thermoelastic stress in concentrating solar receiver tubes: A retrospect on stress analysis methodology, and comparison of salt and sodium. *Solar Energy*, 160:368–379, 2018. (cited on pages 12, 37, 54, 57, 139, 142, 143, 144, and 156)

73. Tim Conroy, Maurice N Collins, and Ronan Grimes. A review of steady-state thermal and mechanical modelling on tubular solar receivers. *Renewable and Sustainable Energy Reviews*, 119:109591, 2020. (cited on page 12)

74. PA González-Gómez, MR Rodríguez-Sánchez, M Laporte-Azcué, and D Santana. Calculating molten-salt central-receiver lifetime under creep-fatigue damage. *Solar Energy*, 213:180–197, 2021. (cited on pages 12 and 146)

75. Germain Augsburger and Daniel Favrat. Modelling of the receiver transient flux distribution due to cloud passages on a solar tower thermal power plant. *Solar Energy*, 87:42–52, 2013. (cited on page 12)

76. Nate Blair, Aron P Dobos, Janine Freeman, Ty Neises, Michael Wagner, Tom Ferguson, Paul Gilman, and Steven Janzou. System advisor model, SAM 2014.1. 14: General description. Technical report, National Renewable Energy Lab.(NREL), Golden, CO (United States), 2014. (cited on pages xxii, 12, 145, and 148)

77. Bruce L Kistler. A user's manual for DELSOL3: a computer code for calculating the optical performance and optimal system design for solar thermal central receiver plants. Technical report, Sandia National Lab.(SNL-CA), Livermore, CA (United States), 1986. (cited on page 12)

78. Birgit Gobereit, Lars Amsbeck, Reiner Buck, and Csaba Singer. Cost analysis of different operation strategies for falling particle receivers. In *Energy Sustainability*, volume 56840, page V001T05A010. American Society of Mechanical Engineers, 2015. (cited on page 13)

79. Peter Schwarzbözl, Reiner Buck, Chemi Sugarmen, Arik Ring, Ma Jesús Marcos Crespo, Peter Altwegg, and Juan Enrile. Solar gas turbine systems: design, cost and perspectives. *Solar energy*, 80(10):1231–1240, 2006. (cited on page 13)

80. Lifeng Li, Bo Wang, John Pye, and Wojciech Lipiński. Temperature-based optical design, optimization and economics of solar polar-field central receiver systems with an optional compound parabolic concentrator. *Solar Energy*, 206:1018–1032, 2020. (cited on pages 13 and 138)

81. Andreas Fritsch, Cathy Frantz, and Ralf Uhlig. Techno-economic analysis of solar thermal power plants using liquid sodium as heat transfer fluid. *Solar Energy*, 177:155–162, 2019. (cited on page 13)

82. Yunes A Cengel and Michael A Boles. Thermodynamics, an engineering approach, mcgraw hill. *Higher education,*, 2011. (cited on page 13)

83. A Bejan, DW Kearney, and F Kreith. Second law analysis and synthesis of solar collector systems. 103(1):23–28, 1981. (cited on page 13)

84. Arif Hepbasli. A key review on exergetic analysis and assessment of renewable energy resources for a sustainable future. *Renewable and sustainable energy reviews*, 12(3):593–661, 2008. (cited on page 13)

85. Chao Xu, Zhifeng Wang, Xin Li, and Feihu Sun. Energy and exergy analysis of solar power tower plants. *Applied Thermal Engineering*, 31(17-18):3904–3913, 2011. (cited on pages 13, 27, 32, 38, 55, and 166)

86. Ricardo Vasquez Padilla, Armando Fontalvo, Gokmen Demirkaya, Arnold Martinez, and Arturo Gonzalez Quiroga. Exergy analysis of parabolic trough solar receiver. *Applied thermal engineering*, 67(1-2):579–586, 2014. (cited on page 13)

87. A Baghernejad and M Yaghoubi. Exergy analysis of an integrated solar combined cycle system. *Renewable Energy*, 35(10):2157–2164, 2010. (cited on page 13)

88. Willem Gabriel Le Roux, Tunde Bello-Ochende, and Josua P Meyer. Operating conditions of an open and direct solar thermal Brayton cycle with optimised cavity receiver and recuperator. *Energy*, 36(10):6027–6036, 2011. (cited on page 13)

89. Soteris A Kalogirou, Sotirios Karellas, Viorel Badescu, and Konstantinos Braimakis. Exergy analysis on solar thermal systems: a better understanding of their sustainability. *Renewable Energy*, 85:1328–1333, 2016. (cited on page 13)

90. M Rodríguez-Sánchez, M Venegas-Bernal, C Marugán-Cruz, and D Santana. Thermal, mechanical and hydrodynamic analysis to optimise the design of molten salt central receivers of solar tower power plants. *ICREPQ*, 13:2172–038, 2013. (cited on pages 14 and 57)

91. MR Rodríguez-Sánchez, A Sánchez-González, C Marugán-Cruz, and D Santana. New designs of molten-salt tubular-receiver for solar power tower. *Energy Procedia*, 49(504-513):6–7, 2014. (cited on page 14)

92. Daniel Potter, Alex Burton, and Jin-Soo Kim. Optimised design of a 1 mw_t liquid sodium central receiver system. In *Proceedings of Asia Pacific Solar Research Conference*, 2015. (cited on page 14)

93. Charles-Alexis Asselineau, Joe Coventry, and John Pye. Exergy analysis of the focal-plane flux distribution of solar-thermal concentrators. *Applied Energy*, 222: 1023–1032, 2018. (cited on pages 14 and 31)

94. Jose Zapata, Charles-Alexis Asselineau, John Pye, Martin Kaufer, Graham Hughes, et al. An integrated optical and thermal model of cavity receivers for paraboloidal dish concentrators. 2014. (cited on pages 14 and 36)

95. María Reyes Rodríguez-Sánchez, Antonio Soria-Verdugo, José Antonio Almendros-Ibáñez, Antonio Acosta-Iborra, and Domingo Santana. Thermal design guidelines of solar power towers. *Applied Thermal Engineering*, 63(1): 428–438, 2014. (cited on pages xv, 14, 27, 28, 49, and 217)

96. M Laporte-Azcué, PA González-Gómez, MR Rodríguez-Sánchez, and D Santana. Exergy analysis of solar central receivers. *Solar Energy*, 207:957–973, 2020. (cited on page 14)

97. Patricia Kuntz Falcone. A handbook for solar central receiver design. Technical report, Sandia National Lab.(SNL-CA), Livermore, CA (United States), 1986. (cited on page 15)

98. Alberto Giaconia, Gaetano Iaquaniello, Amr Amin Metwally, Giampaolo Caputo, and Irena Balog. Experimental demonstration and analysis of a CSP plant with molten salt heat transfer fluid in parabolic troughs. *Solar Energy*, 211:622–632, 2020. (cited on page 16)

99. Olivier Dumont, Sylvain Quoilin, and Vincent Lemort. Importance of the reconciliation method to handle experimental data in refrigeration and power cycle: application to a reversible heat pump/organic rankine cycle unit integrated in a positive energy building. *International Journal of Energy and Environmental Engineering*, 7(2):137–143, 2016. (cited on page 16)

100. Yonghee Ryu, Abhinav Gupta, WooYoung Jung, and BuSeog Ju. A reconciliation of experimental and analytical results for piping systems. *International Journal of Steel Structures*, 16(4):1043–1055, 2016. (cited on page 16)

101. Ye Wang. *Optical and thermal radiative performance of bladed receivers for concentrating solar thermal energy systems.* PhD thesis, 07 2020. (cited on pages xix, xx, xxi, xxviii, 16, 74, 78, 79, 80, 84, 94, 95, 115, 116, and 117)

102. Belen Zalba, Jose Ma Marın, Luisa F Cabeza, and Harald Mehling. Review on thermal energy storage with phase change: materials, heat transfer analysis and applications. *Applied thermal engineering*, 23(3):251–283, 2003. (cited on page 20)

103. Ming Liu, Wasim Saman, and Frank Bruno. Review on storage materials and thermal performance enhancement techniques for high-temperature phase change thermal storage systems. *Renewable and Sustainable Energy Reviews*, 16 (4):2118–2132, 2012. (cited on page 20)

104. Rafael Osuna, R Olavarría, Rafael Morillo, Marcelino Sánchez, Felipe Cantero, Valerio Fernández-Quero, Pedro Robles, T López, Antonio Esteban, Francisco Céron, et al. Ps10, construction of a 11mw solar thermal tower plant in seville, spain. In *Proc. SolarPACES conference, Seville, Spain*, 2006. (cited on pages 20 and 74)

105. Bruno Cárdenas, Noel León, John Pye, and Héctor D García. Design and modeling of a high temperature solar thermal energy storage unit based on molten soda lime silica glass. *Solar Energy*, 126:32–43, 2016. (cited on page 20)

106. Johannes P Kotzé, Theodor W von Backström, and Paul J Erens. A combined latent thermal energy storage and steam generator concept using metallic phase change materials and metallic heat transfer fluids for concentrated solar power. *SolarPACES 2011*, 2011. (cited on page 20)

107. 1414 DEGREES. 1414 degrees, clean scalable energy storage. https://1414degrees.com.au, 2019. Accessed: 2019-09-02. (cited on page 20)

108. U.S. Department of Energy. Generation 3 concentrating solar power systems (Gen3 CSP). https://www.energy.gov/eere/solar/generation-3-concentrating-solar-power-systems-gen3-csp, 2020. Accessed: 2021-02-03. (cited on page 21)

109. Yoonhan Ahn, Seong Jun Bae, Minseok Kim, Seong Kuk Cho, Seungjoon Baik, Jeong Ik Lee, and Jae Eun Cha. Review of supercritical co_2 power cycle technology and current status of research and development. *Nuclear Engineering and Technology*, 47(6):647–661, 2015. (cited on page 21)

110. Yunus A Cengel, Michael A Boles, and Mehmet Kanoğlu. *Thermodynamics: an engineering approach*, volume 5. McGraw-hill New York, 2011. (cited on pages xv and 21)

111. Woo Seok Jeong, Jeong Ik Lee, and Yong Hoon Jeong. Potential improvements of supercritical recompression CO_2 Brayton cycle by mixing other gases for power conversion system of a SFR. *Nuclear Engineering and Design*, 241(6):2128–2137, 2011. (cited on pages xv and 21)

112. Susan Kraemer. Shouhang and edf to test sCO_2 cycle in concentrated solar power. https://www.solarpaces.org/shouhang-and-edf-first-to-test-s-co2-cycle-in-concentrated-solar-power/, 2019. Accessed: 2019-09-02. (cited on page 21)

113. Carmen Margarita Mendez Cruz and Gary E Rochau. sCO_2 Brayton cycle: Roadmap to sCO_2 power cycles ne commercial applications. Technical report, Sandia National Lab.(SNL-NM), Albuquerque, NM (United States), 2018. (cited on page 21)

114. Ales Vojacek, Alexander Johannes Hacks, Tomas Melichar, Otakar Frybort, and Petr Hájek. Challenges in supercritical CO_2 power cycle technology and first operational experience at cvr. In *Proceedings of the 2nd European Supercritical CO_2 Conference, Essen, Germany*, pages 30–31, 2018. (cited on page 21)

115. Ricardo Vasquez Padilla, Yen Chean Soo Too, Regano Benito, Robbie McNaughton, and Wes Stein. Multi-objective thermodynamic optimisation of supercritical CO_2 Brayton cycles integrated with solar central receivers. *International Journal of Sustainable Energy*, 37(1):1–20, 2018. (cited on page 21)

116. Sergio Relloso and Yolanda Gutiérrez. Sener molten salt tower technology. Ouarzazate noor III case. In *AIP Conference Proceedings*, volume 1850, page 030041. AIP Publishing LLC, 2017. (cited on page 22)

117. Kenneth Guy Allen. *Rock bed thermal storage for concentrating solar power plants*. PhD thesis, Stellenbosch: Stellenbosch University, 2014. (cited on page 22)

118. AB Zavoico. Solar power tower design basis document. sandia national laboratories. 2001. (cited on pages xv and 25)

119. JK Fink and L Leibowitz. Thermodynamic and transport properties of sodium liquid and vapor. Technical report, Argonne National Lab., 1995. (cited on pages xv and 25)

120. Roland Span and Wolfgang Wagner. A new equation of state for carbon dioxide covering the fluid region from the triple-point temperature to 1100 k at pressures up to 800 MPa. *Journal of physical and chemical reference data*, 25(6):1509–1596, 1996. (cited on pages xv and 25)

121. A Fenghour, William A Wakeham, and V Vesovic. The viscosity of carbon dioxide. *Journal of physical and chemical reference data*, 27(1):31–44, 1998. (cited on pages xv and 25)

122. V Vesovic, WA Wakeham, GA Olchowy, JV Sengers, JTR Watson, and J Millat. The transport properties of carbon dioxide. *Journal of physical and chemical reference data*, 19(3):763–808, 1990. (cited on pages xv and 25)

123. Hing Y Lo, Daniel L Carroll, and Leonard I Stiel. Viscosity of gaseous air at moderate and high pressures. *Journal of Chemical and Engineering Data*, 11(4): 540–544, 1966. (cited on pages xv and 25)

124. K Kadoya, N Matsunaga, and A Nagashima. Viscosity and thermal conductivity of dry air in the gaseous phase. *Journal of physical and chemical reference data*, 14 (4):947–970, 1985. (cited on pages xv and 25)

125. Freesteam: Steam tables, Open Source, IAPWS-if97. http://freesteam.sourceforge.net/. Accessed: 2022-07-02. (cited on pages xv and 25)

126. Adrian Bejan, George Tsatsaronis, and Michael J Moran. *Thermal design and optimization*. John Wiley & Sons, 1995. (cited on page 24)

127. IE Mouromtseff. Water and forced-air cooling of vacuum tubes nonelectronic problems in electronic tubes. *Proceedings of the IRE*, 30(4):190–205, 1942. (cited on pages 24 and 26)

128. Charles F Bonilla et al. *Nuclear engineering*. McGraw-Hill, 1957. (cited on pages 24 and 26)

129. Andrej Lenert, Youngsuk Nam, and Evelyn N Wang. Heat transfer fluids. *Annual Review of Heat Transfer*, 15, 2012. (cited on pages 24, 25, and 26)

130. J Pye, M Zheng, CA Asselineau, and J Coventry. An exergy analysis of tubular solar-thermal receivers with different working fluids. *Proceedings of SolarPACES 2014*, 2014. (cited on pages xv and 29)

131. ASME. *ASME Boiler and Pressure Vessel Code, Sec. III, Division 5*. American Society of Mechanical Engineers, 2007. (cited on pages xv, xxii, 30, 78, 138, 140, 141, and 145)

132. JK Wright. Draft ASME boiler and pressure vessel code case for use of alloy 617 for class a elevated temperature service construction. Technical report, INL/EXT-15-36305, Idaho National Laboratory, 2015. (cited on pages xv, xxii, 30, 78, 138, 140, 141, 145, and 157)

133. Bipul Barua, Michael McMurtrey, Ryann E Rupp, and Mark C Messner. Design guidance for high temperature concentrating solar power components. Technical report, Argonne National Lab.(ANL), Argonne, IL (United States), 2020. (cited on pages xv, xxii, 30, 78, 138, 140, 141, 145, 146, 157, and 163)

134. Dennis L Siebers and John S Kraabel. Estimating convective energy losses from solar central receivers. Technical report, Sandia National Labs., Livermore, CA (USA), 1984. (cited on pages xxii, 30, 140, and 141)

135. Clifford K Ho, A Roderick Mahoney, Andrea Ambrosini, Marlene Bencomo, Aaron Hall, and Timothy N Lambert. Characterization of Pyromark 2500 paint for high-temperature solar receivers. *Journal of Solar Energy Engineering*, 136(1), 2014. (cited on page 30)

136. Yves Candau. On the exergy of radiation. *Solar Energy*, 75(3):241–247, 2003. (cited on pages 31, 55, and 213)

137. V Gnielinski. Equations for calculating heat transfer in single tube rows and banks of tubes in transverse flow. *Int. Chem. Eng.;(United States)*, 19(3), 1979. (cited on pages 33, 36, 76, 120, 140, and 163)

138. Julio Pacio, Luca Marocco, and Th Wetzel. Review of data and correlations for turbulent forced convective heat transfer of liquid metals in pipes. *Heat and Mass Transfer*, 51(2):153–164, 2015. (cited on page 34)

139. OJ Foust. Sodium-nak engineering handbook. Volume II. sodium flow, heat transfer, intermediate heat exchangers, and steam generators. 1976. (cited on pages xvi, 34, and 35)

140. E Skupinski, J Tortel, and L Vautrey. Determination des coefficients de convection d'un alliage sodium-potassium dans un tube circulaire. *International Journal of Heat and Mass Transfer*, 8(6):937–951, 1965. (cited on pages xvi, 34, 35, 140, 163, and 165)

141. Bernard Lubarsky and Samuel J Kaufman. Review of experimental investigations of liquid-metal heat transfer. 1955. (cited on pages xvi, 34, and 35)

142. Xu Cheng and Nam-il Tak. Investigation on turbulent heat transfer to lead-bismuth eutectic flows in circular tubes for nuclear applications. *Nuclear Engineering and Design*, 236(4):385–393, 2006. (cited on pages xvi and 35)

143. John Downing Pye. *System modelling of the compact linear Fresnel reflector*. PhD thesis, UNSW Sydney, 2008. (cited on page 35)

144. BS Petukhov et al. Heat transfer and friction in turbulent pipe flow with variable physical properties. *Advances in heat transfer*, 6(503):i565, 1970. (cited on page 36)

145. Satish G Kandlikar. Development of a flow boiling map for subcooled and saturated flow boiling of different fluids inside circular tubes. 1991. (cited on page 36)

146. DC Groeneveld. Post-dryout heat transfer at reactor operating conditions. Technical Report No. CONF-730304–, Atomic Energy of Canada Limited, 1973. (cited on page 36)

147. OneSteel Trading Pty Limited. Pipe and fittings data charts. https://www.libertygfg.com/media/163088/onesteel-metalcentre-pipe-and-fittings-data-charts.pdf, 2013. Accessed: 2019-04-03. (cited on pages 36, 150, and 153)

148. St Timoshenko. P, and goodier, jn theory of elasticity, 1970. (cited on page 37)

149. RC Hibbeler. *Mechanics of Materials, SI version*. Pearson Higher Education US., 2005. (cited on page 37)

150. ASME Boiler and Pressure Vessel Code. Section II Part D. *Properties (Metric) Ma*, 2010. (cited on pages xvi and 37)

151. Haynes international. https://www.haynesintl.com/, 2020. Accessed: 2020-09-24. (cited on pages 37, 78, and 163)

152. Art Westerberg, Benjamin Allan, Vicente RicoRamirez, Mark Thomas, and Kenneth Tyner. ASCEND IV: Advanced system for computations in engineering design, 1998. (cited on pages 38 and 163)

153. Drake Tilley, Bruce Kelly, and Frank Burkholder. Baseload nitrate salt central receiver power plant design final report. Technical report, Abengoa Solar LLC, Lakewood, CO (United States), 2014. (cited on pages 40, 50, and 211)

154. Antoni Gil, Marc Medrano, Ingrid Martorell, Ana Lázaro, Pablo Dolado, Belén Zalba, and Luisa F Cabeza. State-of-the-art on high-temperature thermal energy storage for power generation. Part 1 — concepts, materials and modellization. *Renewable and Sustainable Energy Reviews*, 14(1):31–55, 2010. (cited on page 41)

155. Merle C Potter, David C Wiggert, and Bassem H Ramadan. Mechanics of fluids, si edition. *Cengage Learning*, 2012. (cited on pages 41 and 128)

156. Ashish Karn, Venkateshwarlu Chintala, and Suresh Kumar. An investigation into sky temperature estimation, its variation, and significance in heat transfer calculations of solar cookers. *Heat Transfer—Asian Research*, 48(5):1830–1856, 2019. (cited on page 46)

157. B Zavoico Alexis. Solar power tower design basis document. *Sandia National Laboratories. doi*, 10:786629, 2001. (cited on page 53)

158. Keith Lovegrove and John Pye. Fundamental principles of concentrating solar power (CSP) systems. In *Concentrating solar power technology*, pages 16–67. Elsevier, 2012. (cited on page 54)

159. Charles-Alexis Asselineau, William Logie, John Pye, and Joe Coventry. Limits of the cylindrical absorber design for a sodium receiver. In *AIP Conference Proceedings*, volume 2033, page 040006. AIP Publishing LLC, 2018. (cited on page 57)

160. Ye Wang, Joe Coventry, and John Pye. Optical and radiation considerations in bladed receiver designs for central tower systems. In *AIP Conference Proceedings*, volume 2126, page 030063. AIP Publishing LLC, 2019. (cited on page 57)

161. Clifford K Ho, Jesus D Ortega, Joshua M Christian, Julius E Yellowhair, Daniel Ray, John Kelton, Gregory Peacock, Charles Andraka, and Subhash Shinde. Fractal-like materials design with optimized radiative properties for high-efficiency solar energy conversion. *SAND2016-9526, Sandia National Laboratories*, 2016. (cited on page 73)

162. Florian R Menter. Zonal two equation KW turbulence models for aerodynamic flows. In *23rd fluid dynamics, plasmadynamics, and lasers conference*, page 2906, 1993. (cited on page 76)

163. Dmitry A Lysenko, Ivar S Ertesvåg, and Kjell E Rian. Modeling of turbulent separated flows using OpenFOAM. *Computers & Fluids*, 80:408–422, 2013. (cited on page 76)

164. Juan F Torres, Farzin Ghanadi, Ian Nock, Maziar Arjomandi, and John Pye. Mixed convection around a tilted cuboid with an isothermal sidewall at moderate reynolds numbers. *International Journal of Heat and Mass Transfer*, 119:418–432, 2018. (cited on page 76)

165. CSIRO. Concentrated solar thermal research, CSIRO. https://www.csiro.au/en/research/technology-space/energy/Solar-thermal. (cited on page 76)

166. John Pye, Ehsan Abbasi, Maziar Arjomandi, Joe Coventry, Farzin Ghanadi, Graham Hughes, Jin-Soo Kim, Li Ma, Ali Shirazi, Juan F Torres, et al. Towards testing of a second-generation bladed receiver. In *AIP Conference Proceedings*, volume 2126, page 030044. AIP Publishing LLC, 2019. (cited on pages 76 and 88)

167. Ian Nock, William Logie, Joe Coventry, John Pye, et al. A computational evaluation of convective losses from bladed solar thermal receivers. In *Proceedings of the 2016 Asia-Pacific Solar Research Conference*. Australian PV Institute, 2016. (cited on pages 78 and 120)

168. Juan F Torres, Farzin Ghanadi, Maziar Arjomandi, and John Pye. Convective heat loss from a bladed solar receiver. In *AIP Conference Proceedings*, volume 2126, page 030059. AIP Publishing LLC, 2019. (cited on page 78)

169. Ye Wang, Charles-Alexis Asselineau, Joe Coventry, and John Pye. Optical performance of bladed receivers for CSP systems. In *Energy Sustainability*, volume 50220, page V001T04A026. American Society of Mechanical Engineers, 2016. (cited on page 81)

170. Eric O Lebigot. Uncertainties: a python package for calculations with uncertainties. *URL http://pythonhosted. org/uncertainties*, 2010. (cited on page 99)

171. John Pye, Joe Coventry, Jin-Soo Kim, Felix Venn, Meige Zheng, Ye Wang, Daniel Potter, Michael Rae, Mike Collins, and Juan F Torres. Experimental testing of the bladed receiver. In *AIP Conference Proceedings*, volume 2303, page 030030. AIP Publishing LLC, 2020. (cited on page 103)

172. REOTEMP Instrument Corporation. Thermocouple accuracies. https://www.thermocoupleinfo.com/thermocouple-accuracies.htm, 2020. Accessed: 2020-12-02. (cited on page 103)

173. Oval coriolis flow meter. https://www.oval.co.jp/english/products/coriolis_index_e.html, 2019. Accessed: 2019-05-24. (cited on page 103)

174. Omega turbine flow meter. https://au.omega.com/prodinfo/flowmeters.html, 2019. Accessed: 2019-05-24. (cited on page 103)

175. DR Myers and SM Wilcox. Relative accuracy of 1-minute and daily total solar radiation data for 12 global and 4 direct beam solar radiometers. Technical report, National Renewable Energy Lab.(NREL), Golden, CO (United States), 2009. (cited on page 103)

176. Newcastle, New South Wales, Australia – sunrise, sunset, and day length, april 2019. https://www.timeanddate.com/sun/australia/newcastle?month=4&year=2019, 2019. Accessed: 2021-03-27. (cited on page 117)

177. J.P. Holman. *Heat Transfer*. McGraw-Hill, 2002. (cited on page 123)

178. C Crane. Flow of fluids through valves, fittings, and pipe. technical paper No. 410 M, 2009. (cited on pages 129 and 131)

179. Akay Aydin Islek. *The impact of swirl in turbulent Pipe flow*. PhD thesis, Georgia Institute of Technology, 2004. (cited on page 129)

180. Mario Turiso, Martin Straka, Jürgen Rose, Christian Bombis, and Denis F Hinz. The asymmetric swirl disturbance generator: Towards a realistic and reproducible standard. *Flow Measurement and Instrumentation*, 60:144–154, 2018. (cited on page 129)

181. RP Skelton and D Gandy. Creep–fatigue damage accumulation and interaction diagram based on metallographic interpretation of mechanisms. *Materials at High Temperatures*, 25(1):27–54, 2008. (cited on page 145)

182. Rando Tungga Dewa, Jeong Hun Park, Seon Jin Kim, and Sang Yeol Lee. High-temperature creep-fatigue behavior of alloy 617. *Metals*, 8(2):103, 2018. (cited on page 145)

183. Tim Conroy, Maurice N Collins, James Fisher, and Ronan Grimes. Levelized cost of electricity evaluation of liquid sodium receiver designs through a thermal performance, mechanical reliability, and pressure drop analysis. *Solar Energy*, 166:472–485, 2018. (cited on pages 145 and 146)

184. MIT Department of Aeronautics and Astronautics. Module 3: Constitutive equations. http://web.mit.edu/16.20/homepage/3_Constitutive/Constitutive_files/module_3_no_solutions.pdf, 2021. (cited on page 147)

185. Bruce D Kelly. Advanced thermal storage for central receivers with supercritical coolants. Technical report, Abengoa Solar Inc., 2010. (cited on page 147)

186. William M Vatavuk et al. Updating the CE plant cost index. *Chemical Engineering*, 109(1):62–70, 2002. (cited on page 148)

187. Felix Venn. The material costs are provided in personal communication on 17 dec 2020, via email. personal communication. (cited on page 148)

188. Craig Turchi, Samuel Gage, Janna Martinek, Sameer Jape, Ken Armijo, Joe Coventry, John Pye, Charles-Alexis Asselineau, Felix Venn, William Logie, et al. CSP Gen3: Liquid-Phase Pathway to SunShot. Technical report, National Renewable Energy Lab.(NREL), Golden, CO (United States), 2021. (cited on page 148)

189. Ali Ghaheri, Saeed Shoar, Mohammad Naderan, and Sayed Shahabuddin Hoseini. The applications of genetic algorithms in medicine. *Oman medical journal*, 30(6):406, 2015. (cited on page 149)

190. Mylene CAF Rezende, Caliane BB Costa, Aline C Costa, MR Wolf Maciel, and Rubens Maciel Filho. Optimization of a large scale industrial reactor by genetic algorithms. *Chemical Engineering Science*, 63(2):330–341, 2008. (cited on page 149)

191. Angus R Simpson and Stephen D Priest. The application of genetic algorithms to optimisation problems in geotechnics. *Computers and Geotechnics*, 15(1):1–19, 1993. (cited on page 149)

192. Ali Shirazi, Alireza Rahbari, Charles-Alexis Asselineau, and John Pye. A solar fuel plant via supercritical water gasification integrated with Fischer–Tropsch synthesis: System-level dynamic simulation and optimisation. *Energy Conversion and Management*, 192:71–87, 2019. (cited on page 149)

193. John Henry Holland et al. *Adaptation in natural and artificial systems: an introductory analysis with applications to biology, control, and artificial intelligence*. MIT press, 1992. (cited on page 149)

194. Félix-Antoine Fortin, François-Michel De Rainville, Marc-André Gardner, Marc Parizeau, and Christian Gagné. DEAP: Evolutionary algorithms made easy. *Journal of Machine Learning Research*, 13:2171–2175, jul 2012. (cited on page 149)

195. Janna Martinek and Craig Turchi. Salt composition and receiver details provided in personal communication in march. personal communication. (cited on pages xxiii, 155, 162, and 163)

196. Xiaoxin Wang, Jesus Del Rincon, Peiwen Li, Youyang Zhao, and Judith Vidal. Thermophysical properties experimentally tested for NaCl-KCl-$MgCl_2$ eutectic molten salt as a next-generation high-temperature heat transfer fluids in concentrated solar power systems. *Journal of Solar Energy Engineering*, 143(4), 2021. (cited on pages xxiii and 155)

197. Meige Zheng, José Zapata, Charles-Alexis Asselineau, Joe Coventry, and John Pye. Analysis of tubular receivers for concentrating solar tower systems with a range of working fluids, in exergy-optimised flow-path configurations. *Solar Energy*, 211:999–1016, 2020. (cited on pages 161, 163, and 165)

198. Shuang Wang, Charles-Alexis Asselineau, John Pye, and Joe Coventry. An efficient method for aiming heliostats using ray-tracing. In *Proceedings of the SolarPaces Conference, Albuquerque, New Mexico, USA*, 2020. (cited on pages 162, 163, and 166)

199. Salvatore Guccione. Design and optimization of a sodium–molten salt heat exchanger for concentrating solar power applications. In *Proceedings of the SolarPaces Conference, Albuquerque, New Mexico, USA*, 2020. (cited on pages 162 and 164)

200. Armando Fontalvo, Salvatore Guccione, Ye Wang, Shuang Wang, Zebedee Kee, Charles-Alexis Asselineau, Daniel Potter, Felix Venn, Janna Martinek, Craig Turchi, et al. System-level comparison of sodium and salt systems in support of the Gen3 Liquids Pathway. In *AIP Conference Proceedings*, volume 2445, page 030007. AIP Publishing LLC, 2022. (cited on page 163)

201. Armando Fontalvo, Salvatore Guccione, Ye Wang, Shuang Wang, Zabedee Kee, Charles-Alexis Asselineau, Potter Daniel, Felix Venn, Janna Martinek, Craig Truchi, Joe Coventry, and John Pye. System-level comparison of sodium and salt systems in support of the Gen3 Liquids Pathway. In *Proceedings of the SolarPaces Conference, Albuquerque, New Mexico, USA*, 2020. (cited on page 164)

202. Salvatore Guccione, Armando Fontalvo, Rafael Guedez, John Pye, Laura Savoldi, and Roberto Zanino. Techno-economic optimisation of a sodium–chloride salt heat exchanger for concentrating solar power applications. *Solar Energy*, 239:252–267, 2022. (cited on pages 165 and 170)

203. Kuppan Thulukkanam. *Heat exchanger design handbook*. CRC press, 2013. (cited on page 165)

204. J Coventry, Ch Andraka, J Pye, M Blanco, and J Fisher. A review of sodium receiver technologies for central receiver solar power plants. *Solar Energy*, 122: 749–762, 2015. (cited on page 170)

205. Craig Truchi. Molten salt vs. liquid sodium receiver selection using the analytic hierarchy process. In *Proceedings of the SolarPaces Conference, Albuquerque, New Mexico, USA*, 2020. (cited on page 170)

Appendices

Appendix A ASCEND Modelling (example)

```
REQUIRE "johnpye/moltensalt.a4c";
REQUIRE "johnpye/thermo_types.a4c";
IMPORT "johnpye/fprops/fprops";
IMPORT "sensitivity/solve";
IMPORT "johnpye/extpy/extpy";
IMPORT "moltensalt-plot_single_segment";

MODEL fprops_fluid;
    component IS_A symbol_constant;
    type IS_A symbol_constant;
END fprops_fluid;

MODEL fluid_state;
    fluid IS_A symbol_constant;
    state IS_A thermophysical_fluid_base;
    T ALIASES state.T;
    h ALIASES state.h;
    s ALIASES state.s;
    p ALIASES state.p;
    u ALIASES state.u;
    v ALIASES state.v;
    rho ALIASES state.rho;
    mu ALIASES state.mu;
    k ALIASES state.k;
    cp ALIASES state.cp;

    SELECT(fluid)
        CASE 'moltensalt':
            state IS_REFINED_TO moltensalt_fluid;
    END SELECT;
METHODS
METHOD default;
    RUN state.default;
END default;
END fluid_state;

(*
    Fluid state together with an associated flowrate, intended for use as
    part of a flowsheet simulation, eg as a component inlet or outlet.

    We have extended this with reference state (exergy calculation) and
    pipe properties (cross-section area etc)
*)
MODEL fluid_node;
    state IS_A fluid_state;
    fluid ALIASES state.fluid;
    T ALIASES state.T;                h ALIASES state.h;
    s ALIASES state.s;                p ALIASES state.p;
    u ALIASES state.u;                v ALIASES state.v;
    rho ALIASES state.rho;            mu ALIASES state.mu;
    k ALIASES state.k;                cp ALIASES state.cp;

    mdot IS_A mass_rate;
    d, L IS_A distance;
    A IS_A area;
    A_eq: A = 0.25{PI} * d^2;
    vel IS_A speed;
    vel_eq: vel = mdot * v / A;

    Re, Pr, Pe IS_A factor;
    Pr_eq: Pr = cp * mu / k;
    nu IS_A kinematic_viscosity;
    nu_eq: nu = mu / rho;
    Re_eq: Re = vel * d / nu;

    Pe_eq: Pe = Re * Pr;

    ref "exergy reference state" IS_A fluid_state;
    ref.fluid , fluid ARE_THE_SAME;

    X_f "flow exergy" IS_A energy_rate;
    X_f_eq: X_f = mdot * ( h - ref.h - ref.T * (s - ref.s) + 0.5*vel^2 );

METHODS
METHOD solve;
    EXTERNAL do_solve(SELF);
END solve;
METHOD default;
    RUN state.default;
END default;
END fluid_node;
```

```
(*
    A single flow segment in the receiver. Putting everything in here saves us
    from a lot of looping/array statements later on, and we get the side
    benefit of being able to test a single segment in isolation.
*)
MODEL receiver_flow_segment;
    inlet, outlet IS_A fluid_node;
    fluid ALIASES inlet.fluid;
    inlet.mdot, outlet.mdot ARE_THE_SAME;
    inlet.fluid, outlet.fluid, inlet.ref.fluid ARE_THE_SAME;
    inlet.ref, outlet.ref ARE_THE_SAME;
    intconv_corr "correlation for internal convection heat transfer" IS_A symbol_constant;
    fric_corr "correlation for Darcy friction factor" IS_A symbol_constant;
    fric_corr :== 'smooth';

    d_i "pipe inside diameter" ALIASES inlet.d;
    t IS_A distance; (* pipe thickness *)
    L "flow segment length" IS_A distance;
    d_o "pipe outside diameter" IS_A distance;
    d_o_eq: d_o = d_i + 2*t;
    A_ext_slice IS_A area; A_ext_slice = L * 0.5{PI} * d_o; (* back surface is assumed insulated from incident radiation and external losses *)
    A_int_slice IS_A area; A_int_slice = L * 0.5{PI} * d_i; (* front half only, because radial-only wall conduction *)

    k_wall IS_A thermal_conductivity;
    h_ext IS_A heat_transfer_coefficient;
    alpha_eff IS_A fraction;
    T_sun IS_A temperature;

    mdot ALIASES inlet.mdot;
    Nu IS_A factor;
    h_int IS_A heat_transfer_coefficient;
    h_int_eq: h_int = Nu * inlet.k / d_i;

    (* Internal convection correlations: Pr, Re limits for these are defined in the 'default' method below *)
    SELECT(intconv_corr)
    CASE 'dittusboelter':
        (* Dittus-Boelter equation, fluid being heated implies the 0.4 exponent *)
        Nu_DB: Nu = 0.023 * inlet.Re^0.8 * inlet.Pr^0.4;
    CASE 'lyonmartinelli':
        (* as quoted in Pacio et al, 2013, Appl. Thermal Eng 60 and also Liquid Metals Handbook 2nd Ed, 1952. *)
        Nu_int_LM: Nu = 7.0 + 0.025 * (inlet.Re * inlet.Pr/0.85)^0.8;
    CASE 'Gnielinski':
        (* Gnielinski eqn (from Incropera & Dewitt, p 445, all properties are evaluated at the bulk temperature) *)
        Nu_eq: Nu = ((f/8) * (inlet.Re - 1000 ) * inlet.Pr)/( 1 + 12.7 * (f/8)^0.5 * ((inlet.Pr^(2/3)) - 1));
    CASE 'Skupinski':
        (*Liquid metals, turbulent, fully developed, uniform flux*)
        Nu_sku: Nu = 4.82 + 0.0185 * (inlet.Re * inlet.Pr) ^0.827;
    END SELECT;

    (*------------ ENERGY -------------*)

    f "Darcy friction factor" IS_A factor;
    DP_f IS_A delta_pressure;
    SELECT(fric_corr)
    CASE 'smooth':
            (* internal friction factor, using smooth pipe eqn, I&D p 424 *)
            feq_SM: f = (0.790 * ln(inlet.Re) - 1.64 )^-2;
    END SELECT;
    (* pressure drop, use upstream friction factor to simplify calculation? *)
    feq: DP_f = - f * (0.5 * inlet.rho * inlet.vel^2) * L / d_i;

    Q_ext_conv, Q_ext_rad, Q_sun, Q_abs, Q_refl, Q_i IS_A energy_rate;
    T_int, T_ext, T_amb IS_A temperature;
    T_ref ALIASES inlet.ref.T;
    p_ref ALIASES inlet.ref.p;

    Q_abs_eq: Q_abs = Q_sun * alpha_eff;
    Q_refl_eq: Q_refl = Q_sun * (1 - alpha_eff);

    (* external convection *)
    Q_ext_conv_eq: Q_ext_conv = h_ext * A_ext_slice * (T_ext - T_amb);

    eps IS_A factor;
    eps = 0.1477*log10(T_ext-264.6{K}) - 5.671e-6*(T_ext-264.6{K})^1.3078 + 0.4988;
    Q_ext_rad_eq: Q_ext_rad = eps * 1{SIGMA_C} * A_ext_slice * (T_ext^4 - T_amb^4);
```

```
158
159     (* wall conduction, assuming only front half of the pipe *)
160     Q_i_eq0: Q_i = 0.5 * 2{PI} * k_wall * L * (T_ext - T_int) / ln(d_o / d_i);
161     (* wall energy balance *)
162     Q_i_eq1: Q_abs = Q_i + Q_ext_conv + Q_ext_rad;
163     Q_i_eq2: Q_i = h_int * A_int_slice * (T_int - outlet.T);
164     (* MOMENTUM BALANCE *)
165     DP_a IS_A delta_pressure;
166     DP_a = -(outlet.rho*outlet.vel^2 - inlet.rho*inlet.vel^2);
167
168     DP_eq2: outlet.p - inlet.p = DP_f + DP_a;
169
170     (* ENERGY BALANCE *)
171     Q_i_eq3: mdot * ((outlet.h - inlet.h) + 0.5*(outlet.vel^2 - inlet.vel^2) ) = Q_i;
172
173     eta IS_A factor;
174     eta_eq: eta = Q_i / Q_sun; (* sun-to-HTF energy efficiency of a single slice *)
175
176     (*------------ EXERGY --------------*)
177     X_sun, X_abs, X_loss_refl, X_conv, X_dest_abs, X_loss_ext_conv, X_loss_ext_rad
178     , X_dest_wall, X_dest_int_conv, X_dest_flow, X_dest IS_A energy_rate;
179
180     (* Petela's equation for radiation exergy *)
181     X_sun_eq: X_sun = Q_sun * ( 1 - 4./3 * T_ref/T_sun + 1./3 * (T_ref/T_sun)^4);
182
183     (* exergy transfer and destruction over each slice *)
184     X_abs_eq:           X_abs = Q_abs *(1 - T_ref / T_ext); (* exergy transferred from sun to
    pipe exterior *)
185     X_conv_eq:          X_conv = Q_i * (1 - T_ref/outlet.T); (* exergy transferred by
    convection to working fluid *)
186     X_loss_refl_eq:     X_loss_refl = (1 - alpha_eff) * X_sun;
187     X_dest_abs_eq:      X_dest_abs = alpha_eff * X_sun - X_abs; (* destroyed in absorption *)
188     X_loss_ext_conv_eq: X_loss_ext_conv = Q_ext_conv * ( 1 - T_ref / T_ext); (* loss through
    external convection *)
189     X_loss_ext_rad_eq:  X_loss_ext_rad = Q_ext_rad * ( 1 - T_ref/T_ext); (* lost through
    external radiation *)
190     X_dest_wall_eq:     X_dest_wall = Q_i * (T_ref/T_int - T_ref / T_ext); (* destroyed in
    conduction through wall *)
191     X_dest_int_conv_eq: X_dest_int_conv = Q_i * (T_ref/outlet.T - T_ref / T_int); (* destroyed
    in internal convection *)
192     X_dest_flow_eq:     X_dest_flow = X_conv + inlet.X_f - outlet.X_f; (* destroyed due by
    flow friction *)
193
194     (* sum of all exergy destroyed per slice *)
195     X_dest_eq:          X_dest = X_dest_abs + X_dest_wall + X_dest_int_conv + X_dest_flow;
196
197     X_tot_bal IS_A energy_rate;
198     X_tot_bal_eq:       X_tot_bal = X_sun + inlet.X_f - outlet.X_f - X_dest - X_loss_ext_conv
    - X_loss_ext_rad - X_loss_refl;
199
200 METHODS
201 METHOD default;
202     RUN inlet.ref.default;
203     RUN inlet.default;
204     RUN outlet.default;
205 END default;
206 END receiver_flow_segment;
207
208 (*
209     The main receiver model. We will aim to remove the flow segment and put
210     that into a submodel.
211 *)
212 MODEL receiver_base;
213     fluid IS_A symbol_constant;
214     inlet_pu , outlet_pu IS_A fluid_state;
215     inlet_pu.fluid , outlet_pu.fluid, fluid ARE_THE_SAME;
216     T_i, outlet_pu.T ARE_THE_SAME;
217     outlet_pu.p, p_i ARE_THE_SAME;
218     eta_pump IS_A factor;
219     w_pump IS_A negative_specific_work;
220     w_pump = inlet_pu.v * (inlet_pu.p - outlet_pu.p) / eta_pump;
221     outlet_pu.h = inlet_pu.h - w_pump ;
222     outlet_pu_vel ALIASES inlet.vel;
223     inlet_pu_vel ALIASES outlet.vel;
224
225     inlet_pu_X_f, outlet_pu_X_f IS_A energy_rate;
226     inlet_pu_X_f = mdot * ( inlet_pu.h - ref.h - ref.T * (inlet_pu.s - ref.s)+
    0.5*inlet_pu_vel^2);
227     outlet_pu_X_f = mdot * ( outlet_pu.h - ref.h - ref.T * (outlet_pu.s - ref.s)+
    0.5*outlet_pu_vel^2);
228
229     intconv_corr "correlation for internal convection heat transfer" IS_A symbol_constant;
```

```
230
231     (* geometry of the receiver *)
232     W IS_A distance; (* receiver width (flat billboard-style receiver) *)
233     L IS_A distance; (*pipe length *)
234     d_i, d_o IS_A distance; (* pipe outside and inside diameter *)
235     t IS_A distance; (* pipe thickness *)
236     d_o = d_i + 2*t;
237     A_aper IS_A area; (* receiver aperture area *)
238     A_aper = L * W;
239     A_recv IS_A area; (* receiver external surface area, assuming flat cylinder  *)
240     A_recv = 0.5{PI} * A_aper; (* allows for circular tubes, only one half facing outwards *)
241     n_banks IS_A factor; (* number of tube-banks or 'passes' in the receiver*)
242     n_tubes IS_A factor; (* number of parallel tubes in each bank *)
243     n_tubes = W / d_o / n_banks;
244     A_int IS_A area; (* total internal area of receiver pipes *)
245     A_int = (1{PI}* d_i * L) * n_tubes * n_banks;
246
247     L_slice IS_A distance;
248     L_slice_eq: L_slice = L * n_banks / n;
249
250     h_ext IS_A heat_transfer_coefficient;
251     k_wall IS_A thermal_conductivity;
252
253     (* solar input *)
254     C IS_A factor; (* concentration ratio *)
255     G IS_A energy_flux; (* solar irradiance *)
256     alpha IS_A fraction; (* solar-weighted absorptivity of the receiver surface*)
257     alpha_eff IS_A fraction; (* effective solar absorptivity of the receiver surface, assuming
    diffuse and allowing cavity behaviour *)
258     alpha_eff_eq: alpha_eff = alpha /(alpha + 2./1{PI}*(1 - alpha));
259     T_sun IS_A temperature; (* black-body temperature of the sun *)
260     Q_sun, Q_abs, Q_refl IS_A energy_rate; (* incident, absorbed, reflected solar radiation *)
261     Q_eq1: Q_sun = G * C * A_aper;
262     Q_eq2: Q_abs = alpha_eff * Q_sun;
263     Q_eq3: Q_refl = Q_sun - Q_abs;
264     Q_sun_slice IS_A energy_rate;
265     Q_eq4: Q_sun_slice = Q_sun / n / n_tubes;
266
267     (* discretisation of pipes *)
268     n IS_A integer_constant; (* number of slices for calculating pressure drop exergy
    destruction *)
269     seg[0..n-1] IS_A receiver_flow_segment;
270     node[0..n] IS_A fluid_node;
271     inlet, outlet IS_A fluid_node;
272     inlet.fluid, fluid ARE_THE_SAME;
273     inlet.state, node[0].state ARE_THE_SAME;
274     outlet.state, node[n].state ARE_THE_SAME;
275     mdot_1 ALIASES node[0].mdot; (* mass flow rate in ONE of the tubes (n_tubes=# of || paths)
    *)
276     mdot_1 = mdot / n_tubes;
277     mdot ALIASES inlet.mdot;
278     outlet.mdot, inlet.mdot ARE_THE_SAME;
279     FOR i IN [0..n-1] CREATE
280         seg[i].inlet, node[i] ARE_THE_SAME;
281         seg[i].outlet, node[i+1] ARE_THE_SAME;
282         seg[i].intconv_corr, intconv_corr ARE_THE_SAME;
283         seg[i].t, t ARE_THE_SAME;
284         seg[i].L, L_slice ARE_THE_SAME;
285
286         seg[i].h_ext, h_ext ARE_THE_SAME;
287         seg[i].k_wall, k_wall ARE_THE_SAME;
288         seg[i].alpha_eff, alpha_eff ARE_THE_SAME;
289     END FOR;
290
291     seg[0..n-1].Q_sun, Q_sun_slice ARE_THE_SAME;
292
293     node[0..n].d, d_i ARE_THE_SAME;
294     ref IS_A fluid_state;
295     ref.fluid, fluid ARE_THE_SAME;
296     ref, inlet.ref, outlet.ref ARE_THE_SAME;
297     node[0..n].ref, ref ARE_THE_SAME;
298     (*seg[0].T_int, node[0].T ARE_THE_SAME;*)
299
300     (* varying solar flux *)
301     x[0..n-1] IS_A delta_distance;
302     y[0..n-1] IS_A delta_distance;
303     a IS_A integer;
304     (* r[0..n-1] IS_A delta_distance; *)
305
306     T_amb IS_A temperature;
307     ref.T, seg[0..n-1].T_amb, T_amb ARE_THE_SAME;
308     seg[0..n-1].T_sun, T_sun ARE_THE_SAME;
```

```
309
310     p_ref ALIASES ref.p;                T_ref ALIASES ref.T;
311     h_ref ALIASES ref.h;                s_ref ALIASES ref.s;
312     T_i ALIASES inlet.T;                T_o ALIASES outlet.T;
313     p_i ALIASES inlet.p;                p_o ALIASES outlet.p;
314     s_o ALIASES outlet.s;               h_o ALIASES outlet.h;
315     h_i ALIASES inlet.h;                s_i ALIASES inlet.s;
316     vel_out ALIASES outlet.vel;
317
318     T_i_pu ALIASES inlet_pu.T;          P_i_pu ALIASES inlet_pu.p;
319
320     T_amb, T_ref ARE_THE_SAME;
321
322     F_safety IS_A factor;
323     sigma_allow IS_A stress;
324     t_eq: t = 0.5 * p_i * d_o * F_safety / sigma_allow;
325
326     Q_i_tot, Q_ext_conv_tot, Q_ext_rad_tot, Q_tot IS_A energy_rate;
327     Q_i_tot = n_tubes * SUM[seg[i].Q_i | i IN [0..n-1]];
328     Q_ext_conv_tot = n_tubes * SUM[seg[i].Q_ext_conv | i IN [0..n-1]];
329     Q_ext_rad_tot = n_tubes * SUM[seg[i].Q_ext_rad | i IN [0..n-1]];
330     Q_tot = Q_sun - Q_refl - Q_i_tot - Q_ext_conv_tot - Q_ext_rad_tot;
331
332     T_ext_ave IS_A temperature;
333     T_ext_ave = SUM [seg[i].T_ext | i IN [0..n-1]] / n;
334
335     Re_ave IS_A factor;
336     Re_ave = SUM [seg[i].inlet.Re | i IN [0..n-1]] / n;
337
338     T_ext_max ALIASES seg[n-1].T_ext;
339
340
341     DP IS_A delta_pressure;
342     DP = p_o - p_i;
343
344     (* exergy accounting *)
345     X_loss_refl IS_A energy_rate;
346     X_sun IS_A energy_rate;
347     X_sun_1 IS_A energy_rate;
348     X_sun_eq: X_sun_1 = Q_sun * ( 1 - 4./3 * T_ref/T_sun + 1./3 * (T_ref/T_sun)^4);
349     X_in, X_out IS_A energy_rate;
350
351     X_abs_tot, X_dest_tot, X_dest_abs_tot, X_loss_refl_tot, X_loss_ext_conv_tot
352     , X_loss_ext_rad_tot, X_dest_wall_tot, X_dest_int_conv_tot
353     , X_dest_flow_tot, X_net, X_conv_tot IS_A energy_rate;
354
355     X_eq0: X_sun =              n_tubes * SUM[seg[i].X_sun | i IN [0..n-1]];
356     X_eq1: X_abs_tot =          n_tubes * SUM[seg[i].X_abs | i IN [0..n-1]];
357     X_eq2: X_conv_tot =         n_tubes * SUM[seg[i].X_conv | i IN [0..n-1]];
358     X_eq3: X_dest_tot =         n_tubes * SUM[seg[i].X_dest | i IN [0..n-1]];
359     X_eq4: X_dest_abs_tot =     n_tubes * SUM[seg[i].X_dest_abs | i IN [0..n-1]];
360     X_eq5: X_loss_ext_conv_tot=n_tubes * SUM[seg[i].X_loss_ext_conv | i IN [0..n-1]];
361     X_eq6: X_loss_ext_rad_tot= n_tubes * SUM[seg[i].X_loss_ext_rad | i IN [0..n-1]];
362     X_eq7: X_dest_wall_tot =    n_tubes * SUM[seg[i].X_dest_wall | i IN [0..n-1]];
363     X_eq8: X_dest_int_conv_tot=n_tubes * SUM[seg[i].X_dest_int_conv | i IN [0..n-1]];
364     X_eq9: X_dest_flow_tot =    n_tubes * SUM[seg[i].X_dest_flow | i IN [0..n-1]];
365     X_eqa: X_loss_refl_tot =    n_tubes * SUM[seg[i].X_loss_refl | i IN [0..n-1]];
366
367     X_i ALIASES inlet.X_f;
368     X_o ALIASES outlet.X_f;
369     X_i_1 ALIASES node[0].X_f;
370     X_o_1 ALIASES node[n].X_f;
371     X_i_n, X_o_n IS_A energy_rate;
372     X_i_n = X_i_1 * n_tubes;
373     X_o_n = X_o_1 * n_tubes;
374
375     (* exergy that is loss because it leaves the system *)
376     X_loss_refl_eq: X_loss_refl = (1 - alpha_eff) * X_sun;
377     X_in = X_i + X_sun;
378     X_out = X_loss_refl + X_loss_ext_conv_tot + X_loss_ext_rad_tot + X_o;
379     X_net = X_o - X_i;
380
381     X_tot1 IS_A energy_rate;
382     X_tot1 = X_sun + inlet.X_f - outlet.X_f - X_dest_tot - X_loss_ext_conv_tot -
    X_loss_ext_rad_tot - X_loss_refl_tot;
383
384     X_tot2 IS_A energy_rate;
385     X_tot2 = SUM[ seg[i].X_tot_bal | i IN [0..n-1]];
386
387     (* first-law efficiency *)
388     eta_1 IS_A factor;
389     eta_1 = Q_i_tot / Q_sun;
390
```

```
391     (* second-law efficiency *)
392     eta_2  IS_A factor;
393     (*eta_2_eq: eta_2 = X_net/ X_sun;*)
394     eta_2_eq: eta_2 = (outlet.X_f - inlet.X_f)/ X_sun;
395
396     (* size the inlet/outlet pipes to give same flow velocity *)
397     inlet.vel = node[0].vel;
398     outlet.vel = node[n].vel;
399
400     Wdot IS_A energy_rate;
401     Wdot = -mdot * w_pump;
402     eta_2_pump, eta_1_PB, eta_2_PB IS_A factor;
403     (*eta_1_overall, eta_1_overall = (Q_i_tot - Wdot/eta_1_PB) / Q_sun;*)
404     eta_2_pump = (outlet_pu_X_f - inlet_pu_X_f)/ Wdot;
405
406     Wdot_net, Wdot_elec, Wdot_pump, X_dest_PB, X_dest_PU IS_A energy_rate;
407     eta_2_system IS_A factor;
408     Wdot_net = Wdot_elec - Wdot_pump;
409     Wdot_elec = eta_2_PB * (outlet.X_f - inlet_pu_X_f);
410     Wdot_pump = Wdot;
411     eta_2_system = Wdot_net / X_sun;
412     X_dest_PB = (1-eta_2_PB) * (outlet.X_f - inlet_pu_X_f);
413     X_dest_PU = Wdot - (outlet_pu_X_f - inlet_pu_X_f);
414
415
416     (* consistency checks *)
417     X_bal_abs, X_bal_wall, X_bal_flow, X_bal_tot, CV_1_bal_tot, CV_3_bal_tot IS_A energy_rate;
418     X_bal_abs = alpha_eff * X_sun - X_abs_tot - X_dest_abs_tot;
419     X_bal_wall = X_abs_tot - X_loss_ext_conv_tot - X_loss_ext_rad_tot - X_dest_wall_tot -
    X_dest_int_conv_tot - X_conv_tot;
420     X_bal_flow = X_conv_tot + X_i - X_dest_flow_tot - X_o;
421     X_bal_tot = X_in - X_out - X_dest_tot;
422
423     CV_1_bal_tot = inlet_pu_X_f + Wdot_pump - inlet.X_f - X_dest_PU;
424     CV_3_bal_tot = outlet.X_f - inlet_pu_X_f - Wdot_elec - X_dest_PB;
425
426 METHODS
427     METHOD set_common_parameters;
428         FIX C := 800;
429         FIX G := 1000 {W/m^2};
430         FIX T_sun := 5800 {K};
431         FIX A_aper := 100 {m^2};
432         FIX p_ref := 1 {bar};
433         FIX T_ref := 20{K} + 273.15{K};
434         FIX sigma_allow := 32.8{MPa};
435         FIX k_wall := 20 {W/m/K};
436         FIX alpha := 0.95;
437         FIX h_ext := 30 {W/m^2/K};
438         FIX eta_pump:= 0.8;
439         FIX eta_1_PB:= 0.38;
440         FIX eta_2_PB:= 0.75;
441     END set_common_parameters;
442
443     METHOD plot_recv;
444         EXTERNAL plot_receiver_profiles_sodium_corr(SELF);
445     END plot_recv;
446
447     METHOD plot_Sankey;
448         EXTERNAL plot_sankey(SELF);
449     END plot_Sankey;
450
451     METHOD on_load;
452         RUN default;
453     END on_load;
454
455     METHOD default;
456         FOR i IN [0..n] DO
457             RUN node[i].default;
458         END FOR;
459         RUN ref.default;
460
461         SWITCH(intconv_corr)
462         CASE 'dittusboelter':
463             node[0..n].Pr.lower_bound := 0.6;
464             node[0..n].Pr.upper_bound := 160;
465             node[0..n].Re.lower_bound := 10000;
466         CASE 'lyonmartinelli':
467             node[0..n].Pr.lower_bound := 0.0001; (* guess *)
468             node[0..n].Pr.upper_bound := 0.1; (* guess *)
469             node[0..n].Re.lower_bound := 100; (* guess *)
470             node[0..n].Re.upper_bound := 2e6; (* guess *)
```

```
471         CASE 'Gnielinski':
472             node[0..n].Pr.lower_bound := 0.5;
473             node[0..n].Pr.upper_bound := 2000;
474         CASE 'Skupinski':
475             node[0..n].Pr.lower_bound := 3e-3;
476             node[0..n].Pr.upper_bound := 5e-2;
477             node[0..n].Re.lower_bound := 3.6e3;
478         END SWITCH;
479 
480         (* constraints, we want errors if the following aren't satisfied: *)
481         F_safety.lower_bound := 1;
482 
483         (* initial guesses, bounds and scaling, to help model to solve *)
484         Q_abs.nominal := 100 {MW};
485         seg[0..n-1].Q_abs.nominal :=  Q_abs.nominal / n * d_o / W;
486         seg[0..n-1].Q_i.nominal :=  Q_abs.nominal / n;
487         seg[0..n-1].Q_ext_conv.nominal :=  Q_abs.nominal / n;
488         seg[0..n-1].Q_ext_rad.nominal :=  Q_abs.nominal / n;
489         A_recv.nominal := 200 {m^2};
490         A_aper.nominal := 200 {m^2};
491         A_int.nominal := 200 {m^2};
492 
493         seg[0..n-1].T_ext := 701 {K};
494         seg[0..n-1].T_ext.upper_bound := 2000 {K};
495         seg[0..n-1].T_int := 700 {K};
496         seg[0..n-1].h_int.nominal := 500 {W/m^2/K};
497         seg[0..n-1].h_int := 1000 {W/m^2/K};
498         node[0..n].u.lower_bound := -10000 {kJ/kg};
499         node[0..n].p.lower_bound := 1 {bar};
500 
501         X_dest_tot.lower_bound := 0 {W};
502         X_dest_abs_tot.lower_bound := 0 {W};
503         X_dest_int_conv_tot.lower_bound := 0 {W};
504         X_dest_wall_tot.lower_bound := 0 {W};
505         X_loss_refl.lower_bound := 0 {W};
506         X_loss_ext_conv_tot.lower_bound := 0 {W};
507         X_loss_ext_rad_tot.lower_bound := 0 {W};
508         outlet_pu.T.upper_bound := 1000 {K} + 273.15 {K};
509         outlet_pu.T.lower_bound := 290 {K} + 273.15 {K};
510 
511     END default;
512 END receiver_base;
513 
514 MODEL receiver_salt REFINES receiver_base;
515     fluid :== 'moltensalt';
516     intconv_corr :== 'Gnielinski';
517     n :== 100;
518 METHODS
519     METHOD on_load;
520         RUN set_common_parameters;
521         RUN default;
522         node[0..n].Re := 10000;
523 
524         FIX n_banks :=10;
525         FIX t := 3.68 {mm};
526         FIX d_o := 48.3 {mm};
527         FIX L := 10 {m};
528         FIX p_i := 10 {bar};
529         FIX inlet_pu.p := 1{bar};
530         FIX inlet_pu.T := 290 {K} + 273.15 {K};
531         FIX mdot := 150 {kg/s};
532         FOR i IN [1..n] DO
533             node[i].p := node[i-1].p - 0.01 {bar};
534         END FOR;
535         SOLVER QRSlv;
536         OPTION convopt 'RELNOM_SCALE';
537         OPTION iterationlimit 10000;
538         OPTION feastol 1e-8;
539         OPTION maxminor 100;
540     END on_load;
541     METHOD solve_T_o;
542         FREE mdot;
543         FIX T_o := 565 {K} + 273.15 {K};
544         FREE p_i;
545         FIX p_o := 1 {bar};
546         SOLVER QRSlv;
547         OPTION convopt 'RELNOM_SCALE';
548     END solve_T_o;
549 END receiver_salt;
550 
```

Appendix B The internal heat transfer correlation for two-phase water/steam

For $0 < x \leq 0.8$, the Kandlikar correlation is used:

$$h_{TP}/h_{lo} = \text{maximum of} \begin{cases} [h_{TP}/h_{lo}]_{\text{NBD}} \\ [h_{TP}/h_{lo}]_{\text{CBD}} \end{cases} \tag{B.1}$$

where h_{TP} refers to heat transfer coefficient during two-phase flow and h_{lo} refers to heat transfer coefficient with total flow as liquid. The subscripts NBD and CBD indicate the nucleate boiling dominant (NBD) and Convective boiling dominant (CBD) regions, as follow:

NBD region:

$$[h_{TP}/h_{lo}]_{\text{NBD}} = 0.6683 \left(\rho_{\text{L}}/\rho_{\text{V}}\right)^{0.1} x^{0.16} (1-x)^{0.64} + 1058.0\text{Bo}^{0.7} (1-x)^{0.8} \tag{B.2}$$

CBD region:

$$[h_{TP}/h_{lo}]_{\text{CBD}} = 1.1360 \left(\rho_{\text{L}}/\rho_{\text{V}}\right)^{0.45} x^{0.72} (1-x)^{0.08} + 667.2\text{Bo}^{0.7} (1-x)^{0.8} \tag{B.3}$$

where the subscripts L and V refer to liquid and vapour states. Bo refers to boiling number (Bo$= \dot{q}\left(\frac{\rho_{\text{L}} v_{\text{L}}}{h_{\text{V}} - h_{\text{L}}}\right)$).

Therefore, for Re < 10^5:

$$\text{Nu} = (h_{TP}/h_{lo}) \frac{\frac{f_D}{8} (\text{Re}_D - 1000)\,\text{Pr}}{1 + 12.7 \left(\frac{f_{\text{D}}}{8}\right)^{0.5} \left(\text{Pr}^{\frac{2}{3}} - 1\right)} \tag{B.4}$$

for Re$\geq 10^5$:

$$\text{Nu} = (h_{TP}/h_{lo}) \frac{\frac{f_D}{8} (\text{Re}_D \text{Pr})}{1.07 + 12.7 \left(\frac{f_{\text{D}}}{8}\right)^{0.5} \left(\text{Pr}^{\frac{2}{3}} - 1\right)} \tag{B.5}$$

For $0.8 < x \leq 1$, the Groeneveld correlation is used:

$$\text{Nu} = 0.00109 \left[\text{Re}_D \left(x + \rho_{\text{V}}/\rho_{\text{L}} (1-x)^{0.989}\right)\right] \text{Pr}_{\text{V}}^{1.41} \Upsilon^{-1.15} \tag{B.6}$$

where $Y = 1 - 0.1\left(\rho_{\mathrm{V}}/\rho_{\mathrm{L}}\right)^{0.4}(1-x)^{0.4}$

Appendix C The effects of varying the external wall temperatures in the circumferential direction (i.e. $\overline{(T_{\text{ext}})^4}$ vs $\overline{T_{\text{ext}}}^4$)

In Chapter 2, uniform temperature at the outer surface of the tubes is assumed, which might lead to inaccuracies that could ultimately affect the results and the comparison of different HTFs. In order to examine this question, we have had conducted supplementary analyses relating to this effect. We provide five analysis cases:

In the first Case C1, we have the same model and results that are provided in Section 2.5 of Chapter 2. This is the case of a tube supplied with heat either uniformly across its front half, and with effective absorptivity as determined using Eq. C.7. The rear half of the tube is assumed to be adiabatic:

$$\alpha_{\text{eff}} = \frac{\alpha}{\alpha + \frac{2(1-\alpha)}{\pi}} = 0.9676 \tag{C.7}$$

Surface emissivity[1] is determined using Eq. C.8, with no effective emissivity being calculated:

$$\epsilon_i = 0.1477 \log_e \left(T_{\text{ext},i} - 264.6\text{K}\right) - 5.671 \times 10^{-6} \left(T_{\text{ext},i} - 264.6\text{K}\right)^{1.3078} + 0.4988 \tag{C.8}$$

The incident irradiance is determined using the local optical concentration ratio (CG) multiplied by the presented area of the tube (with external diameter d_o). The absorbed energy on each tube element is then calculated using Eq. C.9, where $CG = 800\ \text{kW/m}^2$:

$$\dot{Q}'_{\text{abs},i} = \alpha_{\text{eff}} CG d_o \tag{C.9}$$

The circumferential tube is equally divided into 60 sectors, with uniform flux being applied to the front 30 sectors, while the back 30 sectors are assumed to be adiabatic. The thermal emission loss for the sector i on the external surface is calculated

[1]The emissivity value ϵ_i is given for Pyromark 2500 on cold-rolled steel at 600°C, as a function of external surface temperature in Kelvin, which refers to the total hemispherical emittance.

as:

$$\dot{Q}'_{\text{ext,rad},i} = \epsilon_i \sigma A_{\text{ext},i} \left(T^4_{\text{ext},i} - T^4_{\text{amb},i} \right) \tag{C.10}$$

where $A_{\text{ext},i} = \frac{\pi d_o}{n_{\text{sectors}}}$ and $n_{\text{sectors}} = 60$ in this analysis, and σ is the Stefan-Boltzmann constant. $\dot{Q}'_{\text{ext,rad},i} = 0$ kW/m for the sectors on the rear half of the tube.

External convection loss,$\dot{Q}'_{\text{ext,conv},i}$, on the front half of the tube are calculated as:

$$\dot{Q}'_{\text{ext,conv},i} = h_{\text{ext}} A_{\text{ext},i} \left(T_{\text{ext},i} - T_{\text{amb},i} \right) \tag{C.11}$$

$\dot{Q}'_{\text{ext,conv},i} = 0$ kW/m for the sectors on the rear half of the tube.

We note that, as in Chapter 2, the convection coefficient $h_{\text{ext}} = 30$ W/(m^2·K).

In Case C2, we use the same model of Case C1, but consider effective emissivity at the front half of the tube. If a two-surface diffuse grey-body radiation problem is considered inside a cavity i and the surroundings s. The view factor can be calculated by imagining a surface o covering the opening. We can say that $F_{o\to i} = 0$ for the opening, and hence by reciprocity $F_{o\to i} = A_o/A_i$, and this is equal to $F_{i\to s}$. The net radiation exchange of surface A_i, with a large surrounding surface A_s, is given by:

$$q_{i\to s} = \frac{(E_{bi} - E_{bs})}{[(1-\epsilon_i)/\epsilon_i A_i + 1/A_i] F_{i\to s}} \tag{C.12}$$

and the net radiation exchange of an imaginary surface A_o having an apparent emissivity ϵ_a, is given by:

$$q_{o\to s} = \epsilon_a A_o (E_{bi} - E_{bs}) \tag{C.13}$$

for A_o at the same temperature at the cavity surface A_i.

For the same heat transfer in both cases, we must have:

$$\frac{1-\epsilon_i}{\epsilon_i A_i} = \frac{1-\epsilon_o}{\epsilon_o A_o} \tag{C.14}$$

which, solving for ϵ_o gives

$$\epsilon_o = \frac{\epsilon_i}{\epsilon_i + \frac{A_o(1-\epsilon_i)}{A_o}} \tag{C.15}$$

Thus, in Case C2, the effective emissivity is calculated as follows:

$$\epsilon_{\text{eff},i} = \frac{\epsilon_i}{\epsilon_i + \frac{2(1-\epsilon_i)}{\pi}} \tag{C.16}$$

where $2/\pi$ compensates the cavity behaviour on a per-aperture-area basis at the front half of the tube (πr) to allow for the two-surface radiosity that will occur in the

crevices ($2r$) between tubes.

In Case C3, we consider a non-uniform distribution of absorbed flux across its front half according to a cosine profile ($\dot{Q}'_{abs,i} = \alpha_{eff} C G A_{ext,i} \cos(\theta)$,where the absorbed flux is symmetrical about the angular coordinate $\theta = 0°, 180°$), with scaling applied to ensure the same total absorbed energy per tube section as in Case C1. The cosine profile is applied to estimate the reduction of the absorbed energy due to cosine effect. The cosine profile shows a good match to the flux profile provided in a report by Tilley et al. [153]. The effect of the circumferential variation in effective absorptivity is not considered, which will be higher in the crevices. This is considered to be a second-order effect, due to the small increase arising due to this effect, whereas the cosine distribution is a first-order effect, varying the absorbed flux between zero at the base of the crevice and a peak value at the crest. The emissivity ϵ_i of the receiver surface in Case C3 is considered the same as Case C1, using Eq. C.8.

In Case C4, we consider the same absorbed flux distribution as Case C3, but we additionally make allowances for the varying view factors arising at different circumferential positions. In the crevice between adjacent tubes, the view factor from the tube surface to the surroundings is lower than at the crest of the tube. In this case, we made use of the basic surface emissivity (as defined in Eq. C.8). In addition, we assume the neighbouring tubes are experiencing identical HTF flow and irradiation conditions, such that they establish identical external surface temperature distributions as the present tube. The Hottel crossed-string rule, as shown below in Fig. C.1, is applied in the calculation of 2D view factors. The cases shown in the calculations below Fig. C.1 cover all possible cases. The view factor from the tube to itself is always zero. As L_1 or L_2 moves, the angles α_1–α_4 change accordingly. The view factor between the tube and the surroundings is calculated by elimination ($1 - \sum_{j=0}^{14} F_{i \to j}$).

In Case C5, we consider the uniform absorbed flux distribution as Case C1, but we add view factors in this case.

If $\measuredangle\alpha_1 < \measuredangle\alpha_2$:

$$F_{i \to j} = \frac{(L_5 + L_6) - (L_3 + L_4)}{2L_1} \tag{C.17}$$

else if $\measuredangle\alpha_2 < \measuredangle\alpha_1$ and $\measuredangle\alpha_3 < \measuredangle\alpha_4$:

$$F_{i \to j} = \frac{\left(nL_1 + L_3' + L_6\right) - (L_3 + L_4)}{2L_1} \tag{C.18}$$

else:

$$F_{i \to j} = 0 \tag{C.19}$$

where $n = 2$ in the right example of Fig. C.1, and L_3' is the length of the dashed

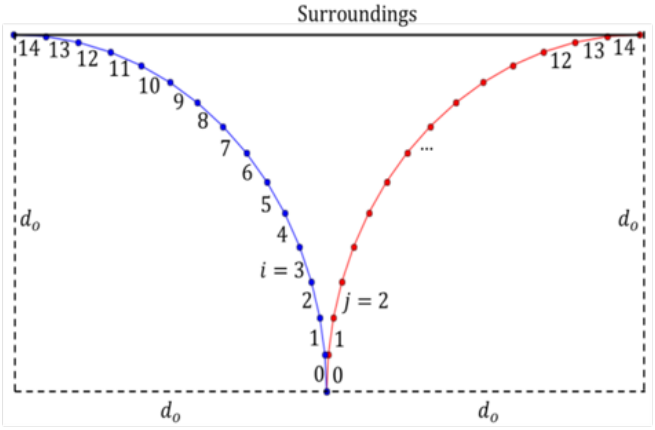

(a) A demonstration of the front quarter-tube and its adjacent quarter-tube and the model notation.

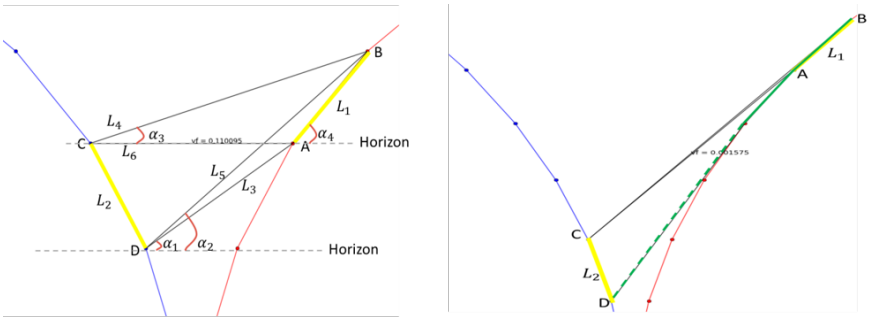

(b) Examples of the calculation of view factors for the space between tubes. In the right figure, L_3 =A-AA (i.e. L_1) + L_3'; $L_4 = L_6 + L_1$; $L_5 = L_1 + L_3$; L_6 = C-A.

Fig. C.1: View factors

green line.

In the radiosity analysis, we assume that in the thermal band, all emission occurs in the >2.5 μm wavelength range, the emissivity and the absorptivity are the same following Kirchhoff's law and are defined as function of temperatures (as shown in Eq. C.8). Incoming radiation, R_i, is the sum of the appropriate share of radiosity from all j surfaces of the other tube ($A_i = A_j$) and from the surrounding surface, which is calculated, using view factor reciprocity ($A_i F_{i\to j} = A_j F_{j\to i}$ and $A_i F_{i\to sur} = A_{sur} F_{sur\to i}$), as:

$$R_i = \sum_{j=1}^{n} J_j F_{i\to j} + \sigma T_{amb}^4 F_{i\to sur} \tag{C.20}$$

The outgoing radiation, J_i is the combination of the local emissive flux and the reflected portion of the irradiance:

$$J_i = \epsilon_i \sigma T_{ext,i}^4 + (1-\epsilon_i)\, R_i \tag{C.21}$$

Total absorbed energy is the sum of the net radiation energy leaving the surface, the external convection loss and the net energy to the fluid, where $\dot{Q}'_{net,leaving,rad,i} = \frac{\epsilon_i A_i \left(\sigma T_{ext,i}^4 - J_i\right)}{1-\epsilon_i}$. The energy balance for the outer surface of the tube wall is:

$$\dot{Q}'_{abs,i} = \dot{Q}'_{net,leaving,rad,i} + \dot{Q}'_{ext,conv,i} + \dot{Q}'_{int,i} \tag{C.22}$$

The local first law efficiency is then:

$$\eta_I = \frac{\sum_i^n \dot{Q}'_{int,i}}{\sum_i^n \dot{Q}'_{inc,i}} \tag{C.23}$$

$\dot{X}'_{sun,i}$ indicates the total exergy in incident sunlight and is calculated using the Petela formula [136], as follows:

$$\dot{X}'_{sun,i} = \dot{Q}'_{inc,i} \left(1 - \frac{4}{3}\frac{T_{ref}}{T_{sun}} + \frac{1}{3}\left(\frac{T_{ref}}{T_{sun}}\right)^4\right) \tag{C.24}$$

$\dot{X}'_{int,i}$ indicates the net exergy gain with the working fluid, as follows:

$$\dot{X}'_{int,i} = \dot{Q}'_{int,i} \left(1 - \frac{T_{ref}}{T_{HTF}}\right) \tag{C.25}$$

The local second law efficiency is then:

$$\eta_{II} = \frac{\sum_i^n \dot{X}'_{int,i}}{\sum_i^n \dot{X}'_{sun,i}} \tag{C.26}$$

We note that the above equations are coupled with the existing model as mentioned in Chapter 2, but Eq. C.17–C.22 are used to re-calculate $\dot{Q}'_{abs,i}$ for Case C4,

instead of using Eq. C.9. The internal convection coefficient is assumed uniform circumferentially even though this may not be true in practice. Tube conduction is assumed to be purely radial.

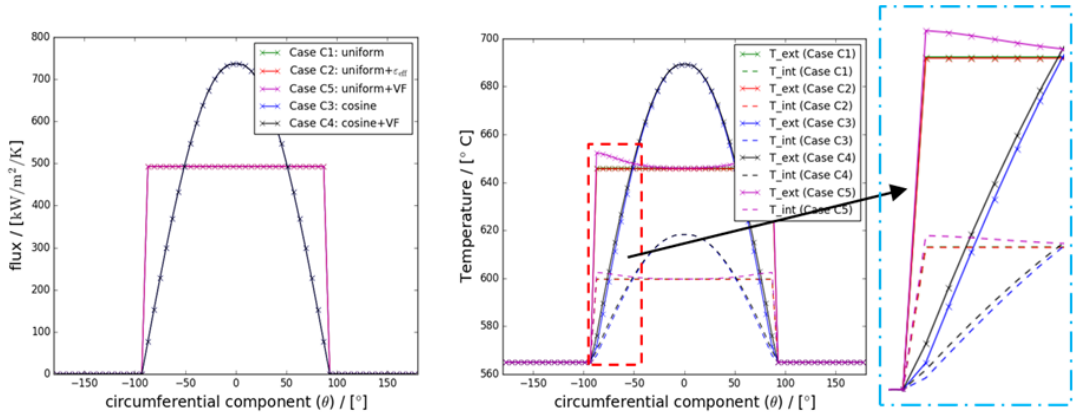

(a) Flux profiles

(b) Temperature profiles

Fig. C.2: Molten salt is selected as the HTF in the receiver, with T_{HTF} = 565°C. (a) flux profiles in the circumferential direction of the tube and (b) the corresponding inner and outer wall temperature profiles. The peak flux ($\dot{q}'_{abs}$) of Case C3 and Case C4 is 736.19 kW/(m^2·K), and of Case C1, Case C2 and Case C5 is 492.79 kW/(m^2·K) on the unfolded surface. The uniform flux is equivalent to the flux used in Chapter 2. The outer diameter of the tube is 10.3 mm and hence, the plot area (i.e. the circumference of a circle) is 32.36 mm (i.e. πd_o) considering the tube as a 2D circle, not a 3D cylinder. The rear half of the tube is assumed to be adiabatic.

Fig.C.2(a) shows the absorbed flux profiles of the five cases. Fig. C.2(b) shows the external and the inner wall temperatures of the five cases. The more detailed external wall temperatures of the quarter-tube are shown in Fig. C.3. For Case C2, the external wall temperatures are slightly lower than they were in Case C1 due to the consideration of the effective emissivity. The wall temperature at the crevice for Case C4 (with the view factor effects) is slightly higher since the radiation is trapped and hence, it is more difficult for it to leave than it was in Case C3 (see Fig. C.3). At the crest of the tube, almost all of the radiation is emitted to the surroundings, and therefore, the wall temperature ($T_{ext,wall,sector\ 14} = 689.20°C$) is as same as it was in Case C3 ($T_{ext,wall,sector\ 14} = 689.20°C$). Detailed $\dot{Q}'_{ext,rad}$ and $\dot{Q}'_{ext,conv}$ breakdown for Case C1, C2, C3, C4 and C5 are shown in Fig. C.3. This figure also compares the difference between different cases.

Energy and exergy accountings for five cases with different flux profiles are shown in Table C.2. To summarise, a cosine circumferential wall temperature profile with no effect of view factors (Case C3) results in a *reduction* in the first- and second-law efficiency by **0.07**% and **0.06**% when compared to the case of uniform wall temperature (Case C1) with no view factor being considered. By adding view factors, the first- and second-law efficiencies are reduced by 0.44% and 0.3% when compare Case C5 and C4. However, if the most realistic case (Case C4) is compared

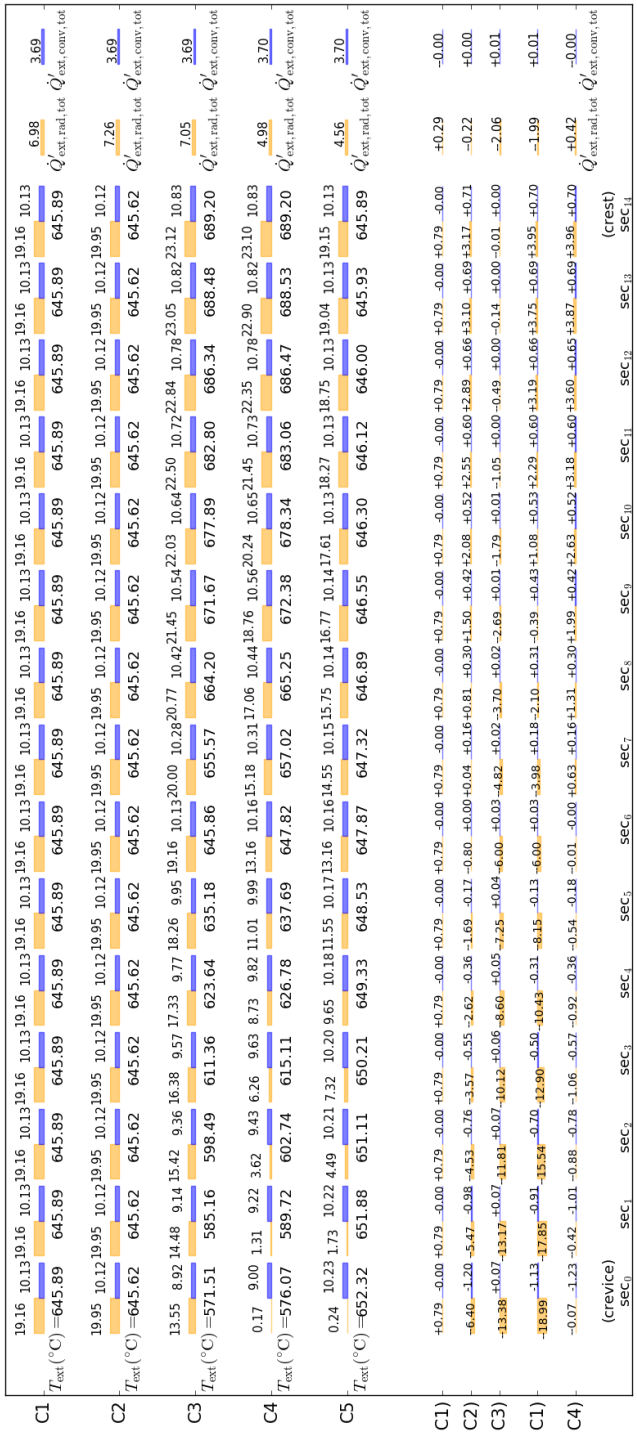

Fig. C.3: Detailed $\dot{Q}'_{\text{ext,rad}}$ and $\dot{Q}'_{\text{ext,conv}}$ breakdown for molten salt Case C1, C2, C3, C4 and C5 at 565°C and the corresponding difference between cases. Units are in %. The corresponding $T_{\text{ext,wall},i}$ are plotted below each case. $\dot{Q}'_{\text{ext,rad}}$ and $\dot{Q}'_{\text{ext,conv}}$ are plotted in orange and blue, respectively. The percentage plots of $\dot{Q}'_{\text{ext,rad},i}$ and $\dot{Q}'_{\text{ext,conv},i}$ on local sectors are the local percentage losses, while $\dot{Q}'_{\text{ext,rad,tot}}$ and $\dot{Q}'_{\text{ext,conv,tot}}$ are the overall percentage losses.

$$\eta_{\text{ext,rad,loss},i} = \frac{\dot{Q}'_{\text{ext,rad},i}}{\dot{Q}'_{\text{inc},i}} \times 100 \text{ and } \eta_{\text{ext,conv,loss},i} = \frac{\dot{Q}'_{\text{ext,conv},i}}{\dot{Q}'_{\text{inc},i}} \times 100.$$

to the case used in the Chapter 2 (Case C1), the first- and second-law efficiency, however, is *increased* by **1.98**% and **1.38**%.

Table C.2: Energy and exergy accounting for five cases with different flux profiles. HTF: molten salt. $T_{HTF} = 565°C$. $d_o = 10.3$ mm, $t = 1.73$ mm. $CG = 800$ kW/m^2

	$\dot{Q}'_{inc}$ kW/m	$\dot{Q}'_{refl}$ kW/m	$\dot{Q}'_{abs}$ kW/m	$\dot{Q}'_{ext,rad}$ kW/m	$\dot{Q}'_{ext,conv}$ kW/m	$\dot{Q}'_{int}$ kW/m	η_I %	$\dot{X}'_{sun}$ kW/m	$\dot{X}'_{int}$ kW/m	$\eta_{I,rec}$ %
C1	8.240	0.267	7.973	0.575	0.304	7.094	86.09	7.68	4.613	60.07
C2	8.240	0.267	7.973	0.599	0.304	7.071	85.81	7.68	4.598	59.87
C3	8.240	0.267	7.973	0.581	0.304	7.088	86.02	7.68	4.609	60.01
C4	8.240	0.267	7.973	0.411	0.305	7.257	88.07	7.68	4.719	61.45
C5	8.240	0.267	7.973	0.376	0.305	7.293	88.51	7.68	4.742	61.74

where in Case C4, $\dot{Q}'_{ext,rad,i} = \left(J_i - \sigma T_{amb}^4\right) F_{i\rightarrow sur} A_i, T_{amb} = 293.15$ K.

Another study is conducted to examine the effect of varying circumferential wall temperature at higher wall temperature and with sodium as the heat transfer fluid, as shown in Fig. C.4 and Fig. C.6. In this scenario, high temperature sodium is selected and T_{HTF} is equal to 740°C. This study (results are shown in Table C.3) shows that, at higher wall temperatures, the effect of applying a view factor on energy efficiencies is higher than at lower wall temperatures. The first- and second-law efficiencies increase from 79.63% (Case C1) to 83.56% (Case C4) and from 60.70% to 63.71%, which give **3.93**% and **3.01**% increase in efficiencies. The study shows that the effect of view factors is more significant than the effect of varying circumferential tube wall temperature, as only 0.43% and 0.33% in the first- and second-law efficiencies reduction (compare Case C4 and C5) are shown due to the variation of the circumferential tube wall temperature.

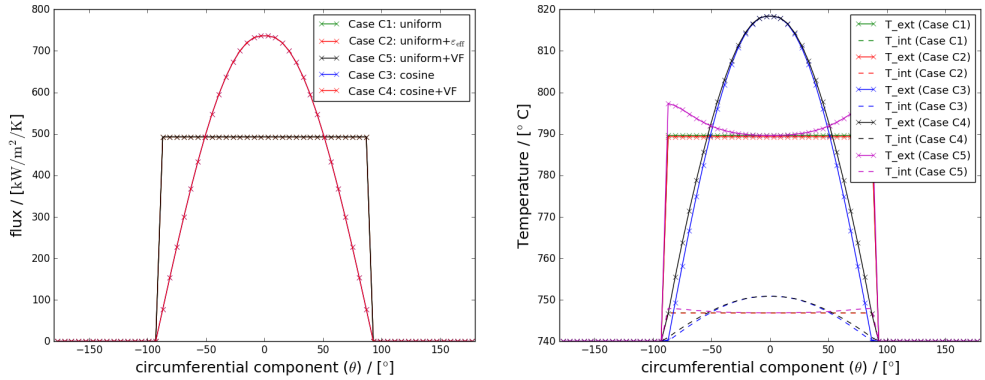

Fig. C.4: Liquid sodium is selected as the HTF in the receiver, with $T_{HTF} = 740°C$. Left: flux profiles in the circumferential direction of the tube. Right: the corresponding inner and outer wall temperature profiles. The peak flux ($\dot{q}'_{abs}$) of Case C3 and Case C4 is 736.19 kW/(m^2·K), and of the uniform flux (Case C1, Case C2 and Case C5) is 492.79 kW/(m^2·K). The outer diameter of the tube is 10.3 mm. The rear half of the tube is assumed to be adiabatic.

Table C.3: Energy and exergy accounting for five cases with different flux profiles. HTF: liquid sodium. $T_{HTF} = 740°C$. $d_o = 10.3$ mm, $t = 1.73$ mm. $CG = 800$ kW/m^2

	$\dot{Q}'_{inc}$ kW/m	$\dot{Q}'_{refl}$ kW/m	$\dot{Q}'_{abs}$ kW/m	$\dot{Q}'_{ext,rad}$ kW/m	$\dot{Q}'_{ext,conv}$ kW/m	$\dot{Q}'_{int}$ kW/m	η_I %	$\dot{X}'_{sun}$ kW/m	$\dot{X}'_{int}$ kW/m	$\eta_{I,rec}$ %
C1	8.240	0.267	7.973	1.038	0.374	6.562	79.63	7.68	4.662	60.70
C2	8.240	0.267	7.973	1.079	0.373	6.531	79.14	7.68	4.634	60.34
C3	8.240	0.267	7.973	1.041	0.374	6.558	79.59	7.68	4.661	60.69
C4	8.240	0.267	7.973	0.713	0.375	6.885	83.56	7.68	4.893	63.71
C5	8.240	0.267	7.973	0.679	0.375	6.921	83.99	7.68	4.918	64.04

Lastly, a study on air (Fig. C.5 and Table C.4) is conducted to examine the effect of varying circumferential wall temperature at higher temperature difference between the front and rear walls and at larger tube diameter, as air has poor heat transfer. In this case, the maximum circumferential ΔT is about 300°C and the outer tube diameter is 48.3 mm. The study shows larger effects on the efficiencies due to the variation of the circumferential tube wall temperature, which results in 1.41% and 0.92% in the first- and second-law efficiencies reduction (compare Case C4 and C5).

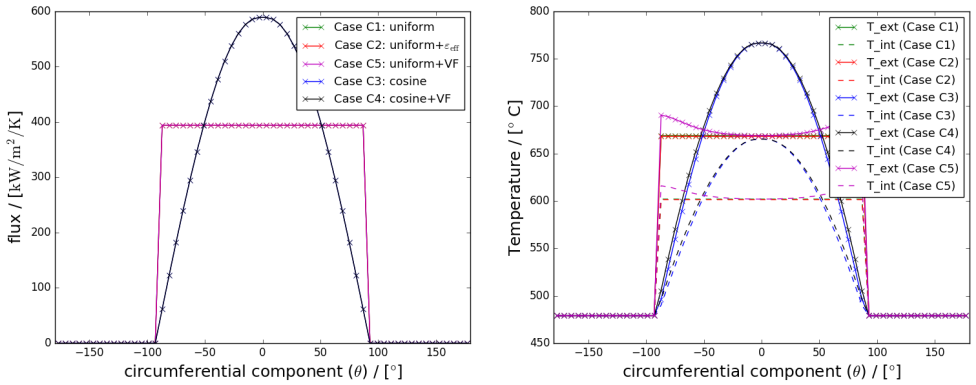

Fig. C.5: Air is selected as the HTF in the receiver, with $T_{HTF} = 479°C$. Left: flux profiles in the circumferential direction of the tube. Right: the corresponding inner and outer wall temperature profiles. The peak flux ($\dot{q}'_{abs}$) of Case C3 and Case C4 is 588.91 kW/(m^2·K), and of the uniform flux (Case C1, Case C2 and Case C5) is 394.20 kW/(m^2·K). The outer diameter of the tube is 48.3 mm.

A study by Rodríguez-Sánchez et al. [95] shows that radiation losses are higher if the tube wall temperature variation is considered by applying view factors to the distribution of the circumferential incident flux. The result from that study agrees with the conclusion from the above analysis (compare Case C3 to C1 or compare Case C4 to C5), even though a different distribution of the absorbed flux is assumed in the above analyses, a cosine distribution. In addition, that study tells that the tube wall temperature variation is a big concern, if the rear temperature of the tubes is much lower than the front temperatures, as under this circumstance, $\overline{(T_{ext})^4}$ would be much greater than $\overline{T_{ext}}^4$ and it seems likely that this effect causes an under-estimation

Fig. C.6: Detailed $\dot{Q}'_{\text{ext,rad}}$ and $\dot{Q}'_{\text{ext,conv}}$ breakdown for high temperature liquid sodium Case C1, C2, C3, C4 and C5 at 740°C and the corresponding difference between cases. Units are in %.

Table C.4: Energy and exergy accounting for five cases with different flux profiles. HTF: air. $T_{HTF} = 479°C$. $d_o = 48.3$ mm, $t = 3.68$ mm. $CG = 640$ kW/m^2

	$\dot{Q}'_{inc}$ kW/m	$\dot{Q}'_{refl}$ kW/m	$\dot{Q}'_{abs}$ kW/m	$\dot{Q}'_{ext,rad}$ kW/m	$\dot{Q}'_{ext,conv}$ kW/m	$\dot{Q}'_{int}$ kW/m	η_I %	$\dot{X}'_{sun}$ kW/m	$\dot{X}'_{int}$ kW/m	$\eta_{I,rec}$ %
C1	30.91	1.00	29.91	2.982	1.477	25.450	82.34	28.83	15.53	53.87
C2	30.91	1.00	29.91	3.097	1.475	25.338	81.97	28.83	15.46	53.62
C3	30.91	1.00	29.91	3.123	1.475	25.312	81.89	28.83	15.45	53.58
C4	30.91	1.00	29.91	2.404	1.487	26.010	84.15	28.83	15.87	55.06
C5	30.91	1.00	29.91	1.973	1.494	26.448	85.56	28.83	16.14	55.98

of the radiative losses. However, in this study, uniform flux is applied on the whole receiver, which means the temperature difference between front and rear wall would be smaller when compared to non-uniform flux. This study shows that, for the cases in Chapter 2, the effect of considering view factors is more significant than circumferential wall variation. For non-uniform flux, the temperature difference between front and rear wall would be larger, imagining the peak flux is on the centre of the receiver and the cold fluid goes from the centre to the outer edges of the receiver.

Appendix D Python codes for a full uncertainty analysis (case: flat air test on the 30 May 2019)

```
import csv,itertools,os
import numpy as np
from collections import defaultdict
import xlrd
from xlwt import Utils
import datetime
import numpy as np
import sys, re
from uncertainties import ufloat,unumpy,nominal_value,std_dev,umath,wrap
import math
import colorama
from uncertainties import *

def bold(s):
    return colorama.Style.BRIGHT + s + colorama.Style.RESET_ALL

class Thermocouple:
    """Define an measurement error for Type K Class 2 thermocouple. Supplied
    values are assumed to be in kelvin.
    """
    def __init__(self,type="K2",cjc=2.5,tag=None):
        assert(type=="K2")
        self.tag = tag
        self.lowr = ufloat(0,2.5,tag="%s_lowr"%(tag)) # low-range absolute error
        self.highr = ufloat(1,0.0075,tag="%s_highr"%(tag)) # high-range relative error
        self.thresh = 333 + 273.15 # boundary value, K
        if isinstance(cjc,float):
            self.cjc = ufloat(0,cjc,tag="%s_cjc"%(tag)) # additional CJC uncertainty, in
  degrees
        else:
            self.cjc=cjc
    def __call__(self,val):
        if val > self.thresh:
            return (val - 273.15) * self.highr + 273.15 + self.cjc
        else:
            return self.lowr + val + self.cjc

    def __repr__(self):
        return "<Thermocouple(tag=%s)>"%(self.tag)

columns = defaultdict(list) # each value in each column is appended to a list
with open('BRRAC_Trend_Export_2019053010_2019053015_30s.csv') as f:
    reader = csv.DictReader(f,delimiter = "\t") # read rows into a dictionary format
    for row in reader: # read a row as {column1: value1, column2: value2,...}
        for (k,v) in row.items(): # go over each column name and value
            columns[k].append(v) # append the value into the appropriate list
                                 # based on column name k

data_1 = ['DNITr           ','TT_762TTr       ','TT_763TTr       ','MFM_701MFCTr
  ','Q_dot_in', 'Q_dot_net','Q_dot_loss','PT_702PTr       ','PT_703PTr       ','TT_704TTr
  ']
data_0 = ['DNI',r'T$_{\rm in}$',r'T$_{\rm out,TT763}$',r'$\dot m$',r'$\dot Q_{\rm in}$', r'$
  \dot Q_{\rm net}$',r'$\dot Q_{\rm loss}$',r'$\Delta (TT763-TT704)$']
data_a = {}

row = 10
col = 10
data_2 = []
data_b = {}
for c in xrange(0,col):
    for r in xrange(0,row):
        name = 'HelioControl_RT_R0%s_P%sTr ' %(r,c)
        data_2.append(name)

for i in xrange(0,4):
    data_a[i] = []
    for value in columns[data_1[i]][0:364]:
        if value == "n/a            ":
            x = data_a[i][-1]
            data_a[i].append(x)
        else:
            x = float(value)
            data_a[i].append(x)

for i in xrange(0,row*col):
    data_b[i] = []
    for value in columns[data_2[i]][0:364]:
        if value == "n/a                    ":
            x = data_b[i][-1]
            data_b[i].append(x)
        else:
            x = float(value)
```

```
            data_b[i].append(x)

for i in xrange(4,14):
    data_a[i] = []

for value in columns[data_1[9]][0:364]:
    if value == "n/a                ":
        x = data_a[12][-1]
        data_a[12].append(x)
    else:
        x = float(value)
        data_a[12].append(x)

T_in = 0.
T_out = 0.
mdot = 0.
Q_in = 0.
Q_net = 0.
Q_loss = 0.

CJC1 = ufloat(0,2.5)
CJC2 = ufloat(0,2.5)
TC_T_in = Thermocouple(tag="T_in",cjc=CJC1) #762&762 share one CJC
TC_T_out = Thermocouple(tag="T_out",cjc=CJC1)
TT704 = Thermocouple(tag="T_out",cjc=CJC2)
DNI_uncert = ufloat(1,0.02)
mdot_uncert = ufloat(1,0.01)
Q_in_uncert = ufloat(1,0.02)

for i in xrange(0,len(data_b[0])):
    Q_dot_in= 0.
    for rc in xrange(0, row * col):
        Q_dot_in = Q_dot_in + data_b[rc][i] * (1.296*1.296/row/col)
    T_in_1 = TC_T_in(data_a[1][i])
    T_out_1 = TC_T_out(data_a[2][i])
    mdot_1 = data_a[3][i]/3600. * mdot_uncert

    T_in = T_in + T_in_1
    T_out = T_out + T_out_1
    mdot = mdot + mdot_1
    Q_dot_in = Q_dot_in * Q_in_uncert
    Q_dot_net = (T_out_1 - T_in_1)* mdot_1 * 1.07
    Q_dot_loss = Q_dot_in - Q_dot_net
    delta_T = T_out_1 - TT704(data_a[12][i])

    DNI = data_a[0][i]*DNI_uncert

    data_a[4].append(Q_dot_in)
    data_a[5].append(Q_dot_net)
    data_a[6].append(Q_dot_loss)
    data_a[7].append(DNI)
    data_a[8].append(T_in_1)
    data_a[9].append(T_out_1)
    data_a[10].append(mdot_1)
    data_a[13].append(delta_T)
    Q_in = Q_in + Q_dot_in
    Q_net = Q_net + Q_dot_net
    Q_loss = Q_loss + (Q_dot_in - Q_dot_net)

data_a[0]=data_a[7]
data_a[1]=data_a[8]
data_a[2]=data_a[9]
data_a[3]=data_a[10]
data_a[7] = data_a[13]
Q_in = Q_in / len(data_b[0])
Q_net = Q_net / len(data_b[0])
Q_loss = Q_loss / len(data_b[0])

T_in = T_in / len(data_b[0])
T_out = T_out / len(data_b[0])
mdot = mdot / len(data_b[0])

print bold("\nExperimental observations")
print "\ndata point(s) = ", len(data_b[0])
print "T_in = %s degC" %T_in
print "T_out = %s degC" %T_out
print "mdot = %s kg/s" %(mdot)
print "Q_inc = %s kW" %Q_in
print "Q_net = %s kW" %Q_net
print "Q_loss = %s kW" %Q_loss

```

```
nominal = {}
std = {}
for i in xrange(0, 8):
    nominal[i] = unumpy.nominal_values(data_a[i])
    std[i] = unumpy.std_devs(data_a[i])
n_elements = np.arange(len(data_b[0]))
n_elements = np.linspace(10.0083, 13.0417,len(data_b[0]))

for i in xrange(0,11):
    data_a[i] = []

for i in xrange(0,4):
    for value in columns[data_1[i]][203:221]: #[166:189] [203:221]
        if value == "n/a            ":
            x = data_a[i][-1]  #last element
            data_a[i].append(x)
        else:
            x = float(value)
            data_a[i].append(x)

for i in xrange(7,10):
    data_a[i+4] = []
    for value in columns[data_1[i]][203:221]:
        if value == "n/a            ":
            x = data_a[i+4][-1]  #last element
            data_a[i+4].append(x)
        else:
            x = float(value)
            data_a[i+4].append(x)

for i in xrange(0,row*col):
    data_b[i] = []
    for value in columns[data_2[i]][203:221]:
        if value == "n/a                    ":
            x = data_b[i][-1]  #last element
            data_b[i].append(x)
        else:
            x = float(value)
            data_b[i].append(x)
T_in = 0.
T_out = 0.
mdot = 0.
Q_in = 0.
Q_net = 0.
Q_loss = 0.
DNI = 0.
for i in xrange(0,len(data_b[0])):
    Q_dot_in= 0.
    for rc in xrange(0, row * col):
        Q_dot_in = Q_dot_in + data_b[rc][i] * (1.296*1.296/row/col)
    T_in_1 = TC_T_in(data_a[1][i])
    T_out_1 = TC_T_out(data_a[2][i])
    T_out_1 = 51.62005 + 0.03016 * TT704(data_a[13][i]) + TT704(data_a[13][i])
    mdot_1 = data_a[3][i]/3600. * mdot_uncert

    T_in = T_in + T_in_1
    T_out = T_out + T_out_1
    mdot = mdot + mdot_1
    Q_dot_in = Q_dot_in * Q_in_uncert
    Q_dot_net = (T_out_1 - T_in_1)* mdot_1 * 1.07
    Q_dot_loss = Q_dot_in - Q_dot_net

    DNI =DNI + data_a[0][i]*DNI_uncert

    data_a[4].append(Q_dot_in)
    data_a[5].append(Q_dot_net)
    data_a[6].append(Q_dot_loss)
    data_a[7].append(DNI)
    data_a[8].append(T_in_1)
    data_a[9].append(T_out_1)
    data_a[10].append(mdot_1)
    Q_in = Q_in + Q_dot_in
    Q_net = Q_net + Q_dot_net
    Q_loss = Q_loss + (Q_dot_in - Q_dot_net)
data_a[0]=data_a[7]
data_a[1]=data_a[8]
data_a[2]=data_a[9]
data_a[3]=data_a[10]
Q_in = Q_in / len(data_b[0])
Q_net = Q_net / len(data_b[0])
Q_loss = Q_loss / len(data_b[0])
DNI  = DNI  / len(data_b[0])
```

```
242 T_in = T_in / len(data_b[0])
243 T_out = T_out / len(data_b[0])
244 mdot = mdot / len(data_b[0])
245
246 P_i = sum(data_a[11])/len(data_b[0])/100.+1
247 P_o = sum(data_a[12])/len(data_b[0])/100.+1
248 print bold("\nExperimental observations")
249 print "\ndata point(s) = ", len(data_b[0])
250 print "DNI = %s +/- %s W/m^2" % (unumpy.nominal_values(DNI), unumpy.std_devs(DNI))
251 print "T_in = %s +/- %s degC" % (unumpy.nominal_values(T_in), unumpy.std_devs(T_in))
252 print "T_out = %s +/- %s degC" % (unumpy.nominal_values(T_out), unumpy.std_devs(T_out))
253 print "mdot = %s +/- %s kg/s" % (unumpy.nominal_values(mdot), unumpy.std_devs(mdot))
254 print "Q_inc = %s +/- %s kW" % (unumpy.nominal_values(Q_in), unumpy.std_devs(Q_in))
255 print "Q_net = %s +/- %s kW" % (unumpy.nominal_values(Q_net), unumpy.std_devs(Q_net))
256 print "Q_loss = %s +/- %s kW" % (unumpy.nominal_values(Q_loss), unumpy.std_devs(Q_loss))
257 print "P_i = %s bar" % P_i
258 print "P_o = %s bar" % P_o
259
260
```